

NORTHWESTERN UNIVERSITY

Mechanical Properties and Microstructure of Al–Sc with Rare-Earth Element
or Al₂O₃ Additions

A DISSERTATION

SUBMITTED TO THE GRADUATE SCHOOL

IN PARTIAL FULFILLMENT OF THE REQUIREMENTS

for the degree

DOCTOR OF PHILOSOPHY

Field of Materials Science and Engineering

By

Richard Albert Karnesky, Jr.

EVANSTON, ILLINOIS

December 2007

© Copyright by Richard Albert Karnesky, Jr. 2007

All Rights Reserved

ABSTRACT

Mechanical Properties and Microstructure of Al–Sc with Rare-Earth Element or Al₂O₃ Additions

Richard Albert Karnesky, Jr.

Aluminum alloys strengthened with coherent (L1₂), nanosize Al₃Sc precipitates may be used as structural materials at elevated temperatures. They are creep resistant at 300°C and exhibit a threshold stress, below which creep is not measurable. Introducing ternary alloying additions, such as rare-earth elements (RE=Y, Dy, Er), that segregate within Al₃Sc precipitates improves this creep resistance by increasing the lattice parameter misfit of precipitates with Al. In this thesis, Al–600 Sc–200 RE and Al–900 Sc–300 Er (at. ppm) are studied. These elements are an order of magnitude less expensive than Sc, so reduce alloy costs. As an alternative or supplement to ternary additions, submicron (incoherent) Al₂O₃ dispersoids impart additional strengthening. The dispersion-strengthened cast alloys, DSC–Al–1100 Sc and DSC–Al–800 Sc–300 Zr, studied in this thesis contain 30 vol.% Al₂O₃.

The temporal evolution of Al–Sc–RE and DSC–Al–Sc(–Zr) alloys are measured using Local-Electrode Atom-Probe tomography, conventional transmission electron microscopy, and

electrical conductivity. These techniques measure the changes in precipitate number density, size, volume fraction, chemical composition, and interprecipitate distance and are compared to models. They are also employed to measure the diffusivity and maximum solubility of Er in α -Al in Al-300 Er, Al-450 Er, and Al-600 Er.

The mechanical behavior (microhardness, yield, and creep) of the alloys is studied at 25, 300, and 350°C. The effect of $\text{Al}_3(\text{Sc}_{1-x}\text{Er}_x)$ precipitate size and interprecipitate distance is studied by varying aging treatments. Various models and simulations are compared to experimental data. These include using experimentally-determined microstructures in a recent dislocation dynamics simulation and a novel model to explain the strengthening that is measured from both populations of strengthening phases in DSC-Al-Sc(-Zr).

Acknowledgements

In loving memory of Richard Albert Karnesky Sr.—father, metallurgical engineer, blacksmith, and friend.

This research was only possible through the guidance and support of my thesis advisors, Profs. David C. Dunand and David N. Seidman. I'd also like to thank my committee members, Profs. Horacio Espinosa and Chris Wolverton for their interest and enthusiasm about this work. Prof. Mark Asta (University of California, Davis) gave insight when on my qualifying committee. Profs. Georges Martin and Joe Jerome; as well as Drs. Dieter Isheim, Chantal K. Sudbrack, and Volker Mohles are thanked for our rewarding collaborations. Dr. Mike Miller and everyone at Imago Scientific deserve appreciation for their willingness to share thoughts and code.

Past and present group members have been nothing but both friendly and helpful. I'd especially like to thank Matt Krug and Drs. Keith E. Knipling and Marsha E. van Dalen for putting themselves into the same boat as me. Thanks also to Drs. Christian B. Fuller and Emmanuel A. Marquis, whose shoulders I stand on.

Many thanks to all family and friends! Beverly put up with living in the midwest so that she could share her love and support. Warm wishes to my mother, grandparents, and brothers; none of whom I see enough of. Thanks also to my “second family,” the Watrouses and to

David Olver and others at IL-855. Jason, Seth, Sue, Clayton, Cev, Ersan, and many others are thanked for long-time encouragement in my career path.

This research was supported by the United States Department of Energy, Basic Sciences Division, under contract DE-FG02-98ER45721. Financial support was also provided by a Walter P. Murphy Fellowship at Northwestern University.

Preface

This thesis examines the improvement of the mechanical properties of Al–Sc by adding rare-earth elements (RE=Y, Dy, and particularly Er (which is fully soluble in Al₃Sc)) and Al₂O₃ dispersoids. Novel strengthening models and atom-probe tomographic analysis techniques are presented.

Chapter 1 provides a short background about this study. Because the literature data for kinetic and thermodynamic variables (particularly the (temperature-dependent) diffusivity in α -Al and the solid solubility in α -Al) are missing, we measure these for the Al–Er binary system in chapter 2. Chapter 3 applies this to study the temporal evolution of the Al–Sc–RE ternary alloys. In chapter 4, a novel algorithm to measure the edge-to-edge interprecipitate distance distributions is presented and applied to Al–Sc–Er and simulated datasets. This quantity is important in predicting the time to reach stationary-state coarsening, as is shown in chapter 5 and in predicting alloy strength or validating the statistical accuracy of simulated obstacle fields, as in chapter 6. This latter chapter compares experimental yield measurements with dislocation dynamics simulations that have been informed by atom-probe tomography data. The study of Al–Sc–RE alloys is concluded in chapter 7, which presents the creep properties of these alloys at 300 °C. Chapter 8 discusses the strengthening

mechanisms at work in alloys that contain two populations of strengtheners: nanometer-sized, coherent $\text{Al}_3(\text{Sc}_{1-x}\text{Zr}_x)$ and submicron, incoherent Al_2O_3 . The work is summarized and possible further research is discussed in chapter 9.

The appendices cover:

- A:** The methodology of the best-fit ellipsoid method, which is used in Chapter 4, and its use in studying preferred orientation of coalesced/coagulated precipitates in Ni–Al–Cr
- B:** Quantification and propagation of error
- C:** Source code for chapter 4, the interprecipitate distance algorithm
- D:** Source code for chapter 8, the dual-strengthening creep model for dislocation detachment from an incoherent particle that is hindered by the additional backstress due to coherent precipitates
- E:** The computing facilities that the author setup for the Northwestern University Center for Atom-Probe Tomography
- F:** The details of the preparation of this thesis

Nomenclature

α	linear thermal expansion coefficient
α_β	parameter describing the geometry of a trailing dislocation, Eq. 6.2 (page 105)
\bar{R}	mean planar radius, Eq. 4.3 (page 80)
ΔC_i	difference in the equilibrium solubility of i in the precipitate and matrix phases
ΔC_i^α	supersaturation of component i in phase α
$\dot{\epsilon}$	strain rate, Eq. 1.1 (page 35)
$\gamma^{\alpha/\beta}$	interfacial free energy
γ_{APB}	anti-phase boundary energy
$\kappa_{i,KV}^\alpha$	coarsening rate constant for $\Delta C_i^\alpha(t)$ from KV model, Eq. 3.7 (page 69)
$\kappa_{i,LSW}^\alpha$	coarsening rate constant for $\Delta C_i^\alpha(t)$ from LSW model, Eq. 2.2 (page 49)
Λ	coarsening coefficient from KV model, Eq. 3.4 (page 67)
$\langle R \rangle$	mean radius
λ_{e-e}^{2D}	edge-to-edge interprecipitate spacing in a plane, Eq. 4.2 (page 80)
λ_{e-e}^{3D}	edge-to-edge interprecipitate spacing in three dimensions, Eq. 4.1 (page 79)
μ	shear modulus
ν	Poisson's ratio
ω_i	i^{th} moment of the precipitate size distribution
ϕ_{eq}	equilibrium volume fraction
σ	applied stress

σ_D	detachment stress for a dislocation to overcome an attractive interface
σ_{Or}	Orowan stress increment, Eq. 6.1 (page 104)
σ_{OS}	long-range-order stress increment, Eq. 6.2 (page 105)
σ_{th}	threshold stress, Eq. 1.3 (page 36)
τ_ε	lattice misfit stress, Eq. 8.5 (page 150)
τ_B	back stress that an array of precipitates exerts onto a dislocation
τ_i	strength increment, Eq. 8.3 (page 145)
τ_t	overall strength, Eq. 8.3 (page 145)
τ_μ	modulus misfit stress, Eq. 8.9 (page 151)
τ_{CRSS}	critically resolved shear stress
τ_{disloc}	stress due to other dislocation segments
τ_{drag}	viscous drag shear stress
τ_{ext}	externally applied shear stress
τ_{obst}	shear stress due to obstacles
ε	constrained lattice misfit, Eq. 8.6 (page 150)
ε'	unconstrained lattice misfit, Eq. 8.7 (page 150)
a	lattice parameter
B	bulk modulus
b	Burgers vector
C	concentration
C_i^α	concentration of component i in phase α
$C_i^{\alpha,eq}$	equilibrium concentration of component i in phase α
$C_i^{\alpha,ff}$	far-field concentration of component i in phase α

D	diffusivity
d	grain diameter
D_0	diffusivity prefactor
E_μ	modulus misfit energy
F_μ	modulus misfit force, Eq. 8.11 (page 151)
$G_{i,j}^\alpha$	partial derivative of the molar Gibbs free energy of the α phase
k_B	Boltzmann constant
K_{KV}	coarsening constant for $\langle R(t) \rangle$ from KV model, Eq. 3.1 (page 64)
K_{LSW}	coarsening constant for $\langle R(t) \rangle$ from LSW model, Eq. 2.1 (page 48)
L	root-mean-squared (RMS) diffusion distance, Eq. 5.4 (page 87)
M	mean Taylor matrix orientation factor
N	coarsening coefficient from KV model, Eq. 3.11 (page 72)
n	stress exponent, Eq. 1.1 (page 35)
N_a	Avogadro's number
N_V	number density of precipitates
p	grain size exponent
Q	activation energy
R_g	ideal gas constant
T	absolute temperature
t	time
t_0	initial time
t_c	minimum time required to reach a stationary state, Eq. 5.6 (page 88)
V_m	molar volume

Table of Contents

ABSTRACT	3
Acknowledgements	5
Preface	7
Nomenclature	9
List of Tables	16
List of Figures	18
Chapter 1. Introduction	27
1.1. Al ₃ Sc Precipitation Strengthened Alloys	27
1.2. Al ₂ O ₃ Dispersoid Strengthened Alloys	31
1.3. Creep Behavior	32
Chapter 2. Aging Behavior and Diffusivity of Al–Er Microalloys	39
2.1. Introduction	39
2.2. Materials and Experimental Methods	40
2.3. Results and Discussion	42
2.4. Conclusions	54
Chapter 3. Precipitate Coarsening in Al–Sc–Er	56

	13
3.1. Introduction	56
3.2. Experimental Methods	57
3.3. Results	58
3.4. Discussion	64
3.5. Conclusions	73
Chapter 4. Interprecipitate distances of Al–600 Sc–200 Er (at. ppm)	75
4.1. Introduction	75
4.2. Methods	76
4.3. Simulated Datasets	80
4.4. Experimentally Obtained Datasets	82
Chapter 5. How Long Does it Take to Achieve a Stationary State in the Solid State?	85
Chapter 6. Precipitation Strengthening in Al–900 Sc–300 Er:	
Experiments and Simulations	92
6.1. Introduction	92
6.2. Experimental Methods	94
6.3. Experimental Results and Discussion	96
6.4. Dislocation Dynamics Simulations	106
6.5. Conclusions	110
Chapter 7. Mechanical Properties of Al–Sc–RE at Ambient and Elevated Temperatures	113
7.1. Introduction	113
7.2. Experimental Methods	115
7.3. Results	118

	14
7.4. Discussion	120
7.5. Conclusions	130
Chapter 8. Strengthening Mechanisms in Aluminum Containing Coherent Al_3Sc Precipitates and Incoherent Al_2O_3 Dispersoids	131
8.1. Introduction	131
8.2. Experimental methods	134
8.3. Results	136
8.4. Discussion	143
8.5. Conclusions	154
Chapter 9. Summary and Future Work	156
References	159
Appendix A. Best-Fit Ellipsoids of Atom-Probe Tomographic Data to Study Coalescence of γ' (L1_2) Precipitates in Ni–Al–Cr	188
Appendix B. Error Analysis	197
B.1. Error Propagation	197
B.2. Least-Squares Fits	198
B.3. Errors in Creep Experiments	199
Appendix C. Source Code for Interprecipitate Distance Measurement	203
Appendix D. Source Code for Dual-Strengthening Creep Model	209
Appendix E. Computing Facilities of the Northwestern University Center for Atom-Probe Tomography	212

	15
E.1. Changes to Imago Computers	212
E.2. Workstations	215
E.3. Server	216
Appendix F. Colophon	226

List of Tables

1.1	Costs of Elements in 2003	29
2.1	Composition of Al–Er alloys as measured by DCP and LEAP	40
2.2	Al_3Er $\langle R \rangle$, $\langle C_{\text{Er}}^{\alpha,ff} \rangle$, and $\Delta C_{\text{Er}}^{\alpha}$ as a function of aging time at 300°C	47
2.3	Diffusion data for rare-earth elements in Al, $D_i(T) = D_0 e^{-\frac{Q}{R_g T}}$	53
3.1	$\text{Al}_3(\text{Sc}_{1-x}\text{Er}_x)$ ϕ , $\langle R \rangle$, and N_V as a function of aging time at 300°C	60
3.2	The Rate Constant, K (m^3s^{-1}) for Al–Sc–Er	66
3.3	The Rate Constant, κ (at. fr. $\text{s}^{\frac{1}{3}}$) for Al–Sc–Er	69
3.4	The Interfacial Free Energy, $\gamma_i^{\alpha/\beta}$ (J m^{-2}) for Al–Sc–Er	70
5.1	t_c compared to measured N_V time exponents	90
6.1	Material Constants Used in Yield Strength Models	104
7.1	Composition of Al–Sc–RE alloys as measured by DCP and LEAP	116
7.2	$\langle R \rangle$, σ_{th} , experimental and calculated σ_{Or} for Al–Sc–RE	126
8.1	Estimated $\langle R \rangle$, n_{ap} , and σ_{th} for DSC–Al(–Sc(–Zr)) creep experiments	142
B.1	Estimates of propagated error for common algebraic manipulations	198

B.2	Example creep data (for Al-600 Sc-200 Gd with $\langle R \rangle = 3.6 \pm 0.4$ nm precipitates [9])	201
-----	--	-----

List of Figures

1.1	Al-rich Al–Sc phase diagram	28
1.2	Lattice parameter as a function of the fraction of Sc replaced	30
1.3	Strain rate dependence on loading direction	34
2.1	Microhardness as a function of isochronal aging temperature for Al–Er, Al–Sc, and Al–Sc–Er alloys	44
2.2	Heterogeneous Al ₃ Er precipitation in of Al ₃ Er precipitates in an Al–450 Er alloy aged for 1,536 h (64 days) at 300°C (superlattice central-dark-field TEM micrograph)	46
2.3	Homogeneous Al ₃ Er precipitates ($\langle R \rangle = 17 \pm 6$ nm) in an Al–450 Er alloy aged for 1,536 h (64 days) at 300°C (superlattice central-dark-field TEM micrograph)	47
2.4	Log-log plot of Al ₃ Er mean precipitate radius as a function of aging time at 300°C	49
2.5	Far-field Er concentration in the α -Al matrix as a function of aging time at 300°C	50
2.6	Log-log plot of the supersaturation of Er in the α -Al matrix as a function of aging time at 300°C	51

		19
2.7	Diffusivity of the lanthanides at 300°C	52
3.1	Two-beam TEM micrographs of $\text{Al}_3(\text{Sc}_{1-x}\text{Er}_x)$ precipitates. In (a), the alloy aged at 300°C for 1,536 h (64 days) still has coherent precipitates, as observed by the Ashby-Brown strain-field contrast. Imaged in bright field along the [100] zone axis using the $\bar{1}11$ reflection. In (b), a high number density $((2.3 \pm 0.9) \times 10^{22} \text{ m}^{-1})$ of small ($\langle R \rangle = 3.7 \pm 0.9 \text{ nm}$) $\text{Al}_3(\text{Sc}_{1-x}\text{Er}_x)$ precipitates is observed after aging for 96 h (4 days). Central-dark-field image using the 110 superlattice reflection on the [100] projection.	59
3.2	Log-log plot of $\text{Al}_3(\text{Sc}_{1-x}\text{Er}_x)$ mean precipitate radius as a function of aging time at 300°C	60
3.3	Semilog plot of volume fraction, ϕ , of $\text{Al}_3(\text{Sc}_{1-x}\text{Er}_x)$ as a function of aging time at 300°C	61
3.4	Log-log plot of $\text{Al}_3(\text{Sc}_{1-x}\text{Er}_x)$ precipitate number density as a function of aging time at 300°C	62
3.5	Far-field Sc and Er concentration in the α -Al matrix as a function of aging time at 300°C	63
3.6	Log-log plot of the supersaturation of Sc and Er in the α -Al matrix as a function of aging time at 300°C	68
4.1	(a) A LEAP [®] tomographic reconstruction of an Al-600 Sc-200 Er (at. ppm) specimen that was homogenized at 640°C for 72 h and aged at 300°C for 24 h. Only Sc atoms are displayed for clarity. (b) The 260	

precipitates are fitted as ellipsoids [1] (c) A Delaunay mesh connects the precipitate centers. This is used to find “interacting precipitates” and to exclude the convex hull. 77

4.2 3D IDD for a simulated data set with an LSW PSD ($\langle R \rangle = 1$ a.u.) and various center-to-center distance distributions (with a mean distance of 10 a.u.). In both cases, $\langle \lambda_{e-e}^{3D} \rangle = 8$ a.u. (as predicted from Eq. 4.1) is preserved. (a) Precipitates on a cubic lattice (b) Precipitates randomly distributed according to algorithm in Ref. [2]. 81

4.3 3D IDD for the data set in Fig. 4.1. (a) IDD of all 3,682 Delaunay lengths, with $\langle \lambda_{e-e}^{3D} \rangle = 25$ nm. (b) Solid: IDD of nearest-neighbor distances for each precipitate that is not on the convex hull, which is sharper than when longer lengths are included ($\langle \lambda_{e-e}^{3D} \rangle = 7.5$ nm). Hollow: IDD of the most-distant Delaunay neighbor for each interior precipitate, which is broader than and slightly overlaps with the shortest distances ($\langle \lambda_{e-e}^{3D} \rangle = 38$ nm). 82

5.1 For a stationary state to be achieved, one constraint is that the diffusion length, L (Eq. 5.4) must exceed the interprecipitate spacing, λ_{e-e} (Eq. 5.5). It takes ca. 8 days for Al–600 Sc–200 Er (at. ppm) to meet this criteria (Eq. 5.6). 89

6.1 Electrical conductivity as a function of aging temperature during isochronal heat treatments for Al–1200 Sc and Al–900 Sc–300 Er. 97

- 6.2 Microhardness as a function of aging temperature during an isochronal heat treatment for Al-1200 Sc and Al-900 Sc-300 Er. 99
- 6.3 (a) A LEAP[®] tomographic reconstruction of an Al-900 Sc-300 Er (at. ppm) specimen that was homogenized at 640°C for 72 h, isochronally aged from 50–300°C in 50°C/2 h steps, and then isothermally aged at 300°C for 24 h. (b) Ellipsoidal fits to precipitates that can be used to measure the interprecipitate distance distribution (Chapter 4) to semi-quantitatively verify randomly generated microstructures. 100
- 6.4 A proximity histogram for the data set in Fig. 6.3, showing the concentration of Sc and Er as a function of distance from the α -Al/Al₃(Sc_{1-x}Er_x) heterophase interface, as defined by a 5 at.% isoconcentration surface. Er segregates to the core of precipitates. Concentration error bars are calculated as $\sigma_C = \sqrt{C(1-C)/N}$, where N is the total number of ions detected in a bin. 101
- 6.5 Microhardness as a function of aging time at 300°C after an isochronal heat treatment described in the text 102
- 6.6 Yield stress increment (as calculated from microhardness and compressive yield experiments) as a function of aging time at 300°C after an isochronal heat treatment described in the text 103
- 6.7 Yield stress increment as a function of precipitate radius. Microhardness, compressive yield, analytical equations, and computer simulations are compared. 105

6.8	Planar experimentally-determined precipitate array extracted from Fig. 6.3.	108
6.9	Simulated planar precipitate array, utilizing statistical information from Fig. 6.3.	111
7.1	Lattice parameter as a function of the fraction of Sc replaced	114
7.2	Microhardness as a function of aging time at 300°C for Al-600 at. ppm Sc-200 at. ppm RE. Error bars are one standard-deviation. The three alloys exhibit similar aging responses, with an incubation period that is followed by hardening, a plateau and then a decrease in microhardness. Al-600 Sc-200 Y has a higher mean peak microhardness than Al-600 Sc-200 Dy, which is harder than Al-600 Sc-200 Er. Al-600 Sc from Ref. [3, 4]	119
7.3	Experimental creep curve for Al-600 Sc-200 Dy aged at 300°C for 16 days ($\langle R \rangle = 5.1 \pm 0.5$ nm). Significant (over 2%) primary creep occurs before the secondary creep rate of $(5.4 \pm 0.1) \times 10^{-8}$.	120
7.4	Double-logarithmic plot of minimum compressive creep strain-rate vs. stress at 300°C for Al-600 at. ppm Sc-200 at. ppm RE. In the left plot, the average precipitate radius, $\langle R \rangle = 3$ nm. In the right plot, $\langle R \rangle = 5$ nm. For a particular size of precipitate, the alloy with the highest lattice parameter misfit between $\text{Al}_3(\text{Sc}_{1-x}\text{M}_x)$ and $\alpha\text{-Al}$ is more creep resistant. For any given alloy, the specimen with the larger diameter precipitates is more creep resistant. High apparent stress exponents are indicative of a	

- threshold stress, σ_{th} . The RE-containing alloys are significantly more resistant to creep than Al–Sc, Al–Sc–Mg, Al–Sc–Zr, and Al–Sc–Ti for a similar volume fraction of precipitates [3–7]. 121
- 7.5 Double-logarithmic plots of minimum compressive creep strain-rate vs. stress at 300°C for Al–900 at. ppm Sc–300 at. ppm Er and Al–600 Sc–200 RE that has been aged at 300°C for 1 day and then aged at 400°C for 1–5 days to coarsen precipitates. 122
- 7.6 Peak Vickers microhardness as a function of the lattice parameter misfit at ambient temperature with Al for Al–600 Sc–200 RE and Al–800 Sc alloys (after Fig. 7.2 and Ref. [8]). Differences in microhardness may be due to (a) precipitate volume fraction differences (as both Sm and Gd have lower solubilities in the Al_3Sc phase, so a reduced volume fraction (the misfit here is calculated at the maximum solubility)) and/or (b) greater resistance to precipitate shearing (directly due to misfit) and/or Orowan looping by dislocations (due to smaller precipitates). 123
- 7.7 Yield stress increment (calculated as Vickers microhardness increment divided by 3) as a function of precipitate size, compared with the calculated Orowan strengthening from Eq. 7.1 for Al–600 at. ppm Sc–200 at. ppm RE (RE=Y, Dy, Er). 124
- 7.8 Creep threshold stress, normalized by the calculated Orowan stress at 300°C, as a function of average precipitate radius, $\langle R \rangle$. Normalized stresses are higher for the three Al–Sc–RE microalloys than any of the previously studied Al–Sc–M alloys [3–7]. 127

- 7.9 Creep threshold stress, normalized by the calculated Orowan stress at 300°C, as a function of average precipitate radius, $\langle R \rangle$ compared with other Al–Sc–RE alloys where RE=Yb, Gd [9]. 129
- 8.1 Vickers microhardness as a function of aging time at (a) 300°C and (b) 350°C. The curves for the DSC–Al–Sc and DSC–Al–Sc–Zr were calculated from Eq. 8.3 with $k = 1.3$, using best-fit curves for DSC–Al, Al–Sc and Al–Sc–Zr. 137
- 8.2 Normalized electrical conductivity as a function of aging time at 300°C for (a) DSC–Al–Sc and Al–Sc and (b) DSC–Al–Sc–Zr and Al–Sc–Zr. 139
- 8.3 Stress dependence of minimum compressive creep strain rate at 300°C. (a) For DSC–Al, DSC–Al–Sc and DSC–Al–Sc–Zr, the latter two alloys being aged to achieve Al_3Sc and $\text{Al}_3(\text{Sc}_{1-x}\text{Zr}_x)$ precipitates with the same radius of ca. 3 nm. (b) For a DSC–Al–Sc sample subjected to three successive aging treatments to coarsen Al_3Sc precipitates (estimated as 3, 10 and 19 nm). DSC–Al curve is reproduced for comparison. 140
- 8.4 Creep threshold stress at 300°C as a function of estimated $\text{Al}_3(\text{Sc}_{1-x}\text{Zr}_x)$ radius for present DSC alloys as well as Al–Sc [3, 4] and Al–Sc–Zr alloys [5] (compositions in at.%). Lines show trends. 146
- 8.5 Schematic of Al_2O_3 dispersoid and $\text{Al}_3(\text{Sc}_{1-x}\text{Zr}_x)$ precipitates illustrating the geometry used in the model. (a) Projection perpendicular to the dislocation glide plane. A dislocation detaching from the departure side of the dispersoid is subjected to an applied resolved shear stress, τ , and a

back-stress, τ_B , imposed by an array of $\text{Al}_3(\text{Sc}_{1-x}\text{Zr}_x)$ precipitates. (b) Three-dimensional schematic, showing all 10 precipitates (3×3 planar array and additional precipitate) contributing to the back-stress on the dislocation. 149

8.6 Comparison between the calculated compressive back-stress (lines connecting individually calculated points) and the experimentally measured compressive threshold stress increments (large squares, found as difference between threshold stresses of DSC–Al–Sc(–Zr) and DSC–Al in Fig. 8.4) as a function of estimated precipitate radius. 153

A.1 The best-fit ellipsoid of a precipitate is determined in three steps: (i) for a reference set of axes (X_1, X_2 , and X_3), identify the x_1, x_2, x_3 coordinates of all atoms in a precipitate and its center of mass to obtain a moment of inertia tensor (L) (Eqs. A.1–A.3); (ii) the orientation of the principle axes (X'_1, X'_2 , and X'_3) of the ellipsoid axes construct a Jacobian transformation matrix that will diagonalize L . (iii) the lengths of the major and minor semi-axes of the best-fit ellipsoid are found from the eigenvalues of the transformed matrix. (Eq. A.4). 191

A.2 A representative data set for a Ni-5.2 Al-14.2 Cr (at.%) alloy, whose thermal history is discussed in the text. The coloring scheme matches that of Fig. A.1, with Ni atoms in green, Al atoms in red, and Cr atoms in blue. The atoms in the γ -matrix (FCC) are omitted for clarity. The

- gold colored best-fit ellipsoids indicate those γ' (L1₂) precipitates that are interconnected by necks. 193
- A.3 An FIM image, centered on the 002 pole, taken before APT analysis. The small square denotes the area and orientation for the data set in Fig. A.1. The larger square connects the 113 family of poles and the edges of this square give the [010] and [100] directions. 194
- A.4 An inverse pole figure for all interconnected γ' (L1₂) precipitates in this study, presented in the standard stereographic triangle. There is a preference for coagulation along and close to $\langle 110 \rangle$ -type directions, which is consistent with a diffusion controlled mechanism for coagulation.195
- B.1 Unweighted and weighted fits for the creep data presented in Table B.2. 201
- E.1 Schematic (not to scale) listing some specifications for NUCAPT computers (facility machines use black text). 213

CHAPTER 1

Introduction

Because of its low density, low cost, and high strength, aluminum and its alloys have been used in numerous engineering applications. The use of conventional precipitation-strengthened aluminum alloys are limited to below approximately 200°C because of the instability of their precipitates and GP zones, which coarsen and/or dissolve at higher temperatures [10]. Selecting precipitates or dispersoids that remain stable at higher use temperatures could improve energy efficiency in aerospace and transportation applications, and Al alloys could replace some of the more expensive and heavier Ti and Ni alloys that are currently in use.

1.1. Al₃Sc Precipitation Strengthened Alloys

Homogenized, dilute Al-Sc alloys (with Sc concentration below the maximum solubility of 0.23 at.% (Fig. 1.1)) can be aged to form a high number density of coherent L1₂ Al₃Sc precipitates that show negligible coarsening rates up to about 300°C [11–17]. Introducing ternary alloying elements that segregate within Al₃Sc precipitates can improve material properties while reducing alloy cost. Elements that increase the lattice parameter of the precipitates can improve lattice mismatch strengthening and elements that either decrease the lattice parameter and/or diffuse slowly in Al can delay coarsening.

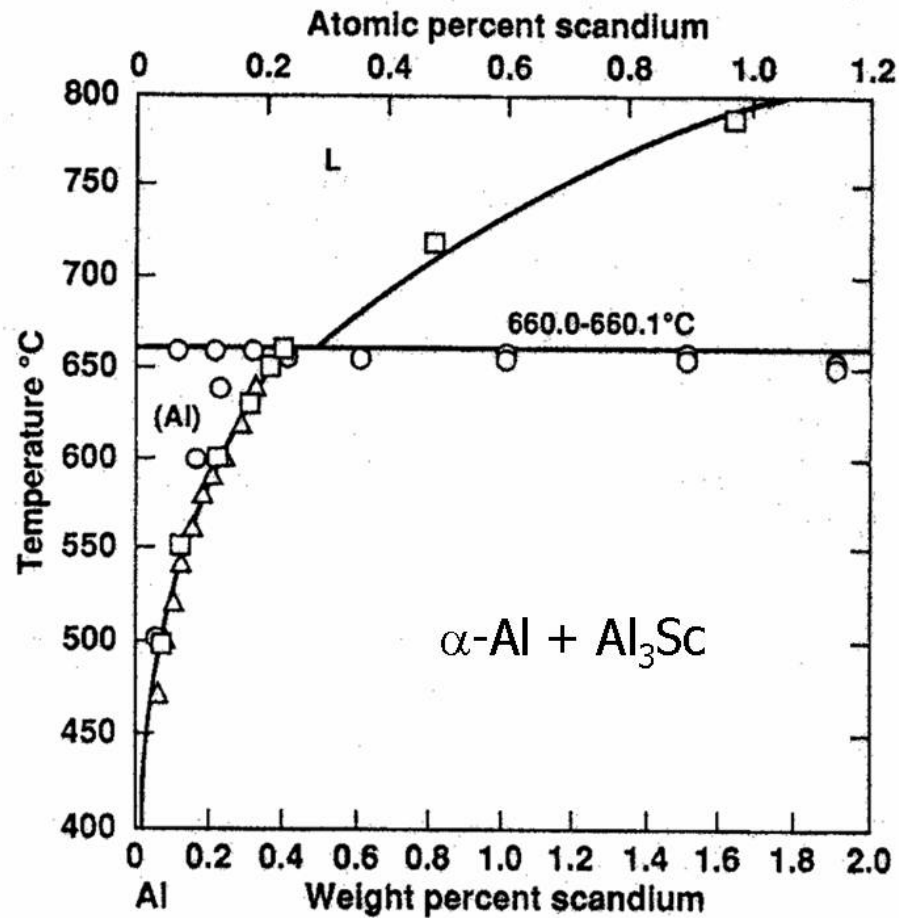


Figure 1.1. Al-rich Al-Sc phase diagram [11]

1.1.1. Zr Additions

Zr can substitute for Sc in precipitates, reducing costs (Table 1.1) and forming $\text{Al}_3(\text{Sc}_{1-x}\text{Zr}_x)$ precipitates with a smaller lattice parameter than Al_3Sc [25–28] (Fig. 1.2). Although this smaller lattice mismatch slightly decreases creep resistance, it also lowers the driving force for coarsening [5]. As the shallow slopes in Fig. 1.2 suggest, this effect is minimal. Furthermore, there is little Zr in the precipitates because Zr has a very small diffusivity in Al.

Table 1.1. Costs of Elements in 2003 [18, 19]

Element	Purity (%)	2003 Price (USD/kg)
Al		1.5
Sc	99.9–99.999	1,750–12,000
Zr		44
Dy	99–99.9	80–142
Er	99.9	160–295
Y	99–99.9	95–115
Gd	99.9–99.9999	225–450
Sm	99–99.9	55–65
Yb	99–99.9	180–320

This slow diffusion rate and the fact that Zr partitions to the precipitate interface blocks Sc diffusion, slowing coarsening even more.

The composite structure of $\text{Al}_3(\text{Sc}_{1-x}\text{Zr}_x)$ (with a large Sc-rich core, surrounded by a thin Zr-rich shell) has been studied using a variety of methods [28–33]. Kinetic Monte Carlo simulations suggest this is due merely to the diffusivity differences between Sc and Zr [31], although others have noted that the Zr-rich shell decreases the interfacial free energy and the lattice misfit between the $\text{Al}_3(\text{Sc}_{1-x}\text{Zr}_x)$ precipitate and the α -Al matrix [29].

1.1.2. Rare-Earth Additions

Several rare-earth (RE) elements are attractive as potential alloying additions. Table 1.1 indicates that REs are orders of magnitude less expensive than Sc. RE are fairly insoluble in Al ($< \approx 0.5$ at.%) [34–36], but are highly soluble in Al_3Sc (≈ 40 – 100 at.%) [20, 21] (Fig. 1.2), leading to strong partitioning to the precipitates. As indicated in Fig. 1.2, REs increase the lattice parameter of $\text{Al}_3(\text{Sc}_{1-x}\text{RE}_x)$ (by ≈ 0.002 – 0.007 Å per at.% RE in the precipitate) [20, 21, 37]. The larger lattice parameter mismatch will lead to greater creep

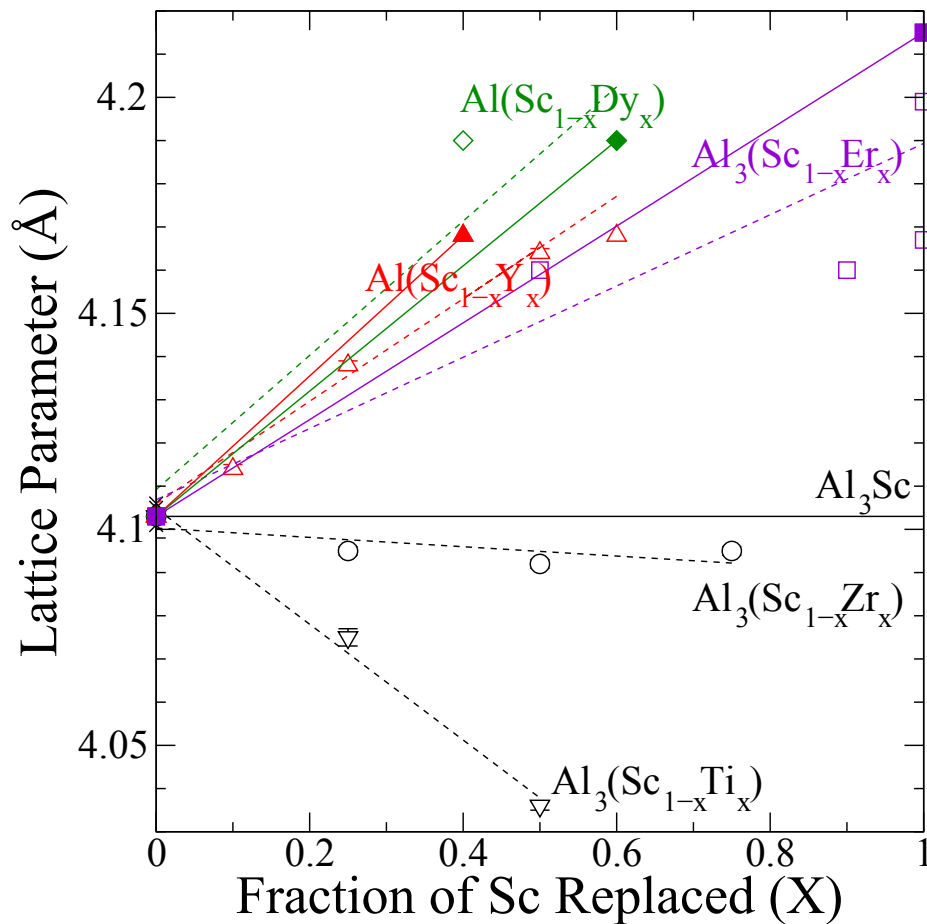


Figure 1.2. Lattice parameter as a function of the fraction of Sc replaced for the elements in this study. The REs have appreciable solubility in Al_3Sc (with Er having 100% solubility) and all increase the lattice parameter. Zr and Ti reduce the lattice parameter. Where two lines exist, the solid lines correspond to Refs. [20, 21] and the dashed lines correspond to fits applied to all available data [22–26].

strength [25, 26]. With the exception of Pr, the lighter lanthanides are also slower diffusers than Sc (by ≈ 1 –20 times at 300°C for La, Ce, Nd, and Sm [38, 39]), which may decelerate the coarsening of $\text{Al}_3(\text{Sc}_{1-x}\text{RE}_x)$ that would otherwise be accelerated due to the larger lattice

parameter mismatch. There is little diffusion data for the REs in this study, but the diffusivity of Er in Al is measured at 300 °C in Chapter 2.

Little research has been done on Al-Sc-RE systems. The research that has been published is very promising. Most US patents on Al-Sc alloys describe their room temperature strength or the superplasticity of the fine-grained alloy [22]. The only US patent on Al-Sc alloys for superior high temperature strength was granted to United Technologies Corporation (Hartford, CT) for alloys that contained some combination of Sc, Er, Lu, Yb, Tm and U [26]. Sawtell and Morris [23, 24] found that additions of 0.3 at.% Er, Gd, Ho, or Y improves the tensile strength of Al–0.3 at.% Sc alloys by ≈ 11 –23%. They note that the electronegativities of the REs are quite similar to that of Sc, so that they should have similar chemical behavior as Sc. The strengthening effects are therefore likely due to elastic effects of the larger REs. Smaller rare earths (with ionic radii < 0.176 nm) are still needed to create $L1_2$ -type precipitates (a notable exception is Yb, which has a radius of 0.179 nm, but still forms $L1_2$ precipitates).

1.2. Al_2O_3 Dispersoid Strengthened Alloys

For over three decades [40], ceramic particles have been introduced into aluminum alloy matrices. Using ceramic dispersoids leads to high strength, high stiffness, and improved wear and corrosion resistance. It is also less expensive to produce and easier to machine discontinuously reinforced aluminum than continuous fiber composites [41]. Although there is little agreement in the literature, “precipitates” will refer to nanosize intermetallic particles formed *in situ* after aging treatments of a supersaturated solid solution. “Dispersoids” will refer to submicron ceramic particles, typically (though not always) added *ex situ*.

Because the dispersoids remain stable, the service temperature for these composites can exceed 400°C. Dispersion strengthened aluminum can therefore be used in housings for rocket motors, the warm areas near turbine engines, and in other aerospace and automotive applications [42]. Creep resistance properties are important for many of these high temperature applications. Experiments and models have shown that dispersion strengthened aluminum is quite creep resistant and exhibit a threshold stress. The degree of creep resistance depends on several particle parameters, as well as on the matrix alloy [43].

1.3. Creep Behavior

At high temperatures, metals may deform through creep at constant applied stresses (or loads). The strain rate decreases with increasing time during primary creep, achieves and essentially maintains a steady-state minimum during secondary creep, and accelerates in tertiary creep until failure by creep rupture. The creep rate in each of these regions is dependent upon the loading direction, as is the duration of each region. The primary and tertiary stages, though still important, are less well documented than the secondary stage, which usually represents the stage that a structure will be subjected for the longest amount of time. The amount of primary creep is important in applications where total accumulated strain is a limiting factor. It is likely dependent on the grain size and the stress state of the composite. The secondary creep rate depends on the composition, method of incorporation, shape, size, volume fraction, and distribution homogeneity of the particles. The properties of the matrix alloy also contributes to it [43].

1.3.1. Dependence on Loading Direction Due to Cavitation

Creep specimens are loaded in either uniaxial tension, uniaxial compression, or shear. In metals and precipitation-strengthened alloys, creep damage (such as void formation or necking) generally only occurs during the late stages of creep (i.e. during the tertiary stage and very late in the secondary stage). Because of this, the creep response is generally independent of how the sample is loaded. This is not the case in dispersion strengthened alloys. Because tensile loading can cause cavitation, the tertiary stage starts earlier than it does in compressive loading. The primary and secondary regions both occur for a shorter duration. During secondary creep, tensile samples exhibit a higher strain rate at a given load than compressive samples. This effect was observed by both Pandey, Mishra, and Mahajan in Al-10 vol.% SiC [45] and Jansen and Dunand in Al-25 vol.% Al₂O₃ [44], as seen in Figure 1.3. It is likely that the magnitude of primary creep would also differ. Shear should also produce different results, and there is some evidence of this in the secondary creep rates reported in the literature.

Care must be taken when comparing the experimental results of dispersion strengthened alloys loaded in different conditions. Because of the effects of cavitation, tensile creep of these composites should be avoided unless attention is paid to the changing microstructure, particularly porosity.

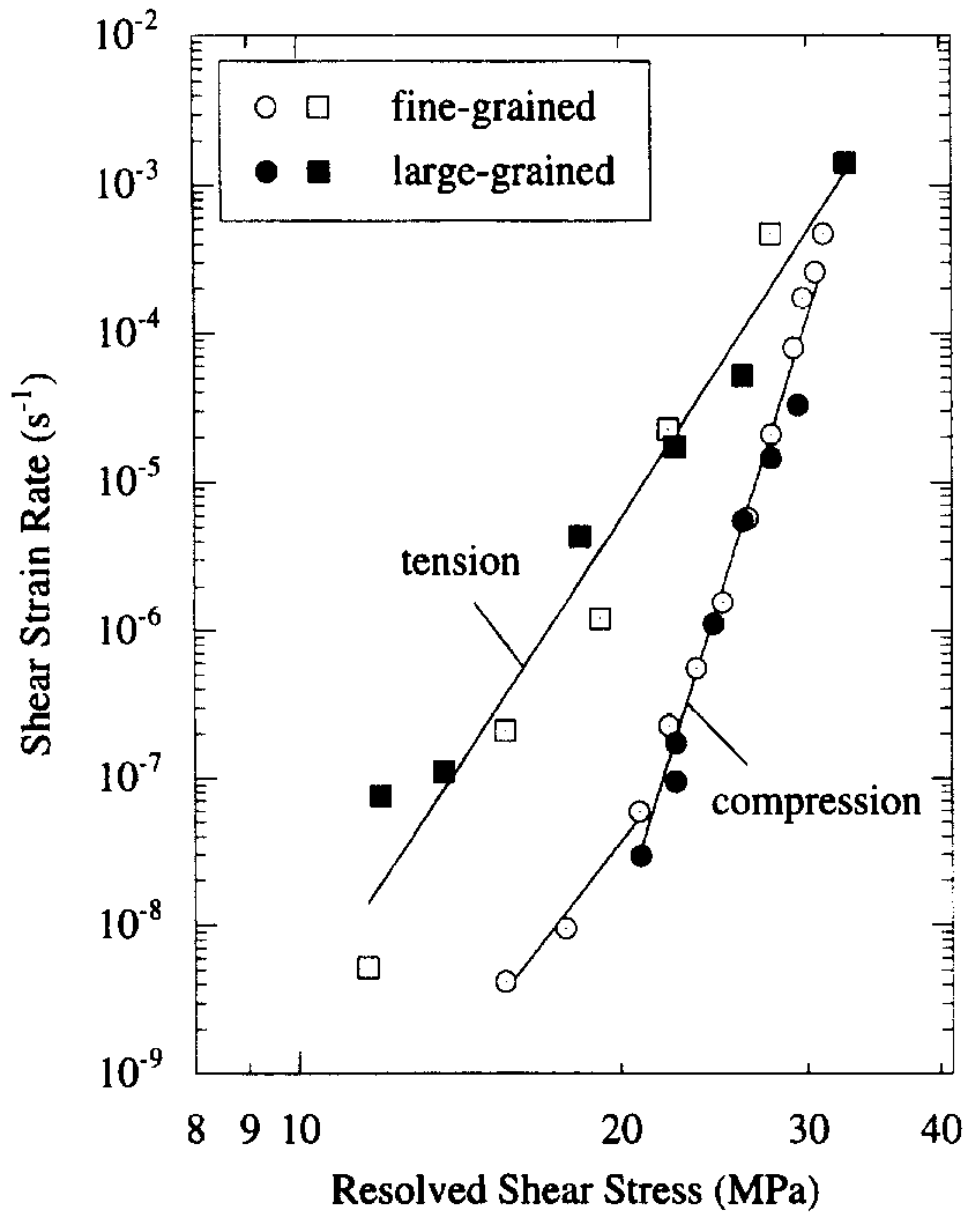


Figure 1.3. Strain rate dependence on the loading direction for Al-25 vol.% Al_2O_3 [44]. Note that tensile samples creep faster due to cavitation.

1.3.2. Secondary Creep

The secondary creep rate, $\dot{\epsilon}$, is usually described by the Mukherjee-Bird-Dorn equation [46]:

$$(1.1) \quad \dot{\epsilon} = A'_{ap} D_{ap} \frac{\mu b}{k_B T} \left(\frac{b}{d} \right)^p \left(\frac{\sigma}{\mu} \right)^{n_{ap}} ;$$

where subscript ap stands for “apparent,” A'_{ap} is a constant, D_{ap} is the appropriate (lattice or grain boundary) diffusion coefficient ($D_{ap} = D_{0_{ap}} \exp\left(-\frac{Q_{0_{ap}}}{R_g T}\right)$, with $D_{0_{ap}}$ being the prefactor, Q_{ap} the activation energy, R_g the ideal gas constant, and T the temperature), μ is the shear modulus, b is the Burgers vector, k_B is Boltzmann’s constant, d is the grain size, p is the grain size exponent, σ is the applied stress, and n_{ap} is the apparent stress exponent. For the ease of discussion, we reduce Eq. 1.1 to the power-law equation:

$$(1.2) \quad \dot{\epsilon} = A_{ap} \sigma^{n_{ap}} \exp\left(-\frac{Q_{ap}}{R_g T}\right);$$

with A_{ap} being a new dimensionless constant ($A_{ap} = A'_{ap} D_{0_{ap}} \frac{\mu b}{k_B T} \left(\frac{b}{d} \right)^p \mu^{-n_{ap}}$).

The value of the stress exponent in high temperature creep depends on the deformation mechanism. At low stresses, diffusional creep and/or Harper-Dorn creep are associated with the “true” stress exponent $n = 1$. At higher stresses and/or grain sizes, deformation occurs by dislocation creep. Dislocations move by either climb or glide, the slowest of the two processes being rate-controlling [47]. Thus, there are three possible values for the stress exponent in this regime: $n = 3$ for viscous glide [48, 49], $n \approx 5$ for dislocation climb controlled by lattice self diffusion (the true value is dependent on the stacking fault energy) [49, 50], and $n = 8$ for constant-structure climb [51, 52]. The experimentally determined exponent for pure aluminum is $n = 4.4$, which is between the model values for

glide and climb. At higher applied stresses, the stress exponent seems to become increasingly larger. This is power-law breakdown, and Eqs. 1.1–1.2 no longer apply [47].

Numerous studies of dispersion strengthened alloys have shown very large apparent stress exponents and apparent activation energies. This dilemma is resolved by introducing the threshold stress.

1.3.3. Threshold Stress

At applied stresses below the threshold stress, σ_{th} , creep is not measurable and Eq. 1.2 becomes:

$$(1.3) \quad \dot{\epsilon} = A(\sigma - \sigma_{th})^n \exp\left(-\frac{Q}{R_g T}\right).$$

The stress, σ_{th} , is not necessarily a “true” threshold, in the sense that at lower applied stresses there is no deformation — this would violate the second law of thermodynamics [53]. There are several ways to measure the threshold stress, and a few models of its origins.

1.3.3.1. Measurement Techniques. The threshold stress can be measured by extrapolation or linear regression. An older technique was to assume a linear superposition of the creep strength of the matrix and of the dispersoids and to estimate the value from a curved double-log plot of $\dot{\epsilon}$ vs. σ [53]. Li and Langdon rediscovered and formalized this technique by extrapolating the curves to and reading the stress at $\dot{\epsilon} = 10^{-10} \text{ s}^{-1}$ [54]. The choice of this strain rate is arbitrary, but approaches the resolution of a strain rate that is measurable in the laboratory. It would take over 3 years for 1% strain to accumulate at this rate. Finally,

extrapolating the non-linear curve is somewhat qualitative and requires data over several orders of magnitude of the strain rate.

The most common technique for finding σ_{th} is to divide the intercept by the slope employing a weighted least-squares linear regression of $\sqrt[n]{\dot{\epsilon}}$ vs. σ [55]. The matrix stress exponent n must be selected *a priori*, and there is no agreement in the literature as to which n to use. (A less common method of avoiding the choice of n is to perform a nonlinear regression analysis using A , σ_{th} , Q , and n as fitting parameters [56].) It is common to either choose n based on the most likely deformation mechanism or to try all reasonable values of n and use the one that gives the best fit. This is the most common technique in the literature. Arzt has attempted to make this process more consistent by normalizing the strain rate to the diffusivity and stress to Young's modulus, and by using the experimental value of n for the matrix alloy (e.g. $n = 4.4$ for aluminum) [53]. This normalization procedure has not been well utilized in the subsequent literature. Arzt also normalized the calculated threshold stress with respect to the calculated Orowan stresses [53]. This procedure is more commonly used, regardless of the method used to obtain the threshold stress.

Two possible mechanisms, and hence two classes of models, have been developed to explain the origin of the threshold stress. Dislocations must first climb over and then may have to detach from dispersoids. Climb models are analogous to those for precipitation-strengthened alloys. Detachment usually has a higher threshold stress in dispersion strengthened alloys, so is usually the controlling mechanism.

Because experimentally determined threshold stresses proved to be significantly lower than the Orowan stress, new models had to be developed to explain the origin of the threshold

stress. Because creep in alloys is generally climb-controlled (i.e. dislocations can quickly and freely glide until they encounter an obstacle, at which point they must climb, which is thermally activated), the early models attempted to model this process.

Early efforts were somewhat flawed. The local climb model assumed a sharp bend in the dislocation, which could be relaxed by diffusion. An equilibrium process, “general climb” was developed.

The general climb model has been successfully modified to include the stresses due to lattice and modulus mismatches of aluminum and a coherent precipitate [57]. Because the threshold originates from the lattice mismatch stress acting in opposition to climb over part of the precipitate, the model is not directly applicable to alloys strengthened with incoherent dispersoids.

Multiple transmission electron micrographs have shown what appears to be dislocations that have successfully climbed over but have adhered to the departure side of the dispersoid. This is explained by the attractive force exerted on a dislocation by the incoherent dispersoid. The controlling mechanism is then the thermally activated detachment from the interface. A model incorporating this concept has proven to be in good agreement with experimental data assuming large grain sizes and low volume fractions. Dunand and Jansen modified the model to work for higher volume fractions by accounting for dislocation pile-ups at the matrix-dispersoid interface. These pile-ups result in a shear stress that is added to the athermal detachment stress of an attached dislocation.

CHAPTER 2

Aging Behavior and Diffusivity of Al–Er Microalloys**2.1. Introduction**

Similar to Sc, Er forms stable and coherent ($L1_2$ structure) trialuminide precipitates [20]. Concentrations of 0.01–0.3 at.% Er are used as an alloying addition to both pure Al and many Al alloys (including Al–Sc, Al–Mg, Al–Cu, Al–Si, Al–Li, Al–Zn–Mg, and Al–Zn–Mg–Cu) [23, 24, 58–65]. In the more highly concentrated of these alloys, eutectic Al_3Er serves as a grain refiner, as in hypereutectic Al–Sc and peritectic Al–Zr alloys. As with the other $L1_2$ formers, nanometer-sized precipitates may form in the alloys upon heat treatment. These two features lead to increased ambient temperature microhardness and yield strength with no detriment to ductility.

The low solid solubility of Er in α -Al leads to small volume fractions of precipitates. However, it may be added as a ternary addition to Al–Sc alloys, which have higher precipitate volume fractions (Chapters 3–7). Erbium is fully soluble in the Al_3Sc phase ($L1_2$ structure) [20]. Replacing the more expensive Sc with Er decreases the cost of the alloy. Erbium also increases the lattice parameter of $Al_3(Sc_{1-x}Er_x)$ precipitates [21–24, 26]. This increased lattice parameter misfit with α -Al (from 1.4% for Al_3Sc to 5% for Al_3Er , as calculated at 0 K [66]) is thought to lead to a larger value of the creep threshold stress at elevated temperatures [57]. The larger lattice parameter misfit is expected to change the maximum precipitate radius that can be achieved while maintaining coherency, but the ratio of Sc to

Table 2.1. Composition of Al–Er alloys as measured by direct coupled plasma (DCP) spectroscopy and by LEAP tomography

Alloy	Er Content from DCP (at. ppm)	Er Content from LEAP tomography (at. ppm)
Al–300 Er	311 ± 8	292 ± 5
Al–450 Er	442 ± 8	453 ± 7
Al–600 Er	590 ± 8	—

Er and the aging treatments can be used to obtain an optimal combination of precipitate size and lattice parameter mismatch.

Despite this promise as an alloying element, much of the thermodynamic and kinetic information for Er in Al is still unknown. The eutectic temperature is 655°C, but the solid solubility at this temperature and the solvus curve for lower temperatures have not been determined [35]. This chapter presents measurements of the solubility of Er in Al at 640°C and at 300°C. The diffusivity of Er in α -Al is also not previously known, but we determined it at 300°C using measurements of the temporal evolution of the average precipitate radius, $\langle R(t) \rangle$, and the supersaturation of Er in α -Al.

2.2. Materials and Experimental Methods

Three alloys with compositions between 300–600 at. ppm Er were prepared, with their compositions measured by direct-current plasma (DCP) emission spectroscopy by ATI Wah Chang (Albany, Oregon) and by LEAP tomography, Table 2.1. The LEAP tomography measurement of the Er concentration for Al–600 Er is not reported in the table, as the technique does not measure large enough specimen volumes to accurately account for the Er that is in the eutectic precipitates that are present in the homogenized sample. The Er

concentration in α -Al for the alloy, as measured by LEAP tomography, is however reported below.

The alloys were dilution-cast in a zirconia-coated alumina crucible in a resistively-heated furnace at 750°C in air, using 99.999 at.% Al (the largest elemental impurity being 1 at. ppm Si, as confirmed by glow-discharge mass spectrometry conducted by Shiva Technologies (now the Evans Analytical Group) and an Al-1 at.% Er master alloy. This master alloy was produced by non-consumable electrode arc-melting from the same 99.999 at.% Al and 99.9 at.% Er, the latter supplied by Stanford Materials (Aliso Viejo, California). After thoroughly stirring, the melt was cast into either a graphite mold resting on a large copper platen (for the Al-300 Er alloy) or into a copper wedge with a 7° angle (for the Al-450 Er and Al-600 Er alloys); the Er values are in atomic parts per million. The copper wedge was used because solidification and cooling rates of the two more concentrated alloys are not sufficiently rapid when prepared in a graphite mold, as micron-sized eutectic precipitates are observed with scanning electron microscopy (SEM) at grain boundaries in the as-cast alloys when prepared in this manner.

All alloys were homogenized at 640°C (which is 15°C below the eutectic temperature) for 72 h (3 days) and water-quenched to ambient temperature.

Vickers microhardness measurements were conducted on isochronally aged specimens using a 200 g weight at ambient temperature on samples ground to a 1 μ m surface finish. The Al-300 Er alloy was aged isochronally in air in 50°C increments for 2 h each. All alloys were aged isochronally in 25°C increments for 1 h each in air. For terminal temperatures above 100°C, specimens were mounted in a quick-set acrylic. For lower aging temperatures

(including as-homogenized specimens), an epoxy mounting compound that sets at ambient temperature was used to prevent aging during the mounting procedure. The Al–1200 Sc and Al–900 Sc–300 Er alloys were also tested after this same aging treatment and are discussed at more depth in Chapter 6.

Transmission electron microscopy (TEM) and local-electrode atom-probe (LEAP) tomography were performed on specimens that were first aged at 50°C for 1 h, 75°C for 1 h, 100°C for 240 h (10 days), and then 300°C for between 24 h (1 day) and 1,536 h (64 days). TEM foils were mechanically ground to a thickness of ca. 200 μm and then electropolished in a solution of 5 vol.% perchloric acid in methanol that was cooled to -40°C in a methanol/dry ice bath. LEAP tomographic sample blanks were produced by mechanically grinding material to a square cross-section of ca. $200 \times 200 \mu\text{m}^2$. An initial electropolishing with a solution of 10 vol.% perchloric acid in acetic acid was followed by a final polishing with a solution of 2 vol.% perchloric acid in butoxyethanol. Three-dimensional tomographic reconstructions were obtained, using Imago's computer program IVAS and proximity histograms (proxigrams) [67] were calculated employing both IVAS and APEX software [68] to determine the far-field Er concentration in α -Al.

2.3. Results and Discussion

2.3.1. Solid Solubility at the Homogenization Temperature

Despite casting into a copper wedge, micron-sized precipitates were observed in the as-cast Al–600 Er alloy. This implies that the maximum solubility limit had been exceeded or that the rate of solidification and cooling was not rapid enough to keep Er in solution. This alloy was

homogenized at 640°C for 72 h (3 days) and water-quenched to ambient temperature. The α -Al matrix concentration from LEAP tomographic measurements is 0.0461 ± 0.006 at.%. This measured solubility is consistent with the eutectic precipitates that are observed in Al-600 Er, but not in Al-450 Er. Because the homogenization temperature is close to the eutectic temperature ($T/T_e = 0.98$), the maximum solid solubility is expected to not be significantly greater than this value. This concentration is 5 times smaller than the maximum solubility of Sc in Al (0.23 at.%) at the eutectic temperature of the Al-Sc system and 4 times smaller than the solubility of Sc at 640°C (0.18 at.%) [36, 69, 70]. The Al-450 Er alloy was selected for the isothermal coarsening study to maximize the precipitate volume fraction and to promote homogeneous precipitation (by maximizing the supersaturation of Er in α -Al).

2.3.2. Microhardness and Minimizing Heterogeneous Precipitation

The solid solubility of Er in α -Al is smaller at lower temperatures, thereby promoting homogeneous precipitation. However, the kinetics of precipitation are diminished. Isochronal aging promotes homogeneous nucleation at lower temperatures and allows the precipitates to grow and coarsen more rapidly at higher temperatures, permitting us to study the precipitation kinetics at 300°C.

Figure 2.1 displays the microhardness response to isochronal aging. The two curves for the different isochronal step sizes (50°C/2 h and 25°C/1 h) show reasonably good agreement as they use the same net heating rate. The Al-600 Er alloy shows a smaller peak microhardness value than the more dilute alloys. This may be related to the presence of eutectic precipitates, which may have been formed due to the solubility limit of Er in α -Al being exceeded

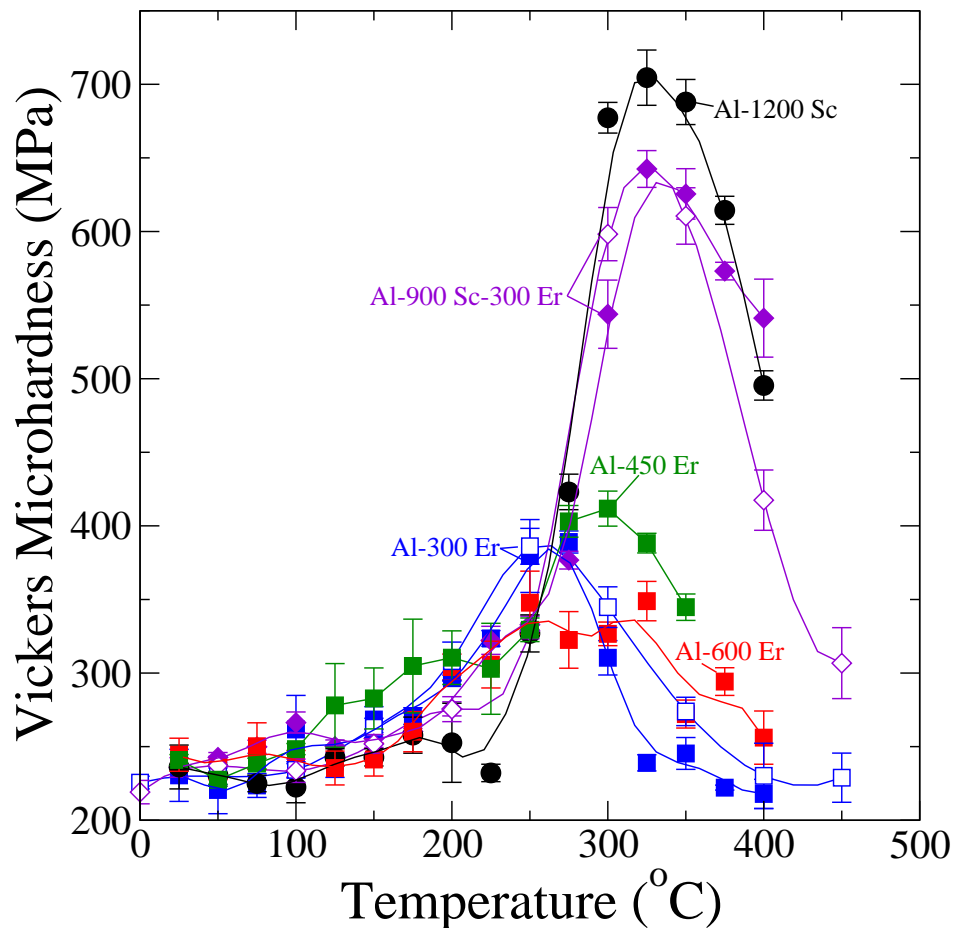


Figure 2.1. Microhardness as a function of isochronal aging temperature for Al–Er, Al–Sc, and Al–Sc–Er alloys. 2 h, 50°C steps are hollow and 1 h, 25°C steps are filled. There is reasonable agreement in the two treatments for any particular alloy. The Er binary alloys peak before the Sc-containing alloys (discussed more in Chapter 6), implying a smaller activation energy for precipitate growth.

or because of different solidification or cooling kinetics. The cause of the smaller peak microhardness is not studied, as it is the kinetics of homogenized alloys (with Er content less than the solid solubility of Er in α -Al at the homogenization temperature) is of interest.

An incubation period is observed at lower temperatures, which is short for the Er-containing alloys that exhibit hardness increases as low as 100°C. The Al–1200 Sc binary exhibits a longer incubation time, despite the higher solute concentration. Additionally, the Al–Er binary alloys achieve peak hardness between 250–300°C, which is at a lower temperature than the aging peak at 325–350°C in the Sc-containing alloys (see Chapter 6). These results suggest that Er might have a lower activation enthalpy for diffusion than Sc, which is consistent with the lighter REs (Table 2.3). After the aging peak, the microhardness values immediately decrease, as shear-resistant precipitates grow and coarsen.

Precipitates were found heterogeneously distributed on dislocations in specimens isochronally aged to 300°C. They were larger (having mean radius values, $\langle R \rangle > 30$ nm) than precipitates farther away from the dislocations, which appeared to have been homogeneously precipitated. To further promote homogeneous precipitation, the Al–450 Er alloy was isochronally aged up to 100°C (the temperature for which a microhardness response is first observed) and held at 100°C for 240 h (10 days) prior to aging at 300 °C. Despite this treatment, there was a small amount of heterogeneous nucleation, as can be observed in Fig. 2.2. The Akaiwa-Voorhees model for coarsening demonstrates that there is a screening distance, beyond which precipitates do not have significant interactions [71]. Using a volume fraction of 0.2% (close to the estimated volume fraction of 0.14%), the screening distance was calculated to be about $40\langle R \rangle$ [72]. For longer aging times, precipitates at this distance away from precipitate-free zones are not observed with TEM. Precipitates from multiple locations were, however, measured and found to be in agreement.

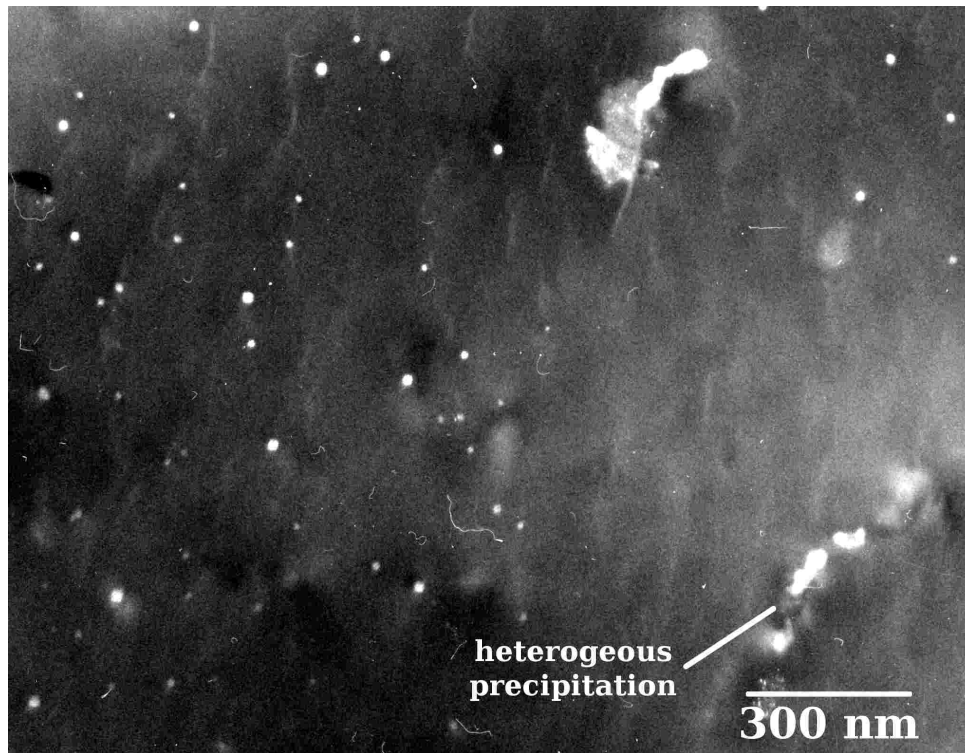


Figure 2.2. Superlattice central-dark-field TEM micrograph of Al_3Er precipitates in an Al-450 Er alloy aged for 1,536 h (64 days) at 300°C after an aging treatment described in the text. There are heterogeneously distributed precipitates and precipitate free zones, in addition to the smaller, more homogeneously distributed precipitates. Imaged using the 110 superlattice reflection for the [100] projection.

2.3.3. Temporal Evolution of Al_3Er

The size of Al_3Er precipitates in Al-450 Er was measured as a function of aging time using super-lattice dark-field imaging (Fig. 2.3). The precipitates grew from having an initial average radius, $\langle R \rangle = 3.9 \pm 0.9$ nm after 24 h (1 day) to $\langle R \rangle = 17 \pm 6$ nm after 1,536 h (64 d), as shown in Table 2.2 and in Fig. 2.4. The coarsening models developed by Lifshitz

Table 2.2. Al_3Er precipitate average radius, Er far-field concentration in the $\alpha\text{-Al}$ matrix, and Er matrix supersaturation in an Al-450 at. ppm Er alloy as a function of aging time at 300°C after being aged at lower temperatures, as described in the text.

Aging Time (h)	$\langle R \rangle$ (nm)	$\langle C_{Er}^{\alpha,ff} \rangle$ (10^{-6} at. fr. Er)	ΔC_{Er}^{α} (10^{-6} at. fr. Er)
24	4 ± 1	30 ± 8	26 ± 11
96	6 ± 2	24 ± 7	20 ± 10
384	10 ± 3	17 ± 6	13 ± 9
1,536	17 ± 6	8 ± 4	4 ± 7

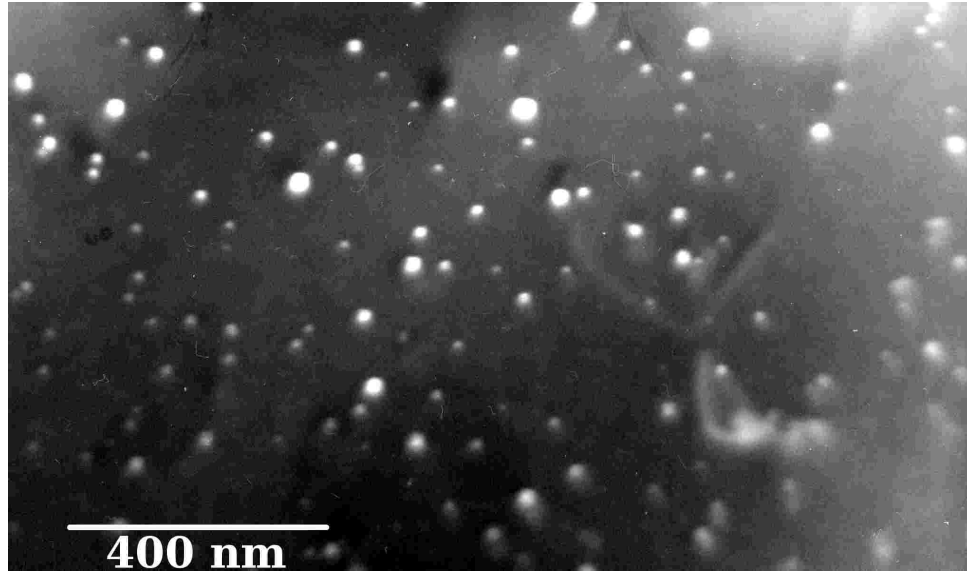


Figure 2.3. Superlattice central-dark-field TEM micrograph of Al_3Er precipitates in an Al-450 Er alloy aged for 1,536 h (64 days) at 300°C after an aging treatment described in the text. The precipitates have a mean radius of $\langle R \rangle = 17 \pm 6$ nm and were imaged using the 110 superlattice reflection on the $[100]$ projection.

and Slyozov [73] and Wagner [74] (abbreviated as LSW) predict:

$$(2.1) \quad \langle R(t) \rangle^3 - \langle R(t_0) \rangle^3 = K_{LSW} (t - t_0)$$

for binary alloys, where K_{LSW} is a system-dependent coarsening constant. Assuming that $\langle R(t_0) \rangle$ and t_0 are negligible, a regression of $\langle R(t) \rangle = (Kt)^n$ to the data was performed. The time exponent, n , was found to be 0.36 ± 0.03 , which is in good agreement with the model exponent of $\frac{1}{3}$. The coarsening constant, K , was determined to be $(2 \pm 1) \times 10^{-31} \text{ m}^3\text{s}^{-1}$, which is ca. 26 times larger than the model K_{LSW} for Al–Sc and an order of magnitude larger than the experimentally measured K for Al–Sc alloys at 300°C and two orders of magnitude larger than the model values for Al–Sc at 300°C [75]. In conjunction with the time exponents, this means that Al_3Er precipitates in Al–Er coarsen faster than Al_3Sc precipitates in Al–Sc.

The Er concentration in α -Al was measured by LEAP tomography in Al–450 Er. Due to the small sampling volumes inherent in this technique (the diameter of the analyzed volume is only 50–100 nm) and the possible heterogeneous distribution of Er in the alloy, data sets that had one or more nanometer-scale precipitates (the size of which is consistent with what is measured by TEM) in the volume were used. Due to the low concentration of Er in the alloy and the fact that Er has six isotopes (not including possible hydrides), background subtraction was critical to obtain accurate measurements. The proxigram was used to measure the far-field concentration of Er in the α -Al matrix, $C_{Er}^{\alpha,ff}$. The concentration systematically decreases from $C_{Er}^{\alpha,ff} = (30 \pm 8) \times 10^{-3}$ at.% Er (30 ± 8 at. ppm Er) after 24 h (1 day) to $C_{Er}^{\alpha,ff} = (8 \pm 4) \times 10^{-4}$ at. % Er (8 ± 4 at. ppm Er) after 3840 h (64 days) (Table 2.2 and Figs. 2.5–2.6). The supersaturation of element i in phase α is given by $\Delta C_i^\alpha(t) = \langle C_i^{\alpha,ff}(t) \rangle - C_i^{\alpha,eq}(\infty)$ (where $C_i^{\alpha,eq}$ is the equilibrium concentration of element

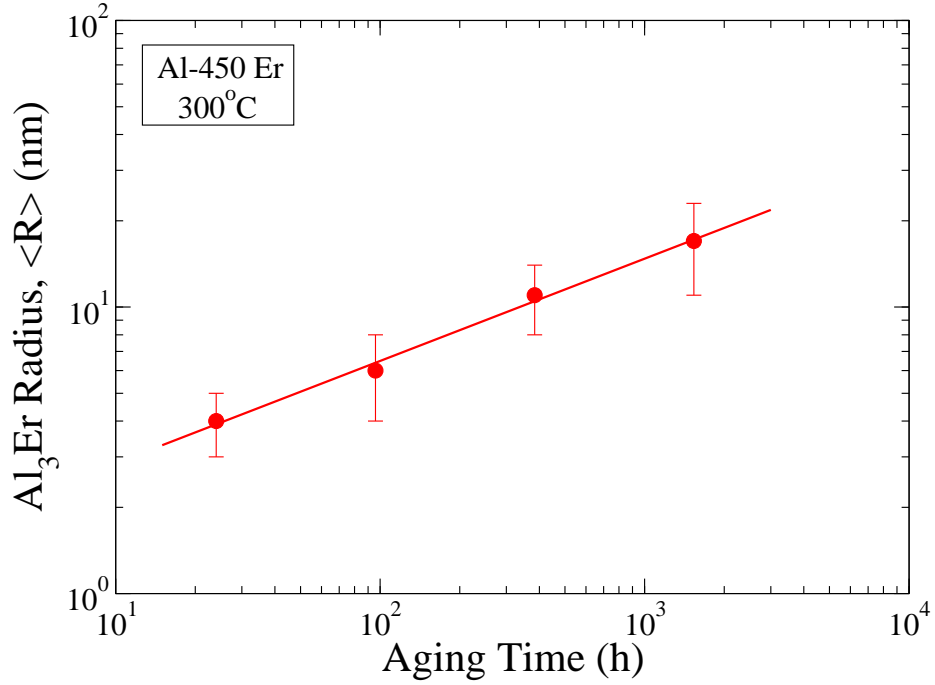


Figure 2.4. Log-log plot of Al₃Er mean precipitate radius, $\langle R \rangle$, as a function of aging time at 300°C after aging at lower temperatures, as described in the text. The quantity $\langle R \rangle$ coarsens with a time exponent of 0.36 ± 0.03 , in good agreement with the LSW model's value of $\frac{1}{3}$ (Eq. 2.1).

i in phase α). The LSW model predicts that this varies as:

$$(2.2) \quad \Delta C_i^\alpha(t) = \kappa_{i,LSW}^\alpha (t)^{-\frac{1}{3}};$$

where $\kappa_{i,LSW}^\alpha$ is a system-dependent coarsening constant. Because there is no theoretical or previously obtained experimental data for $C_{Er}^{\alpha,eq}$, it was obtained by fitting Eq. 2.2 to the experimental data (assuming the model time exponent of $-\frac{1}{3}$), as in Fig. 2.5, to be $(4 \pm 3) \times 10^{-4}$ at.% Er (4 ± 3 at. ppm Er). The temporal evolution of the supersaturation

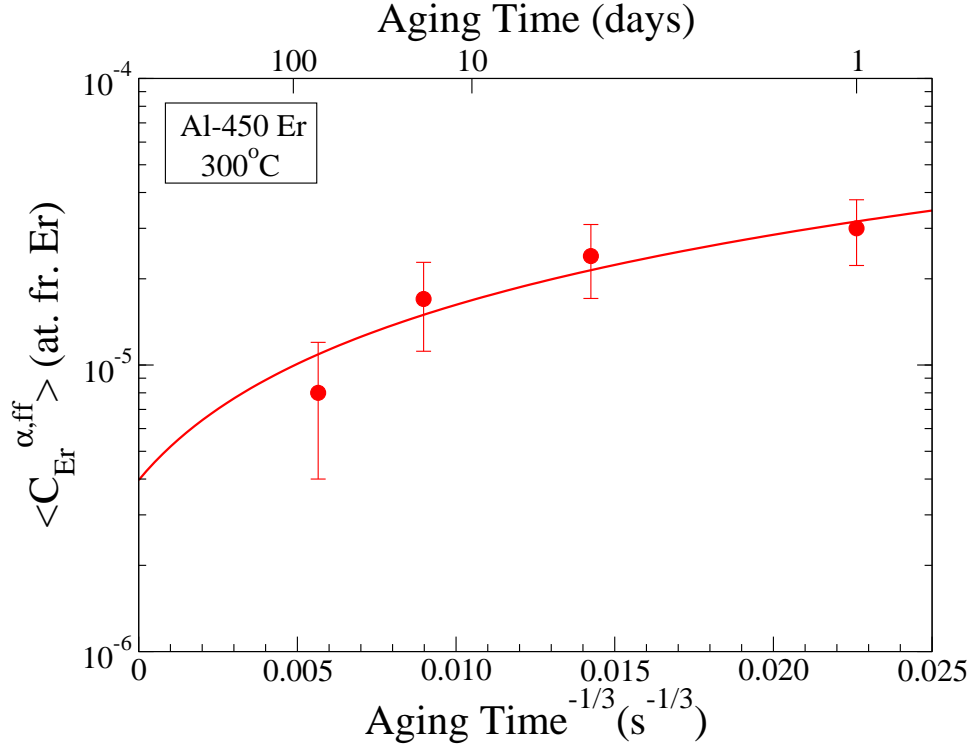


Figure 2.5. The far-field Er concentration, $\langle C_{Er}^{\alpha,ff} \rangle$, in the α -Al matrix as a function of aging time at 300°C (after aging at lower temperatures to nucleate precipitates, as described in the text). The concentration steadily decreases with increasing aging time and the y-intercept of the fitting line (Eq. 2.2 gives the solid solubility of Er in Al at 300°C. $C_{Er}^{\alpha,eq} = (4 \pm 3) \times 10^{-4}$ at. % Er (4 ± 3 at. ppm Er).

is given in Table 2.2 and in Fig. 2.6. A least-squares linear regression was made on log-transformed data in order to test how well the calculated supersaturation obeyed the $-\frac{1}{3}$ time exponent and to obtain a refined measurement of κ_{Er}^{α} . The time exponent is found to be -0.30 ± 0.09 , which exhibits good agreement with the LSW model and confirms that the $C_{Er}^{\alpha,eq}$ remains self-consistent with the refined fitting procedure. The regression analysis yields $\kappa_{Er}^{\alpha} = (1.1 \pm 0.9) \times 10^7$ at. fr. Er s⁻¹.

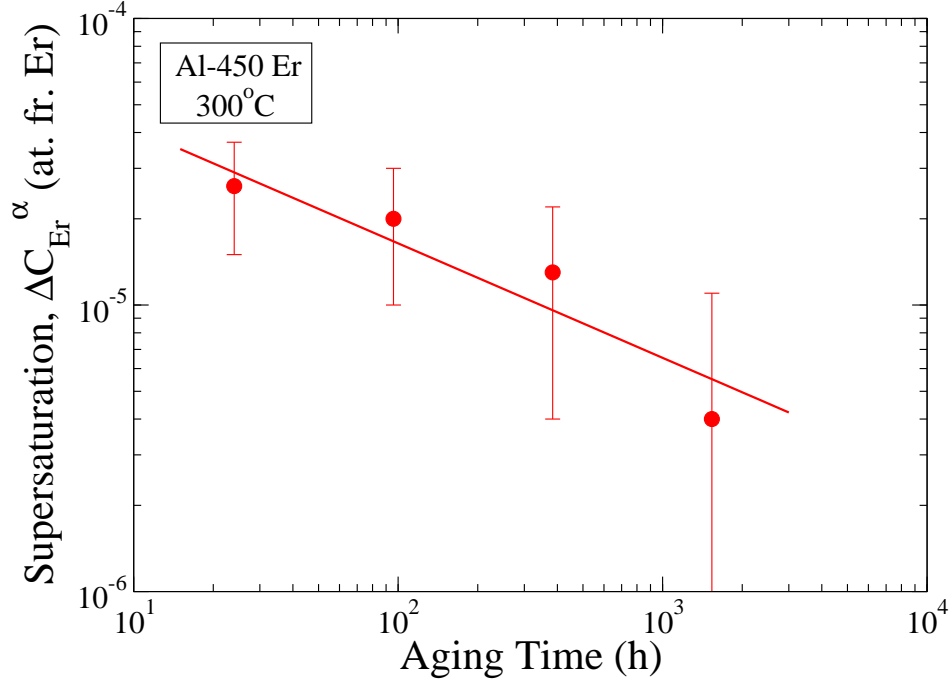


Figure 2.6. Log-log plot of the supersaturation of Er, ΔC_{Er}^{α} , in the α -Al matrix as a function of aging time at 300°C (after aging at lower temperatures to nucleate precipitates, as described in the text). The solid solubility of Er in α -Al is determined from Fig. 2.5 and a second refinement was made to fit the coarsening prefactor and time exponent. The supersaturation steadily decreases with aging with a time exponent of -0.30 ± 0.09 , in agreement with the LSW model and the first fit.

2.3.4. Er Diffusivity in Al at 300°C

Ardell showed that the diffusivity, D , at the aging temperature is related by the K and κ coarsening coefficients [76, 77]. Assuming a quasi-stationary state:

$$(2.3) \quad D_i^{\alpha} = \frac{9(C_i^{\beta,eq} - C_i^{\alpha,eq})}{4} (K^2 \kappa_i^{\alpha})^{\frac{1}{3}}.$$

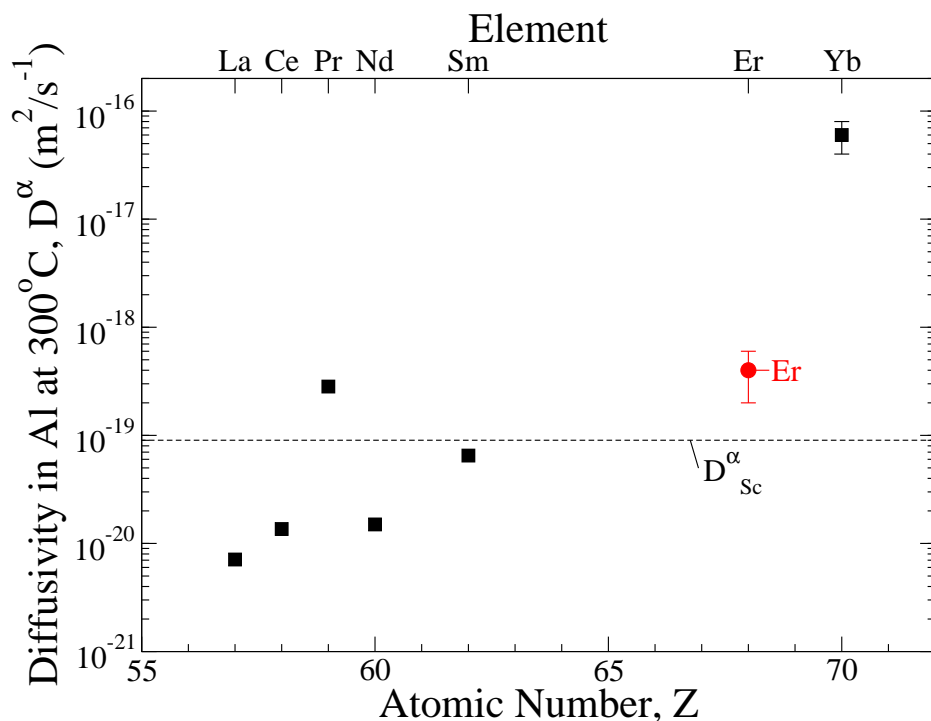


Figure 2.7. Diffusivity of the lanthanides at 300°C

Using the experimentally determined values for K and κ_{Er}^α , D_{Er}^α at 300°C is $(4 \pm 1) \times 10^{-19} \text{ m}^2\text{s}^{-1}$.

Similar to Pr and Yb but unlike the other rare-earth elements for which diffusivity data is known, Er is a faster diffuser in Al at 300°C than Sc (Table 2.3 and Fig. 2.7). At 300°C, it is measured to have approximately the same diffusivity as Pr, half of an order of magnitude larger than the diffusivity of Sc, and two orders of magnitude smaller than the diffusivity of Yb. The similarity of Er's diffusivity to the other lanthanides and the very large diffusivity of Yb in Al are consistent with the physical properties of the lanthanides, which depend upon bonding. Ytterbium has a low melting temperature (824°C) compared with Er (1497°C) and the other lanthanides (which increase from 920–1545°C with increasing Z number, with the

Table 2.3. Diffusion data for rare-earth elements in Al, $D_i(T) = D_0 e^{-\frac{Q}{R_g T}}$

Element	Technique	Temperature Range (°C)	D_0 (m^2s^{-1})	Q (kJ mol^{-1})	D_i at 300°C (m^2s^{-1})	Source
Sc	residual activity	540–655	5.31×10^{-4}	173	9.01×10^{-20}	[39]
La	residual activity	500–630	1.40×10^{-10}	110	7.1×10^{-21}	[38, 78]
Ce	residual activity	450–630	1.90×10^{-10}	111	1.36×10^{-20}	[38, 78]
Pr	residual activity	520–630	3.58×10^{-10}	99.87	2.83×10^{-19}	[38, 78]
Nd	residual activity	450–630	4.80×10^{-11}	100	1.4×10^{-20}	[38, 78]
Sm	residual activity	450–630	3.45×10^{-11}	95.73	6.50×10^{-20}	[38, 78]
Er	precipitate coarsening	300	—	—	$(4 \pm 2) \times 10^{-19}$	This Work
Yb	precipitate coarsening	300	—	—	$(6 \pm 2) \times 10^{-17}$	[9]

exceptions of Ce (795°C), Eu (826°C), and Yb). The crystal structures of Yb (F.C.C.) and Eu (B.C.C.) are also different from the rest of the lanthanides (all others are H.C.P except Sm (trigonal)).

2.4. Conclusions

This study of the aging behavior of Al–Er microalloys aged at 300°C (after pre-aging at lower temperatures to enhance homogeneous nucleation of Al₃Er) yields thermodynamic and kinetic parameters that can aid in understanding Er's role as an addition in both present and future Al alloys.

- The solid solubility of Er in Al at 640°C (only 15°C below the eutectic temperature) is found to be 0.0461 ± 0.006 at.%, which is 4 times smaller than that of Sc at 640°C.
- Microhardness measurements throughout an isochronal heat treatment demonstrate that Al–Er alloys age harden due to precipitation and that the kinetics of precipitation are faster at lower temperatures than Al–Sc alloys.
- The evolution of the mean precipitate radius, $\langle R \rangle$, with aging time at 300°C obeys the LSW coarsening model with a time exponent of 0.36 ± 0.03 a rate constant value, $K = (2 \pm 1) \times 10^{-31} \text{ m}^3\text{s}^{-1}$.
- Using LEAP tomography, the maximum solid solubility of Er in Al at 300°C, $C_{Er}^{\alpha,eq}$, is found to be $(4 \pm 3) \times 10^{-4}$ at.% Er (4 ± 3 at. ppm Er).
- Using the previous finding, the supersaturation of Er in α -Al obeys the LSW model with a time exponent of 0.30 ± 0.09 and $\kappa_{Er}^{\alpha} = (1.1 \pm 0.9) \times 10^7 \text{ at. fr. Er s}^{-1}$.

- Using these latter two findings, the diffusivity of Er in α -Al at 300°C is calculated to be $(4 \pm 2) \times 10^{-19} \text{m}^2 \text{s}^{-1}$, which is half an order of magnitude larger than that of Sc and two orders of magnitude slower than that of Yb in α -Al.

CHAPTER 3

Precipitate Coarsening in Al–Sc–Er**3.1. Introduction**

Because Al–Sc alloys are candidates for high temperature (300–400°C) use [5–7, 57, 79–83] (Chapters 7–8), the coarsening behavior of precipitates in these alloys is of great scientific and technological interest. Binary Al–Sc alloys coarsen in approximate agreement with the LSW coarsening model [73, 74] when aged at 300°C and above. Experimentally measured time exponents for the average precipitate radius vary between 0.18 [75, 84] and 0.5, with many researchers reporting the model value of $\frac{1}{3}$ [15, 75, 85–88]. The change in the matrix supersaturation of Al–Sc has been studied between 400–500°C, and this data has been used to calculate independently the diffusivity of Sc in α -Al and the interfacial free energy [88]. The impact of additional alloying elements on Al–Sc has also been studied. In ternary systems, the Kuehmann-Voorhees (KV) modifications to coarsening models [89] should be used, but are sometimes neglected. Mg is a solid-solution strengthener that is found to decrease the coarsening rate of Al_3Sc precipitates [84, 90]. Zr substitutes for Sc on the L1_2 Al_3Sc precipitate sublattice. These $\text{Al}_3(\text{Sc}_{1-x}\text{Zr}_x)$ precipitates exhibit very slow coarsening kinetics due to the very small diffusivity of Zr in α -Al, which segregates to the shell of core-shell precipitates [28–31, 33, 86, 91]. Hf and Ti similarly decrease the coarsening rate of Al_3Sc [7, 32].

Unlike Ti, and Zr, in ternary Al–Sc–M alloys, Er is a faster diffuser in α -Al at 300°C ($(4 \pm 2) \times 10^{-19} \text{ m}^2\text{s}^{-1}$, Chapter 2) than Sc ($9.01 \times 10^{-20} \text{ m}^2\text{s}^{-1}$ [39]). The impact of Er on the coarsening kinetics may therefore be detrimental, but the large lattice parameter misfit between $\text{Al}_3(\text{Sc}_{1-x}\text{Er}_x)$ and α -Al improves the elevated temperature mechanical properties (Chapter 7).

3.2. Experimental Methods

An Al–1 at.% Er master alloy was produced by non-consumable electrode arc-melting in argon from 99.99 at.% Al (the only impurity elements that are found with more than 10 at. ppm concentrations are Fe, Cu, and Si (49, 42, and 40 at. ppm, respectively), as confirmed by glow-discharge mass spectrometry performed by Shiva Technologies (Syracuse, NY)) and 99.9 at.% Er; the latter was supplied by Stanford Materials. The nominal Al–600 at. ppm Sc–200 at. ppm Er alloy was dilution cast from this master alloy, the same stock of 99.99 at.% Al, and an Al–1.2 at.% Sc master alloy. The small solute concentration was chosen to increase the probability of being in the single-phase α -Al field during the homogenization treatment at 640°C, as the dilute ternary phase diagram is unavailable. In binary Al–Sc alloys, the maximum solubility of Sc is 2,300 at. ppm at the eutectic temperature of 640°C (almost four times the concentration in the alloy in this study). In Chapter 2, the solubility of Er in α -Al is found to be 461 ± 6 at. ppm at 640°C (over twice the concentration of Er in this alloy). The alloy was melted in a zirconia-coated alumina crucible in a resistively-heated furnace at 750°C in air. The melt was stirred to ensure proper mixing and then cast into a graphite mold resting on a copper plate to insure both relatively rapid cooling and solidification rates. The chemical composition of the alloy was measured by ATI Wah

Chang (Albany, OR) and by LEAP tomography, and is presented in Table 7.1. The alloys were homogenized in air at 640°C for 72 h and then quenched into ambient-temperature water. Aging of each microalloy specimen was performed at 300°C in air for 24–1,536 h (1–64 days) and was terminated by an ambient-temperature water quench.

TEM foils were prepared by mechanical grinding sections of aged specimens to a thickness of ca. 100 μm . Discs of ca. 3 mm diameter were then cut or punched. These discs were twin-jet electropolished at 20 Vdc using a 10 vol.% solution of perchloric acid in methanol chilled by a dry ice/methanol bath to -40°C. Conventional TEM was performed with a Hitachi 8100 operating at 200 kV.

Tips for LEAP tomography were prepared by cutting and grinding aged needles to a cross-sectional area of ca. 300 \times 300 μm^2 . These needles were initially electropolished in a 10 vol.% perchloric acid in acetic acid solution and then in a solution of 2 vol.% perchloric acid in butoxyethanol. Three-dimensional reconstructions were obtained using Imago's computer program IVAS.

The far-field concentration of Sc and Er in α -Al were obtained from proximity histograms (proxigrams) [67] that were calculated employing both IVAS and APEX software [68].

3.3. Results

3.3.1. Precipitate Morphology

A uniform distribution of spheroidal $\text{Al}_3(\text{Sc}_{1-x}\text{Er}_x)$ precipitates is observed after aging the alloy at 300°C for all aging times (24–1,536 h), as can be seen in a representative TEM micrograph in Fig. 3.1. In Fig. 3.1a, Ashby-Brown [92, 93] or “coffee-bean” strain-field

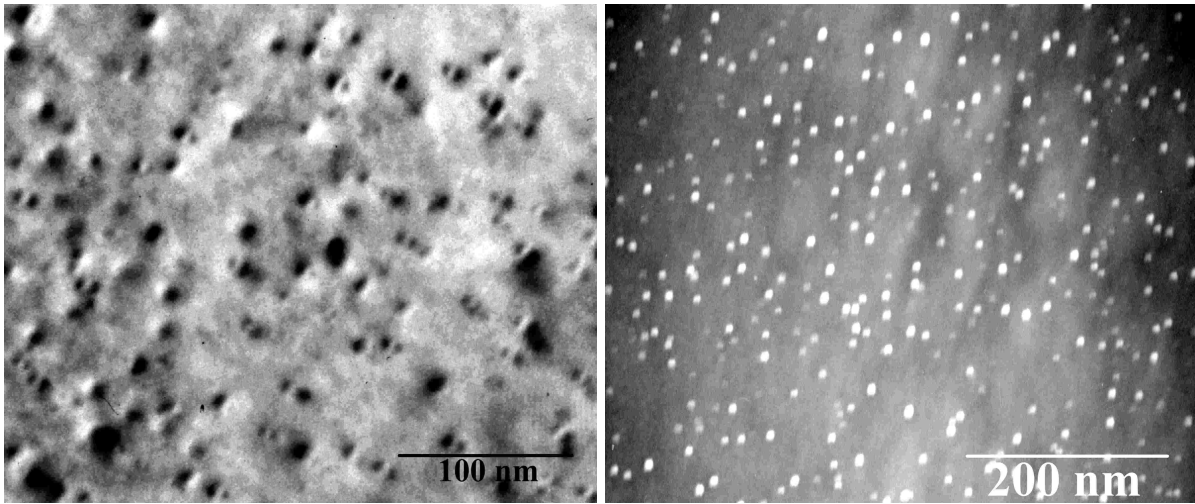


Figure 3.1. Two-beam TEM micrographs of $\text{Al}_3(\text{Sc}_{1-x}\text{Er}_x)$ precipitates. In (a), the alloy aged at 300°C for 1,536 h (64 days) still has coherent precipitates, as observed by the Ashby-Brown strain-field contrast. Imaged in bright field along the $[100]$ zone axis using the $\bar{1}11$ reflection. In (b), a high number density $((2.3 \pm 0.9) \times 10^{22} \text{ m}^{-3})$ of small $(\langle R \rangle = 3.7 \pm 0.9 \text{ nm})$ $\text{Al}_3(\text{Sc}_{1-x}\text{Er}_x)$ precipitates is observed after aging for 96 h (4 days). Central-dark-field image using the 110 superlattice reflection on the $[100]$ projection.

contrast is observed, with lines of no contrast normal to the diffraction vector. This indicates that the precipitates are coherent ($L1_2$). The average precipitate radius, $\langle R \rangle$, increases with aging time at 300°C , from $3.3 \pm 0.2 \text{ nm}$ after 24 h to $7 \pm 3 \text{ nm}$ after 1,536 h (Table 3.1 and Fig. 3.2). TEM was not performed on specimens aged for 192 h (8 days) or 768 h (32 days) and the LEAP data sets had only a few precipitates that were uncut by the boundary of the analysis volume and therefore we do not report $\langle R \rangle$ for those aging treatments.

As is seen in Table 3.1 and Fig. 3.3, the volume fraction of precipitates, ϕ , as measured by LEAP tomography, increases slightly from $0.31 \pm 0.01\%$ after 24 h to 0.33% after 96 h, where it remains constant (within the experimental uncertainty of ca. 0.02% per data point) through 1,536 h. This constant value of ϕ is the same as the equilibrium volume fraction,

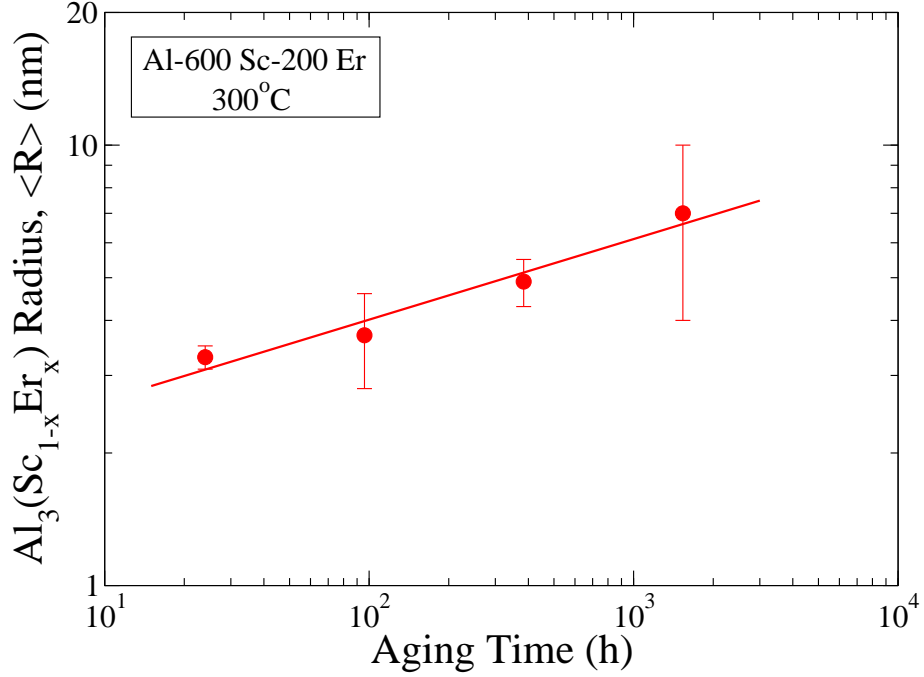


Figure 3.2. Log-log plot of $\text{Al}_3(\text{Sc}_{1-x}\text{Er}_x)$ mean precipitate radius, $\langle R \rangle$, as a function of aging time at 300°C . The quantity $\langle R \rangle$ coarsens with a time exponent of 0.24 ± 0.03 , found by a regression of Eq. 3.1. This differs from the model KV value of $\frac{1}{3}$.

Table 3.1. $\text{Al}_3(\text{Sc}_{1-x}\text{Er}_x)$ precipitate volume fraction (ϕ), average radius ($\langle R \rangle$), and number density (N_V) as a function of aging time at 300°C

Aging Time (h)	ϕ (%)	$\langle R \rangle$ (nm)	N_V (m^{-3})
24	0.31 ± 0.01	3.3 ± 0.2	$(1.1 \pm 0.1) \times 10^{23}$
96	0.33 ± 0.02	3.7 ± 0.9	$(2.3 \pm 0.9) \times 10^{22}$
168	0.32 ± 0.01	—	$(2 \pm 1) \times 10^{22}$
384	0.34 ± 0.02	4.9 ± 0.6	$(8 \pm 1) \times 10^{21}$
744	0.33 ± 0.02	—	$(5 \pm 2) \times 10^{21}$
1,536	0.33 ± 0.02	8 ± 2	$(2 \pm 1) \times 10^{21}$

$\phi_{eq} = 0.33\%$ for an Al–800 Sc binary alloy, as calculated using the lever rule [70]. This is most likely because both Sc and Er have low solid solubilities in α -Al and because Er is fully

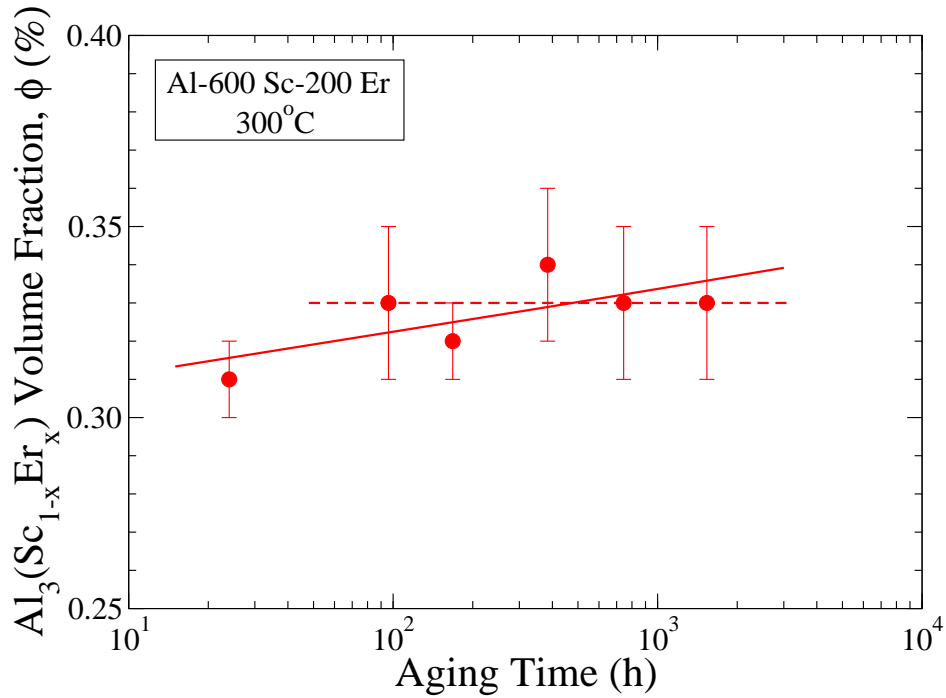


Figure 3.3. Semilog plot of $\text{Al}_3(\text{Sc}_{1-x}\text{Er}_x)$ volume fraction, ϕ , as a function of aging time at 300°C . The alloy is in a quasi-stationary state, and the mean values of the precipitate volume fraction, ϕ , are within 0.01% (less than the uncertainty in each data point, ca. 0.02%) of 0.33% for all but the first point, aged for 24 h (dashed line). The solid line is a power-law fit to all data points.

soluble in Al_3Sc [20]. Thus, Er acts as a less expensive substitute for Sc. It can be assumed that the system is, at least, in a quasi-stationary state, thus satisfying an assumption made by the KV coarsening model (see Chapter 5).

The $\text{Al}_3(\text{Sc}_{1-x}\text{Er}_x)$ precipitate number density may be found by using the ENVELOPE method [94, 95] to isolate individual precipitates and then dividing by the volume of a LEAP tomographic data set (as obtained by the total number of atoms in the data set, taking the instrument efficiency of 0.5 into account). This quantity is plotted against aging time in Fig. 3.4 and

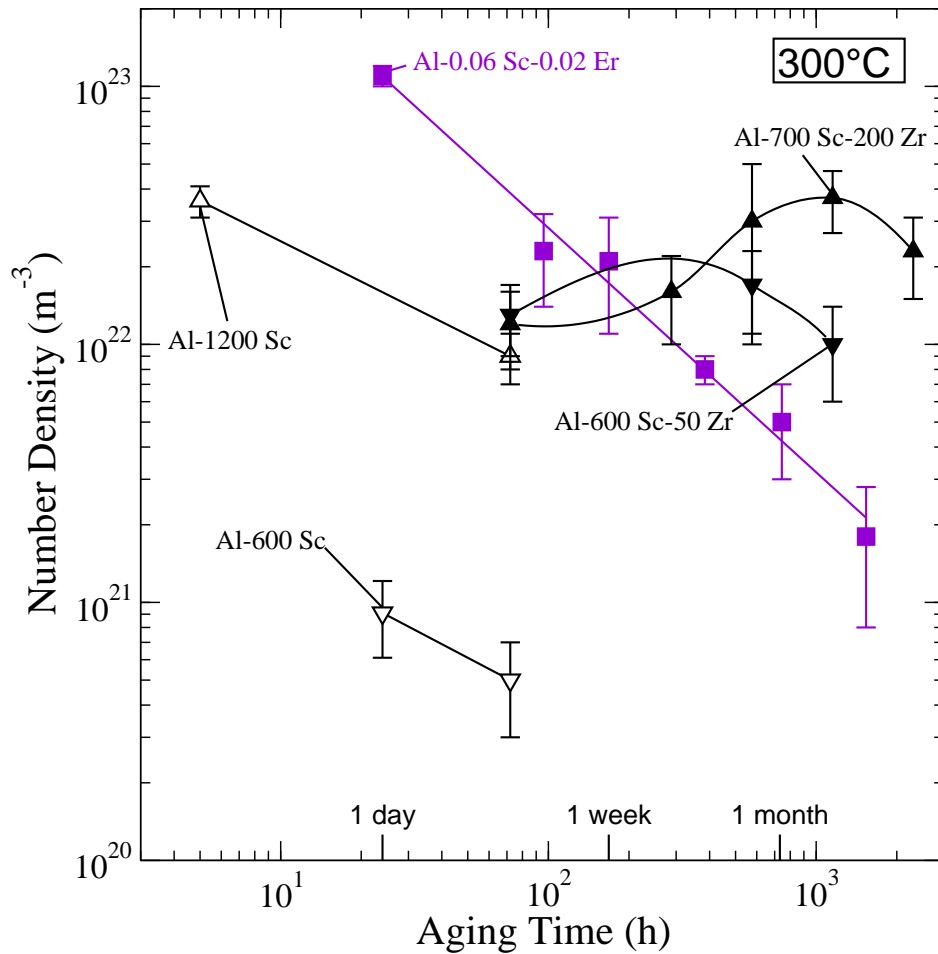


Figure 3.4. Log-log plot of $\text{Al}_3(\text{Sc}_{1-x}\text{Er}_x)$ precipitate number density, N_V , as a function of aging time at 300°C . The number density decreases steadily with a time exponent of -0.9 ± 0.1 , found by fitting Eq. 3.2. This is close to the model value of -1 , suggesting that the alloy is in the coarsening regime with little growth. The number density of $\text{Al}_3(\text{Sc}_{1-x}\text{Zr}_x)$ precipitates in Al-Sc [75] and Al-Sc-Zr [91] alloys with similar solute content exhibit shallower slopes over this time scale.

is compared to other Al-Sc-X alloys [75, 91]. Zr additions increase the coarsening resistance, as the number density of $\text{Al}_3(\text{Sc}_{1-x}\text{Zr}_x)$ does not decrease significantly over this timescale [91]. For the shallow slopes of the limited amount of binary Al-Sc data available,

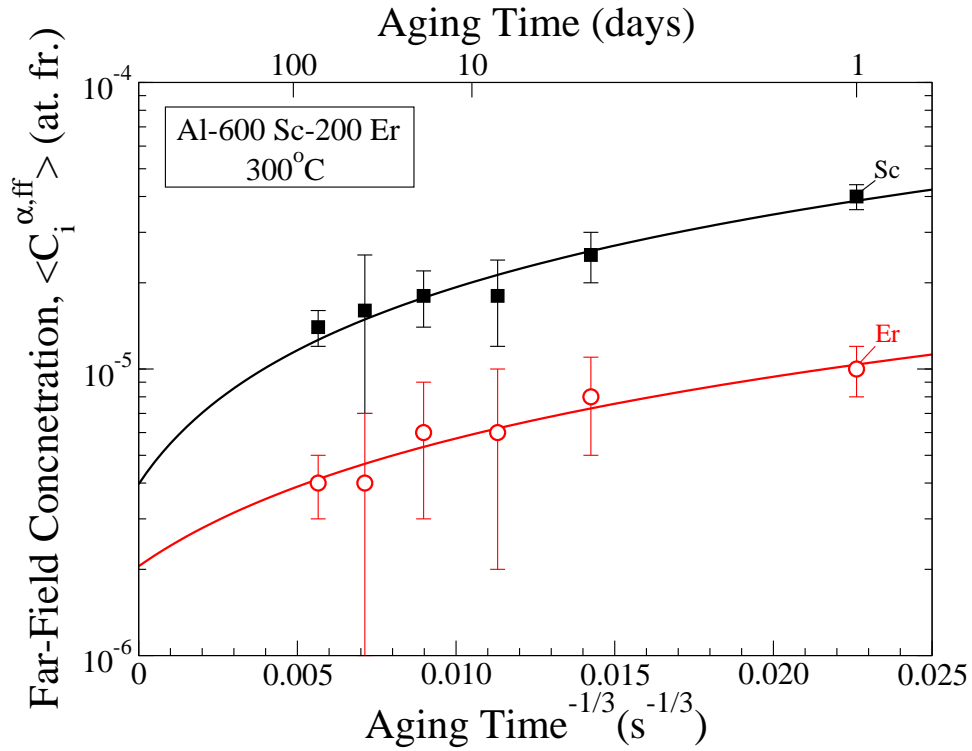


Figure 3.5. The far-field concentration, $\langle C_i^{\alpha,ff} \rangle$, of Sc and Er in the α -Al matrix as a function of aging time at 300°C. The concentration of Sc and Er steadily decrease with increasing aging time and the ordinate-intercept of the fitting line (Eq. 3.7 gives the solid solubility in α -Al at 300°C): $C_{Sc}^{\alpha,eq} = (4 \pm 2) \times 10^{-4}$ at. % Sc (4 ± 2 at. ppm Sc) and $C_{Er}^{\alpha,eq} = (2 \pm 1) \times 10^{-4}$ at. % Er (2 ± 1 at. ppm Er).

it seems that Al-Sc-Er coarsens more rapidly. This is consistent with the larger diffusivity of Er in Al (Chapter 2).

3.3.2. Composition

The proxigram methodology was used to measure the far-field matrix concentrations of Sc and Er in LEAP tomographic reconstructions. These concentrations are plotted in Fig. 3.5. Because of the low concentration of Er in the alloy and the fact that Er has six stable isotopes

(not including Er hydrides that are also detected by LEAP tomography), background subtraction in the mass spectra is critical to obtain accurate measurements. The Sc concentration decreases with aging at 300°C from 40 ± 4 at. ppm after 24 h (1 day) to 14 ± 2 at. ppm after 1,536 h (64 days). This 65% decrease is greater than the average uncertainty of 30% (the standard deviation from counting statistics). The Er concentration decreased 60% from 10 ± 2 to 4 ± 1 over the same time period. Due to the smaller concentrations and the many isotopes, this decrease is approximately equal to the mean relative uncertainty.

3.4. Discussion

3.4.1. $\text{Al}_3(\text{Sc}_{1-x}\text{Er}_x)$ Precipitate Radius

The KV model for coarsening predicts that $\langle R(t) \rangle$ has the time dependence [89]:

$$(3.1) \quad \langle R(t) \rangle^3 - \langle R(t_0) \rangle^3 = K_{KV} (t - t_0)$$

where t_0 is any time at or after the initiation of quasi-stationary state coarsening and K_{KV} is the coarsening constant for $\langle R(t) \rangle$. Here, the model time exponent is $n = \frac{1}{3}$. A non-linear optimizer that minimizes the sum of squares error is used to fit reasonable values for $\langle R(t_0) \rangle^n$ and t_0 in a four-parameter refinement. Once these two variables are found, they are used in a conventional power law fit that yields to $n = 0.24 \pm 0.03$ and $K = (7 \pm 1) \times 10^{-31} \text{ m}^3\text{s}^{-1}$.

This n value is smaller than both the model value and the value found for an Al–Er binary alloy (Chapter 2). It is, however, slightly greater than the exponent found for a binary Al–1800 at. ppm Sc alloy aged at 300°C ($n = 0.18 \pm 0.01$) [75, 84]. In the coarsening

study of Al–Sc–Mg, the disagreement with the model time exponent was attributed to either being in a transient coarsening regime (with precipitate growth) or that the exact details of diffusion (off-diagonal terms of the diffusion tensor, vacancy chemical potential, and diffusivity within the precipitate phase) must be taken into account [84]. There may also not be good agreement because the radius only increases by a factor of ca. 2.4, whereas an order of magnitude increase is preferred. That the Al–Sc–Er system achieves a time exponent closer to the model value may be due to the faster diffusion of Er in α -Al (Chapter 2). In the Al–Er binary, the model time exponent was obtained for a similar aging time range at 300°C. Although the measured time exponent was not found to be identically equal to the model value in Al–Sc–Er, quasi-stationary state coarsening is still assumed due to the results obtained for $\phi(t)$ and the number density, $N_V(t)$.

3.4.2. $\text{Al}_3(\text{Sc}_{1-x}\text{Er}_x)$ Precipitate Number Density

The KV model for coarsening predicts that $\langle N_V(t) \rangle$ decreases with aging time according to [89]:

$$(3.2) \quad N_V(t)^{-1} - N_V(t_0)^{-1} = 4.74 \frac{K_{KV}}{\phi_{eq}} (t - t_0).$$

A regression analysis similar to that performed for $\langle R(t) \rangle$ was performed on $N_V(t)$, yielding a time exponent of -0.9 ± 0.1 , which is close to the model value of -1 . This good agreement suggests that the system may be nearing a true stationary state, which is in agreement with the very small changes in ϕ , and the matrix supersaturation. Still, that ϕ and ΔC change at all and that $\langle R(t) \rangle$ does not have a $\frac{1}{3}$ time dependence implies that it is only in a

Table 3.2. The Rate Constant, K (m^3s^{-1})

Measured from $N_V(t)$, K^{N_V}	$(7 \pm 1) \times 10^{-32}$
Measured from $\langle R(t) \rangle$, K^R	$(7 \pm 1) \times 10^{-31}$
$\frac{K^{N_V}}{K^R}$	0.10 ± 0.02
Calculated from Eq. 3.3, K_{KV}	$(1.7 \pm 0.7) \times 10^{-32}$
$\frac{K^{N_V}}{K_{KV}}$	4 ± 2
Measured for Al-1800 Sc binary, K^{Sc} [75]	$(2.0 \pm 0.4) \times 10^{-32}$
$\frac{K^{N_V}}{K^{Sc}}$	3.5 ± 0.9
Measured for Al-450 Er binary, K^{Er1}	$(2 \pm 1) \times 10^{-31}$
$\frac{K^{N_V}}{K^{Er}}$	0.4 ± 0.2

quasi-stationary state. The minimum time to reach a true stationary state, estimated as the time for the RMS diffusion distance to equal the edge-to-edge interprecipitate spacing, is ca. 200 h (ca. 8 days, Chapter 5). This is consistent with the smaller value of ϕ with shorter aging times.

A rate constant of $K = (7 \pm 1) \times 10^{-32} \text{ m}^3\text{s}^{-1}$ was obtained from the fitting procedure. That this differs by an order of magnitude from what was found using $\langle R(t) \rangle$ suggests that either the regression of Eq. 3.1 was not as good as the regression of Eq. 3.2 (possibly due to the fewer data points and a smaller span in $\langle R(t) \rangle$) or that the KV model does not describe this system well.

3.4.3. The Rate Constant, K

Table 3.2 lists the experimental and model values found for K . The model value is found assuming dilute ideal solution theory [89]:

$$(3.3) \quad K_{KV} = \frac{8\gamma^{\alpha/\beta} V_m^\beta}{9\Lambda}$$

where $\gamma^{\alpha/\beta}$ is the isotropic interfacial free energy, V_m^β is the molar volume of $\text{Al}_3(\text{Sc}_{1-x}\text{Er}_x)$ ($V_m^\beta = \frac{N_a a^3}{4} = 1.06 \times 10^{-5} \text{ m}^3 \text{ mol}^{-1}$, where N_a is Avogadro's number and a is the lattice parameter of $\text{Al}_3(\text{Sc}_{1-x}\text{Er}_x)$, found by assuming Vegard's law [20, 21]), and Λ is given by:

$$(3.4) \quad \Lambda = \frac{\Delta C_{Sc}}{D_{Sc}} \left(\Delta C_{Sc} G_{Sc,Sc}^\alpha + \Delta C_{Er} G_{Sc,Er}^\alpha \right) + \frac{\Delta C_{Er}}{D_{Er}} \left(\Delta C_{Er} G_{Er,Er}^\alpha + \Delta C_{Sc} G_{Sc,Er}^\alpha \right);$$

with $\Delta C_i = C_i^\beta - C_i^\alpha$, being the difference in the equilibrium solid-solubility of component i between the $\text{Al}_3(\text{Sc}_{1-x}\text{Er}_x)$ precipitate phase β and the α -Al matrix phase $C_{Sc}^{\alpha,eq} = 7.2 \times 10^{-6}$ at. fr. [84] and $C_{Er}^{\alpha,eq} = 4 \times 10^{-6}$ at. fr. (Chapter 2) and for C_i^β it is assumed that the precipitate phase is a trialuminide with the Er/Sc ratio of the overall alloy composition (as Er is fully soluble in Al_3Sc). D_i is the diffusivity of species i in α -Al ($D_{Sc} = 9.01 \times 10^{-20} \text{ m}^2 \text{ s}^{-1}$ [39] and $D_{Er} = 4 \times 10^{-19} \text{ m}^2 \text{ s}^{-1}$ (Chapter 2) at 300°C) and $G_{i,j}^\alpha$ is the partial derivative of the molar Gibbs free energy of the α phase with respect to components i and j . For an ideal dilute solution, it is given by:

$$(3.5) \quad G_{i,i}^\alpha = \frac{R_g T (1 - C_j^{\alpha,eq})}{C_i^{\alpha,eq} (1 - C_i^{\alpha,eq} - C_j^{\alpha,eq})}$$

$$(3.6) \quad G_{i,j}^\alpha = \frac{R_g T}{1 - C_i^{\alpha,eq} - C_j^{\alpha,eq}}.$$

Because the interfacial free energy, $\text{Al}_3(\text{Sc}_{1-x}\text{Er}_x)/\alpha$ -Al is unknown, the experimental value of $(0.5 \pm 0.2) \text{ J m}^{-2}$, determined below is utilized. The model K_{KV} is calculated to be $(1.7 \pm 0.7) \times 10^{-32} \text{ m}^3 \text{ s}^{-1}$, which is between the two experimentally measured values (from $\langle R(t) \rangle$ and $N_V t$).

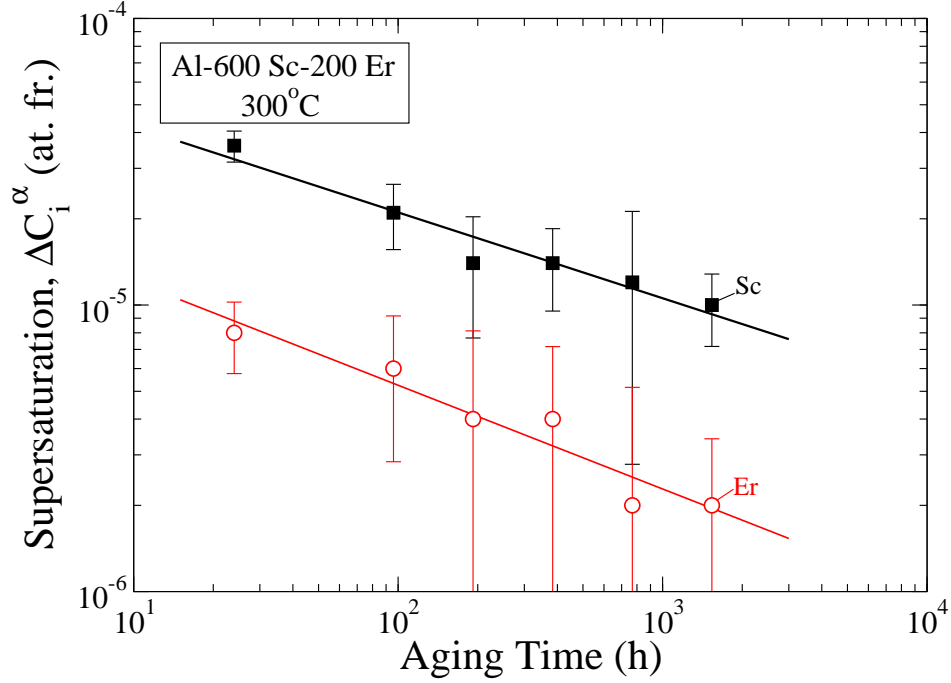


Figure 3.6. Log-log plot of the supersaturation of Sc and Er, ΔC_i^α , in the α -Al matrix as a function of aging time at 300°C. The solid solubility of Er in α -Al is determined from Fig. 3.5 and a second refinement was made to fit the coarsening prefactor and time exponent. The supersaturation of Sc and Er decreases with aging with time exponents of -0.35 ± 0.03 and $0 - 0.32 \pm 0.04$, respectively. This is in agreement with KV model and the first fit.

3.4.4. Temporal Evolution of Concentration

A linear regression was performed on C as a function of $t^{\frac{1}{3}}$, as in Fig. 3.5, to find the solid solubilities of Sc and Er in α -Al, $C_{Sc}^{\alpha,eq}$. $C_{Sc}^{\alpha,eq}$ was determined to be $(4 \pm 2) \times 10^{-4}$ at. % Sc (4 ± 2 at. ppm Sc), which is slightly less than the calculated value of 7.2 at. ppm Sc in the Al-Sc binary system [84]. $C_{Er}^{\alpha,eq}$ was determined to be $(2 \pm 1) \times 10^{-4}$ at. % Er (2 ± 1 at. ppm Er), which is in agreement with the measured value of 4 ± 3 at. ppm Sc in the Al-Er binary system (Chapter 2).

Table 3.3. The Rate Constant, κ (at. fr. $s^{\frac{1}{3}}$)

Measured κ_{Sc}^{α}	$(1.8 \pm 0.8) \times 10^{-3}$
Calculated $\kappa_{Sc,KV}^{\alpha}$ from Eq. 3.8	$(2.3 \pm 0.8) \times 10^{-3}$
Measured κ_{Er}^{α}	$(3 \pm 2) \times 10^{-3}$
Calculated $\kappa_{Er,KV}^{\alpha}$ from Eq. 3.8	$(9 \pm 3) \times 10^{-4}$

In Fig. 3.6, these experimentally-determined solid solubility values are used to find the supersaturation of Sc and Er in α -Al, $\Delta C_i^{\alpha}(t)$ [89]:

$$(3.7) \quad \Delta C_i^{\alpha}(t) = \langle C_i^{\alpha,ff}(t) \rangle - C_i^{\alpha,eq}(\infty) = \kappa_{i,KV}^{\alpha}(t)^{-\frac{1}{3}};$$

where $\kappa_{i,KV}^{\alpha}$ is a rate constant for component i , which is different from K_{KV} . A power-law regression is performed and the time exponents for Sc and Er are found to be -0.35 ± 0.03 and -0.32 ± 0.04 , respectively. This exhibits good agreement with the model value of $-\frac{1}{3}$ and confirms that the $C_{Er}^{\alpha,eq}$ remains self-consistent with the refined fitting procedure. The rate constants are found to be $\kappa_{Sc}^{\alpha} = (1.8 \pm 0.8) \times 10^{-3}$ at. fr. $s^{\frac{1}{3}}$ and $(\kappa_{Er}^{\alpha} = 3 \pm 2) \times 10^{-3}$ at. fr. $s^{\frac{1}{3}}$. The expression for κ_i^{α} is [89]:

$$(3.8) \quad \kappa_{i,KV}^{\alpha} = \frac{(3\gamma^{\alpha/\beta} V_m^{\beta})^{\frac{2}{3}} \Lambda^{\frac{1}{3}} \Delta C_i}{\Delta C_i (\Delta C_i G_{i,i}^{\alpha} + \Delta C_j G_{i,j}^{\alpha}) + \Delta C_j (\Delta C_j G_{j,j}^{\alpha} + \Delta C_i G_{i,j}^{\alpha})}.$$

3.4.5. The Rate Constant, κ

The calculated interfacial free energy, $\gamma_i^{\alpha/\beta}$, is used to find the model $\kappa_{i,KV}^{\alpha}$. Values of $\kappa_{Sc,KV}^{\alpha} = (2.3 \pm 0.8) \times 10^{-3}$ at. fr. $s^{\frac{1}{3}}$ and $\kappa_{Er,KV}^{\alpha} = (3 \pm 1) \times 10^{-3}$ at. fr. $s^{\frac{1}{3}}$ were calculated, in excellent agreement with the experimentally measured values. When $\gamma_{Sc}^{\alpha/\beta}$ is used in Eq. 3.7, $\kappa_{Er,KV}^{\alpha} = (9 \pm 3) \times 10^{-4}$ at. fr. $s^{\frac{1}{3}}$. This is in poorer quantitative agreement with the measured

Table 3.4. The Interfacial Free Energy, $\gamma_i^{\alpha/\beta}$ (J m^{-2})

$\gamma_{Sc}^{\alpha/\beta}$ in Al–Sc–Er aged at 300°C	0.5 ± 0.2
$\gamma_{Er}^{\alpha/\beta}$ in Al–Sc–Er aged at 300°C	3 ± 2

value, but is more consistent with how the other parameters are obtained. This may suggest that the actual interfacial free energy falls somewhere in between the two calculated values and/or merely that the significant uncertainty in the Er concentration measurements makes the KV analysis more problematic. Values of κ_i^α are listed in Table 3.3.

3.4.6. Interfacial Free Energy

Following Ref. [84], the interfacial free energy, $\gamma_i^{\alpha/\beta}$, is found from the above equations:

$$(3.9) \quad \gamma_i^{\alpha/\beta} = \frac{\kappa_{i,KV}^\alpha K_{KV}^{\frac{1}{3}} \left(\Delta C_i \left(\Delta C_i G_{i,i}^\alpha + \Delta C_j G_{i,j}^\alpha \right) + \Delta C_j \left(\Delta C_j G_{j,j}^\alpha + \Delta C_i G_{i,j}^\alpha \right) \right)}{2V_m^\beta \Delta C_i}.$$

Using the experimentally determined values of $K^{Nv} = (7 \pm 1) \times 10^{-32} \text{ m}^3 \text{ s}^{-1}$, $\kappa_{Sc}^\alpha = (1.8 \pm 0.8) \times 10^{-3} \text{ at. fr. s}^{\frac{1}{3}}$, and $\kappa_{Er}^\alpha = (3 \pm 2) \times 10^{-3} \text{ at. fr. s}^{\frac{1}{3}}$, it is found that $\gamma_{Sc}^{\alpha/\beta} = (0.5 \pm 0.2) \text{ J m}^{-2}$ and $\gamma_{Er}^{\alpha/\beta} = (3 \pm 2) \text{ J m}^{-2}$ (where the uncertainty is propagated from the uncertainties in K^{Nv} and κ_i^α only). The mean value found for $\gamma_{Sc}^{\alpha/\beta}$ is larger than the values found for other Al–Sc alloys, but is still comparable when the uncertainty is taken into account. In the Al–Sc binary system, $\gamma_{Sc}^{\alpha/\beta}$ has been found to be between 20–300 mJ m^{-2} [15, 17, 69, 87, 88, 96–98], with values of ca. 200 mJ m^{-2} being most reasonable (as experimental measurements near this value have been relied on extrapolation of the high temperature diffusivity and first principle calculations in this range have used more accurate values for the formation energy of Al_3Sc [99]). In Al–Sc–Mg, $\gamma_{Sc}^{\alpha/\beta}$ has been determined to be between 150–225 mJ m^{-2} [84,

90]. The larger value of $\gamma_{Sc}^{\alpha/\beta}$ is consistent with the smaller value of the solid solubility of Sc in α -Al that is found in this study.

The value found for $\gamma_{Er}^{\alpha/\beta}$ is extremely large (the surface energy of pure Al is only ca. 1 J m^{-2} [100, 101]), although there is a significant uncertainty due to the large uncertainty in κ_{Er}^{α} (which is because of the small concentration of Er). This large value suggests that assumptions of Eq. 3.9 are not met by this system. In particular, the segregation of Er to the core of $\text{Al}_3(\text{Sc}_{1-x}\text{Er}_x)$ precipitates might change the dependence of K and κ on $\gamma_{Er}^{\alpha/\beta}$ (Eqs. 3.3, 3.8). There might also be solute-vacancy interactions, despite the assumption of dilute ideal solution theory. Because Sc segregates to the precipitate shell, the inter-diffusion within the precipitates may matter less. This could explain why the experimentally determined values of $\gamma_{Sc}^{\alpha/\beta}$ and D_{Sc} are in more reasonable agreement with past studies of Al-Sc alloys.

The result that $\gamma_{Er}^{\alpha/\beta} > \gamma_{Sc}^{\alpha/\beta}$ is consistent with Sc segregating to the shell and Er segregating to the core of precipitates. First-principles calculations using the generalized gradient approximation implemented in the Vienna *ab initio* simulation package at 0 K have found the lattice parameter misfit with the α -Al matrix and Al_3Er to be 5%, while the misfit between α -Al and Al_3Sc is only 1.4% [66]. Because of the segregation, the experimentally measured value of $\gamma_{Sc}^{\alpha/\beta}$ is used to calculate the model coarsening rate constants.

3.4.7. Diffusivity

Unlike Sc and Mg in Ref. [84], the measured diffusivities and solid solubilities of Er and Sc in α -Al for a binary alloy at 300°C are similar. A more complicated equation for the

diffusivity of the species i , D_i is given by:

$$(3.10) \quad D_i = \frac{9 \left(\Delta C_i G_{i,i}^\alpha + \Delta C_j G_{i,j}^\alpha \right) \Delta C_i^3 K_{KV}^{\frac{2}{3}}}{4\kappa_{i,KV}^\alpha N - 9 \frac{\Delta C_j}{D_j} \left(\Delta C_j G_{j,j}^\alpha + \Delta C_i G_{i,j}^\alpha \right) \Delta C_i^2 K_{KV}^{\frac{2}{3}}};$$

where:

$$(3.11) \quad N = \Delta C_i \left(\Delta C_i G_{i,i}^\alpha + \Delta C_j G_{i,j}^\alpha \right) + \Delta C_j \left(\Delta C_j G_{j,j}^\alpha + \Delta C_i G_{i,j}^\alpha \right).$$

This analysis yields $D_{Sc} = (6 \pm 3) \times 10^{-20} \text{ m}^2\text{s}^{-1}$, which is in good agreement with the diffusivity of Sc in pure Al ($9.01 \times 10^{-20} \text{ m}^2\text{s}^{-1}$ [39]). Er thus has a negligible effect on the slower Sc. The calculated value of $D_{Er} = (9 \pm 6) \times 10^{-22} \text{ m}^2\text{s}^{-1}$ in Al–Sc–Er is three orders of magnitude smaller than the value that was measured in the Al–Er binary in Chapter 2 ($D_{Er} = (4 \pm 2) \times 10^{-19} \text{ m}^2\text{s}^{-1}$). This much smaller value is consistent with the greater coarsening resistance of Al–Sc–Er as compared to Al–Er and may arise from the core-shell structure of precipitates and/or to the vacancy–solute and solute–solute interactions that are not considered in Eq. 3.10. Similar phenomena have been observed in Al–Sc–Zr, where the slower Zr partitions to a shell around the $\text{Al}_3(\text{Sc}_{1-x}\text{Zr}_x)$ precipitates and slows coarsening considerably as compared to Al–Sc binary alloys [28–31, 33, 91]. This analysis also disregards the off-diagonal terms of the diffusivity tensor, which may be important in this system.

3.5. Conclusions

This study of coarsening kinetics in a ternary Al–600 Sc–200 Er (at. ppm) alloy by local-electrode atom-probe tomography and transmission electron microscopy revealed quantitative differences from the coarsening behavior of binary Al–Sc [75] and Al–Er (Chapter 2) alloys. The following conclusions are reached about this Al–Sc–Er system:

- A high number density $((2 \pm 1) \times 10^{21} - (1.1 \pm 0.1) \times 10^{23})$ of coherent $(L1_2)$ $\text{Al}_3(\text{Sc}_{1-x}\text{Er}_x)$ precipitates is formed after the alloy is homogenized at 640°C for 72 h (3 days) and aged at 300°C for 24–1,536 h (1–64 days).
- A quasi-stationary state is also obtained after this aging treatment, as is evidenced by a nearly constant $\text{Al}_3(\text{Sc}_{1-x}\text{Er}_x)$ precipitate volume fraction, $\phi = 0.33\%$, and the nearly constant composition of the α -Al matrix.
- The measured time exponent for the mean radius, $\langle R \rangle$, of $\text{Al}_3(\text{Sc}_{1-x}\text{Er}_x)$ precipitates, $n = 0.24 \pm 0.03$ is smaller than the value of $\frac{1}{3}$ predicted by the KV model and is in-between values measured for an Al–Er ($n = 0.36 \pm 0.03$) and an Al–Sc ($n = 0.18 \pm 0.01$) alloy aged at 300°C .
- The precipitate number density was found to have a time exponent of -0.9 ± 0.1 , in agreement with the KV model value of -1.
- The measured time exponents for the matrix supersaturation, -0.35 ± 0.03 for Sc and -0.32 ± 0.04 for Er, are in good agreement with the value predicted by the KV model $(-\frac{1}{3})$.

- The coarsening rate is slower in Al–Sc–Er than an Al–Er binary alloy, but is more rapid than in an Al–Sc binary alloy, as can be seen from the measured time exponents. This may be because of the core-shell structure of the precipitates.
- The measured rate constants differ from one another and the rate constants predicted by the KV model by, at most, one order of magnitude.
- Utilizing the experimentally-measured coarsening constants, a larger value for the interfacial free energy, $0.5 \pm 0.2 \text{ J m}^{-2}$, is found than for previous Al–Sc alloys ($0.02\text{--}0.3 \text{ mJ m}^{-2}$).
- The diffusivity of Sc is measured to be $D_{Sc} = (6 \pm 3) \times 10^{-20} \text{ m}^2\text{s}^{-1}$, which is in good agreement with the diffusivity of Sc in pure Al ($9.01 \times 10^{-20} \text{ m}^2\text{s}^{-1}$ [39]).
- The calculated value of $D_{Er} = (9 \pm 6) \times 10^{-22} \text{ m}^2\text{s}^{-1}$ in Al–Sc–Er is three orders of magnitude slower than the value that was measured in the Al–Er binary in Chapter 2 ($D_{Er} = (4 \pm 2) \times 10^{-19} \text{ m}^2\text{s}^{-1}$) at 300°C . This may be due to solute–solute or solute–vacancy interactions and/or to the core/shell structure of precipitates.

CHAPTER 4

Interprecipitate distances of Al–600 Sc–200 Er (at. ppm)**4.1. Introduction**

Many physical properties of materials depend on the edge-to-edge interprecipitate distance, λ_{e-e} . The applied stress required for a dislocation to glide past or climb over precipitates depends on λ_{e-e} [102], as does precipitate coarsening (Chapter 5) and electrical conductivity. Frequently, λ_{e-e} is merely approximated by assuming the precipitates form a cubic array or a square array in a plane [103]. It is also assumed that precipitates are spherical with a known precipitate size distribution (PSD) (usually either all precipitates are the same size or they obey the PSD derived by Lifshitz and Slyozov [73] and Wagner [74] (LSW)). Real materials are almost always more complicated.

Much of the past work on calculating the distance between precipitates or other microstructural features of interest [104, 105] (whether interprecipitate distances [103], mean free paths or chord lengths [106], or nearest-neighbor distribution functions [107–110]) has been theoretical. Experimental characterization of λ_{e-e} requires a microscopic technique that has: (i) a high enough spatial resolution to define clearly each and every precipitate and (ii) a large enough analysis volume to capture many precipitates and to exclude boundary effects. Furthermore, 3-dimensional (3D) information (without suffering from precipitate overlap or truncation) makes determining the 3D distance distributions easier. For nanometer-sized precipitates, the local-electrode atom-probe (LEAP[®]) tomograph (Imago Scientific Instruments)

satisfies these requirements [111, 112]. Despite these capabilities, it has not been previously utilized to gather this information and the little available experimental data for λ_{e-e} comes from 2D techniques. These cannot be compared directly to models of 3D microstructure, but only to 2D slices from simulated 3D microstructures [113] (although a stereological transformation might be possible [114]).

In this chapter, an algorithm to calculate λ_{e-e} from LEAP tomographic reconstructions is presented and applied to a Al-600 Sc-200 Er (at. ppm) alloy. As discussed in this thesis, this alloy is strengthened by a high number density of nanometer-sized $\text{Al}_3(\text{Sc}_{1-x}\text{Er}_x)$ precipitates.

4.2. Methods

4.2.1. Materials, Aging Treatment, and LEAP Tomography

An Al-600 Sc-200 Er (at. ppm) alloy whose casting is described in Chapter 3 was homogenized in air at 640°C for 72 h, water quenched to ambient temperature, and aged in air at 300°C for 24 h and 96 h before a terminal water quench to ambient temperature. As discussed in Chapter 3, these treatment lead to a high number density of nanometer-sized precipitates. The specimens were cut, ground, and then electropolished into tips. The LEAP tomographic experiment was conducted with a 30 K specimen temperature, a 5–15 kV specimen voltage, pulse fraction of 15%, and a pulse repetition rate of 200 kHz. The computer program *IVAS* (Imago Scientific Instruments) was used to analyze the data. Precipitates are isolated using a modified envelope algorithm [115]. Because Sc and Er partition strongly to

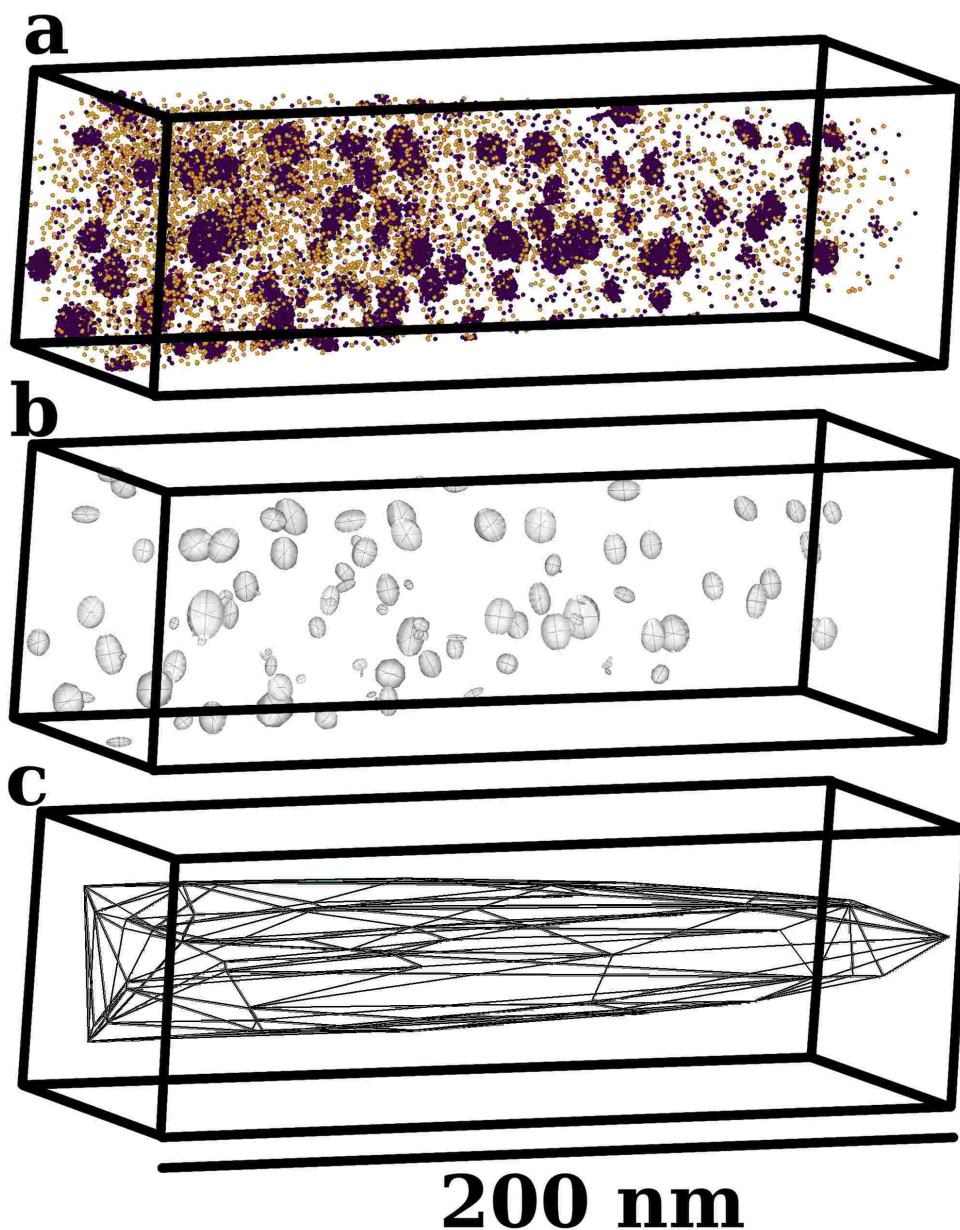


Figure 4.1. (a) A LEAP[®] tomographic reconstruction of an Al-600 Sc-200 Er (at. ppm) specimen that was homogenized at 640°C for 72 h and aged at 300°C for 24 h. Only Sc atoms are displayed for clarity. (b) The 260 precipitates are fitted as ellipsoids [1] (c) A Delaunay mesh connects the precipitate centers. This is used to find “interacting precipitates” and to exclude the convex hull.

precipitates (Chapter 3, an isoconcentration surface was not necessary to distinguish the precipitates in this data set.

4.2.2. Direct Measurement of Interprecipitate Distance Distributions

The interprecipitate distance algorithm begins by representing these precipitates with simpler geometric shapes. While λ_{e-e} between spheres is simple (it being the difference of the center-to-center distance and the precipitate radii), spheres do not adequately represent many precipitate morphologies. Instead, best-fit ellipsoids to the precipitates are calculated (Fig. 4.1b) employing a recently presented algorithm [1]. The 4×4 transformation matrix calculated with that algorithm translates, rotates, and scales a unit sphere centered at the origin to an ellipsoid that preserves the centroid, principle axes, and moments of inertia of a precipitate.

A Delaunay tetrahedral mesh is generated from the precipitate centroids (Fig. 4.1c) [116, 117]. The Delaunay mesh is the geometric dual of the Voronoi diagram; mesh segments connect neighboring precipitates whose Voronoi cells touch. It decreases the number of precipitate pairs for which λ_{e-e} is calculated to a group of neighbors. The mesh also finds the 75 precipitates that make up the convex hull. These outer-most precipitates are allowed to be nearest neighbors of the inner precipitates, but their own nearest neighbors are not calculated, as they might fall outside the volume of the analysis.

The distance between two ellipsoids is found utilizing the constrained optimization by linear approximation (COBYLA) algorithm [118]. This general optimization algorithm is chosen over more efficient algorithms that calculate explicitly the distance between ellipsoids [119,

120], so that it can be used with other abstractions of precipitate morphology (such as the isoconcentration surface) and additional constraints (such as calculation of interplanar edge-to-edge distances) and because a gratis implementation exists [121]. COBYLA minimizes the distance between two points, x and y in the analysis space, $\sqrt{\sum_j (x_j - y_j)^2}$. The constraints are that x and y must fall on the ellipsoid. This is simplified by the fact that applying the inverse transformation of ellipsoids transforms them back into unit spheres, centered at the origin (so $\sum_j x_j^{T_x} = 1$ and $\sum_j y_j^{T_y} = 1$, where the superscript T_i is the inverse transform of the best-fit ellipsoid for precipitate i). The initial guess is chosen as the two closest points that satisfy these constraints that lie on the line that connects the precipitate centers.

In certain cases, it is not $\langle \lambda_{e-e}^{3D} \rangle$ that is of interest, but rather the interplanar edge-to-edge distance, $\langle \lambda_{e-e}^{2D} \rangle$. This might, for instance, be a glide plane of a dislocation. This 2D distance can be calculated by imposing an additional constraint for COBYLA—that x and y values must fall on a particular plane. For comparison, $\langle \lambda_{e-e}^{3D} \rangle$ and $\langle \lambda_{e-e}^{2D} \rangle$ can be calculated from one another by assuming precipitates are distributed on a cubic lattice [103],

$$(4.1) \quad \langle \lambda_{e-e}^{3D} \rangle = \left(\sqrt[3]{\frac{4\pi}{3\phi}} - 2 \right) \langle R \rangle;$$

where ϕ is the volume fraction of precipitates. Assuming a square array of precipitates,

$$(4.2) \quad \langle \lambda_{e-e}^{2D} \rangle = \left(\sqrt{\frac{\pi}{\phi}} - 2 \right) \bar{R};$$

where the mean planar radius, \bar{R} , is given by:

$$(4.3) \quad \bar{R} = \frac{\pi}{4} \omega_2 \langle R \rangle;$$

with ω_2 being the second moment of the PSD [103]. Values for ω_2 for the LSW distribution and for the case where all precipitates are the same size are given in Ref. [103]. Equating the ϕ s in Eqs. 4.1–4.2 leads to a cubic equation relating $\langle \lambda_{e-e}^{2D} \rangle$ and $\langle \lambda_{e-e}^{3D} \rangle$. Solving for $\langle \lambda_{e-e}^{2D} \rangle$:

$$(4.4) \quad \langle \lambda_{e-e}^{2D} \rangle = \frac{\pi \left(-4\omega_2 \langle R \rangle^2 + \sqrt{3\omega_2^2 \langle R \rangle \left(2\langle R \rangle + \langle \lambda_{e-e}^{3D} \rangle \right)^3} \right)}{8\langle R \rangle}.$$

4.3. Simulated Datasets

An interprecipitate distance distribution (IDD) is the cross-correlation (covariance) of the PSD and the center-to-center distance distribution. Assuming one of these distributions is an even function (for example, a δ distribution or a normal Gaussian distribution), the convolution is the same as this cross-correlation. Many coarsening models require the system to be in a stationary state, which causes the PSDs to be self-similar with aging time. The IDD will therefore also be self-similar if the center-to-center distance distribution is also self-similar.

Simulated data sets with spherical precipitates (in this case, drawn from distributions where $\langle R \rangle = 1$ a.u. and a mean center-to-center distance of 10 a.u. (and thus a volume fraction of 0.42%)) can be used to test the methodology.

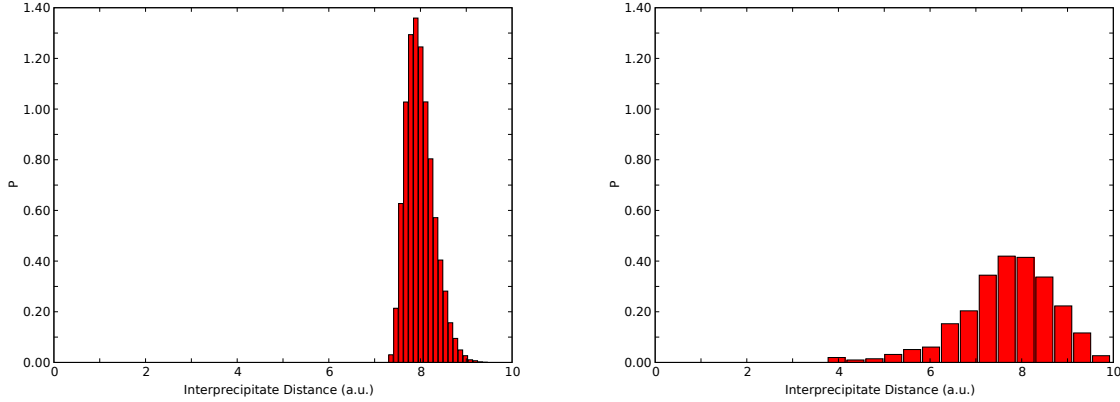


Figure 4.2. 3D IDD for a simulated data set with an LSW PSD ($\langle R \rangle = 1$ a.u.) and various center-to-center distance distributions (with a mean distance of 10 a.u.). In both cases, $\langle \lambda_{e-e}^{3D} \rangle = 8$ a.u. (as predicted from Eq. 4.1) is preserved. (a) Precipitates on a cubic lattice (b) Precipitates randomly distributed according to algorithm in Ref. [2].

The simplest case is when the PSD is a monodispersion (δ function) and the precipitates are arranged on a simple cubic lattice (so that the center-to-center distance distribution is also a δ function). The resulting IDD is also a δ function with $\langle \lambda_{e-e}^{3D} \rangle = 8$ a.u. This is the same spacing found using Eq. 4.1. Figure 4.2 presents more interesting cases, where the PSD is the LSW precipitate size distribution. Two separate histograms are depicted for different possible center-to-center distance distributions. In the first case, precipitates are again in a simple cubic array. Because the center-to-center distribution is a δ function, the shape of the LSW PSD can readily be seen in the resulting IDD. In (b), precipitates are packed into space based on their relative size (representative of large precipitates “sweeping up” solute, so being further away from other precipitates than smaller precipitates) and then randomized, as is described in detail in Ref. [2]. In this case, the IDD is wider because the randomized center-to-center distributions are wider.

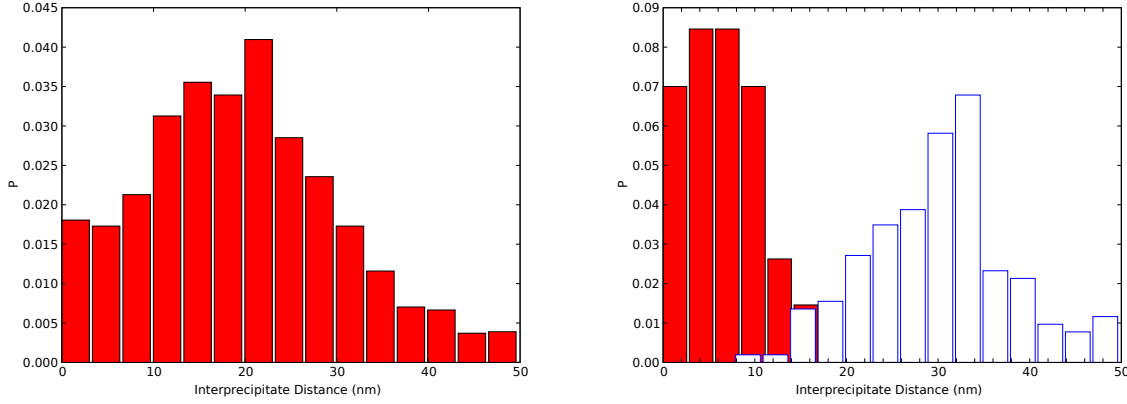


Figure 4.3. 3D IDD for the data set in Fig. 4.1. (a) IDD of all 3,682 Delaunay lengths, with $\langle \lambda_{e-e}^{3D} \rangle = 25$ nm. (b) Solid: IDD of nearest-neighbor distances for each precipitate that is not on the convex hull, which is sharper than when longer lengths are included ($\langle \lambda_{e-e}^{3D} \rangle = 7.5$ nm). Hollow: IDD of the most-distant Delaunay neighbor for each interior precipitate, which is broader than and slightly overlaps with the shortest distances ($\langle \lambda_{e-e}^{3D} \rangle = 38$ nm).

Using Eq. 4.2 or Eq. 4.4, $\langle \lambda_{e-e}^{2D} \rangle^* = 21$ a.u. These equations assume a square lattice spacing, which is the same particle distribution that was used in Fig. 4.2a. Direct measurement of this data set unsurprisingly yields the same $\langle \lambda_{e-e}^{2D} \rangle$. For the array of randomly oriented precipitates that was used to generate Fig. 4.2b, $\langle \lambda_{e-e}^{2D} \rangle = 13 \pm 5$ a. u. Due to differences between the way precipitates are distributed in space (the distribution of center-to-center distances), the mean values is smaller and the standard deviation of the 2D IDD is broader than when precipitates fall on a lattice.

4.4. Experimentally Obtained Datasets

Interprecipitate distance distributions (IDDs) may be generated using different combinations of Delaunay neighbors, as in Fig. 4.3. In Fig. 4.3a, an IDD for all 3,682 Delaunay neighbor

distances yields a mean 3D interprecipitate distance, $\langle \lambda_{e-e}^{3D} \rangle$, of 25 nm. For the $\langle R \rangle$ and volume fraction for this specimen, Eq. 4.1 yields $\langle \lambda_{e-e}^{3D} \rangle = 25$ nm, which is in excellent agreement with what has been measured experimentally.

Figure 4.3b displays two subsets of this IDD, each with 99 lengths because there is one distance associated with each of the 99 interior precipitates that are not on the convex hull. The distance between nearest precipitates is often used to calculate precipitate-dislocation interactions. The IDD for this is much sharper and $\langle \lambda_{e-e}^{3D} \rangle = 7.5$ nm. Precipitates that are very close to one another might be bypassed as a pair by a dislocation. The longest Delaunay distances provide an upper bound to the interactive distance. This is probably not physically important for plastic deformation, but may be relevant for other physical phenomena. The IDD for this case is broader, and overlaps slightly with the shortest distances, and has a mean value that is several times larger ($\langle \lambda_{e-e}^{3D} \rangle = 38$ nm). While 84% of the distances are shorter than this mean value, the distribution has a long tail that extends to beyond the diameter of the analysis volume. This may suggest that, for this number density of precipitates, larger analysis volumes might be useful to analyze the longer Delaunay distances. However, because the percentage of lengths within this tail are small and because the longer lengths are of little interest for mechanical properties and coarsening, they are not analyzed more deeply here.

For the specimen aged for 96 h, only 35 precipitates were in the data set. For this aging treatment, Eq. 4.1 yields $\langle \lambda_{e-e}^{3D} \rangle = 30$ nm. The mean value of the shortest Delaunay spacings from the experimental data set is $\langle \lambda_{e-e}^{3D} \rangle = 18$. However, taking all Delaunay spacings yielded $\langle \lambda_{e-e}^{3D} \rangle = 74$ nm, which is in poor agreement. This poor agreement may come from the small number of precipitates, which leads to a Delaunay mesh that has much longer lengths than

if the analyzed volume were larger (as more precipitates might fall on the convex hull). This highlights a limitation of this technique, which is that hundreds of precipitates must be contained in the analysis volume for an accurate measurement. Even with this limitation, the method described here can accurately find IDD for the minimum Delaunay lengths and the IDD found for all Delaunay lengths might be useful as an upper bound.

$\langle \lambda_{e-e}^{2D} \rangle$ is measured directly by imposing the additional constraint on COBYLA that the two points must lie in the same plane, which is radial to the analysis direction. The entire tip is sampled by taking 180 1° steps. This process samples the precipitates toward the center of the tip more than those toward the hull, but has fewer edge artifacts than parallel slices would have. λ_{e-e}^{2D*} is calculated from what is displayed in Fig. 4.3b by applying Eq. 4.4 with $\omega_2 = 1.046$ [103] (the superscript * denotes this transformation). Despite the simple geometrical assumptions involved in deriving Eq. 4.4, the mean values are in reasonable agreement (with the “direct” method yielding $\langle \lambda_{e-e}^{2D} \rangle = 56$ nm and with the conversion leading to $\langle \lambda_{e-e}^{2D} \rangle^* = 60$ nm). Despite this similarity in the mean values, the distributions are different. The converted IDD is narrower and weighted towards shorter distances than the IDD that is directly calculated. A more complicated stereological transformation might be needed to preserve the distribution [114]. Because the LEAP tomograph gathers 3D experimental data, it allows direct measurement of λ_{e-e}^{2D} from planar slices taken from the 3D reconstruction and λ_{e-e}^{3D} .

In Chapter 5, interprecipitate distances are used to predict the time to reach a stationary state during precipitate coarsening. In Chapter 6, the technique is used to evaluate the statistical accuracy of simulated microstructures, which are used in a continuum dislocation dynamics simulation that calculates a stress-strain curve [122].

CHAPTER 5

How Long Does it Take to Achieve a Stationary State in the Solid State?

A common assumption in materials science and engineering is that a system can achieve a stationary state because the ensuing partial differential equation is mathematically easier to solve. This assumption implies that the time to achieve a stationary state can be estimated with some degree of confidence [123]. In this chapter, we address this question for the coarsening model developed by Lifshitz and Slyozov [73] and Wagner [74] (abbreviated as LSW), because it is heavily used to explain diffusion-controlled Ostwald ripening of precipitates in many alloy systems. Despite this wide application, the LSW model makes a number of physical assumptions that are not always applicable. The LSW model assumes that:

- (1) Precipitates are spherical, although in nature they are sometimes not [1]
- (2) Dilute solution theory applies to the thermodynamics of the two phases
- (3) There are no elastic interactions among precipitates
- (4) The diffusion fields of individual precipitates do not overlap
- (5) The volume fraction of the precipitating phase approaches zero
- (6) The alloy is a binary
- (7) The precipitates have the equilibrium composition at the initiation of coarsening
- (8) The equilibrium volume fraction of precipitates is achieved (a stationary state)

This chapter will estimate the time it takes to achieve a stationary state, satisfying assumption 8.

The LSW model has been modified many times to remove some of the other restrictions. In the LSW model, the time is allowed to approach infinity to achieve a solution. Calderon *et al.* [124] removed the necessity of ideal solution theory (assumption 2). Umantsev and Olson [125] showed that the coarsening of multi-component alloys obey the same temporal power laws (removing assumption 6). Kuehmann and Voorhees (KV) [89] considered capillarity effects in ternary alloys, where the matrix and precipitate compositions can deviate from their equilibrium values (assumption 7). With these modifications, only the amplitudes (coarsening rate constants) of the time-dependent coarsening laws have changed. Thus, for ternary alloys, the time-dependent (t) equations for the mean radius ($\langle R \rangle$), number density (N_V), and supersaturation (ΔC_i^α) after an initial time (t_0) are (Eq. 3.1–3.7):

$$(5.1) \quad \langle R(t) \rangle^3 - \langle R(t_0) \rangle^3 = K_{KV} (t - t_0)$$

$$(5.2) \quad N_V(t)^{-1} - N_V(t_0)^{-1} = 4.74 \frac{K_{KV}}{\phi_{eq}} (t - t_0)$$

$$(5.3) \quad \Delta C_i^\alpha(t) = \langle C_i^{\alpha,ff}(t) \rangle - C_i^{\alpha,eq}(\infty) = \kappa_{i,KV}^\alpha (t)^{-\frac{1}{3}};$$

where K_{KV} is the coarsening constant for $\langle R(t) \rangle$, ϕ_{eq} is the equilibrium volume fraction, C_i^α is the concentration of component i in the matrix phase α (with the superscripts *eq* denoting equilibrium and *ff* indicating the far-field concentrations), and $\kappa_{i,KV}^\alpha$ is the coarsening rate constant for the supersaturation (Eq. 5.3).

Many experiments have found the time exponent predicted in Eq. 5.1. The time exponent predicted in Eq. 5.2 has sometimes been close to -1 , but it is more often than not in poor

agreement. The experimental measurement of the supersaturation (Eq. 5.3) requires either techniques that require external calibration (such as measuring the change of conductivity or Curie temperature) or a technique that has both high spatial resolution and high compositional precision (such as atom-probe tomography). Because of this, its measurement is relatively rare.

Ardell has ascribed the chronic disagreement with the time exponent in Eq. 5.2 to the fact that many coarsening experiments have been conducted over time scales where the volume fraction is not constant (the stationary-state assumption 8 does not apply) and has proposed a modified form of 5.2 equation, which attempts to account for this fact [126–128]. Since these nonstationary-state solutions have often not been applied and because the temporal evolution of the precipitate volume fraction and the supersaturation of solute elements have not always been measured, it is useful to calculate the time to approach a stationary state.

To estimate the time to approach a stationary state for any nonstationary state diffusion-limited process, Balluffi *et al.* propose equating the diffusion distance of the slowest species to the largest characteristic length [123]. The root-mean-squared (RMS) diffusion distance, $L(t)$ is:

$$(5.4) \quad L(t) = \sqrt{4Dt};$$

where D is the diffusivity of the slowest diffusivity. In coarsening, the mean edge-to-edge interprecipitate distance, $\langle \lambda_{e-e}(t) \rangle$, is continuously increasing as $N_v(t)$ decreases and $\langle R(t) \rangle$ increases. The largest characteristic length of a coarsening system is the average distance a particular atom on the edge of a precipitate would travel along a randomly oriented

straight line before coming into contact with the edge of any other precipitate, $\langle \lambda_{e-e}^{1D} \rangle$, which is significantly greater than the minimum distance between two nearest-neighbor precipitates, $\langle \lambda_{e-e}^{3D} \rangle$. The actual diffusion path might be between $\langle \lambda_{e-e}^{3D} \rangle$ and $\langle \lambda_{e-e}^{1D} \rangle$ due to the attractive interactions due to the diffusion gradient. The interprecipitate distance may be measured directly [129] or can be calculated from the average radius, $\langle R(t) \rangle$ and the volume fraction, $\phi(t)$ by assuming a particular distribution of precipitate sizes (typically either a monodispersion or the LSW distribution) via the equation [130]:

$$(5.5) \quad \lambda_{e-e}^{1D}(t) = \left(\frac{1}{\phi(t)} - 1 \right) \frac{4}{3} \frac{\omega_3}{\omega_2} \langle R(t) \rangle;$$

where ω_i is the i^{th} moment of the precipitate size distribution. For the LSW distribution, $\omega_2 = 1.046$ and $\omega_3 = 1.130$ [130].

In a stationary state, Eq. 5.5 has the same time dependence as Eq. 5.1. By equating the interprecipitate distance (Eq. 5.5) as a function of time with the RMS diffusion distance (Eq. 5.4) and solving for t , we are able to find a criteria for the onset of stationary-state coarsening, t_c , that is consistent with both diffusion and stationary-state coarsening models. Assuming that t_0 and $\langle R(t_0) \rangle$ are negligible and that $\phi(t) = \phi_{eq}$ (which is an assumption implicitly made in KV and a number of other coarsening models, and most deviations from it would increase the time to achieve a stationary state), t_c is given by:

$$(5.6) \quad t_c = \frac{64}{729} \left(\frac{\omega_3}{\omega_2} \right)^6 \left(\frac{1}{\phi_{eq}} \right)^6 \frac{K_{KV}^2}{D^3}.$$

Figure 5.1 demonstrates that it takes ca. 8 days to reach t_c in the Al–600 Sc–200 Er system aged at 300°C.

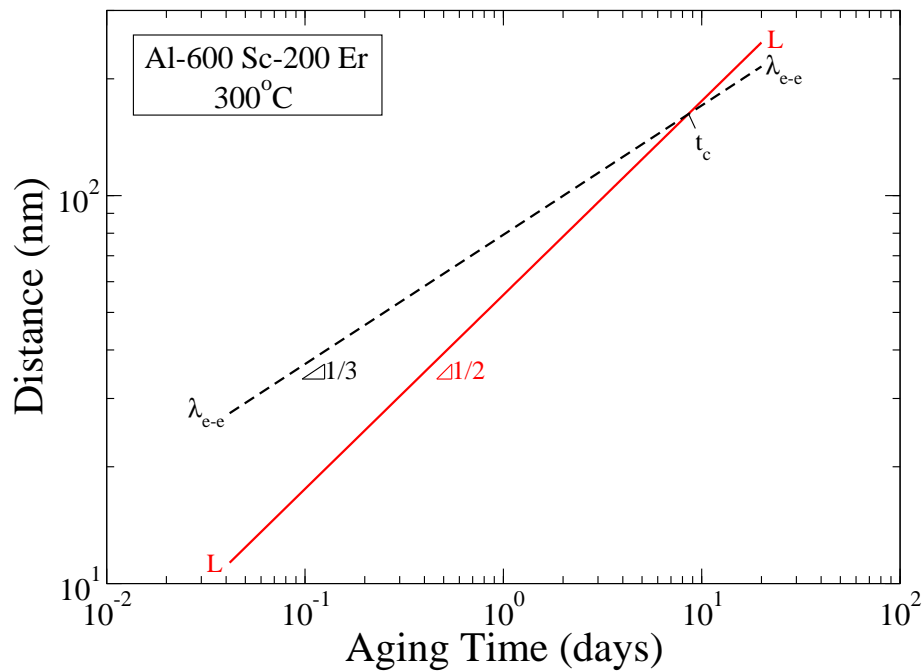


Figure 5.1. For a stationary state to be achieved, one constraint is that the diffusion length, L (Eq. 5.4) must exceed the interprecipitate spacing, λ_{e-e} (Eq. 5.5). It takes ca. 8 days for Al-600 Sc-200 Er (at. ppm) to meet this criteria (Eq. 5.6).

It is noted that, in addition to assuming an equilibrium volume fraction of precipitates, the kinetics inside the precipitate and at the precipitate/matrix interface are not taken into account. Because of this, t_c is a lower bound on the time to reach a stationary state with the equilibrium volume fraction. Interface-controlled coarsening and slower diffusion within precipitates would increase the time to reach the equilibrium compositions of the matrix and precipitate phase. Table 5.1 lists the ranges of t_c and the reported time exponent for the number density of precipitates for several material systems with L1₂ precipitates.

Table 5.1. Minimum time to reach a stationary state, t_c , compared to measured N_v time exponents in alloys strengthened by $L1_2$ precipitates

Reference	Alloy (at.%)	Temperature (°C)	t_c (h)	Exponent for N_v
Al Alloys				
[131]	Al-7 Li	190	3×10^2	-0.55
[91]	Al-0.06 Sc-0.005 Zr	300	9×10^{10}	-0.04 ± 0.03
		350	9×10^9	-0.20 ± 0.04
		375	3×10^9	-0.20 ± 0.04
	Al-0.07 Sc-0.019 Zr	300	3×10^9	0.28 ± 0.01
		350	3×10^8	-0.31 ± 0.03
		375	1×10^8	-0.29 ± 0.02
	Al-0.09 Sc-0.047 Zr	300	3×10^7	0.32 ± 0.09
		350	3×10^6	-0.39 ± 0.06
		375	1×10^6	-0.19 ± 0.05
	Al-0.14 Sc-0.012 Zr	300	5×10^8	0.0007 ± 0.0007
		350	4×10^7	-0.13 ± 0.08
		375	1×10^7	-0.04 ± 0.03
Chapter 3	Al-0.06 Sc-0.02 Er	300	2×10^2	-0.9 ± 0.01
Ni Alloys				
[132]	Ni-7.5 Al-8.5 Cr	600	8×10^6	-0.42 ± 0.03
[132, 133]	Ni-5.2 Al-14.2 Cr	600	2×10^6	-0.67 ± 0.01
[134]	Ni-9.8 Al-8.3 Cr	800	1×10^{-2}	-0.84 ± 0.04
	Ni-9.7 Al-8.5 Cr-2 W	800	4×10^{-2}	-0.88 ± 0.07
[135, 136]	Ni-10 Al-8.5 Cr-2 Re	800	2×10^{-2}	-0.75 ± 0.04

It can be seen that, when t_c is small compared to the aging times, the time exponent is closer to -1 , the value predicted by the KV model for a stationary state. It thus serves as a pragmatic semi-quantitative tool to test the stationary-state assumption made by many coarsening models, despite the caveats listed above. In addition to checking whether it is possible that the equilibrium volume fraction of precipitates has been achieved and is maintained for the duration of a coarsening experiment, the careful researcher who may wish to claim that they have aged an alloy into a stationary state will want to confirm that precipitate-size distributions are self-similar and that $N_v(t)$ has a time exponent of

–1. The experimental edge-to-edge interprecipitate distance distribution (Chapter:4) or the precipitate pair correlation function may also be checked against precipitate coarsening simulations that assume a stationary state [137, 138].

CHAPTER 6

Precipitation Strengthening in Al–900 Sc–300 Er:**Experiments and Simulations****6.1. Introduction**

Aluminum alloys with Sc additions have excellent mechanical properties at ambient temperature due to coherent (L1₂) precipitates [3–8, 12, 13, 139–148]. The precipitates are very resistant to shear due, in part, to their large anti-phase boundary (APB) energy, $0.3 \leq \gamma_{APB} \leq 0.7 \text{ J/m}^2$ [3, 4, 149–153] (as both calculated theoretically and measured by the distance between paired dislocations). This long-range order strengthening establishes the peak strength of the alloy and the Orowan bypass mechanism (of an unpaired dislocation) becomes the controlling deformation process even for very small precipitates (as small as ca. $\langle R \rangle = 2 \text{ nm}$, depending on the precipitate volume fraction). However, the actual transition between these two strengthening mechanisms is less well understood.

Mohles has modelled this transition in Ni-base superalloy NIMONIC PE16, using simulated obstacle arrays [38]. An intermediate “slightly overaged” regime is observed in these simulations, where dislocations bypass arrays of precipitates in pairs, shearing some precipitates. However, they are separated from each other due to Orowan looping. This differs from the peak-aged state, in which precipitates are nearly always sheared by a pair of dislocations and

also from the “highly overaged” state, where precipitates are nearly always bypassed by a single dislocation bowing past them. Both of these cases have also been modelled [154–156]. The stresses exerted on a 2D glide plane originate from a 3D arrangement of precipitates. In part due to the lack of experimental 3D data, the precipitate arrays are typically generated in a random or pseudo-random fashion. In dislocation dynamics simulations, both completely randomized precipitate arrays and more orderly arrays that are intended to relate the center-to-center precipitate distance with the size of the precipitate (to mimic growth and coarsening, where there is a larger depleted region of solute around larger precipitates than around smaller ones) have been used [157]. In the latter case, a “sphere of influence” is assigned to a precipitate based on the radius (drawn from the LSW precipitate size distribution) such that packing of these spheres in a rectangular prism is very dense. The location of each sphere is randomized, and overlaps are prohibited. These spheres are then scaled to obtain the desired volume fraction, ϕ , for the simulation. Comparing 2D slices of these generated obstacle fields with AFM and SEM micrographs has shown that these more orderly arrays are closer to “real” data sets, but are not random enough [122]. In more recent simulations, a small random displacement is made to the scaled down precipitate within its “sphere of influence” [122].

Because the LEAP tomograph can collect data sets with many hundreds of precipitates in 3D within a single data set, it has the promise of being used to experimentally generate precipitate arrangements for direct use in dislocation dynamics simulations. Even larger arrays are needed to study precipitate shearing by a pair of dislocations effectively to accurately average over the stresses on dislocation segments inside many precipitates due to the APB and the stress between the two dislocations. The data sets generated by the LEAP

tomograph can also be quantitatively compared (such as through use of the interprecipitate distance distribution, Chapter 4) with simulated precipitate arrangements.

The goal of this chapter is to use experimental measurements of mechanical properties, analytical strengthening equations, and dislocation dynamics simulations that have been informed by experimentally-determined microstructure to better understand the strengthening mechanisms in Al–Sc–Er at ambient temperature.

6.2. Experimental Methods

6.2.1. Alloy Preparation and Aging

An Al–1200 Sc (at. ppm), produced by Dr. Emmanuelle Marquis, was used as a control. The preparation of this (Al–0.2 wt.% Sc) alloy is described in Refs. [3, 4]. An Al–900 Sc–300 Er alloy was conventionally cast in a zirconia-coated alumina crucible at 750°C in air using 99.999 at.% Al (the largest elemental impurity being 1 at. ppm Si, as confirmed by glow-discharge mass spectrometry conducted by Shiva Technologies (now the Evans Analytical Group (Syracuse, NY)) and an Al–1 at.% Er master alloy. The preparation of this master alloy by arc melting is described in Chapter 2. The melt was poured into a graphite mold resting on a copper plate at ambient temperature. The final alloy composition was confirmed in homogenized samples to be very close to the nominal compositions by direct coupled plasma spectroscopy (Al–(890 ± 30) Sc–(311 ± 8) Er) performed by ATI Wah Chang (Albany, OR) and by Local-Electrode Atom-Probe (LEAP) tomography measurements (Al–(904 ± 4) Sc–(291 ± 5) Er).

The two alloys were homogenized in air at 640 °C for 72 h (3 days). Although the Al–1200 Sc alloy was previously aged, the re-homogenization dissolved precipitates, as confirmed by electrical conductivity measurements. After homogenization, the alloys were water-quenched to ambient temperature and isochronally aged in air from 50°C to at least 400°C, using both 25°C increments every 1 h and 50°C increments every 2 h (the two treatments have the same effective step size). After this ramp heat treatment up to 300°C, the Al–900 Sc–300 Er alloy was aged isothermally at 300°C. The isochronal pre-treatment helped to maximize the number density of precipitates (by allowing them to nucleate at lower temperatures).

6.2.2. Conductivity Measurements

Electrical conductivity was measured at ambient temperature on discs that were least 11 mm in diameter and 5 mm wide that were polished to a 1 μm surface finish. An ambient temperature eddy-current instrument (Sigmatest 2.069, from Foerster Instruments Inc. (Pittsburgh, PA)) was used on both sides of the discs at operating frequencies of 60, 120, 240, 480, and 960 kHz. Errors reported are for one standard deviation from the mean value.

6.2.3. Mechanical Properties Measurements

Vickers microhardness measurements were made at ambient temperature on the same specimens used for conductivity measurements using a 200 g load for 5 s. One standard deviation errors are reported.

Cylindrical specimens (with 8.10 mm diameter and 16.10 mm length) were machined with their axes parallel to that of the cast billet prior to the aging treatment described, above. They

were tested in uniaxial compression cage at ambient temperature with constant cross-head speed of 0.5 mm/min. Strain was measured by an extensometer and the yield stress was determined as the first deviation from linearity. A different specimen was used for each test, but three aging treatments used two specimens to estimate repeatability. Errors reported are from this determination.

6.2.4. Microstructure

Specimens for LEAP tomography were prepared at ambient temperature by sectioning blanks of the aged alloy to a ca. $200 \times 200 \mu\text{m}^2$ square cross section. These blanks were thinned and rounded by electropolishing in a 10 vol.% perchloric acid in acetic acid solution. The tips were completed with a final polishing in a solution of 2 vol.% perchloric acid in botoxyethanol. They were analyzed by LEAP tomography at 30 K. Proxigrams [67] were calculated in IVAS and a modified version of the ENVELOPE [94, 95, 158] method isolated precipitates to that they could be fit as ellipsoids [158] for the calculation of interprecipitate distance distributions (Chapter 4) and for direct use in a dislocation dynamics simulation.

6.3. Experimental Results and Discussion

6.3.1. Isochronal Heat Treatment

Figure 6.1 shows the change in electrical conductivity as a function of aging temperature during isochronal aging in the two alloys. After homogenization, Al-1200 Sc has a smaller value of conductivity than Al-900 Sc-300 Er. The smaller conductivity value is caused by

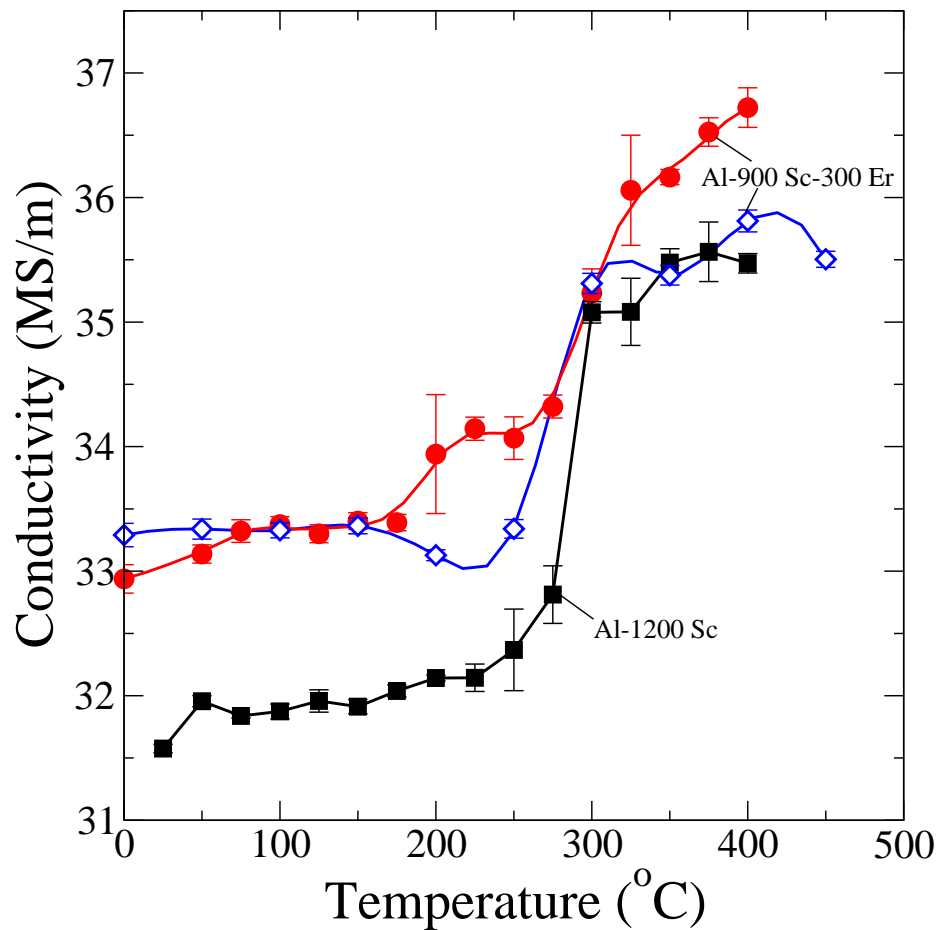


Figure 6.1. Electrical conductivity as a function of aging temperature during isochronal heat treatments for Al-1200 Sc and Al-900 Sc-300 Er.

more Sc and Er atoms in solution (rather than in $\text{Al}_3(\text{Sc}_{1-x}\text{Er}_x)$ precipitates). Since each element has a different contribution to resistivity, the difference in as-homogenized conductivity does not reflect a difference in the solute content. The as-homogenized conductivity of the Al-1200 Sc alloy is very similar to past ambient temperature measurements of a solutionized alloy with the same composition (32.2 MS/m) [17], suggesting that the re-homogenization of the alloy was effective at dissolving precipitates. Neither alloy shows significant change in

conductivity (reflecting very slow precipitation) until ca. 200°C, when the Al-900 Sc-300 Er with 25°C/1 h steps has a ca. 5% increase. This is a similar temperature to that which Al-Er binary alloys were observed to start having microhardness and conductivity increases (Chapter 2). This could reflect a smaller activation energy for Er diffusion, but a finer temperature step size would be needed to quantify this.

The largest relative change in conductivity for all alloys and treatments happens after the 300°C step, when diffusivity of Sc becomes more significant [39]. Even at the termination of isochronal heat treatments, the conductivity is still increasing, indicating that there is still precipitate growth and possibly nucleation. Since we only wished to pre-age at lower temperatures to increase the number density of $\text{Al}_3(\text{Sc}_{1-x}\text{Er}_x)$ precipitates, this does not matter. After 6–12 h at 300°C, the conductivity of Al-900 Sc-300 Er reached a plateau that lasted through the last point at 1,536 h (64 days). Specimens aged 24 h or longer are therefore assumed to have nearly reached the equilibrium volume fraction. The two specimens (aged at 300°C for 24 h and 384 h (16 days)) that were analyzed by LEAP tomography had the same ϕ within experimental uncertainty of ca. 0.01%.

In Fig. 6.2, the microhardness is shown over the same isochronal heat treatment as Fig. 6.1. Again, precipitation of Al_3Er might have cause the ca. 24% increase in hardness between 150-200°C in Al-900 Sc-300 Er alloy, but not in the Al-1200 Sc alloy. A finer temperature resolution would be needed to be certain. The two Al-900 Sc-300 Er curves show relatively good agreement until the alloys begin to weaken at 350–400°C. The curve with a finer step size also shows a higher peak microhardness, lending support to needing an even finer temperature resolution to capture and compare true microhardness peaks. All alloys achieve peak microhardness at about the same temperature of 300–350°C, which is when

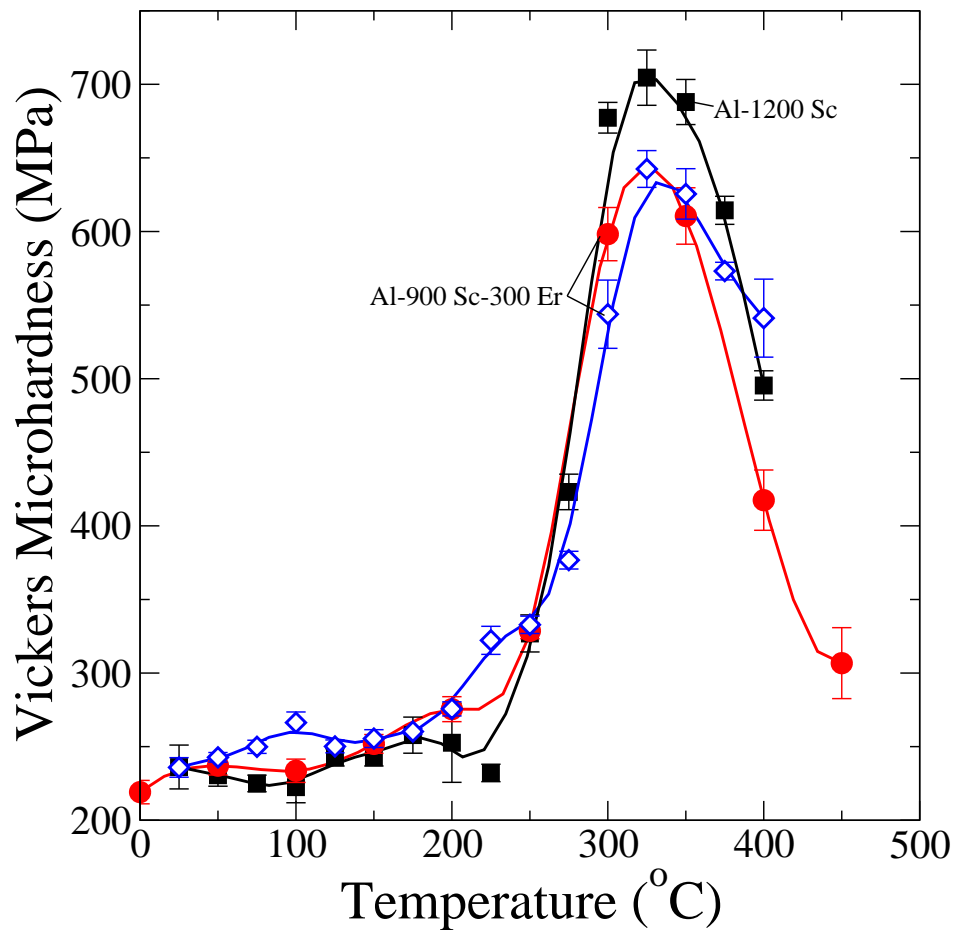


Figure 6.2. Microhardness as a function of aging temperature during an isochronal heat treatment for Al-1200 Sc and Al-900 Sc-300 Er.

much of the Sc has precipitated out and the precipitates begin to grow and coarsen, based on previous studies [3, 4]. The peak microhardness of Al-1200 Sc is ca. 9% larger than Al-900 Sc-300 Er with the same nominal solute content, which is different than the trend observed for isothermal aging at 300 °C for more dilute alloys (Chapter 7). Since the alloys quickly lose microhardness in these isochronal treatments, but have a microhardness plateau in the isothermal treatments, this does not necessarily contradict those results.

6.3.2. Microstructure

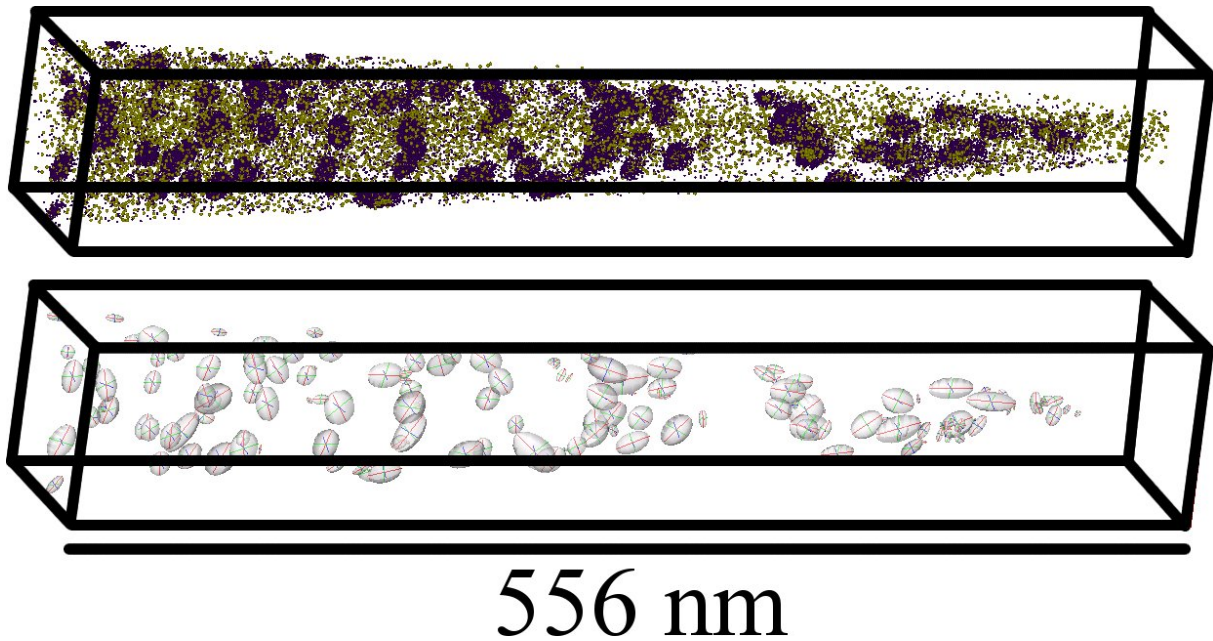


Figure 6.3. (a) A LEAP[®] tomographic reconstruction of an Al-900 Sc-300 Er (at. ppm) specimen that was homogenized at 640°C for 72 h, isochronally aged from 50–300°C in 50°C/2 h steps, and then isothermally aged at 300°C for 24 h. (b) Ellipsoidal fits to precipitates that can be used to measure the interprecipitate distance distribution (Chapter 4) to semi-quantitatively verify randomly generated microstructures.

Figure 6.3 displays the LEAP tomographic reconstruction for Al-900 Sc-300 Er after being aged at 300°C for 24 h following the isochronal treatment described above. A large number density of precipitates with mean radius value, $\langle R \rangle = 4.1 \pm 0.5$ nm are observed. The measured value $\phi = (0.50 \pm 0.01)\%$, is comparable to the value $\phi = 0.49\%$ calculated by the lever rule on the Al-Sc binary phase diagram for the same total solute content. This similarity is most likely due to both Sc and Er having extremely small solubilities in α -Al at 300°C and having aged for long enough for most of the solute to precipitate out. In binary alloys, the solid solubilities in α -Al are 7.2 at. ppm Sc [84] and 4 ± 3 at. ppm Er (Chapter 2).

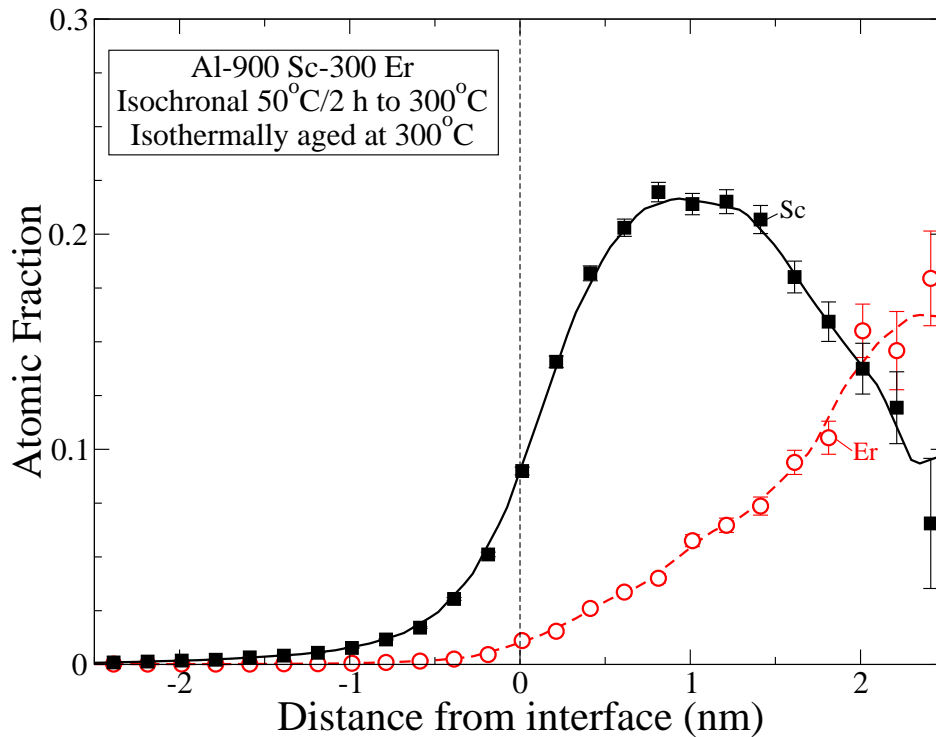


Figure 6.4. A proximity histogram for the data set in Fig. 6.3, showing the concentration of Sc and Er as a function of distance from the $\alpha\text{-Al}/\text{Al}_3(\text{Sc}_{1-x}\text{Er}_x)$ heterophase interface, as defined by a 5 at.% isoconcentration surface. Er segregates to the core of precipitates. Concentration error bars are calculated as $\sigma_C = \sqrt{C(1-C)/N}$, where N is the total number of ions detected in a bin.

The same core-shell precipitates observed in more dilute Al-600 Sc-200 Er alloys are observed in this alloy. This is apparent in a proxigram (Fig. 6.4), showing the concentration of Sc and Er as a function of radial distance from the $\alpha\text{-Al}/\text{Al}_3(\text{Sc}_{1-x}\text{Er}_x)$ precipitate interface. The Er may segregate to the core because Er is a faster diffuser in $\alpha\text{-Al}$ at 300°C ($(4 \pm 2) \times 10^{-19} \text{ m}^2\text{s}^{-1}$, Chapter 2) than Sc ($9.01 \times 10^{-20} \text{ m}^2\text{s}^{-1}$ [39]) and/or because of the larger lattice parameter misfit at 300°C with $\alpha\text{-Al}$ of Al_3Er ($\epsilon' = 3.0\%$ [20]) than of Al_3Sc ($\epsilon' = 1.1\%$ [25]).

6.3.3. Mechanical Properties During Isothermal Aging

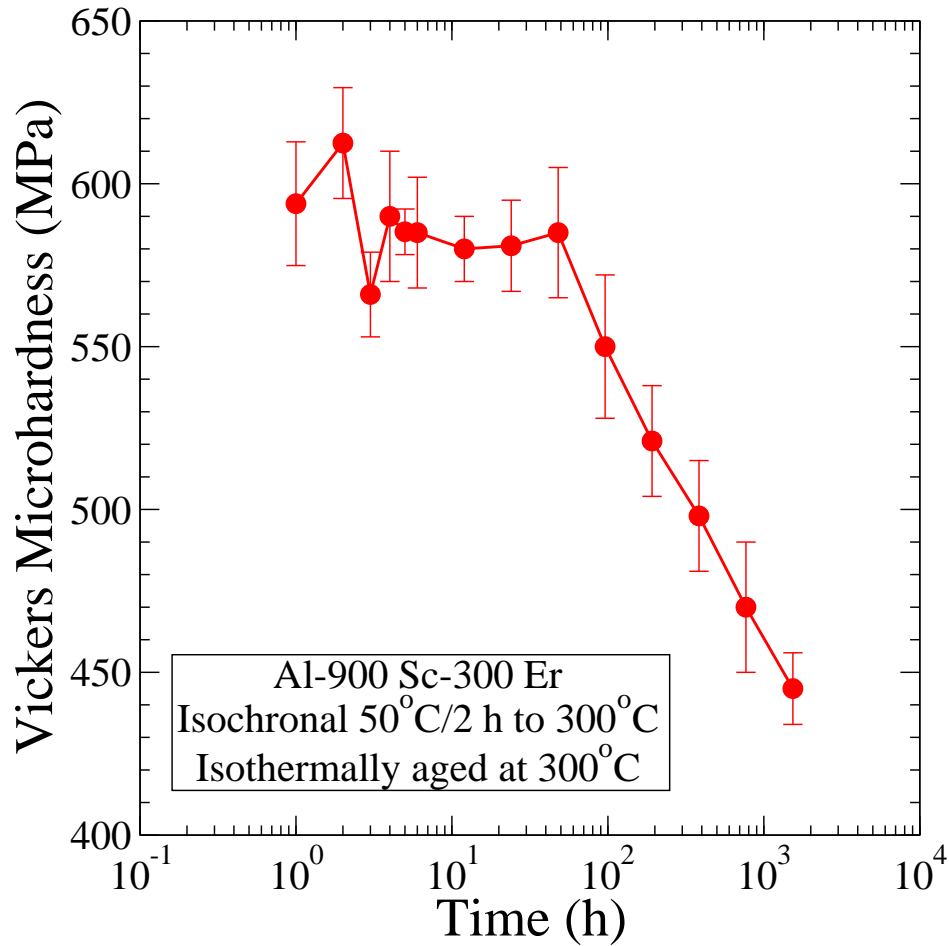


Figure 6.5. Microhardness as a function of aging time at 300°C after an isochronal heat treatment described in the text

The microhardness of Al-900 Sc-300 Er reached a plateau of 600 ± 20 MPa after being isothermally aged to 300°C (Fig. 6.5). The microhardness then rapidly drops after ca. 48 h until the last measurement of 440 ± 10 MPa after 1,536 h. Even this last data point is ca. 200 MPa stronger than the unaged alloy.

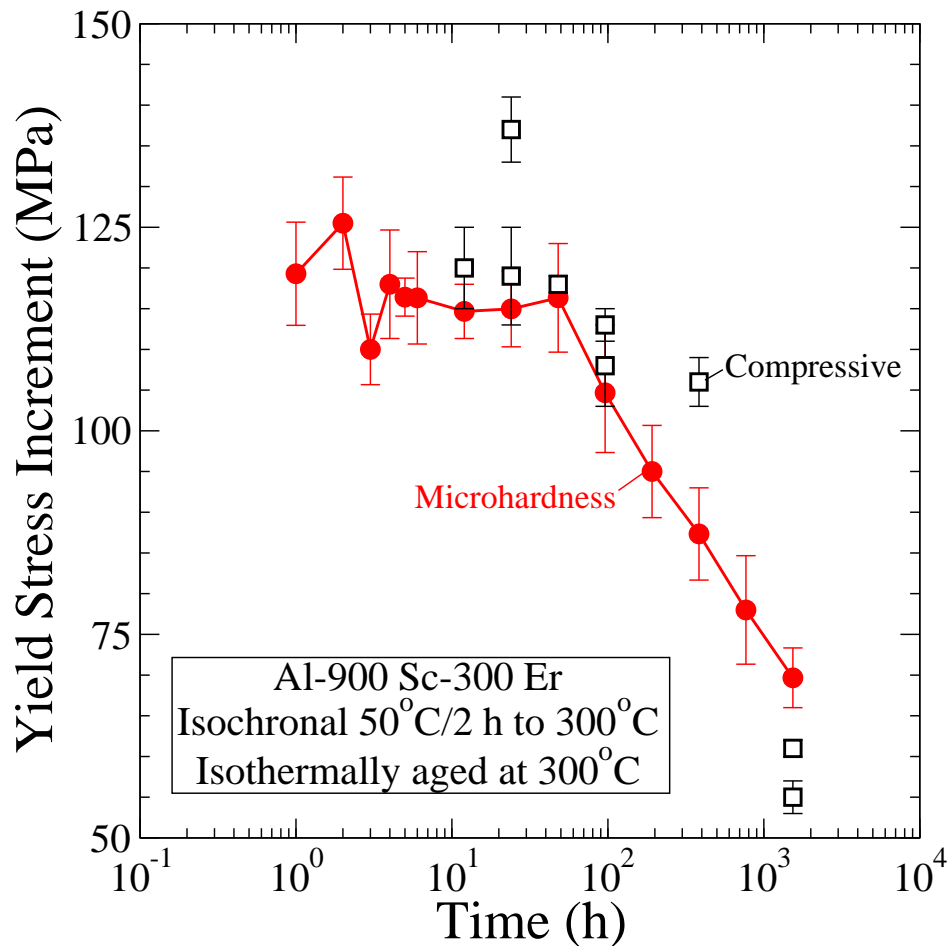


Figure 6.6. Yield stress increment (as calculated from microhardness and compressive yield experiments) as a function of aging time at 300°C after an isochronal heat treatment described in the text

The compressive yield stress increment is obtained by subtracting the as-homogenized yield stress (205 ± 2 MPa) from each data point and is shown in Fig. 6.6. The measurements show the same strength plateau followed by weakening with aging time. The microhardness may be compared to the compressive yield stress measurements using the linear relationship $\sigma_{YS} \approx \frac{HV}{3}$ [159]. This conversion is fairly satisfactory for Al-900 Sc-300 Er, but appears to consistently underestimate the yield strength increment. This under-estimate was also

Table 6.1. Material Constants Used in Yield Strength Models

Constant	Value	Reference
μ (GPa)	25.4	[47]
γ_{APB} (J/m ²)	0.5	[3, 4]
b (nm)	0.286	[47]
M	3.06	[161]
ν	0.345	[161]
ϕ (%)	0.49	

observed for two yield measurements of an Al–1800 Sc (0.3 wt.%) alloy [3, 4], and when a divisor of 2.8 was used instead of 3 for Al–Sc–Zr alloys [160], there was better agreement between the strength increment measured by microhardness with those calculated from analytical equations.

For larger precipitates, the Orowan strengthening mechanism is dominant. The strengthening increment is given as [102, 162]:

$$(6.1) \quad \Delta\sigma_{Or} = M \frac{0.4}{\pi} \frac{\mu b}{\sqrt{1-\nu}} \frac{\ln\left(\frac{2\bar{R}}{b}\right)}{\langle\lambda_{e-e}^{2D}\rangle};$$

where M is the mean Taylor matrix orientation factor, μ is the shear modulus, b is the magnitude of the Burger's vector, ν is Poisson's ratio, \bar{R} is the mean radius for circular cross-sections of precipitates ($\bar{R} = 0.822\langle R \rangle$ assuming an LSW precipitate size distribution [130]), and $\langle\lambda_{e-e}^{2D}\rangle$ is the mean edge-to-edge interprecipitate spacing in a glide plane ($\langle\lambda_{e-e}^{2D}\rangle = \left(1.538\phi^{-\frac{1}{2}} - 1.643\right)\langle R \rangle$ [130] assuming an LSW precipitate size distribution falls on a square lattice of precipitates). Values for these constants are given in Table 6.1.

For smaller precipitates that are still shearable, a pair of dislocations bypasses precipitates (restoring the ordering). The long-range order strengthening increment, σ_{OS} , is given

as [2, 122]:

$$(6.2) \quad \sigma_{OS} = \frac{M}{2} \left(\left((0.79 + 0.9\phi) \sqrt{\frac{3\pi\omega_2^2\phi}{8\omega_3} \frac{\gamma_{APB}}{b}} \right) - \alpha_\beta \phi \frac{\gamma_{APB}}{b} \right);$$

where ω_i is the i^{th} moment of the precipitate size distribution and $0 \leq \alpha_\beta \leq 1$ is a parameter used to describe the fraction of a precipitate's diameter in the glide plane that the trailing dislocation is in. In past articles on Al-Sc alloys, $\alpha_\beta = 0$ was assumed, meaning that the trailing dislocation does not touch precipitates, has been used.

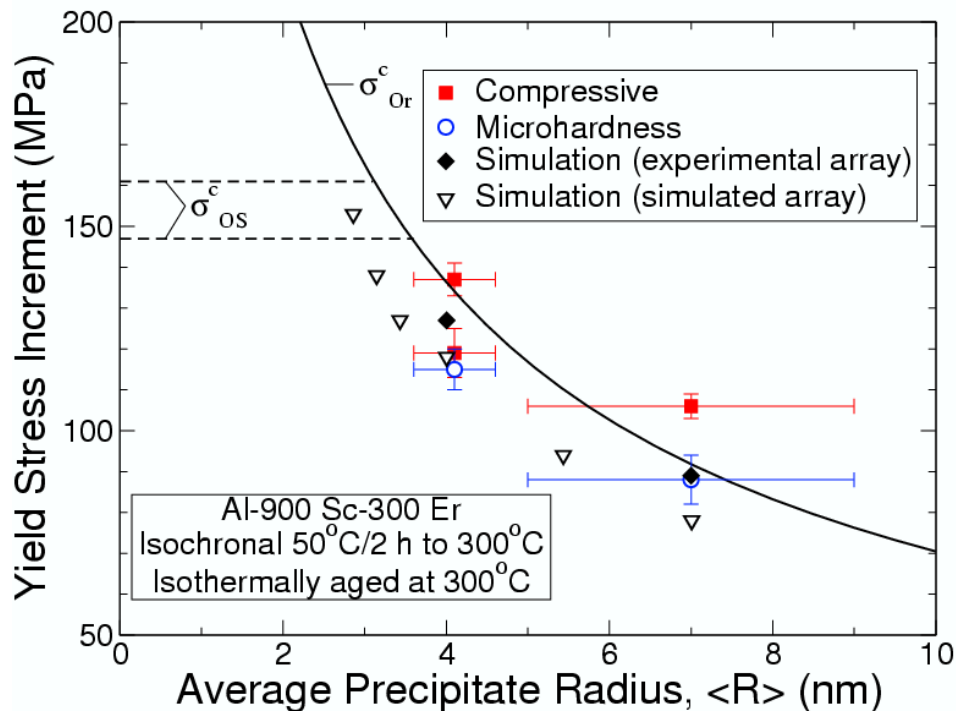


Figure 6.7. Yield stress increment as a function of precipitate radius. Microhardness, compressive yield, analytical equations, and computer simulations are compared.

These equations describe the experimentally measured yield stresses well, as is indicated for specimens aged for 24 h (1 day) and 384 h (16 days) in Fig. 6.7. However, dislocation dynamics simulations have the advantage of being able to test the effects of a combination of the strengthening mechanisms.

6.4. Dislocation Dynamics Simulations

6.4.1. Methods

The details of the dislocation dynamics situations have been given in Refs. [2, 122, 154–156, 163–168]. Simulations take place in a continuum. Precipitate fields are computer generated in 3D with periodic boundary conditions and the stress-field, τ_{obst} , due to long-range ordered (or unsharable) precipitates are calculated in a single plane ($z = 0$). This plane maintains the periodic boundary conditions over x (the direction perpendicular to the applied stress) and y (the direction of the applied stress). Dislocations are placed in this plane, segmented, and the stress on each dislocation segment is calculated. There must be a balance of stresses on every dislocation segment, such that:

$$(6.3) \quad \tau_{ext} + \tau_{drag} + \tau_{obst} + \tau_{disloc} = 0;$$

where τ_{ext} is the externally applied stress (the maximum value of which is the critically resolved shear stress, τ_{CRSS}), τ_{drag} is the viscous drag experienced by a dislocation segment, τ_{obst} is the stress calculated on the dislocation segment due to the plane of precipitates (periodic in x and y for most simulations), and τ_{disloc} is the stress on a dislocation segment to the other dislocation segments (typically periodic in x , but not in y). The dislocation

can be thought of as a loop around a cylinder whose circumference is the extent of x and that is travelling up the axis (the height of which is the extent of y). A small initial value of τ_{ext} is calculated based on the analytical value of τ_{CRSS} . The dislocation segments move with a velocity determined by τ_{drag} until a static equilibrium is reached, and then τ_{ext} is incremented slightly. The simulation ends when $\tau_{ext} = \tau_{CRSS}$ causes the first dislocation segment to reach the end of the precipitate array.

The materials constants used in the simulations are listed in Table 6.1. We assume the single γ_{APB} value of Al_3Sc , and do not try to mimic the core-shell structure of precipitates. The value of γ_{APB} for Al_3Er is unknown. A smaller γ_{APB} for the precipitate core might slightly decrease the strength increment found in the simulations, but the already large γ_{APB} value of the Al_3Sc shell would, for the most part, control the strength. A larger value of γ_{APB} for Al_3Er would increase the strength increments found by simulations, as the dislocation segments would get trapped in the precipitate core.

In addition to γ_{APB} , changing any of the other constants listed in Table 6.1 would change the outcome of the simulation. In particular, ϕ has been determined from LEAP tomography on two specimens with different aging treatments and by using the lever rule on the Al–Sc binary system. There is no ternary phase diagram to consult and longer-term coarsening studies have not been conducted on this particular alloy system. Increasing or decreasing ϕ would cause a systematic shift in calculated τ_{CRSS} up or down, respectively, for all values of $\langle R \rangle$. The finite size of the τ_{ext} increment ultimately determines the resolution to which one might find τ_{CRSS} to. This may be adjusted, but is chosen to be 3% of the estimated alloy strength using Eqs. 6.1–6.2.

Different arrangements of precipitates will also change the results. Larger arrays of precipitates will lead to asymptotically increasing values of τ_{CRSS} (assuming that the resolution in the τ_{ext} increment is high enough). Within the same size precipitate arrays with a similar degree of randomness, a ca. 6% scatter has been found [2, 122, 155, 156]. For small precipitate arrays, changing the degree of randomness of the array has the most substantial impact on τ_{CRSS} , as less regular arrays will have more and larger soft spots. It is therefore important that precipitate arrays accurately fit what is experimentally observed.

6.4.2. Experimental Array of Precipitates

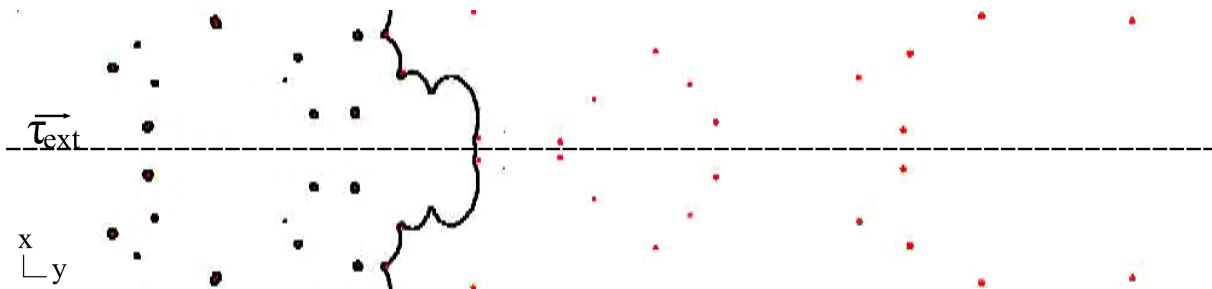


Figure 6.8. Planar experimentally-determined precipitate array extracted from Fig. 6.3.

Rather than simulating an array of precipitates, one can be found experimentally. The largest rectangular cross-section of Fig. 6.3 is taken and the precipitates that intersect the plane are fit as spheres. This plane is then mirrored across the axis of analysis to generate a precipitate array that is periodic in x , but not in y . Such a precipitate array is shown in Fig. 6.8. Depending on the number density of precipitates and the dimensions of the tip, there can be ca. 50–300 precipitates in the glide plane after mirroring for typical specimens reported in this thesis, with $0.3 < \phi < 0.5$ and $\langle R \rangle < 6$ nm. This is significantly smaller than the glide planes that contain 350–900 precipitate cross sections have been used with

this dislocation dynamics simulation in the past [122, 155]. The larger field-of-view now available on atom-probe tomographs and alloys with larger volume fractions of precipitates can improve on this. For alloys with limited volume fractions such as this one, the array of precipitates is too small to pass two dislocations through to model the peak strength. However, the precipitates are large enough that the large γ_{APB} causes all of the precipitates to be bypassed through the Orowan process for the precipitate sizes plotted in Fig. 6.7. Therefore, only a single dislocation is used with this experimentally-determined precipitate array.

Because coarsening models predicts that precipitate size distributions are self-similar with aging time, a single experimentally determined precipitate array within a quasi-stationary-state coarsening regime may be used for a wide variety of precipitate sizes within that regime. This also relaxes the need to keep the precipitate size exactly the same, when it is normalized by b and rescaled for the simulation. The best data set to use with this method would be one with a wide field of view through-out a long analysis length for an alloy aged to the very onset of quasi-stationary state coarsening (when the number density is large). The same data set used to predict the strength for an alloy with $\langle R \rangle = 4$ nm precipitates (Fig. 6.8) is used to simulate $\langle R \rangle = 7$ nm precipitates.

Both edge and screw dislocations were simulated and τ_{CRSS} is taken as the geometric mean of the two. There is a 28% difference between the two. This large difference is most likely due to the small size of the array. The yield stress is taken from $\sigma_{YS} = M\tau_{CRSS}$ and is plotted in Fig. 6.7. It is apparent that even a modestly sized array of precipitates can be used to simulate the overaged yield stress increment due to Orowan bowing, as long as the precipitate sizes and spatial distributions are well-characterized. That the geometric

mean for τ_{CRSS} is still in good agreement most likely reflects the ease with which overaged specimens where the Orowan mechanism dominates may be simulated. Even for a 1-D array of incoherent precipitates (where precipitates may only be bypassed through Orowan looping), the geometric mean yields consistent results with a 2-D array [155].

6.4.3. Simulated Array of Precipitates

Due to the size limitations of experimentally measured data sets, simulated precipitate arrays are still useful, particularly in the peak-aged state and slightly overaged states, when dislocation shear ordered precipitates in pairs. However, these simulated arrays can be informed by experimental data. Discrete, experimentally-determined precipitate size distributions are used instead of the LSW size distribution, and the edge-to-edge interprecipitate distance distribution (IDD) is used to semi-quantitatively check the location of precipitates in the simulated array after precipitates have been randomly displaced by a certain amount. Such an obstacle field is shown in Fig. 6.9. This array has an order of magnitude more precipitate cross sections than in the experimentally determined array (Fig. 6.8). We are in the midst of using arrays such as this one to more accurately determine the theoretical strength of the alloy nearer to peak aging, using a pair of dislocations.

6.5. Conclusions

Precipitation strengthening of dilute Al-900 Sc-300 Er (at. ppm) that was aged isochronally to 300°C and then aged isothermally at 300°C was studied at ambient temperatures utilizing

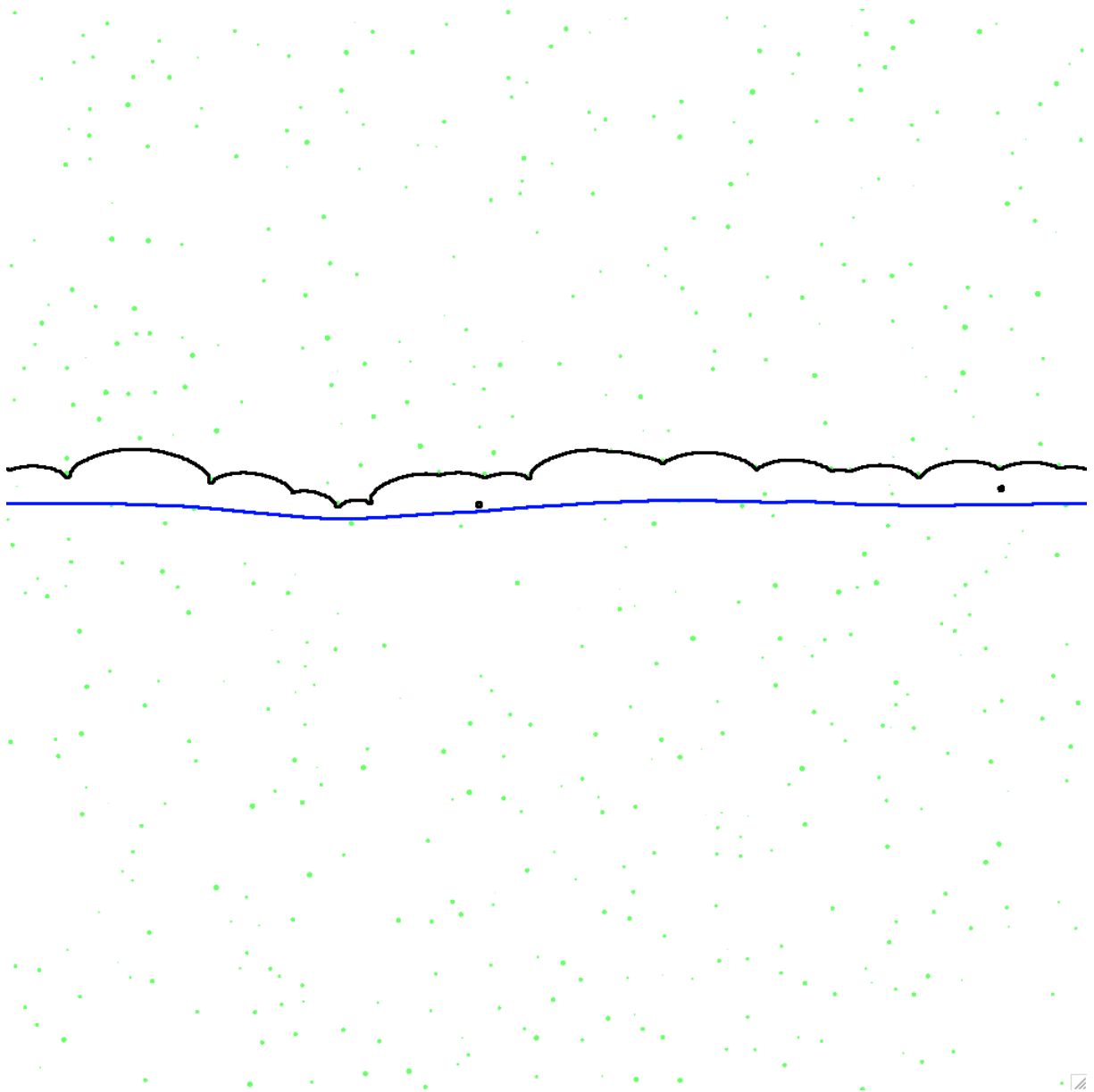


Figure 6.9. Simulated planar precipitate array, utilizing statistical information from Fig. 6.3.

microhardness, compression, atom-probe tomography, and continuum dislocation dynamics simulations. The following conclusions are made:

- Core-shell precipitates $\text{Al}_3(\text{Sc}_{1-x}\text{Er}_x)$, with Er segregating to the center of precipitates and Sc segregating around it, are formed with the aging treatment.
- After the isochronal heat treatment of 50°C increments every 2 h 300°C, the Al-900 Sc-300 Er achieves a peak strengthening increment of ca. 120 MPa over the homogenized strength.
- After aging for longer than 48 h at 300°C, the strength decreases due to coarsening of the $\text{Al}_3(\text{Sc}_{1-x}\text{Er}_x)$ precipitates that causes the Orowan strengthening mechanism to become dominant.
- A dislocation dynamics simulation using an experimentally-determined 3D precipitate array yielded values consistent with experimental measurements and analytical equations for the overaged alloy strength, despite its small size.
- Precipitate size and distribution statistics have been used to generate precipitate arrays of larger size to simulate the peak strength and the transition to the overaged regime.

CHAPTER 7

Mechanical Properties of Al–Sc–RE at Ambient and Elevated Temperatures

7.1. Introduction

In Chapter 6, it was shown that Al–900 Sc 300 Er has excellent mechanical properties at ambient temperatures due to $\text{Al}_3(\text{Sc}_{1-x}\text{RE}_x)$ (L1_2) precipitates. These precipitates can impede dislocation motion at elevated temperatures also. As in Al–Sc binary alloys, Al–Sc–RE (RE=Y, Dy, or Er) forms a coarse-grained (≈ 1 mm diameter) structure after conventional casting of hypoeutectic alloys and homogenization at 640°C (in the single-phase α -Al region of Al–Sc alloys). Because of the precipitates and the large grains, Al–Sc alloys are resistant to creep at high temperatures [3, 6, 79].

Other ternary additions to Al–Sc microalloys have improved mechanical properties at both ambient and elevated temperatures. Mg additions impart solid-solution strengthening [4]. Zr [5] or Ti [7] substitute for Sc in Al_3Sc precipitates. These elements are slow diffusers in Al [169] and decrease the lattice-parameter misfit between $\text{Al}_3(\text{Sc}_{1-x}\text{M}_x)$ precipitates and the α -Al matrix [25]. These traits both lead to increased resistance to precipitate coarsening. However, the decrease in misfit reduces the elastic stresses between dislocations and precipitates during climb bypass, decreasing creep resistance, as modeling [57] and experiments [5, 7] have shown.

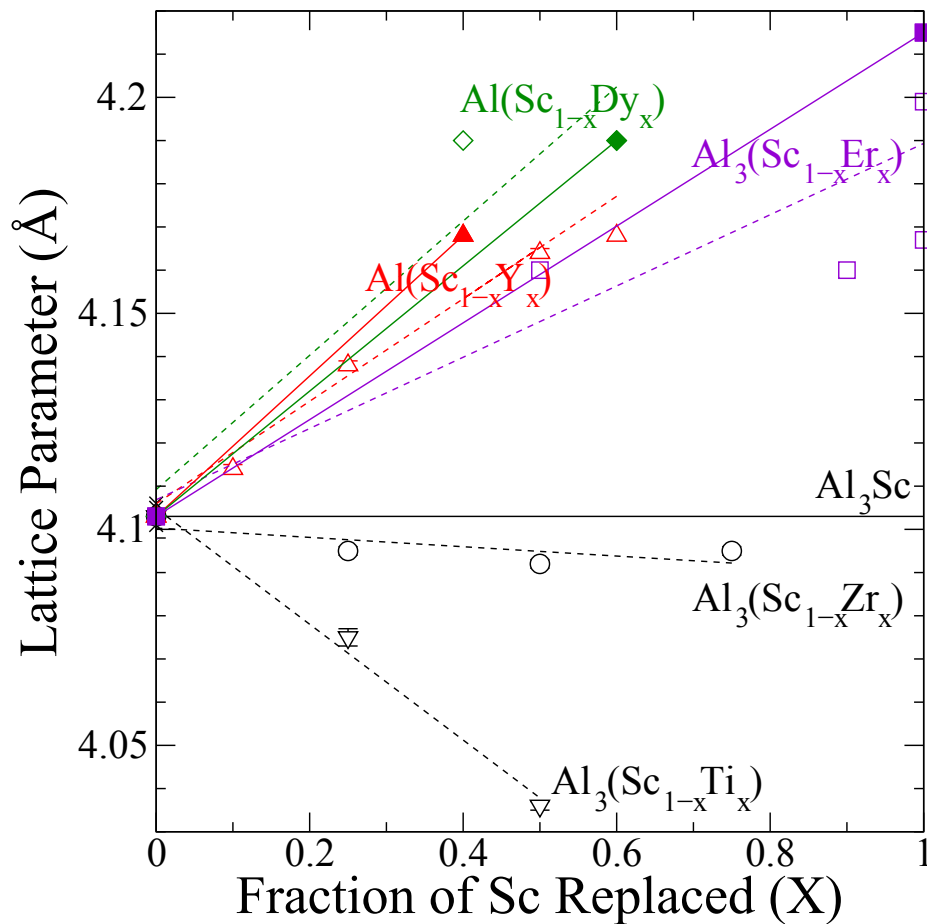


Figure 7.1. Lattice parameter of $\text{Al}_3(\text{Sc}_{1-x}\text{RE}_x)$ at ambient temperature as a function of the fraction of Sc replaced for the elements in this study. The REs have appreciable solubility in Al_3Sc (with Er having 100% solubility) and all increase the lattice parameter. Zr and Ti reduce the lattice parameter. Where two lines exist, the solid lines and filled symbols correspond to Refs. [20] and the dashed lines and hollow symbols correspond to fits applied to all available data [22–26, 170].

As is shown in Fig. 7.1 (reproduced from Fig. 1.2 and discussed in section 1.1.2 of the introduction), RE additions to Al–Sc alloys increase the lattice parameter mismatch, and so should improve creep resistance [20, 21, 37].

In the present chapter, we investigate hypoeutectic Al–600 at. ppm Sc alloys, with additions of 200 at. ppm RE (RE=Y, Dy, or Er) and Al–900 at. ppm Sc 300 at. ppm Er and report on the ambient temperature microhardness and the compressive creep properties of these microalloys at 300°C.

7.2. Experimental Methods

7.2.1. Materials and Heat Treatments

Al–600 at. ppm Sc–200 at. ppm RE alloys were studied with three RE additions (Y, Dy, or Er). An Al–800 Sc was used as a control. The low solute concentration was chosen to increase the probability of being in the single-phase α -Al field during the homogenization treatment at 640°C, as the dilute ternary phase diagrams are unavailable. For binary Al–Sc alloys, the maximum solubility of Sc is 2,300 at. ppm at the eutectic temperature. In Chapter 2, the solubility of Er in Sc was found to be 461 ± 6 at. ppm at 640°C. To investigate an alloy with a larger volume fraction of precipitates, an Al–900 at. ppm Sc–300 at. ppm Er alloy was also used.

The microalloys were dilution-cast from the same 99.99 at.% Al alloy described previously, Al–1.2 at.% Sc and, in the case of Al–Sc–RE, Al–1 at.% RE master alloys. The Al–1 at.% RE master alloys were produced by non-consumable electrode arc-melting from 99.99 at.% Al and 99.9 at.% RE; the latter were supplied by Stanford Materials. Each alloy was melted in a zirconia-coated alumina crucible in a resistively-heated furnace at 750°C in air. After thoroughly stirring, the melt was cast into a graphite mold resting on a large copper plate to insure both relatively rapid solidification and cooling rates. The chemical compositions of

Table 7.1. Composition of Al-Sc-RE alloys as measured by direct coupled plasma (DCP) spectroscopy and by LEAP spectrometry

Alloy	Sc Content from DCP (at. ppm)	RE Content from DCP (at. ppm)	Sc Content from DCP (at. ppm)	Sc Content from LEAP (at. ppm)	RE Content from LEAP (at. ppm)
Al-600 Sc	600(30)	—	—	571(4)	—
Al-800 Sc	820(30)	—	—	865(6)	—
Al-600 Sc 200 Y	610(30)	188(15)	188(15)	622(13)	191(11)
Al-600 Sc 200 Dy	580(30)	236(8)	236(8)	618(9)	208(9)
Al-600 Sc 200 Er	640(30)	220(8)	220(8)	695(5)	220(10)
Al-900 Sc 300 Er	890(30)	311(8)	311(8)	904(4)	291(5)

arc-melted master alloys and cast microalloys were determined by ATI Wah Chang (Albany, OR). Exact alloy compositions are listed in Table 7.1.

Test specimens were machined from the cast billets. Hardness specimens were larger than $5 \times 5 \times 3 \text{ mm}^3$. Cylindrical compression and creep specimens (8.10 mm diameter and 16.10 mm length) were machined with their long axis in the main billet direction. The dimensions of each specimen were measured before and after each test. The density of a creep specimen was measured before and after creep via the Archimedes method.

The alloys were homogenized in air at 640°C for 72 h and then quenched into ambient-temperature water. Aging of each microalloy specimen was performed at 300°C in air for different times and was terminated by an ambient-temperature water quench. After being aged at 300°C for 24 h, some specimens were aged at 400°C to coarsen precipitate radii.

The mean radius of $\text{Al}_3(\text{Sc}_{1-x}\text{RE}_x)$ precipitates was measured by TEM using the same procedures described in Chapter 3. Errors reported are one standard deviation.

7.2.2. Mechanical Properties

Ten Vickers microhardness measurements were made on each specimen and were measured using a 200 g load at ambient temperature on samples ground to a $1 \mu\text{m}$ surface finish.

Compressive creep experiments at constant load were performed at 300°C in air in a three-zone resistively-heated furnace with a temperature stability of $\pm 1^\circ\text{C}$. A superalloy compression-cage was used with boron-nitride-lubricated alumina platens. The platen displacement was transmitted by an extensometer connected to a linear voltage displacement transducer ($1.0 \mu\text{m}$ resolution). Strain and loading times were continuously monitored

and recorded by a computer. At any given stress level, sufficient creep time was allowed to establish a minimum creep-rate by a linear-regression analysis. The steady-state creep-rate was determined after at least 2 % strain, over approximately the last 0.5 % strain range. The load was then increased and another minimum creep rate was measured. This procedure was repeated until a strain of 10 % was accumulated or the sample had failed. Thus, a single specimen yielded minimum creep rates for up to five different stress levels.

7.3. Results

7.3.1. Microhardness

Fig. 7.2 displays the microhardness of Al-600 Sc-200 RE alloys after aging at 300°C. The microhardness response of Al-900 Sc-300 Er is reported in Chapter 6.

The four anticipated stages of precipitation strengthening are observed: (a) a short incubation period (0.2 h) where the microhardness does not vary; (b) an under-aged regime where there is a rapid increase in microhardness; (c) a plateau of peak aging at ca. 400 MPa h higher than the as-homogenized microhardness; and (d) overaging, where the microhardness decreases. At 300°C, overaging is slow—the microhardness is 200 MPa higher than the as-homogenized state after 1,536 h (64 days).

7.3.2. Creep

The first two classic stages of creep were observed: (a) primary creep, where the strain decreases continuously followed by (b) the steady-state creep regime, where the strain rate is constant (Fig. 7.3). Due to the high applied stresses, significant strain was incurred in

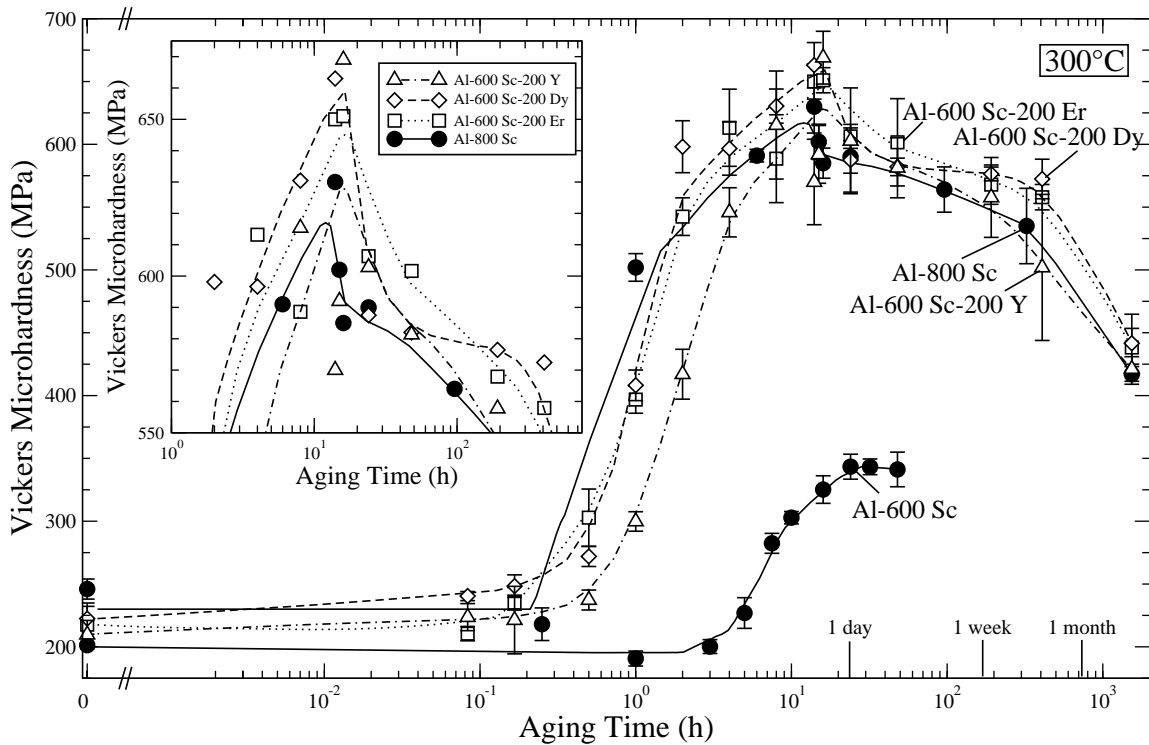


Figure 7.2. Microhardness as a function of aging time at 300°C for Al-600 at. ppm Sc-200 at. ppm RE. Error bars are one standard-deviation. The three alloys exhibit similar aging responses, with an incubation period that is followed by hardening, a plateau and then a decrease in microhardness. Al-600 Sc-200 Y has a higher mean peak microhardness than Al-600 Sc-200 Dy, which is harder than Al-600 Sc-200 Er. Al-600 Sc from Ref. [3, 4]

the primary regime. However, the secondary creep regime still reached low minimum strain rates. All alloys and aging treatments exhibit significant creep resistance at 300°C, as shown in Figs. 7.4–7.5. High ($n_{ap} = 8\text{--}40$) apparent stress exponents were observed, which is indicative of a threshold stress, below which creep is not measurable.

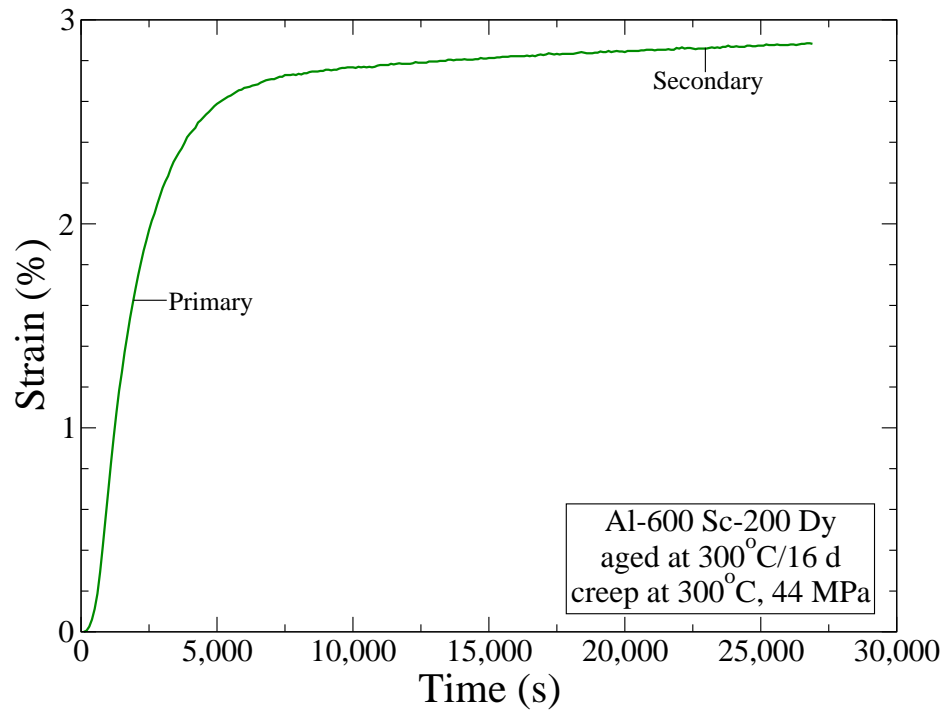


Figure 7.3. Experimental creep curve for Al-600 Sc-200 Dy aged at 300°C for 16 days ($\langle R \rangle = 5.1 \pm 0.5$ nm). Significant (over 2%) primary creep occurs before the secondary creep rate of $(5.4 \pm 0.1) \times 10^{-8}$.

7.4. Discussion

7.4.1. Microhardness

Although there is a significant sampling error, the mean measured peak microhardnesses for the microalloys increase with the α -Al/Al₃(Sc_{1-x}RE_x) lattice-parameter mismatch determined from Vegard's law [20–26, 37, 170] as shown in Fig. 7.6. This may be fortuitous and due to precipitate volume fraction differences. Al-600 Sc-200 Sm and Al-600 Sc-200 Gd [9] have 118 and 94 at. ppm RE in excess of the maximum solubility in Al₃Sc phase, respectively [21]. However, Sawtell and Morris [23] also found Al-Sc-Y to be harder

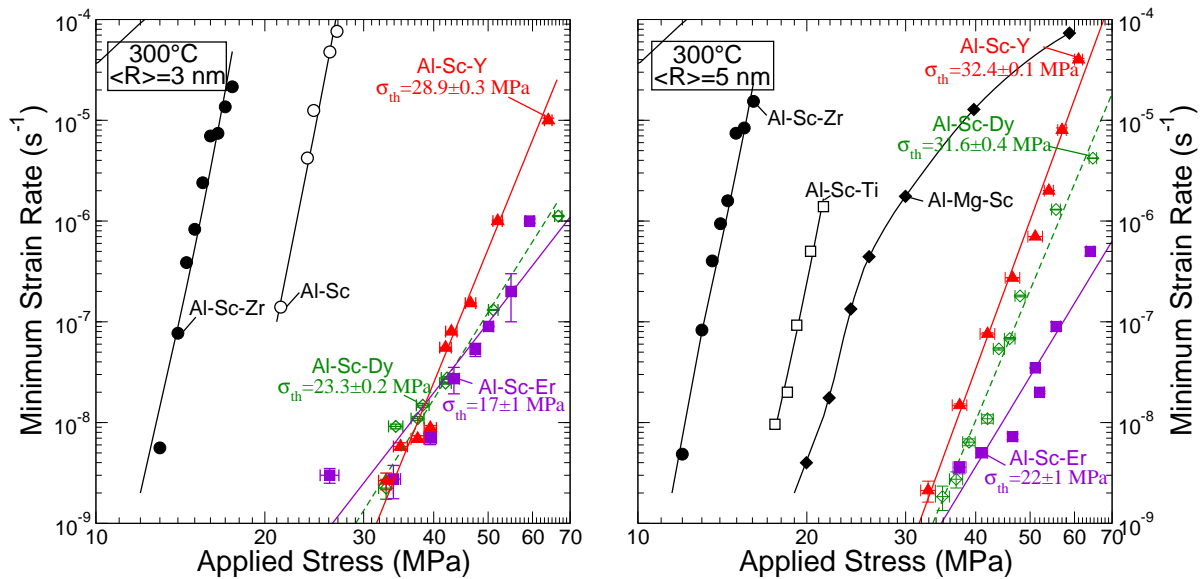


Figure 7.4. Double-logarithmic plot of minimum compressive creep strain-rate vs. stress at 300°C for Al–600 at. ppm Sc–200 at. ppm RE. In the left plot, the average precipitate radius, $\langle R \rangle = 3\text{ nm}$. In the right plot, $\langle R \rangle = 5\text{ nm}$. For a particular size of precipitate, the alloy with the highest lattice parameter misfit between $\text{Al}_3(\text{Sc}_{1-x}\text{M}_x)$ and $\alpha\text{-Al}$ is more creep resistant. For any given alloy, the specimen with the larger diameter precipitates is more creep resistant. High apparent stress exponents are indicative of a threshold stress, σ_{th} . The RE-containing alloys are significantly more resistant to creep than Al–Sc, Al–Sc–Mg, Al–Sc–Zr, and Al–Sc–Ti for a similar volume fraction of precipitates [3–7].

than Al–Sc–Er and predicted (from RE atomic radii) that Al–Sc–Dy should have a strength between the two. Our experimental results for these alloys are consistent with their simple model.

If there are differences, they could be due to (a) shearing of small precipitates; and/or (b) Orowan bypass of large precipitates (the transition between shearing and bypassing occurring at radii of ca. 2 nm in prior studies of Al–Sc alloys [3–6, 23]). The shearing stress scales with the $\frac{3}{2}$ power of the constrained lattice parameter mismatch [130] due to

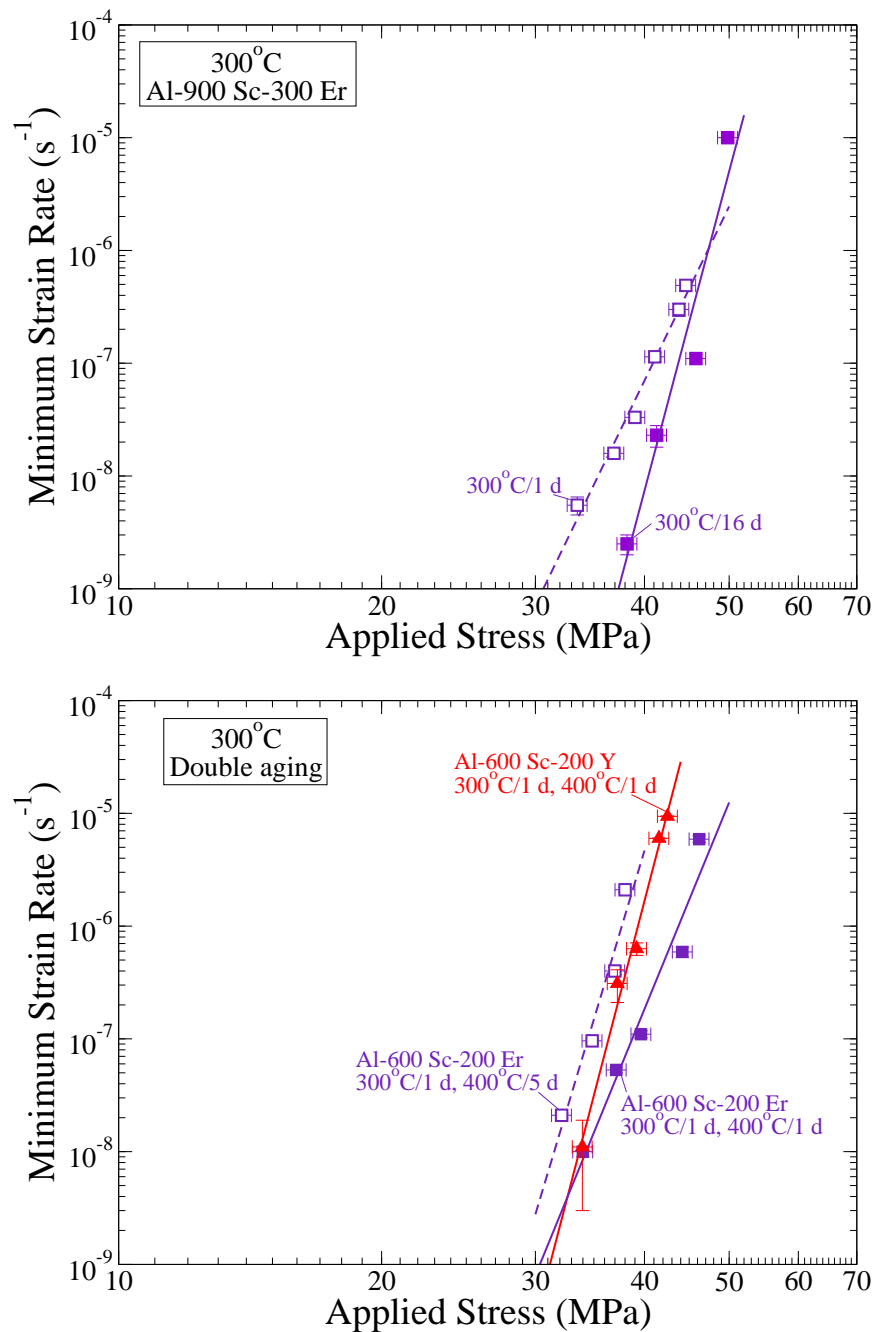


Figure 7.5. Double-logarithmic plots of minimum compressive creep strain-rate vs. stress at 300°C for Al-900 at. ppm Sc-300 at. ppm Er and Al-600 Sc-200 RE that has been aged at 300°C for 1 day and then aged at 400°C for 1-5 days to coarsen precipitates.

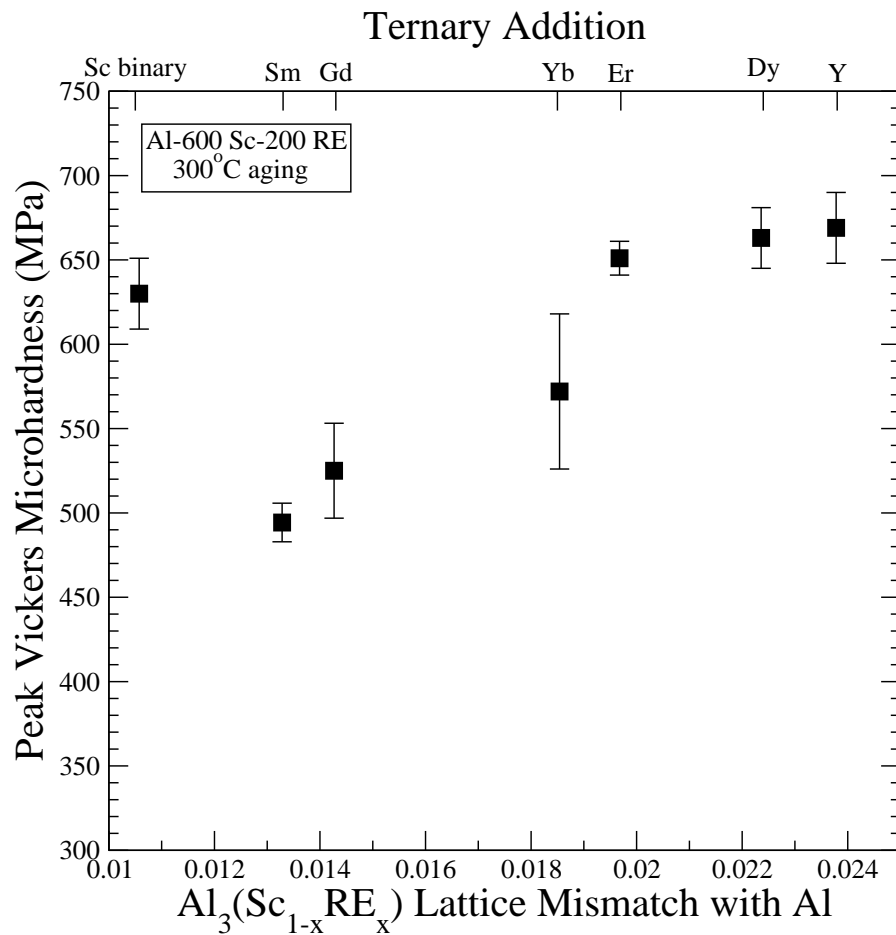


Figure 7.6. Peak Vickers microhardness as a function of the lattice parameter misfit at ambient temperature with Al for Al-600 Sc-200 RE and Al-800 Sc alloys (after Fig. 7.2 and Ref. [8]). Differences in microhardness may be due to (a) precipitate volume fraction differences (as both Sm and Gd have lower solubilities in the Al_3Sc phase, so a reduced volume fraction (the misfit here is calculated at the maximum solubility)) and/or (b) greater resistance to precipitate shearing (directly due to misfit) and/or Orowan looping by dislocations (due to smaller precipitates).

coherency strengthening, and the $Al_3(Sc_{1-x}RE_x)$ phases have a greater lattice parameter mismatch with Al than Al_3Sc [20–26, 37, 170]. The Orowan strengthening scales with $\frac{\ln(R)}{\langle R \rangle}$, where $\langle R \rangle$ is the mean precipitate radius [130], so the higher strengths could be the result

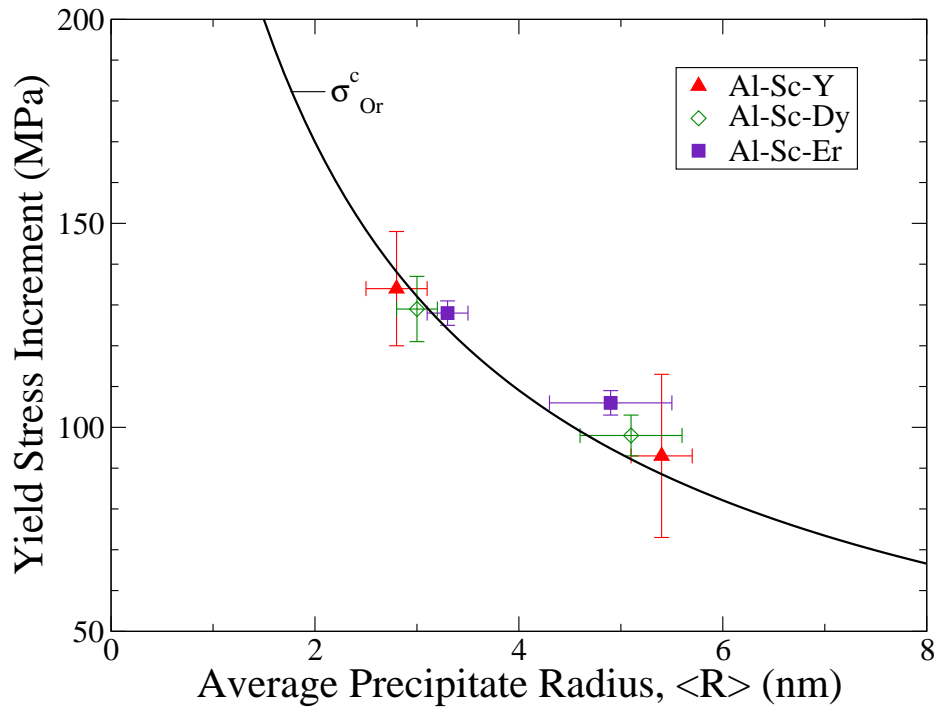


Figure 7.7. Yield stress increment (calculated as Vickers microhardness increment divided by 3) as a function of precipitate size, compared with the calculated Orowan strengthening from Eq. 7.1 for Al-600 at. ppm Sc-200 at. ppm RE (RE=Y, Dy, Er).

of smaller precipitates, assuming a similar volume fraction of precipitates. Indeed, for the same aging treatment near peak microhardness (300°C/24 h), the mean precipitate size for the Dy, Er, and Y containing alloys goes inversely with misfit (Table 7.2), but sampling error is again significant and there may be difference in precipitate volume fraction.

The calculated increase in yield strength due to Orowan dislocation looping, σ_{Or}^c , is given by [102]:

$$(7.1) \quad \sigma_{Or}^c = M \frac{0.4}{\pi} \frac{\mu b}{\sqrt{1-\nu}} \frac{\ln\left(\frac{2\bar{R}}{b}\right)}{\langle \lambda_{e-e}^{2D} \rangle};$$

where M is the mean Taylor matrix orientation factor ($M = 3.06$ for Al [161]), μ is the shear modulus ($\mu = 25.4$ GPa for Al at 24°C [47]), b is the magnitude of the Burger's vector ($b = 0.286$ for Al [47]), ν is Poisson's ratio ($\nu = 0.345$ for Al [161]), \bar{R} is the mean radius for circular cross-sections of precipitates ($\bar{R} = 0.822\langle R \rangle$ ($\langle R \rangle$ is the mean precipitate radius) assuming an LSW precipitate size distribution [130]), and $\langle \lambda_{e-e}^{2D} \rangle$ is the mean edge-to-edge interprecipitate spacing in a glide plane (for volume fraction, ϕ , $\langle \lambda_{e-e}^{2D} \rangle = \left(1.538\phi^{-\frac{1}{2}} - 1.643\right)\langle R \rangle$ [130] assuming an LSW precipitate size distribution falls on a square lattice of precipitates). Because the dilute ternary phase diagrams for Al-Sc-RE have not been calculated, ϕ was taken from the lever-rule on the binary Al-Sc phase diagram with the total solute content. This is thought to be a good approximation as most Sc and RE do precipitate out and the volume fractions are comparable to those measured with LEAP tomography (Chapter 3). For the Al-600 Sc-200 RE, $\phi = 0.33\%$ and for the Al-900 Sc-300 Er, $\phi = 0.49\%$. The experimental increment in yield stress, σ_{Or}^e , was found by dividing the peak microhardness increment by 3 [159], and is in good agreement with the calculated Orowan strengthening (Fig. 7.7 and Table 7.2).

7.4.2. Creep

A modified version of the Mukherjee-Bird-Dorn power-law equation states that the minimum strain rate, $\dot{\epsilon}$, is (Eq 1.3):

$$(7.2) \quad \dot{\epsilon} = A(\sigma - \sigma_{th})^n \exp\left(-\frac{Q}{R_g T}\right);$$

Table 7.2. Mean radius, creep threshold stress, experimentally determined Orowan strength increment, and calculated Orowan strength increments for the Al-Sc-RE specimens in this study.

Alloy	Aging treatment	$\langle R \rangle$ (nm)	σ_{th} (MPa)	σ_{Or}^e at 24°C (MPa)	σ_{Or}^c at 24°C (MPa)	σ_{Or}^c at 300°C (MPa)
Al-600 Sc 200 Y	300°C, 1 d	2.8(3)	28.9(3)	134(14)	137(17)	118(15)
	300°C, 16 d	5.4(3)	32.4(1)	93(20)	88(6)	75(5)
Al-600 Sc 200 Dy	300°C, 1 d + 400°C, 1 d	9(2)	33(1)	—	61(15)	52(13)
	300°C, 1 d	3.0(2)	23.3(2)	129(8)	132(10)	113(9)
Al-600 Sc 200 Er	300°C, 16 d	5.1(5)	31.6(4)	98(5)	92(10)	79(9)
	300°C, 1 d	3.3(2)	17(1)	128(3)	124(9)	106(8)
	300°C, 16 d	4.9(6)	22(1)	106(3)	95(13)	81(11)
Al-900 Sc 300 Er	300°C, 1 d + 400°C, 1 d	10(2)	29(3)	—	56(12)	48(11)
	300°C, 1 d + 400°C, 5 d	15(2)	28(1)	—	41(6)	35(5)
	300°C, 1 d	4.1(5)	30.0(6)	115(5) ^a	132(19)	113(16)
	300°C, 16 d	7(2)	36(2)	128(4) ^b	91(29)	77(24)
				88(6) ^c		
				106(3) ^d		

^amicrohardness

^bcompressive yield

^cmicrohardness

^dcompressive yield

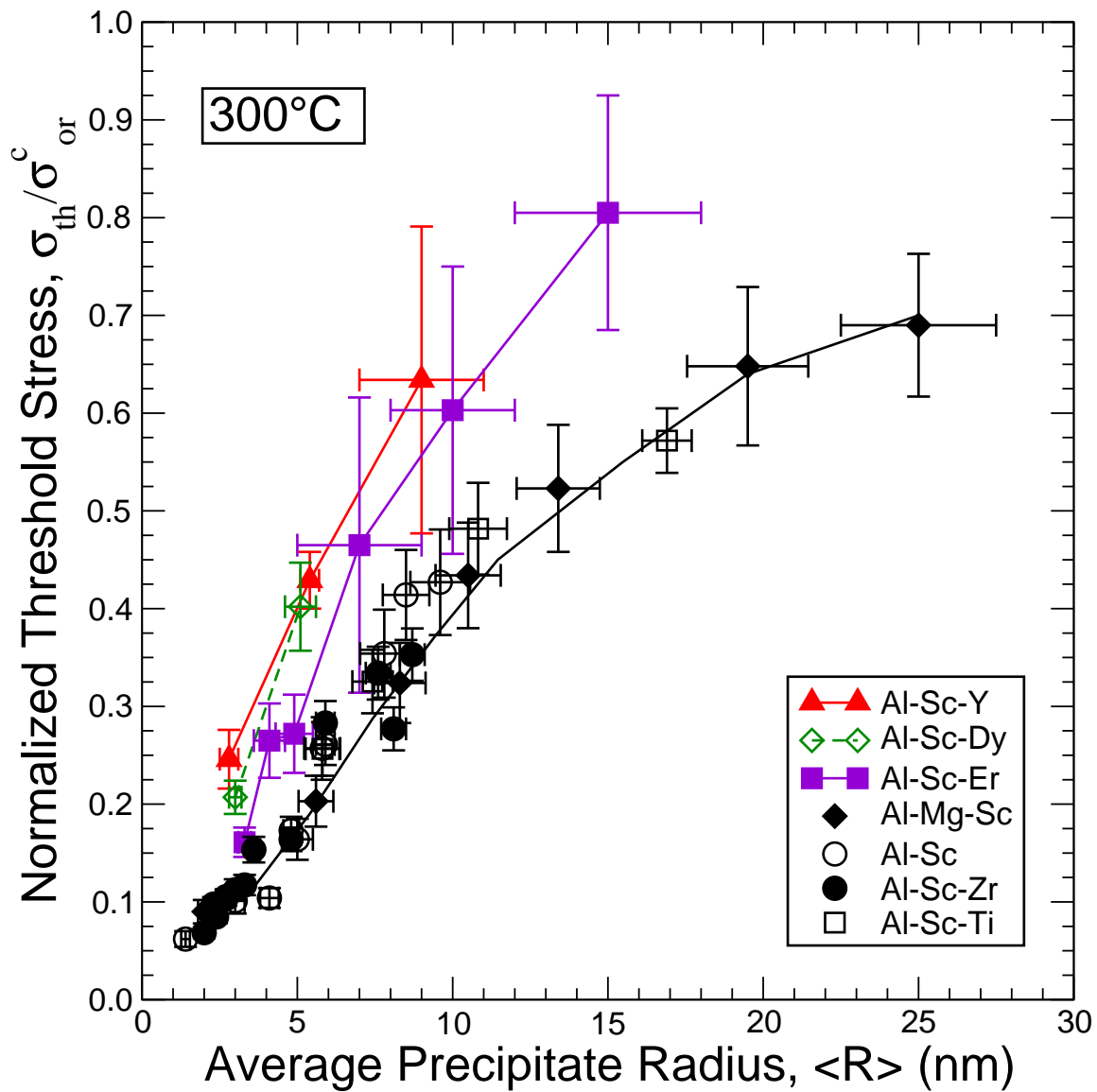


Figure 7.8. Creep threshold stress, normalized by the calculated Orowan stress at 300°C, as a function of average precipitate radius, $\langle R \rangle$. Normalized stresses are higher for the three Al-Sc-RE microalloys than any of the previously studied Al-Sc-M alloys [3-7].

where A is a constant, σ is the applied stress, σ_{th} the threshold stress, n is the stress exponent, Q the activation energy, R_g the ideal gas constant, and T the absolute temperature. The value of σ_{th} is calculated by dividing the intercept by the slope employing a weighted least-squares linear-regression of $\sqrt[n]{\dot{\epsilon}}$ vs. σ [55]. The experimental value for the Al matrix, $n = 4.4$, is used [53]. Threshold stresses increase with increasing precipitate size, as shown in Table 7.2. This is consistent with previous results for smaller precipitates in Al–Sc [3, 6], Al–Mg–Sc [4], Al–Sc–Zr [5], and Al–Sc–Ti [7] alloys. Larger precipitates in these alloys begin to have decreasing threshold stresses when the precipitates lose coherency with α -Al. As was previously observed for the Al–Sc–M alloys, the threshold stresses predicted for shearing and the general dislocation climb models [171] do not explain our results: the former predicts stresses that are too high and the latter does not explain the precipitate radius dependence. The experimental behavior is, however, consistent with a modified general climb model [57], which considers the elastic interactions due to the lattice-parameter and modulus mismatches between the α -Al matrix and the $\text{Al}_3(\text{Sc}_{1-x}\text{RE}_x)$ precipitates. Based on the larger lattice-parameter mismatch exhibited by Al–Sc–RE alloys, this model also predicts correctly the trend of larger threshold stresses for these alloys as compared to Al–Sc, Al–Mg–Sc, Al–Sc–Zr, and Al–Sc–Ti alloys. This trend is evident in a normalized threshold plot (Fig. 7.8), where σ_{th} is divided by σ_{Or}^c (Eq. 7.1). Similar mean values of the normalized threshold stress are displayed in other Al–Sc–RE alloys where RE=Gd or Yb (Fig. 7.9) [9]. Due, in part, to the high reported errors in threshold stress of these alloys and also to the strong dependence on $\langle R \rangle$, trends between Al–Sc–RE with five different REs are more difficult to assess. The normalized threshold stresses for a particular $\langle R \rangle$ could be the same within experimental uncertainty. However, the mean values of the normalized

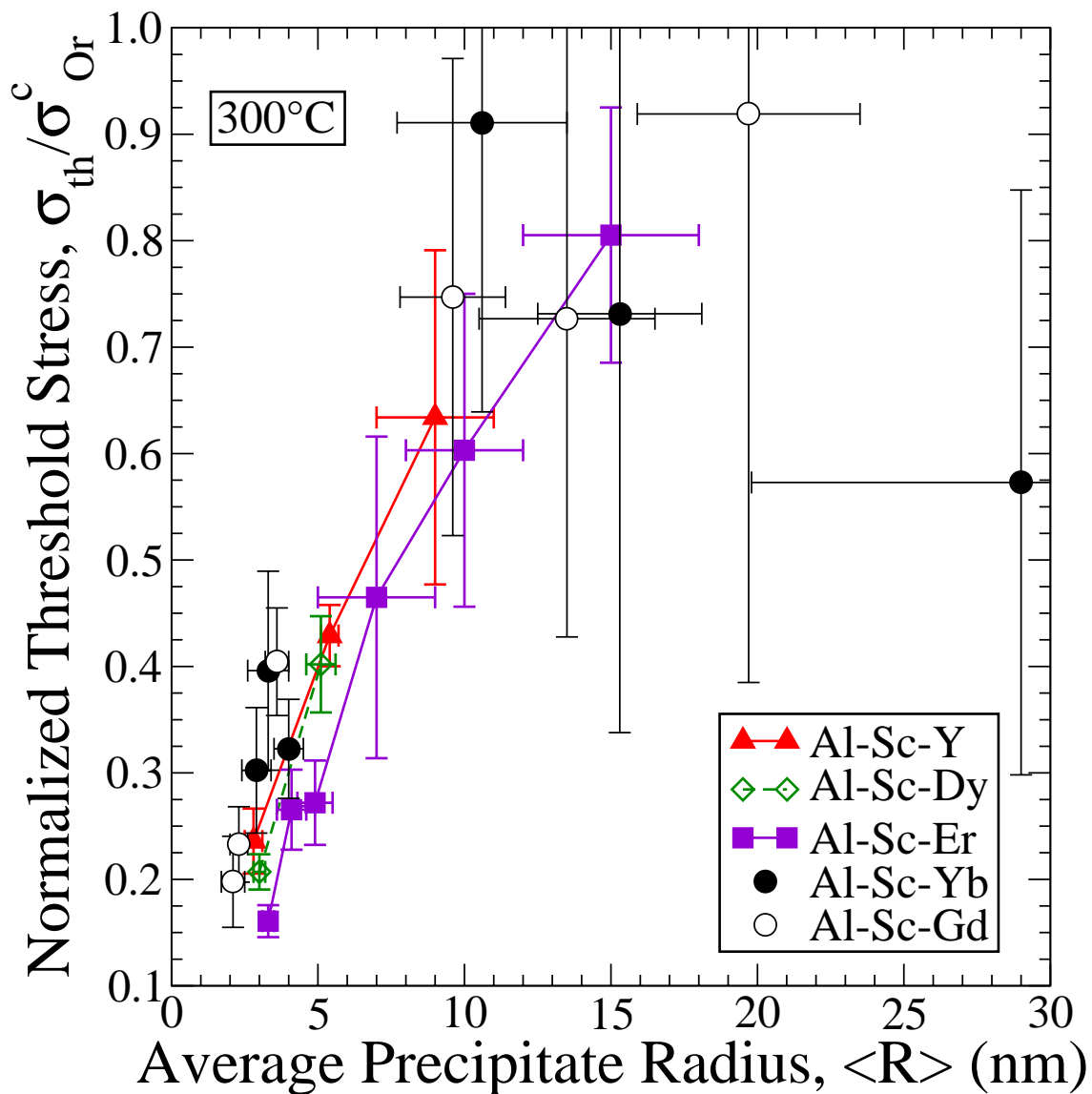


Figure 7.9. Creep threshold stress, normalized by the calculated Orowan stress at 300°C, as a function of average precipitate radius, $\langle R \rangle$ compared with other Al-Sc-RE alloys where RE=Yb, Gd [9].

threshold for precipitates ca. $\langle R \rangle < 12$ are higher in Al-Sc-Yb and Al-Sc-Gd, despite their lower lattice parameter misfit with α -Al. As $\langle R \rangle$ increases past this size in Al-Sc-Yb and Al-Sc-Gd, the mean value of the normalized threshold stress decreases. This might be

due to the loss of coherency of $\text{Al}_3(\text{Sc}_{1-x}\text{RE}_x)$ precipitates with respect to the α -Al matrix. As precipitates become semi-coherent, the lattice stresses that impede dislocation climb decrease. However, misfit dislocations at the interface may also impede dislocation motion. Also, when precipitates become completely incoherent, the departure interface becomes attractive to dislocations (see Chapter 8). The transition between these several possible origins of the threshold stress are difficult to model, which makes the highest normalized threshold stresses difficult to compare.

7.5. Conclusions

The mechanical properties of Al-600 at. ppm Sc-200 at. ppm RE (RE=Y, Dy, or Er) and Al-900 at. ppm Sc-300 at. ppm Er were studied at ambient temperature and at 300°C, leading to the following conclusions:

- $\text{Al}_3(\text{Sc}_{1-x}\text{RE}_x)$ precipitates, created by aging at 300°C, lead to high ambient temperature strengths, as measured by Vickers microhardness.
- Even though the Al-Sc-RE microalloys overage when exposed at 300°C for over 96 h, the microhardness is greater than the as-homogenized hardness after aging times as long as 1,536 h.
- Al-Sc-RE alloys are creep resistant at 300°C and exhibit a threshold stress that increase with increasing mean precipitate radius. This same trend was observed in Al-Sc, Al-Mg-Sc, Al-Sc-Zr, and Al-Sc-Ti microalloys studied previously. This trend is also in agreement with a modified general climb model that includes elastic interactions between dislocations and the stress fields of $\text{Al}_3(\text{Sc}_{1-x}\text{RE}_x)$ precipitates in an α -Al matrix.

CHAPTER 8

Strengthening Mechanisms in Aluminum Containing Coherent Al_3Sc Precipitates and Incoherent Al_2O_3 Dispersoids

8.1. Introduction

Incoherent ceramic dispersoids (with size below ca. 1 μm) distributed within a coarse-grained metallic matrix provide high strength at ambient and elevated temperatures, as they impede dislocation glide and climb [172]. Choosing chemically stable and coarsening-resistant submicron dispersoids such as Al_2O_3 allows for dispersion-strengthened aluminum with creep-resistance to high temperatures (500°C and above [44, 173–180]). When creep is controlled by dislocation motion, the minimum strain rate, $\dot{\epsilon}$, of dispersion-strengthened aluminum can be described by a power-law equation [46]:

$$(8.1) \quad \dot{\epsilon} = A_{ap} \sigma^{n_{ap}} \exp\left(-\frac{Q_{ap}}{R_g T}\right);$$

where subscript ap stands for “apparent,” A is a dimensionless constant (calculated from the diffusion coefficient, shear modulus, test temperature, Burgers vector and grain size of the matrix), σ is the applied stress, n is the matrix stress exponent (which is mechanism- and material-dependent), Q is the matrix creep activation energy, R_g is the ideal gas constant and T is the absolute temperature. Dispersion-strengthened aluminum exhibits much lower strain rates than pure aluminum in the low-stress regime, as well as higher apparent stress-

and temperature-dependence (n_{ap} and Q_{ap}). This behavior can be modeled by introducing in Eq. 8.1 a threshold stress, σ_{th} , below which creep is not measurable experimentally (Eq. 1.3):

$$(8.2) \quad \dot{\epsilon} = A(\sigma - \sigma_{th})^n \exp\left(-\frac{Q}{R_g T}\right).$$

For dispersion-strengthened alloys, the origin of the threshold stress has been shown to be the detachment of the dislocations from the incoherent dispersoids [181]. This detachment model, some versions of which consider thermally activated detachment of dislocations [182], was recently modified to take into account the effect of dislocation pile-up in dispersion-strengthened-cast aluminum (DSC–Al) consisting of unalloyed aluminum with high volume fractions (>20%) of submicron alumina dispersoids [183].

Whereas dispersoids are typically added *ex situ* in aluminum by powder or liquid metallurgy and are thus incoherent with the matrix, precipitates are created *in situ* in aluminum by heat-treatment and can remain coherent when their size is small. The low precipitate volume fractions achievable in conventionally cast aluminum alloys dictate that the precipitates must remain nanometric in size to maintain their effectiveness against dislocation motion. For long-term creep resistance, alloying additions producing slow-coarsening precipitates are thus essential and among various candidates [169], scandium has been the focus of recent research for creep-resistant aluminum alloys [3–7, 79–81, 184].

Homogenized, dilute Al–Sc alloys (with Sc concentration below the maximum solubility of 0.23 at.%) can be aged to form a high number density of coherent $L1_2$ Al_3Sc precipitates which show negligible coarsening rates up to about 300°C [11–17]. Zirconium can partially

substitute for Sc in precipitates, forming coherent $L1_2$ $Al_3 (Sc_{1-x}Zr_x)$ precipitates with improved coarsening resistance up to at least 350°C. This is due to the much lower diffusivity of Zr as compared to Sc, and to Zr partitioning to the precipitate interface which inhibits Sc diffusion [25, 28–30, 39, 185, 186]. Coherent precipitates have been shown to increase the creep-resistance of cast, coarse-grained Sc-containing alloys with additions of Mg, Zr, Ti, or rare-earth elements by introducing a threshold stress [3–7, 79–81, 184]. Because these precipitates are coherent, detachment cannot be invoked as a threshold mechanism. Previous studies showed that precipitate cutting is not operative, leaving precipitate bypass by dislocation climb as the most likely threshold mechanism [3–6, 57]. A small threshold stress (ca. 2% of the Orowan stress) is expected for this general-climb mechanism, independently of precipitate radius [5, 6, 57, 171]. However, these dilute Al–Sc alloys show a threshold stress increasing with precipitate radius to much higher fractions of the Orowan stress (up to 70%) [6]. This behavior was explained by extending the general-climb model to include back-stresses acting on the dislocations, originating from the lattice and modulus mismatches between the aluminum matrix and the coherent Al_3Sc precipitates [57].

The present research examines DSC–Al–Sc(–Zr) alloys which contain two distinct populations of dislocation-impeding particles: a high volume fraction of submicron, incoherent Al_2O_3 dispersoids and a low volume fraction of nanometer-size, coherent Al_3Sc or $Al_3 (Sc_{1-x}Zr_x)$ precipitates. The microhardness and compressive properties at ambient temperature and the creep-resistance at elevated temperatures are measured for these alloys and compared to existing data on control alloys containing only one population of particles, i.e., Al–Sc(–Zr) alloys (with Al_3Sc or $Al_3 (Sc_{1-x}Zr_x)$) precipitates but without Al_2O_3 dispersoids) and DSC–Al (with Al_2O_3 dispersoids but without Al_3Sc or $Al_3 (Sc_{1-x}Zr_x)$ precipitates). Existing models

for the strengthening effect of each type of particles are combined to explain the synergistic strengthening found in the DSC–Al–Sc(–Zr) alloys with both types of particles.

8.2. Experimental methods

8.2.1. Materials preparation

An Al–0.11 at.% Sc (Al–0.18 wt.% Sc) alloy was created by dilution of small quantities of Al–0.5 wt. Sc master alloy to 99.9% pure Al. The melt was cast in an alumina crucible and solidified in air. This alloy is referred to as Al–Sc in the following. An Al–0.08 at.% Sc–0.03 at.% Zr alloy (Al–0.13 wt.% Sc–0.10 wt.% Zr, referred to as Al–Sc–Zr) was cast from 99.99% Al, an Al–1.7 wt.% Sc master alloy and an Al–4.4 wt.% Zr master alloy. This material was melted in a zirconia-coated alumina crucible, stirred and poured into a boron-nitride-coated graphite mold resting on a copper plate. The typical grain size of the resulting alloys was 1–2 mm. Alloy compositions were determined by plasma emission spectroscopy by Luvak Inc. (Boylston, MA, USA).

Chesapeake Composites Corp. (New Castle, DE, USA) supplied several dispersion-strengthened-cast (DSC) billets produced by melt infiltration of preforms of Al_2O_3 particles with a $0.3\ \mu\text{m}$ average size [41]. Two billets, referred to as DSC–Al–Sc and DSC–Al–Sc–Zr, were fabricated from the above Al–Sc and Al–Sc–Zr cast alloys. Three control billets, all referred to as DSC–Al, were fabricated from 99.98% pure Al. All DSC billets contained $30.1 \pm 0.2\ \text{vol.}\% \text{Al}_2\text{O}_3$ dispersoids, as determined from mass density measurements by the Archimedes method.

The unalloyed DSC–Al specimens were tested in the as-cast condition. Aging treatments for the other alloys consisted of homogenization at 640°C in air for 24 h for the alloys without

Zr and for 120 h for the alloys with Zr (due to the lower diffusivity), water-quenching to ambient temperature, aging in air at 300–450°C for various times, terminated by a water-quench to ambient temperature.

8.2.2. Conductivity measurements

Electrical conductivity was measured at ambient temperature on coupons (with at least 11 mm diameter, 5 mm width and polished to a 1 μm surface finish) aged in air at 300°C for various times after homogenization, using an eddy-current instrument (Sigmatest 2.069, from Foerster Instruments Inc. (Pittsburgh, PA)). Both sides of the coupons were measured at operating frequencies of 60, 120, 240, 480, and 960 kHz. Errors reported are for one standard deviation from the mean value.

8.2.3. Mechanical properties

Vickers microhardness measurements were performed with a 500 g load for 5 s on coupons (with size at least $5 \times 5 \times 3 \text{ mm}^3$ and polished to a 1 μm surface finish) aged in air at 300 and 350°C for various times after homogenization. Errors reported are for one standard deviation from the mean value.

Cylindrical DSC specimens (with 8.10 mm diameter and 16.10 mm length) were electro-discharge machined with their axes parallel to that of the cast billet. DSC–Al–Sc specimens, homogenized and aged at 350°C for 24 h and 450°C for 60 h, were tested in uniaxial compression at ambient temperature, using a constant rate of crosshead displacement of 1.0 mm/min. Compressive creep experiments at constant load were performed in air at

300 and 350°C for the three DSC alloys, using a three-zone, resistively heated furnace with a temperature stability of $\pm 1^\circ\text{C}$. A superalloy compression-cage was used with boron-nitride-lubricated alumina platens. The platen displacement, transmitted by an extensometer connected to a linear voltage displacement transducer, was continuously monitored and recorded by computer to 2.5 μm resolution. At any given stress level, sufficient time was allowed to establish a minimum creep rate, as determined by weighted linear regression. If the sample had not failed, the load was increased. Therefore, a single specimen could be utilized to obtain minimum creep rates at multiple stress levels. Typically, steady-state creep rate was determined after ca. 2% strain, over approximately the last 0.5% strain range. Different aging treatments were utilized for the DSC–Al–Sc(–Zr) specimens, in order to study the effects of distribution and size of $\text{Al}_3(\text{Sc}_{1-x}\text{Zr}_x)$ precipitates. Some specimens were used repeatedly in creep tests after intermediate aging treatments, as described later.

8.3. Results

8.3.1. Microhardness and strength at ambient temperature

Fig. 8.1 shows the evolution of microhardness with aging time at 300 and 350°C for all alloys in this study. The four expected regimes for precipitation strengthening (due to formation of Al_3Sc or $\text{Al}_3(\text{Sc}_{1-x}\text{Zr}_x)$ precipitates) can be observed sequentially: (i) a short region where hardness remains equal to the as-cast value (incubation); (ii) a rapid increase in hardness (under-aging); (iii) a plateau in hardness values (peak-aging); and (iv) a slow decrease in hardness (over-aging).

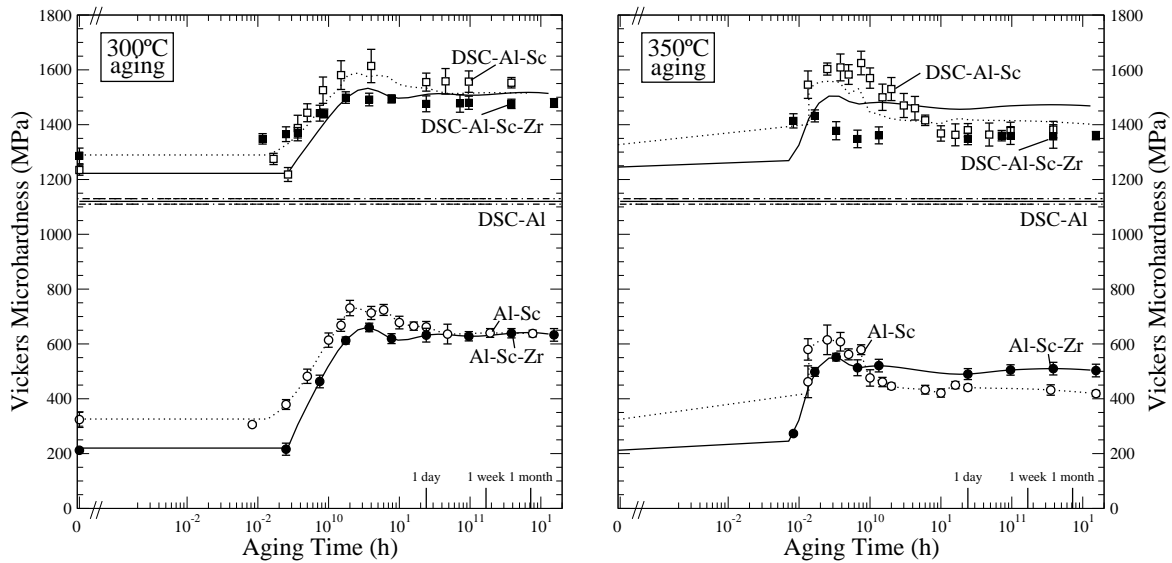


Figure 8.1. Vickers microhardness as a function of aging time at (a) 300°C and (b) 350°C. The curves for the DSC–Al–Sc and DSC–Al–Sc–Zr were calculated from Eq. 8.3 with $k = 1.3$, using best-fit curves for DSC–Al, Al–Sc and Al–Sc–Zr.

In Al–Sc, peak-aging occurs after ca. 2 h at 300°C and ca. 0.25 h at 350°C. Also, onset of overaging occurs earlier at 350°C. The overaged microhardness appears stable for times longer than 16 h at 300°C or 6 h at 350°C. The peak hardness for aging at 350°C is lower than that at 300°C by about 16%, while the overaged hardness at 350°C is lower than that at 300°C by about 31%.

Al–Sc–Zr achieves peak-aging after ca. 4 h at 300°C and ca. 0.3 h at 350°C, the same times as Al–Sc within experimental error. The peak hardness is slightly lower in Al–Sc–Zr at both aging temperatures. Over-aging in Al–Sc–Zr does not cause as much of a decrease of hardness as in Al–Sc and the hardness remains stable when aged for 1,536 h (64 days).

In DSC–Al–Sc, hardness peaks after ca. 4 h at 300°C and ca. 0.4 h at 350°C. The hardness decreases slightly after achieving its peak value and then remains almost constant for over 384 h (16 days) at either 300 or 350°C. The time span of this plateau is longer than a creep experiment, so precipitate radii can safely be assumed to remain constant through a creep test. The peak hardness for aging at 350°C is the same as at 300°C, within experimental error, while the stable hardness for aging at 350°C is lower than that at 300°C by about 14%. The DSC–Al–Sc peak hardness is about three times higher than that of Al–Sc when aged at 350°C and about twice as high when aged at 300°C. This illustrates the hardening contribution from the Al₂O₃ dispersoids, which is independent of aging time or temperature. DSC–Al–Sc–Zr reaches peak-aging after ca. 2 h at 300°C and after 0.2 h at 350°C. Both of these times, though shorter, are within experimental error of the peak-aging times for DSC–Al–Sc. The peak hardness of DSC–Al–Sc–Zr is lower than that of DSC–Al–Sc by ca. 7% when aged at 300°C and ca. 12% when aged at 350°C. At 300°C, hardness remains constant at the peak value when overaged for as long as 1,536 h (64 days), as with Al–Sc–Zr. Thus, the assumption that precipitate size is constant through a creep experiment is safe. Although there is little change in hardness when aged at 350°C, DSC–Al–Sc–Zr is always harder than the as-homogenized alloy. This trend of lower hardness for higher aging temperatures was previously observed for Al–Sc–Zr alloys and was attributed to coarsening [5].

In Fig. 8.2, the normalized electrical conductivity, $\sigma_n(t) = \frac{\sigma(t) - \sigma(t=0)}{\sigma(t=t_{max})}$, is plotted against aging time at 300°C, where $\sigma(t)$ is the electrical conductivity at time $t = 0$ (no aging), t or t_{max} (longest aging time). The conductivity increases with aging, as the concentration of Sc and Zr atoms in solid-solution within the matrix decreases from the as-homogenized values due to precipitation. The curves of the DSC alloys overlap those of their matrix alloys,

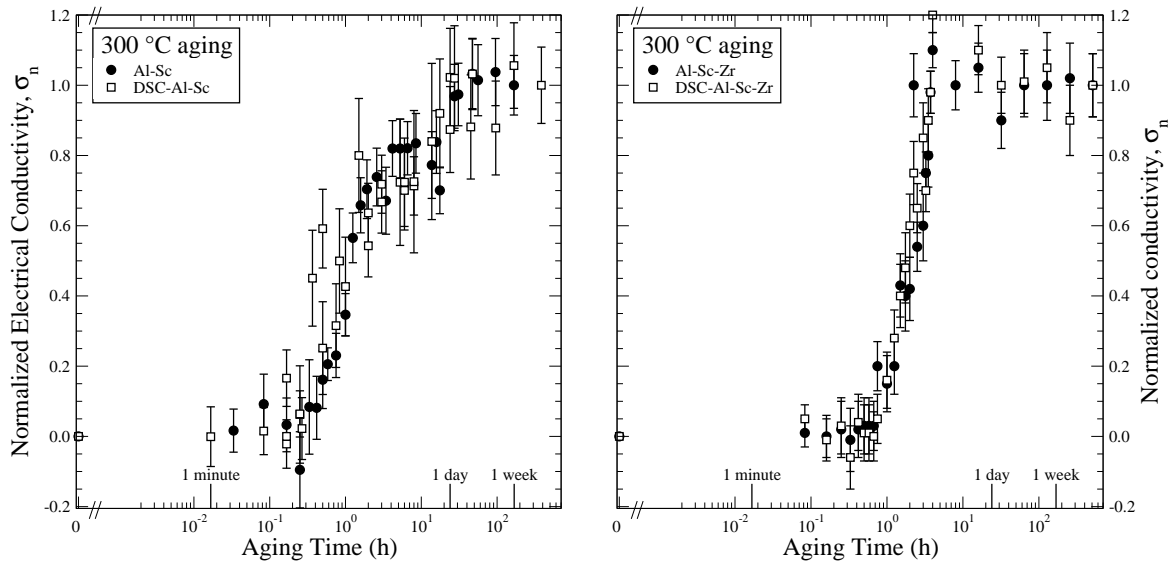


Figure 8.2. Normalized electrical conductivity as a function of aging time at 300°C for (a) DSC–Al–Sc and Al–Sc and (b) DSC–Al–Sc–Zr and Al–Sc–Zr.

indicating that the Al_2O_3 dispersoids do not significantly modify the nucleation and growth of Al_3Sc or $\text{Al}_3(\text{Sc}_{1-x}\text{Zr}_x)$ precipitates.

The compressive yield stress, as measured by the first detectable deviation from the linear portion of the stress-strain curve, is 350 ± 10 MPa for DSC–Al aged at 350°C for 24 h and 270 ± 10 MPa when aged at 450°C for 60 h. The 0.2% proof stresses were 357 ± 2 and 275 ± 2 MPa, respectively. The ultimate compressive strengths were 609 and 500 MPa. These strengths are slightly higher than those reported for DSC–Al with 32 vol.% Al_2O_3 [42]. Direct comparison is not possible, since this previous alloy had been extruded and thus exhibited a very small grain size ($0.88 \mu\text{m}$) contributing to its strength. However, the drop in strength observed upon overaging in the present alloys is a clear indication that precipitates contribute to ambient-temperature strength. The Young's modulus, found from

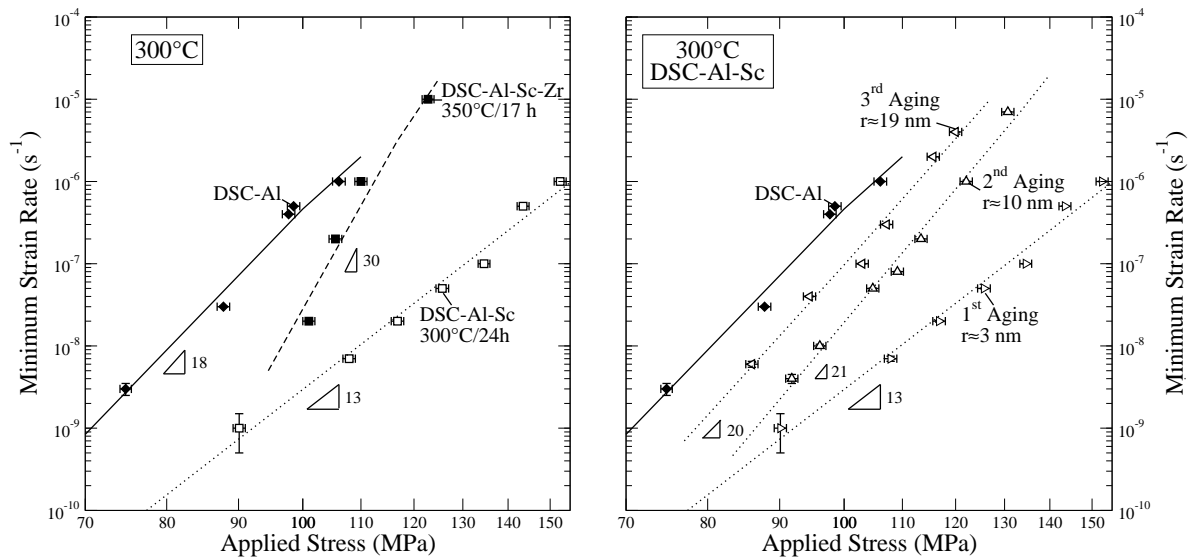


Figure 8.3. Stress dependence of minimum compressive creep strain rate at 300°C. (a) For DSC–Al, DSC–Al–Sc and DSC–Al–Sc–Zr, the latter two alloys being aged to achieve Al₃Sc and Al₃(Sc_{1-x}Zr_x) precipitates with the same radius of ca. 3 nm. (b) For a DSC–Al–Sc sample subjected to three successive aging treatments to coarsen Al₃Sc precipitates (estimated as 3, 10 and 19 nm). DSC–Al curve is reproduced for comparison.

the elastic slope of the stress-strain curve, is 103 ± 5 GPa for both samples, in good agreement with previous results on DSC–Al without alloying additions to the matrix [187, 188].

8.3.2. Creep properties

Fig. 8.3(a) displays the steady-state creep behavior at 300°C—plotted as minimum creep rate, $\dot{\epsilon}$, vs. applied stress, σ , on double-logarithmic axes—for DSC–Al, DSC–Al–Sc (aged at 300°C for 24 h) and DSC–Al–Sc–Zr (aged at 350°C for 17 h). The aging treatments were selected to yield approximately the same 3 nm precipitate radius for both Sc-containing alloys, based on measurements reported in Refs. [75, 91]. All three alloys have high apparent stress

exponents, indicative of a threshold stress. DSC–Al–Sc is significantly more creep-resistant than Sc-free DSC–Al. DSC–Al–Sc–Zr is less creep-resistant than DSC–Al–Sc, but still more creep-resistant than DSC–Al at strain rates below about 10^6 s^{-1} .

After creep testing, the above DSC–Al–Sc sample, which had been aged at 300°C for 24 h prior to testing, was reaged at 450°C for 24 h and creep tested again. Finally, the same sample was subjected to a third aging treatment at 450°C for 24 h and creep tested for a third time. Creep results are plotted in Fig. 8.3(b), which shows that creep-resistance decreases with increased aging, as expected if precipitates are coarsening during the second and third heat-treatments. Nevertheless, the overaged DSC–Al–Sc sample which had been subjected to three aging treatments remained more creep-resistant than the precipitate-free DSC–Al samples.

The threshold stress was found by plotting creep data as $\dot{\epsilon}$ vs. $\sigma^{\frac{1}{n}}$, and extrapolating to $\dot{\epsilon} = 0$ using a weighted least-squares linear regression [55]. Since diffusional creep is not active given the large grain size, we use here the experimentally-determined exponent for dislocation creep of pure aluminum, $n = 4.4$ [47], which is between the theoretical values for glide ($n = 3$ [48, 49]) and climb ($n = 5$ [49, 50]) and which has been used successfully in previous studies on DSC–Al without precipitates [44] and on Al–Sc(–Zr) alloys without dispersoids [3–5]. The threshold stresses for creep at 300°C are listed in Table 8.1. Good linear fits were obtained for all samples, except for one case marked in Table 8.1. Also given in Table 8.1 are threshold values for DSC–Al and DSC–Al–Sc–Zr at 350°C ; data for DSC–Al–Sc are omitted due to coarsening of the precipitates (Fig. reffig:dsc-mh(b)).

Table 8.1. Aging treatment, estimated precipitate radius, apparent stress exponent and threshold stresses for DSC-Al(-Sc(-Zr)) creep experiments at 300 and 350°C

Material	Aging treatment (°C)	300°C Creep Experiments	Estimated radius (nm)	n_{ap}	σ_{th} (MPa)
DSC-Al	As-cast		0	18	59 ± 3
	450°C/24 h		0	15	57 ± 2
DSC-Al-Sc	300°C/24 h		3	13	97 ± 8
	As previous, crept 300°C, aged 400°C/24 h		10	21	86 ± 6
	As previous, crept 300°C, aged 400°C/24 h		19	20	84 ± 7
	300°C/24 h		3	13	76 ± 3
DSC-Al-Sc-Zr	As previous, crept 300°C, aged 450°C/2 h		6	25	110 ± 20 ^a
	As previous, crept 300°C, aged 450°C/24 h		30	22	91 ± 4
	300°C/24 h		3	13	76 ± 3
	350°C/24 h		4	13	79 ± 2
	300°C/72 h		2	25	77 ± 2
	300°C/72 h		2	26	77 ± 1
	350°C/17 h		3	30	94 ± 7
	375°C/3 h		8	25	78 ± 3
	350°C/192 h		12	22	83 ± 2
	375°C/48 h		24	21	85 ± 1
DSC-Al	As cast	350°C Creep Experiments	0	21	52 ± 1
	450°C/24 h		0	20	52 ± 3
DSC-Al-Sc-Zr	350°C/17 h		3	28	71 ± 3
	350°C/17 h		3	25	75 ± 2
	375°C/3 h		8	33	78 ± 2
	350°C/192 h		12	26	79 ± 2

^anot plotted in Fig. 8.4 and Fig. 8.6 due to high error

8.4. Discussion

8.4.1. Ambient temperature hardness

Fig. 8.1 shows that, in all four cases (aged at 300 and 350°C, with and without Al₂O₃ dispersoids), the Zr-containing samples exhibit lower hardness than their Zr-free counterparts. This can be explained by the tendency, during aging, for most of the Zr atoms to remain in solid-solution while Sc precipitates, so that only a small amount of the Zr available in the alloy is found in the Al₃(Sc_{1-x}Zr_x) precipitates. For example, it has been observed in Al-0.09 Sc-0.047 Zr that, after aging for 2412 h (ca. 100 days) at 300°C, the value of x is only 0.042 ± 0.007 , indicating that Zr substitutes only 1 in 24 ± 4 Sc atoms in the precipitates [29]. Thus, the volume fraction of precipitates in the DSC-Al-Sc-Zr matrix is, to a good approximation, reduced to that of a Al-0.08 at.% Sc alloy and is lower than that of DSC-Al-Sc containing 0.11 at.% Sc. At 300°C, the precipitate volume fractions in the matrix are thus 0.33 and 0.45 vol.%, respectively, as calculated from the lever rule. However, even at these low substitution levels, it is known that Zr is very effective at slowing the coarsening kinetics of the precipitates [91]. This is indeed observed in Fig. 8.1, which show no overaging for DSC-Al-Sc-Zr, unlike DSC-Al-Sc which overages slightly at 300°C and noticeably at 350°C.

Although the nominal peak-aging times seem to differ among samples with and without Al₂O₃ dispersoids (e.g., 2 h for Al-Sc and 4 h for DSC-Al-Sc at 300°C), the peak times are in fact undistinguishable when considering error bars on the hardness values in Fig. 8.1. This is confirmed by the conductivity curves for aging at 300°C (Fig. 8.2), which also show no significant difference between samples with and without Al₂O₃ dispersoids. The lack

of influence of the incoherent Al_2O_3 particles upon the precipitation kinetics of Al_3Sc precipitates is in disagreement with several previous studies which found that ceramic particulates (with a wide range of size and volume fraction) accelerate precipitation [43, 189–192]. This effect is often assigned to the presence of mismatch dislocations punched by the dispersoids into the matrix, which allow discontinuous nucleation and enhance growth of precipitates. However, other studies have shown that, for some matrix materials, aging is slowed or unaffected by dispersoids [43]. The lack of effect on the kinetics of precipitation observed in the present study may be due to the propensity for Al–Sc and Al–Sc–Zr alloys to exhibit a very high number density of homogeneously nucleated precipitates [12, 13, 15, 17, 75, 91], so that heterogeneous nucleation on mismatch dislocations produced by dispersoids does not contribute appreciably to the final number density. We thus assume in the following that the Al_2O_3 dispersoids do not alter the temporal evolution of Al_3Sc size, thus allowing for the direct comparison of specimens with and without Al_2O_3 at the same aging treatment. Fig. 8.1 illustrates that the majority of the hardness of the DSC alloys originates from the Al_2O_3 dispersoids ($\text{HV} = 1120 \pm 10$ MPa for DSC–Al). At peak-aging, however, the Al_3Sc precipitates boost hardness by ca. 50% (to $\text{HV} = 1614 \pm 61$ MPa for DSC–Al–Sc aged at 300°C), thus contributing a substantial fraction of the total hardness, despite a 100-fold smaller volume fraction (0.32 vol.% Al_3Sc in DSC–Al–Sc aged at 300°C vs. 30 vol.% for Al_2O_3). This illustrates that the fine size of the precipitates (with mean radius of ca. 2 nm at peak aging [3–6, 8], as compared to ca. 150 nm for Al_2O_3) is essential to their effectiveness as strengtheners in the alloy.

The overall strength τ_t of a material with various operative strengthening mechanisms, each with a characteristic strength increment τ_i , can be described by the empirical equation [6,

193, 194]:

$$(8.3) \quad \tau_t^k = \sum_i \tau_i^k;$$

with an exponent $1 \leq k \leq 2$. All hardness values for DSC–Al–Sc fall within the upper and lower bounds for τ_t , given by exponents $k = 1$ (linear sum) and $k = 2$ (Pythagorean sum), respectively. A least-squares refinement gives $k = 1.30 \pm 0.05$ for DSC–Al–Sc and DSC–Al–Sc–Zr, and the resulting lines are given in Fig. 8.1. This value compares well with an earlier experimentally-determined value $k = 1.4$ for aluminum alloys with a bimodal distribution of precipitates [195]. Other combinations of strengthening mechanisms provide different values for the exponent. For example, $k = 1$ was found for an aluminum alloy strengthened both by nanoscale Al_3Sc precipitates and Mg in solid-solution [6].

8.4.2. High temperature strength

8.4.2.1. Threshold stress. The threshold stresses at 300 and 350°C listed in Table 8.1 for precipitate-free DSC–Al are in agreement with those in the literature [44]. DSC–Al–Sc(–Zr) alloys have significantly higher threshold stresses than DSC–Al or literature data for Al–Sc(–Zr) alloys [3–5, 79]. This indicates that, as for hardness at ambient temperature, high-temperature strengthening occurs at both length scales, due to the two populations of nanometer-sized $\text{Al}_3(\text{Sc}_{1-x}\text{Zr}_x)$ precipitates and the submicrometer Al_2O_3 particles. This case is different from that considered by previous authors on dual-population strengthening [196–199], where the two populations consist of dispersoids impeding dislocations and

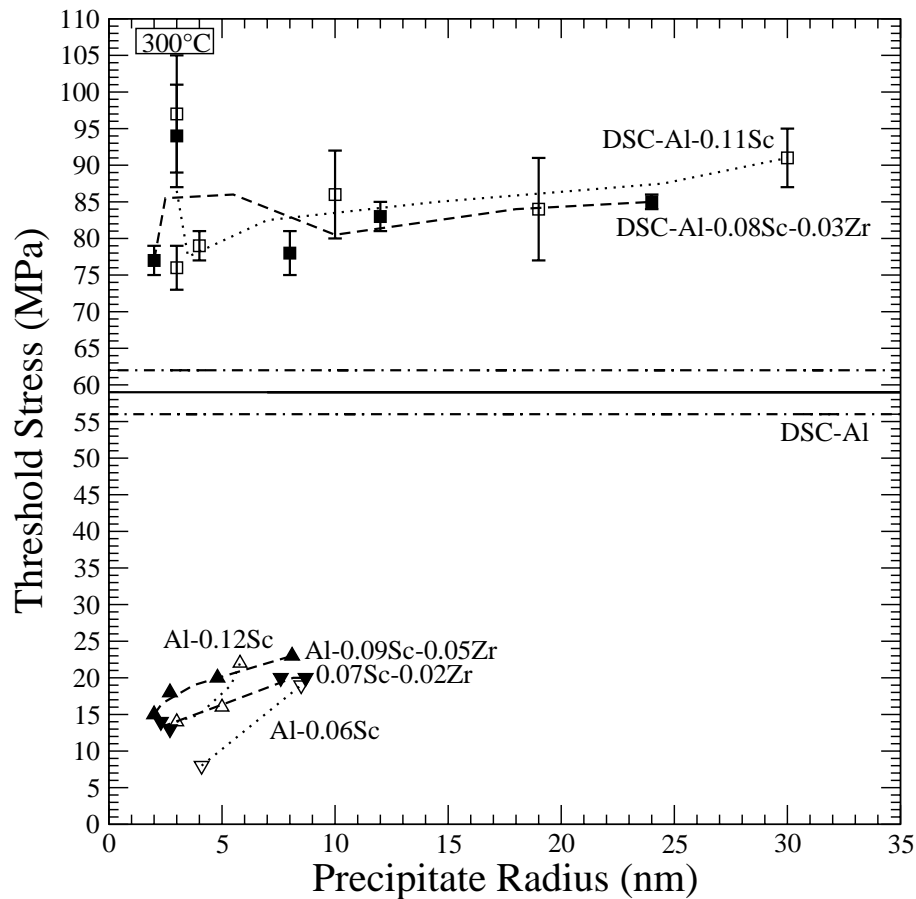


Figure 8.4. Creep threshold stress at 300°C as a function of estimated $\text{Al}_3(\text{Sc}_{1-x}\text{Zr}_x)$ radius for present DSC alloys as well as Al–Sc [3, 4] and Al–Sc–Zr alloys [5] (compositions in at.%). Lines show trends.

supramicrometer reinforcements which strengthen the material by load transfer (rather than nanometer-size precipitates, as considered here, which also impeded dislocations).

The threshold stresses at 300°C are plotted for all materials in Fig. 8.4 against the precipitate radius, estimated based on coarsening kinetics in Al–Sc [75] and Al–Sc–Zr [91] alloys. One micrograph by Marquis [200] for DSC–Al–Sc aged at 350°C for 2 h confirms that these

estimates are realistic. The threshold stress of DSC–Al–Sc(–Zr) shows a mildly increasing trend with aging time. A similar stronger trend exists for Al–Sc and Al–Sc–Zr alloys [5], as also shown in Fig. 8.4 and has been modeled previously by considering the elastic interactions between dislocations and precipitates [57]. Fig. 8.4 also shows that, within error, the threshold stresses for DSC–Al–Sc(–Zr) are equal to the sum of the threshold stresses for DSC–Al and Al–Sc(–Zr). At first view, this is an unexpected result, as it may be expected that the overall threshold stress should be the higher of the threshold stress for the two active mechanisms. This prediction is based on the assumption that dislocation motion is impeded sequentially by each population of particles. Dislocations first climb over the many fine precipitates present between the larger dispersoids. Then, after they encounter and climb over a coarser dispersoid, they detach from it. As the two types of obstacles are overcome sequentially by the dislocations, the overall threshold stress is the higher of the two mechanisms, which is the detachment from the dispersoid in the present case. This approach predicts that the precipitates have no effect on the threshold stress of DSC–Al–Sc(–Zr), which is not supported by the experimental results (Table 8.1 and Fig. 8.4). The following section presents a possible explanation for this discrepancy.

8.4.2.2. Extension of the detachment model to include precipitate back-stress. Here, we consider that dislocation motion is impeded simultaneously, rather than sequentially, by both dispersoids and precipitates, which leads to a threshold stress higher than for a dislocation interacting with either type of particles, a trend in agreement with experimental data. This situation occurs when the dislocations are pinned at the departure side of the Al_2O_3 dispersoids (after having climbed over them), while concurrently being subjected to the elastic back-stress from nearby $\text{Al}_3(\text{Sc}_{1-x}\text{Zr}_x)$ precipitates. If that back-stress is negative,

i.e., opposite in sign to the shear stress externally applied to the dislocations, it impedes the dislocation detachment process so that the overall threshold stress is the sum of the true detachment stress from the dispersoids and the back-stress from the nearby precipitates. If the former is expressed as a tensile value, σ_D , and the latter is expressed as a shear value, τ_B , the overall threshold stress in tension, σ_{th} , is:

$$(8.4) \quad \sigma_{th} = \sigma_D + M\tau_B;$$

where M is the mean matrix orientation factor ($M = 3.06$ for Al [161])).

We do not seek to determine the tensile detachment threshold stress σ_D in DSC-Al, as this has been done previously by using the original detachment model [181, 182] with the additional consideration of dislocation pileups [183]. Rather, we consider a dislocation pinned at the departure side of an Al_2O_3 dispersoid and calculate the shear back-stress τ_B acting on this detaching dislocation by the first four nearest neighbor $\text{Al}_3(\text{Sc}_{1-x}\text{Zr}_x)$ precipitates (totaling 10 nearest precipitates), with other farther precipitates assumed to have a negligible back-stress. The overall threshold stress can then be calculated from Eq. 8.4. As for a previous model [57], we consider stresses associated with lattice and modulus misfit of Al_3Sc precipitates in the Al matrix. We assume an idealized, highly simplified geometry, sketched in Fig. 8.5, where any segment of an edge dislocation pinned at the departure side of the dispersoid is subjected to the stress field of 10 neighboring precipitates. The precipitates are assumed to have a constant radius and to be arranged on a cubic lattice, as used previously [57]. Thus, no enrichment of precipitates around the dispersoid is assumed, as supported by the unchanged precipitation kinetics with and without Al_2O_3 dispersoids (Fig. 8.1 and Fig. 8.2).

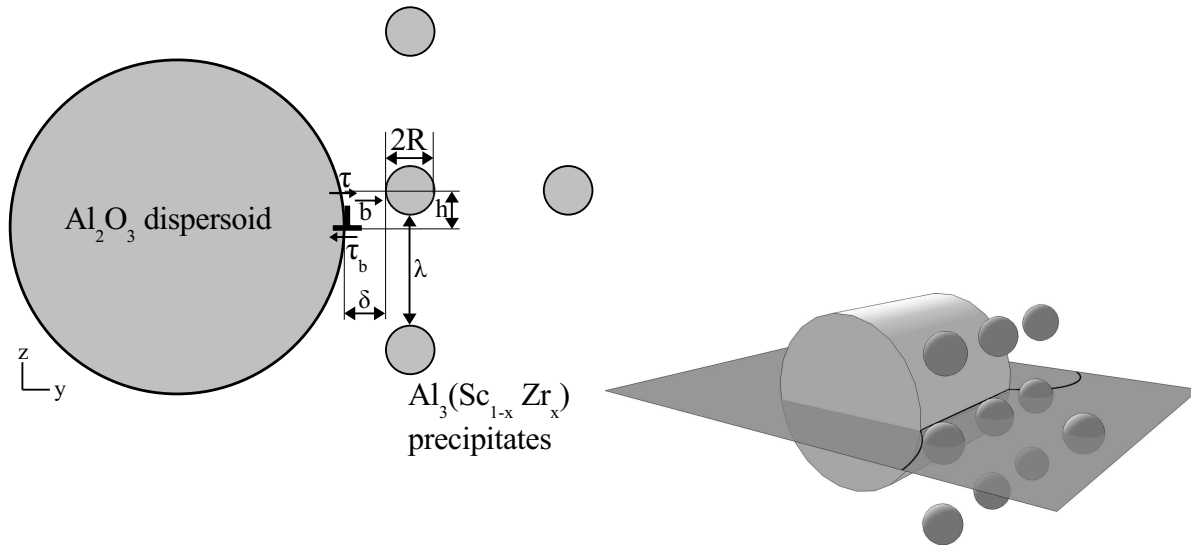


Figure 8.5. Schematic of Al_2O_3 dispersoid and $\text{Al}_3(\text{Sc}_{1-x}\text{Zr}_x)$ precipitates illustrating the geometry used in the model. (a) Projection perpendicular to the dislocation glide plane. A dislocation detaching from the departure side of the dispersoid is subjected to an applied resolved shear stress, τ , and a back-stress, τ_B , imposed by an array of $\text{Al}_3(\text{Sc}_{1-x}\text{Zr}_x)$ precipitates. (b) Three-dimensional schematic, showing all 10 precipitates (3×3 planar array and additional precipitate) contributing to the back-stress on the dislocation.

As shown in Fig. 8.5(a), there are four main geometric parameters for the calculation of the back-stress: the precipitate radius R , the spacing λ between the precipitates, and the spacing δ and height h between the dislocation slip plane and the nearest precipitate. Assuming a cylindrical shape for the alumina dispersoid (with diameter and height D) allows us to use a constant distance δ between the dislocation pinned at the departure side of the dispersoid and the nearest row of precipitate, as shown in Fig. 8.5(b). Then, a segment of the dislocation pinned at the interface, with length λ , is representative of the whole pinned dislocation length (neglecting end segments near the edge of the dispersoid).

The first component of the back-stress is due to the lattice mismatch between the precipitates and the matrix. Any point on the segment of length λ of the straight edge dislocation (with Burgers vector normal to the x-axis) is subjected to a shear stress τ_ε [130]:

$$(8.5) \quad \tau_\varepsilon = \frac{6C_{44}^{Al}\varepsilon R^3}{r^5}yz;$$

where R is the precipitate radius and r is the distance from the center of the precipitate to the point on a dislocation (given by $r = (x^2 + y^2 + z^2)^{\frac{1}{2}}$, where x , y and z are the coordinates of the center of the precipitate if the point on a dislocation is at the origin) and μ^{Al} is the temperature-dependent matrix shear modulus (given as $\mu^{Al} = 25.4 [1 - 0.5(T - 300)]/933$ with GPa units [47]). The temperature-dependent constrained lattice mismatch of the precipitate with the matrix, ε , is given by [130]:

$$(8.6) \quad \varepsilon = \frac{\varepsilon'}{1 + \frac{4\mu^{Al}}{3B_{Al_3(Sc_{1-x}Zr_x)}}}.$$

In this equation, $B_{Al_3(Sc_{1-x}Zr_x)}$ is the bulk modulus of the precipitate (taken as 100 GPa [96, 201, 202]) and the unconstrained mismatch is given by [203, 204]:

$$(8.7) \quad \varepsilon' = \left(\frac{a_{Al_3(Sc_{1-x}Zr_x)}}{a_{Al}} \right) - 1$$

with a_i as the temperature-dependent lattice parameter of phase i given by:

$$(8.8) \quad a_i = a_{i0} (1 + \alpha_i(T - 300));$$

where a_{i0} is the lattice parameter at 300 K for phase i ($a_{i0} = 0.4049$ nm for Al [47] and 0.4013 nm for Al_3Sc [25]) and α_i is the linear thermal expansion given in Ref. [204]. The

Al₃Sc lattice parameter was used for both DSC–Al–Sc and DSC–Al–Sc–Zr (the latter because of the very small amount of Zr in Al₃(Sc_{1-x}Zr_x) precipitates).

The second contribution to the back-stress on the detaching dislocation originates from the modulus mismatch between the precipitate ($C_{44}^{\text{Al}_3(\text{Sc}_{1-x}\text{Zr}_x)} = 68.0$ GPa [96]) and the matrix ($C_{44}^{\text{Al}} = 21.7$ GPa at 300°C). For a dislocation in the matrix, it is given by τ_μ as:

$$(8.9) \quad \tau_\mu = F_\mu b \lambda;$$

where $b = \frac{a_{\text{Al}}}{\sqrt{2}}$ is the magnitude of the Burgers vector, F_μ is the force acting on the dislocation and λ is the length of the dislocation segment under consideration. This length is taken as the interprecipitate spacing, which can be calculated as [195]:

$$(8.10) \quad \lambda = 2R \left(\sqrt{\frac{\pi}{4\phi}} - 1 \right);$$

where ϕ is the volume fraction of precipitates in the matrix calculated through the lever rule from the Al–Sc binary diagram for both Al–Sc and Al–Sc–Zr (the latter assuming 0.08 at.% Sc, thus ignoring the small amount of Zr in the precipitates). Because no simple exact solution exists for spherical or cylindrical particles, the two-dimensional (2D) solution given by Dundurs [205] for a circular precipitate interacting with a straight edge dislocation is used:

$$(8.11) \quad F_\mu = -R \frac{\partial E_\mu}{\partial y};$$

where E_μ is a function of dislocation–precipitate distance, precipitate radius and elastic constants for Al and Al₃Sc, given in Refs. [57, 205]. The above approach follows that used by

Marquis and Dunand [57] to calculate the forces impeding the climb of dislocations around coherent precipitates. The modulus mismatch stresses are symmetric in the z -direction and always oppose detachment, but they are orders of magnitude lower than the lattice mismatch stresses for the present case (Al and Al₃Sc at 300°C), so that the 2D modulus mismatch assumption is expected to introduce negligible errors in the final calculations.

The shear back-stress is the sum of the back-stresses from the lattice and modulus mismatches given by Eqs. 8.5 and 8.9:

$$(8.12) \quad \tau_B = -(\tau_\varepsilon + \tau_\mu);$$

where the negative sign is used because Eqs. 8.5, 8.9, and 8.11 define a repulsive stress (against the applied stress) with a negative sign, whereas in Eq. 8.4 a positive back-stress (which is repulsive) increases the threshold stress.

Eq. 8.12 was evaluated numerically and averaged over $-\frac{\lambda}{2} < x < \frac{\lambda}{2}$ to obtain the average back-stress. Furthermore, z is set to $(R + \delta)\tan\theta\dot{y}$ and is averaged over the interval $0 < \theta < \frac{\pi}{2}$. The interval $-\frac{\pi}{2} < \theta < 0$ is ignored since the anti-symmetric nature of τ_ε (which is much higher than τ_μ) provides a positive shear stress which helps the detachment of the dislocation. This is equivalent to considering that only half the dispersoids sampled by the dislocation during its glide through the matrix have a precipitate configuration which prevents detachment, with $h > 0$ and a repulsive τ_ε .

The only adjustable parameter is δ , the distance between the pinned dislocation and the nearest precipitate in the matrix (Fig. 8.5(a)). Computations were performed for a series of values ($\delta = b$, $\delta = 5b$, and $\delta = 10b$) and are plotted in Fig. 8.6. With increasing values

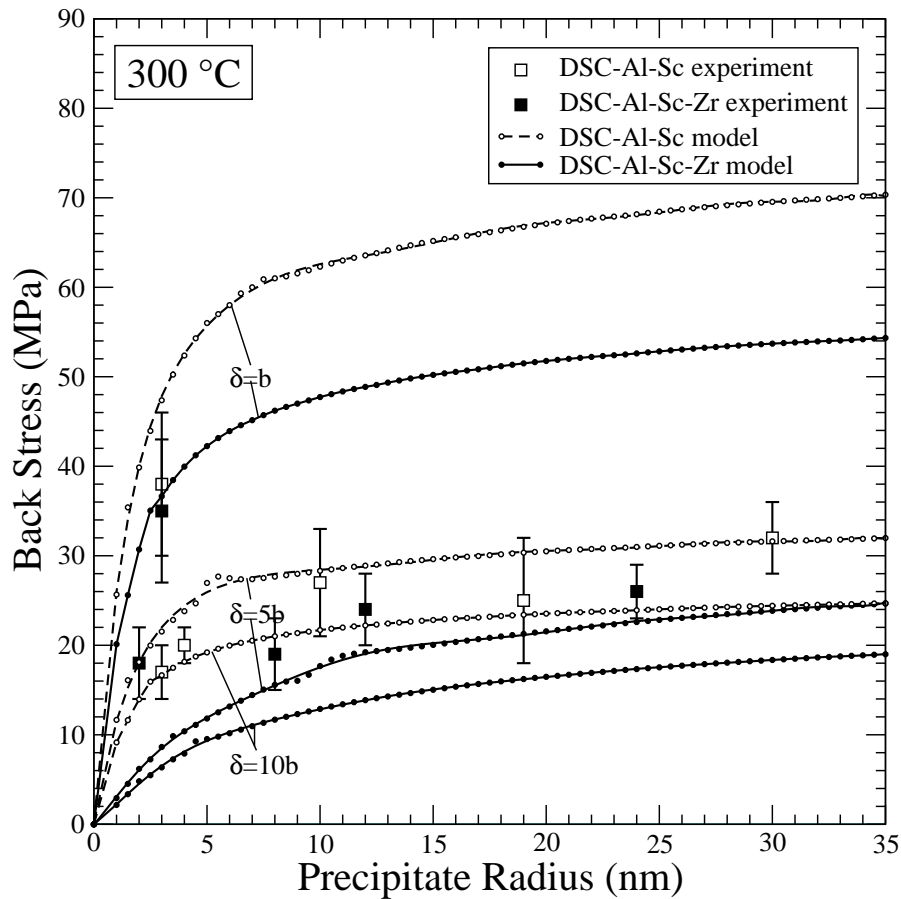


Figure 8.6. Comparison between the calculated compressive back-stress (lines connecting individually calculated points) and the experimentally measured compressive threshold stress increments (large squares, found as difference between threshold stresses of DSC–Al–Sc(–Zr) and DSC–Al in Fig. 8.4) as a function of estimated precipitate radius.

of δ , the back-stress becomes smaller, as expected. We consider here the lowest range of δ values (within the possible range $b < \delta < \frac{\lambda}{2}$) because the dislocation sequentially bypasses a large number of obstacles placed in series and becomes pinned at those obstacles with lowest values of δ , where the back-stress is maximum. As shown in Fig. 8.6, the model seems to capture the main trend of the experimental data, i.e., the threshold stress increases

with increasing precipitate radius R . The model also predicts a somewhat lowered threshold stress for DSC–Al–Sc–Zr as compared to DSC–Al–Sc, a trend that is too weak to be detectable within experimental errors.

Because of the many simplifications and assumptions made in the model, our aim is limited to seeking a conceptual understanding about the back-stress rather than achieving quantitative predictions. We thus do not seek here to improve the model by considering further refinements, e.g., enhanced density of precipitates around dispersoids or interactions between non-attached segments of the dislocation and precipitates. It is therefore perhaps fortuitous that a good quantitative agreement exists between the experimentally measured and numerically modeled threshold stresses for a value of $\delta = 5b$. Nonetheless, the model provides a simple explanation of the synergy observed in the creep threshold stress of DSC–Al–Sc, and by extension other metals, strengthened with two populations of coherent precipitates (providing a back-stress) and incoherent dispersoids (acting through a detachment stress).

8.5. Conclusions

This study examines dispersion-strengthened-cast aluminum (DSC–Al) containing two populations of particles: 30 vol.% submicron, incoherent Al_2O_3 dispersoids and 0.2–0.3 vol.% nanosize, coherent Al_3Sc precipitates (with and without small Zr additions in solid-solution). The following conclusions can be drawn:

- DSC–Al–Sc(–Zr) exhibits strengthening at ambient temperature from both the Al_3Sc precipitates and the Al_2O_3 dispersoids, as measured by microhardness and uniaxial

compressive testing. The Al_3Sc precipitation kinetics are unaffected by the presence of Al_2O_3 .

- Partial replacement of Sc with Zr in DSC–Al–Sc–Zr is the likely explanation for the observed lower peak hardness (due to lower volume fraction of precipitates) and elimination of overaging at 300 or 350°C (due to slower coarsening kinetics), as compared to DSC–Al–Sc.
- DSC–Al–Sc(–Zr) tested under compressive creep conditions at 300 and 350°C exhibits high stress exponents, which are characteristic of materials with a threshold stresses (as also exhibited by DSC–Al and Al–Sc(–Zr) alloys).
- Partial replacement of Sc with Zr in Al–Sc–Zr and DSC–Al–Sc–Zr slightly decreases the creep-resistance and threshold stress, as expected from the decrease of volume fraction and lattice mismatch of the precipitates.
- The threshold stress of DSC–Al–Sc(–Zr) is greater than either that of precipitate-free DSC–Al or dispersoid-free Al–Sc(–Zr) alloys. This indicates that both populations of particles (precipitates and dispersoids) affect the threshold mechanism, despite their very different size, volume fraction and coherency with the matrix.
- This dual-strengthening effect is modeled by considering dislocations pinned at the departure side of Al_2O_3 dispersoids while being subjected to a back-stress from the nearby Al_3Sc precipitates, due to the strain field originating from their lattice and modulus mismatches with the matrix.

CHAPTER 9

Summary and Future Work

This thesis demonstrates that rare-earth elements (RE=Y, Dy, Er) improve the creep performance of Al–Sc alloys at 300°C. Er is found to be a fast diffuser in α -Al ($(4 \pm 2) \times 10^{-19} \text{ m}^2 \text{ s}^{-1}$ at 300°C), and forms coherent Al_3Er precipitates when added to Al up to its experimentally-measured solubility limit of 461 ± 6 at. ppm at 640°C. When added to Al–Sc alloys (which have a solubility that is four times larger), they substitute for Sc in the L1_2 precipitate phase. At ambient temperature, these $\text{Al}_3(\text{Sc}_{1-x}\text{RE}_x)$ precipitates strengthen the alloy due to their high antiphase boundary energy, which prevents shearing. At elevated temperatures, the high lattice parameter misfit between $\text{Al}_3(\text{Sc}_{1-x}\text{RE}_x)$ and α -Al causes high creep threshold stresses.

Additionally, submicron, incoherent Al_2O_3 dispersoids are found to complement the strengthening due to $\text{Al}_3(\text{Sc}_{1-x}\text{Zr}_x)$ precipitates at both ambient and elevated temperatures. Higher creep thresholds are measured in the dual-strengthened alloy that are in agreement with a model of the precipitates exerting a back stress on dislocations, preventing detachment from the incoherent interface of α -Al/ Al_2O_3 .

A better-understanding of the Al–RE binaries would be of fundamental interest. Little thermodynamic and kinetic information exists on the heavier lanthanides. Dr. Zugang Mao is currently performing first-principle calculations to find the α -Al/ Al_3Er interfacial free energy to compare with the high experimentally measured values presented here. Additionally,

calculations to find the antiphase boundary energy of Al_3Er will better inform dislocation dynamics simulations and analytical expressions for the peak strength of Al–Sc–Er alloys that have very fine precipitates [66].

The mechanism for precipitate nucleation in Al–Sc–Er is of interest. Unlike other systems that exhibit core-shell precipitation (such as Al–Sc(–Zr)(–Ti) and Al–Sc–Yb), the diffusivities of Er and Sc are only separated by half an order of magnitude. The very large lattice parameter misfits may be a more significant factor than solute diffusion in the creation of the core-shell precipitates in this system.

A determination of the Al–Sc–Er ternary phase diagram would assist in better alloy design. In particular, alloys with more solute content (within the solubility limits of the ternary alloy) would cause a higher volume fraction of precipitates to form on aging to improve strength and ambient and elevated temperatures and to aid in the understanding of the microstructure of the alloy.

Various quaternary alloying elements could be used to improve the volume fraction of strengthening phase (as in the case of Li) or to slow coarsening kinetics (as in the case of Ti and Zr). A careful selection of elements based on diffusivities and lattice misfit, as well as careful aging treatments, might create precipitates with multiple shells. Such complex precipitates might have interesting effects on mechanical properties. It might require the use of dislocation dynamics simulations or improvements to the existing analytical expressions for strength to understand these effects. A suitably chosen outer-shell (that is slow and impermeable) might also aid in an understanding of the intermixing between segregated elements in the precipitate core.

There is growing demand for a better understanding of alloy behavior over timespans longer than those presented in this thesis. While there are few other Al-base alloys that can operate at service temperatures of 300°C and above, that might be the only niche for Al-Sc. Their extremely slow coarsening kinetics at temperatures lower than 300°C suggest they may be suitable replacements (with longer lifetimes and/or greater strength) at these moderate temperatures.

References

- [1] R. A. Karnesky, C. K. Sudbrack, and D. N. Seidman, “Best-Fit Ellipsoids of Atom-Probe Tomographic Data to Study Coalescence of γ' (L1₂) Precipitates in Ni-Al-Cr,” *Scripta Materialia*, **57**, pp. 353–356 (2007).
- [2] V. Mohles and B. Fruehstorfer, “Computer Simulations of Orowan Process Controlled Dislocation Glide in Particle Arrangements of Various Randomness,” *Acta Materialia*, **50**, pp. 2503–2516 (2002).
- [3] D. N. Seidman, E. A. Marquis, and D. C. Dunand, “Precipitation Strengthening at Ambient and Elevated Temperatures of Heat-Treatable Al(Sc) Alloys,” *Acta Materialia*, **50**(16), pp. 4021–4035 (2002).
- [4] E. A. Marquis, D. N. Seidman, and D. C. Dunand, “Precipitation Strengthening at Ambient and Elevated Temperatures of Heat-Treatable Al(Sc) Alloys [Acta Materialia 50(16), pp. 4021–4035],” *Acta Materialia*, **51**(1), pp. 285–287 (2003).
- [5] C. B. Fuller, D. N. Seidman, and D. C. Dunand, “Mechanical Properties of Al(Sc,Zr) Alloys at Ambient and Elevated Temperatures,” *Acta Materialia*, **51**(16), pp. 4803–4814 (2003).
- [6] E. A. Marquis, D. N. Seidman, and D. C. Dunand, “Effect of Mg Addition on the Creep and Yield Behavior of an Al–Sc Alloy,” *Acta Materialia*, **53**(16), pp. 4751–4760 (2003).

- [7] M. E. van Dalen, D. C. Dunand, and D. N. Seidman, "Effects of Ti Additions on the Nanostructure and Creep Properties of Precipitation-Strengthened Al–Sc Alloys," *Acta Materialia*, **53**, pp. 4225–4235 (2005).
- [8] R. A. Karnesky, M. E. van Dalen, D. C. Dunand, and D. N. Seidman, "Effects of Substituting Rare-Earth Elements for Scandium in a Precipitation-Strengthened Al 0.08 at.% Sc Alloy," *Scripta Materialia*, **55**, pp. 437–440 (2006).
- [9] M. van Dalen, "Personal Communication," (2007).
- [10] R. S. Mishra, "Designing DRA Composites for High Creep Strength," *JOM*, **51**(11), pp. 65–68 (1999).
- [11] R. W. Hyland, "Homogeneous Nucleation Kinetics of Al₃Sc in a Dilute Al–Sc Alloy," *Metallurgical Transactions A-Physical Metallurgy and Materials Science*, **23**(7), pp. 1947–1955 (1992).
- [12] J. Røyset and N. Ryum, "Scandium in Aluminium Alloys," *International Materials Reviews*, **50**, pp. 19–44 (2005).
- [13] L. S. Toropova, D. G. Eskin, M. L. Kharakterova, and T. V. Dobatkina, *Advanced Aluminum Alloys Containing Scandium: Structure and Properties*, Gordon & Breach Science Publishers (1998).
- [14] N. Blake and M. A. Hopkins, "Constitution and Age Hardening of Al–Sc Alloys," *Journal of Materials Science*, **20**(8), pp. 2861–2867 (1985).
- [15] G. M. Novotny and A. J. Ardell, "Precipitation of Al₃Sc in binary Al–Sc alloys," *Materials Science and Engineering A*, **318**, pp. 144–154 (2001).

- [16] E. Clouet, A. Barbu, L. La, and G. Martin, "Precipitation kinetics of Al_3Zr and Al_3Sc in Aluminum Alloys Modeled with Cluster Dynamics," *Acta Materialia*, **53**, pp. 2313–2325 (2005).
- [17] J. Røyset and N. Ryum, "Kinetics and Mechanisms of Precipitation in an Al–0.2 wt.% Sc Alloy," *Materials Science and Engineering A*, **396**, pp. 409–422 (2005).
- [18] High Tech Materials, "Rare Earths and Specialty Metals Market Prices," (2003).
- [19] USGS, *Mineral Commodity Summaries* (2007).
- [20] O. I. Zalutskaya, V. R. Ryabov, and I. I. Zalutsky, "The X-Ray Analysis of Aluminum-Rich Ternary Alloys of Aluminium and Rare-Earth Metals of the Yttrium Subgroup and Scandium," *Dopovidi Akademii Nauk Ukrainskoi RSR Seriya A-Fiziko-Matematichni Ta Technichni Nauki*, (3), pp. 255–259 (1969).
- [21] O. I. Zalutskaya, V. G. Kontsevov, N. I. Karamyshev, V. R. Ryabov, and I. I. Zalutsky, "Ternary Systems Gd–(Y,Tb,Dy,Ho,Er,Sc)–Al in the Region to 25 at.% Rare-Earth Metals," *Dopovidi Akademii Nauk Ukrainskoi RSR Seriya A-Fiziko-Matematichni Ta Technichni Nauki*, (8), pp. 751–753 (1970).
- [22] R. R. Sawtell, P. E. Bretz, and C. L. Jensen, "Superplastic Aluminum Alloys Containing Scandium," US Patent 4,689,090 (1987).
- [23] R. R. Sawtell, *Exploratory Alloy Development in the System Al–Sc–X*, Ph.D. thesis, University of California, Berkeley (1988).
- [24] R. R. Sawtell and J. W. Morris, Jr., "Exploratory Alloy Development in the System Al–Sc–X," in *Dispersion Strengthened Aluminum Alloys* (edited by Y. W. Kim and W. M. Griffith), pp. 409–420, TMS, Warrendale (1988).

- [25] Y. Harada and D. C. Dunand, "Microstructure of Al_3Sc with Ternary Transition-Metal Additions," *Materials Science and Engineering A*, **329–331**, pp. 686–695 (2002).
- [26] T. J. Watson, "High Strength Aluminum Alloy," US Patent 6,248,453 (2001).
- [27] C. B. Fuller, A. R. Krause, D. C. Dunand, and D. N. Seidman, "Microstructure and Mechanical Properties of a 5754 Aluminum Alloy Modified by Sc and Zr Additions," *Materials Science and Engineering A*, **338**(1–2), pp. 8–16 (2002).
- [28] B. Forbord, W. Lefebvre, F. Danoix, H. Hallem, and K. Marthinsen, "Three Dimensional Atom Probe Investigation on the Formation of $\text{Al}_3(\text{Sc}, \text{Zr})$ -Dispersoids in Aluminium Alloys," *Scripta Materialia*, **51**(4), pp. 333–337 (2004).
- [29] C. B. Fuller, J. L. Murray, and D. N. Seidman, "Temporal Evolution of the Nanostructure of $\text{Al}(\text{Sc}, \text{Zr})$ Alloys: Part I—Chemical Compositions of $\text{Al}_3(\text{Sc}_{1-x}\text{Zr}_x)$ Precipitates," *Acta Materialia*, **53**, pp. 5401–5413 (2005).
- [30] A. Tolley, V. Radmilovic, and U. Dahmen, "Segregation in $\text{Al}_3(\text{Sc}_{1-x}\text{Zr}_x)$ Precipitates in Al–Sc–Zr Alloys," *Scripta Materialia*, **52**, pp. 621–625 (2005).
- [31] E. Clouet, L. Lae, T. Epicier, W. Lefebvre, M. Nastar, and A. Deschamps, "Complex Precipitation Pathways in Multi-Component Alloys," *Nature Materials*, **5**, pp. 482–488 (2006).
- [32] H. Hallem, W. Lefebvre, B. Forbord, F. Danoix, and K. Marthinsen, "The Formation of $\text{Al}_3(\text{Sc}_x\text{Zr}_y\text{Hf}_{1-x-y})$ -Dispersoids in Aluminium Alloys," *Materials Science and Engineering A*, **421**, pp. 154–160 (2006).
- [33] A. Deschamps, L. Lae, and P. Guyot, "In Situ Small-Angle Scattering Study of the Precipitation Kinetics in an Al–Zr–Sc alloy," *Acta Materialia*, **55**, pp. 2775–2783 (2007).

- [34] W. G. Moffatt, *The Handbook of Binary Phase Diagrams*, Genium Publishing Corporation, Schenectady (1976).
- [35] T. B. Massalski, H. Okamoto, P. R. Subramanian, and L. Kacprzak, *Binary Alloy Phase Diagrams*, ASM International, Materials Park (1990).
- [36] H. Okamoto, *Phase Diagrams of Dilute Binary Alloys*, ASM International, Materials Park (2002).
- [37] A. Palenzon, "Ytterbium–Aluminum System," *Journal of the Less Common Metals*, **29**(3), pp. 289–292 (1972).
- [38] L. F. Mondolfo, *Aluminum Alloys: Structures and Properties*, Butterworth, London (1976).
- [39] S. I. Fujikawa, "Impurity Diffusion of Scandium in Aluminum," *Defect and Diffusion Forum*, **143**, pp. 115–120 (1997).
- [40] K. Milička, J. Čadek, and P. Rýs, "Creep of Aluminum Strengthened by Alumina Particles," *Acta Metallurgica*, **18**(7), pp. 733–746 (1970).
- [41] A. Kelly, "Composites in Context," *Composites Science and Technology*, **23**(3), pp. 171–199 (1985).
- [42] W. H. Hunt, Jr. and B. Maruyama, "The World Still Won't Beat a Path to Your Door: Transitioning DRA to the Marketplace," *JOM*, **51**(11), pp. 62–64 (1999).
- [43] D. J. Lloyd, "Particle Reinforced Aluminium and Magnesium Matrix Composites," *International Materials Reviews*, **39**(1), pp. 1–23 (1994).
- [44] A. M. Jansen and D. C. Dunand, "Creep of Metals Containing High Volume Fractions of Unshearable Dispersoids—Part II. Experiments in the Al–Al₂O₃ System and Comparison to Models," *Acta Materialia*, **45**(11), pp. 4583–4592 (1997).

- [45] A. B. Pandey, R. S. Mishra, and Y. R. Mahajan, "Creep Behaviour of an Aluminium–Silicon Carbide Particulate Composite," *Scripta Metallurgica et Materialia*, **24**(8), pp. 1565–1570 (1990).
- [46] A. K. Mukherjee, J. E. Bird, and J. E. Dorn, "Experimental Correlations for High-Temperature Creep," *ASM Transactions Quarterly*, **62**(1), p. 155 (1969).
- [47] H. J. Frost and M. F. Ashby, *Deformation-Mechanism Maps*, Pergamon Press, Oxford (1982).
- [48] J. Weertman, "Steady-State Creep of Crystals," *Journal of Applied Physics*, **28**(10), pp. 1185–1189 (1957).
- [49] F. A. Mohamed and T. G. Langdon, "Transition from Dislocation Climb to Viscous Glide in Creep of Solid-Solution Alloys," *Acta Metallurgica*, **22**(6), pp. 779–788 (1974).
- [50] J. Weertman, "Steady-State Creep through Dislocation Climb," *Journal of Applied Physics*, **28**(3), pp. 362–364 (1957).
- [51] G. Gonzalez-Doncel and O. D. Sherby, "High Temperature Creep-Behavior of Metal Matrix Aluminum-SiC Composites," *Acta Metallurgica et Materialia*, **41**(10), pp. 2797–2805 (1993).
- [52] O. D. Sherby, R. H. Klundt, and A. K. Miller, "Flow-Stress, Subgrain Size, and Subgrain Stability at Elevated-Temperature," *Metallurgical Transactions A*, **8**(6), pp. 843–850 (1977).
- [53] E. Arzt, "Mechanical Properties of Metallic Composites," in *Mechanical Properties of Metallic Composites* (edited by S. Ochiai), chap. 8, pp. 205–223, Marcel Dekker, Inc., New York (1994).

- [54] Y. Li and T. G. Langdon, "A Simple Procedure for Estimating Threshold Stresses in the Creep of Metal Matrix Composites," *Scripta Materialia*, **36**(12), pp. 1457–1460 (1997).
- [55] R. Lagneborg and B. Bergman, "The Stress/Creep Rate Behaviour of Precipitation-Hardened Alloys," *Metal Science*, **10**(1), pp. 20–28 (1976).
- [56] M. W. Decker, J. R. Groza, and J. C. Gibeling, "Creep Properties of an Extruded Copper–8% Chromium–4% Niobium Alloy," *Materials Science and Engineering A*, **369**(1–2), pp. 101–111 (2004).
- [57] E. A. Marquis and D. C. Dunand, "Model for Creep Threshold Stress in Precipitation-Strengthened Alloys with Coherent Particles," *Scripta Materialia*, **47**(8), pp. 503–508 (2002).
- [58] Z. Nie, T. Jin, J. Fu, G. Xu, J. Yang, J. Zhou, and T. Zuo, "Research on Rare Earth in Aluminum," *Materials Science Forum*, **396–402**, pp. 1731–1735 (2002).
- [59] Z.-R. Nie, T.-N. Jin, J.-X. Zou, J.-B. Fu, J.-J. Yang, and T.-Y. Zuo, "Development on Research of Advanced Rare-Earth Aluminum Alloy," *Transactions of Nonferrous Metals Society of China*, **13**, pp. 509–514 (2003).
- [60] J. J. Yang, Z. R. Nie, T. N. Jin, G. F. Xu, J. B. Fu, H. Q. Ruan, and T. Y. Zuo, "Effect of Trace Rare Earth Element Er on High Pure Al," *Transactions of Nonferrous Metals Society of China*, **13**, pp. 1035–1039 (2003).
- [61] Z. R. Nie, J. B. Fu, J. X. Zou, T. N. Jun, J. J. Yang, G. F. Xu, H. Q. Ruan, and T. Y. Zuo, "Advanced Aluminum Alloys Containing Rare-earth Erbium," *Aluminium Alloys: Their Physical and Mechanical Properties*, **28**, pp. 197–201 (2004).

- [62] J. B. Fu, Z. R. Nie, T. N. Jin, J. X. Zou, and T. Y. Zou, "Effect of Er on aging behavior of 1420 alloy," *Journal Of Rare Earths*, **23**, pp. 430–433 (2005).
- [63] J. W. Mao, T. N. Jin, G. F. Xu, and Z. R. Nie, "As-Cast Microstructure of Al–Zn–Mg and Al–Zn–Mg–Cu Alloys Added Erbium," *Transactions of Nonferrous Metals Society of China*, **15**, pp. 1341–1345 (2005).
- [64] H. Na, X. F. Bian, K. B. Yin, and X. J. Yao, "Modification Effect of Er on Hypoeutectic Al–8Si Alloy," *Journal Of Rare Earths*, **23**, pp. 474–477 (2005).
- [65] G. F. Xu, S. Z. Mou, J. J. Yang, T. N. Jin, Z. R. Nie, and Z. M. Yin, "Effect of Trace Rare Earth Element Er on Al–Zn–Mg Alloy," *Transactions of Nonferrous Metals Society of China*, **16**, pp. 598–603 (2006).
- [66] Z. Mao, "Personal Communication," (2007).
- [67] O. C. Hellman, J. A. Vandenbroucke, J. Rusing, D. Isheim, and D. N. Seidman, "Analysis of Three-dimensional Atom-probe Data by the Proximity Histogram," *Microscopy & Microanalysis*, **6**, pp. 437–444 (2000).
- [68] O. Hellman, J. Vandenbroucke, J. B. du Rivage, and D. N. Seidman, "Application Software for Data Analysis for Three-Dimensional Atom Probe Microscopy," *Materials Science and Engineering A*, **327**, pp. 29–33 (2002).
- [69] H.-H. Jo and S.-I. Fujikawa, "Kinetics of Precipitation in Al–Sc alloys and Low Temperature Solid Solubility of Scandium in Aluminium Studied by Electrical Resistivity Measurements," *Materials Science and Engineering A*, **171**, pp. 151–161 (1993).
- [70] J. L. Murray, "The Al–Sc (Aluminum–Scandium) System," *Journal of Phase Equilibria*, **19**(4), pp. 380–384 (1998).

- [71] N. Akaiwa and P. W. Voorhees, "Late-Stage Phase Separation: Dynamics, Spatial Correlations, and Structure Functions," *Physical Review E*, **49**, pp. 3860–3880 (1994).
- [72] S. Farjami, "Personal Communication," (2007).
- [73] I. M. Lifshitz and V. V. Slyozov, "The Kinetics of Precipitation from Supersaturated Solid Solutions," *Journal of Physics and Chemistry of Solids*, **19**, pp. 35–50 (1961).
- [74] C. Wagner, "Theorie der Alterung von Niederschlägen durch Umlösen," *Zeitschrift für Elektrochemie*, **65**, pp. 581–591 (1961).
- [75] E. A. Marquis and D. N. Seidman, "Nanoscale Structural Evolution of Al₃Sc Precipitates in Al(Sc) Alloys," *Acta Materialia*, **49**(11), pp. 1909–1919 (2001).
- [76] A. J. Ardell, "An Application of the Theory of Particle Coarsening: The γ' Precipitate in Ni–Al Alloys," *Acta Metallurgica*, **16**, pp. 511–516 (1968).
- [77] A. J. Ardell, "Interfacial Free Energies and Solute Diffusivities from Data on Ostwald Ripening," *Interface Science*, **3**, pp. 119–125 (1995).
- [78] S. P. Murarka and R. P. Agarwala, "Diffusion of Rare Earth Elements in Aluminum," (1968).
- [79] C. B. Fuller, D. N. Seidman, and D. C. Dunand, "Creep Properties of Coarse-Grained Al(Sc) Alloys at 300°C," *Scripta Materialia*, **40**(6), pp. 691–696 (1999).
- [80] S. P. Deshmukh, R. S. Mishra, and K. L. Kendig, "Creep Behavior and Threshold Stress of an Extruded Al–6Mg–2Sc–1Zr alloy," *Materials Science and Engineering A*, **381**, pp. 381–385 (2004).
- [81] S. P. Deshmukh, R. S. Mishra, and K. L. Kendig, "Creep Behavior of Extruded Al–6Mg–1Sc–1Zr–10 vol.% SiCp Composite," *Materials Science and Engineering A*, **410-411**, pp. 53–57 (2005).

- [82] M. E. van Dalen, D. C. Dunand, and D. N. Seidman, "Nanoscale Precipitation and Mechanical Properties of Al–0.06 at.% Sc Alloys Micro-Alloyed with Yb or Gd," *Journal of Materials Science*, **41**, pp. 7814–7823 (2006).
- [83] M. E. van Dalen, T. Gyger, D. C. Dunand, and D. N. Seidman, "Effects of Zr on the Microstructure and Mechanical Properties of Al–Sc–Yb Alloys," *Microscopy and Microanalysis* (2007).
- [84] E. A. Marquis and D. N. Seidman, "Coarsening Kinetics of Nanoscale Al₃Sc Precipitates in an Al–Mg–Sc Alloy," *Acta Materialia*, **53**, pp. 4259–4268 (2005).
- [85] M. Y. Drits, L. B. Ber, Y. G. Bykov, L. S. Toropova, and G. K. Anastas'eva, "Ageing of Al–0.3 at.% Sc," *The Physics of Metals and Metallography*, **57**, pp. 118–126 (1984).
- [86] Y. W. Riddle and T. H. Saunders Jr., "A Study of Coarsening, Recrystallization, and Morphology of Microstructure in Al–Sc–(Zr)–(Mg) Alloys," *Metallurgical and Materials Transactions A*, **35**, pp. 341–350 (2004).
- [87] S. Iwamura and Y. Miura, "Loss in Coherency and Coarsening Behavior of Al₃Sc Precipitates," *Acta Materialia*, **52**(3), pp. 591–600 (2004).
- [88] C. Watanabe, T. Kondo, and R. Monzen, "Coarsening of Al₃Sc Precipitates in an Al–0.28 Wt Pct Sc Alloy," *Metallurgical and Materials Transactions A*, **35**, pp. 3003–3008 (2004).
- [89] C. J. Kuehmann and P. W. Voorhees, "Ostwald Ripening in Ternary Alloys," *Metallurgical and Materials Transactions*, **27A**, pp. 937–943 (1996).
- [90] C. Watanabe, D. Watanabe, and R. Monzen, "Coarsening Behavior of Al₃Sc Precipitates in an Al–Mg–Sc Alloy," *Materials Transactions*, **47**, pp. 2285–2291 (2006).

- [91] C. B. Fuller and D. N. Seidman, "Temporal Evolution of the Nanostructure of Al(Sc,Zr) Alloys: Part II—Coarsening of $\text{Al}_3\text{Sc}_{1-x}\text{Zr}_x$ Precipitates," *Acta Materialia*, **53**, pp. 5415–5428 (2005).
- [92] M. F. Ashby and L. M. Brown, "Diffraction Contrast from Spherically Symmetrical Coherency Strains," *Philosophical Magazine*, **8**, pp. 1083–1102 (1963).
- [93] M. F. Ashby and L. M. Brown, "On Diffraction Contrast from Inclusions," *Philosophical Magazine*, **8**, pp. 1649–1676 (1963).
- [94] J. M. Hyde and C. A. English, "An Analysis of the Structure of Irradiation Cu-enriched Clusters in Low and High Nickel Welds," in *Microstructural Processes in Irradiated Materials—2000*, vol. 650 of *Materials Research Society Symposia Proceedings* (edited by G. E. Lucas, L. Snead, M. A. Kirk, and R. G. Ellman), pp. R.6.6.1–12, Materials Research Society, Warrendale, PA (2001).
- [95] M. K. Miller, *Atom Probe Tomography: Analysis at the Atomic Level*, Kluwer Academic, New York (2000).
- [96] R. W. Hyland, Jr. and R. C. Stiffler, "Determination of the Elastic Constants of Polycrystalline Al_3Sc ," *Scripta Metallurgica et Materialia*, **25**, pp. 473–477 (1991).
- [97] M. Asta, V. Ozolins, and C. Woodward, "A First-Principles Approach to Modeling Alloy Phase Equilibria," *JOM*, **53**, pp. 16–19 (2001).
- [98] J. D. Robson, M. J. Jones, and P. B. Prangnell, "Extension of the N-model to predict competing homogeneous and heterogeneous precipitation in Al–Sc alloys," *Acta Materialia*, **51**, pp. 1453–1468 (2003).
- [99] M. Asta, S. M. Foiles, and A. A. Quong, "First-Principles Calculations of Bulk and Interfacial Thermodynamic Properties for fcc-Based Al–Sc Alloys," *Physical Review B*,

- 57, pp. 11,265–11,275 (1998).
- [100] M. Baskes, “Modified Embedded-Atom Potentials for Cubic Materials and Impurities,” *Physical Review B*, **46**, p. 2727 (1992).
- [101] Z. Jian-Min, M. Fei, and X. Ke-Wei, “Calculation of the Surface Energy of fcc Metals with Modified Embedded-Atom Method,” *Chinese Physics*, p. 1082 (2004).
- [102] L. M. Brown and R. K. Ham, “Dislocation-Particle Interactions,” in *Strengthening Methods in Crystals* (edited by A. Kelly and R. B. Nicholson), chap. 2, pp. 9–135, Elsevier, Amsterdam (1971).
- [103] E. Nembach, *Particle Strengthening of Metals and Alloys*, Wiley-Interscience, New York (1996).
- [104] S. Torquato, “Statistical Description of Microstructures,” *Annual Review of Materials Research*, **32**, pp. 77–111 (2002).
- [105] J. Quintanilla, “Microstructure and Properties of Random Heterogeneous Materials: A Review of Theoretical Results,” *Polymer Engineering and Science*, **39**, pp. 559–585 (2004).
- [106] B. Lu and S. Torquato, “Chord-Length and Free-Path Distribution Functions for Many-Body Systems,” *Journal of Chemical Physics*, **98**, pp. 6472–6482 (1993).
- [107] S. Torquato, “Mean Nearest-Neighbor Distance in Random Packings of Hard D-Dimensional Spheres,” *Physical Review Letters*, **74**, pp. 2156–2159 (1995).
- [108] J. R. Macdonald, “Nearest-Neighbor Distribution Functions for Impenetrable Particles in One to Three Dimensions,” *Journal of Physical Chemistry*, **96**, pp. 3861–3864 (1996).

- [109] Z. H. Liu, Y. Li, and K. W. Kowk, "Mean Interparticle Distances Between Hard Particles in One to Three Dimensions," *Polymer*, **42**, pp. 2701–2706 (2001).
- [110] A. Tewari and A. M. Gokhale, "Nearest-Neighbor Distances Between Particles of Finite Size in Three-Dimensional Uniform Random Microstructures," *Materials Science and Engineering A*, **385**, pp. 332–341 (2004).
- [111] T. F. Kelly and D. J. Larson, "Local Electrode Atom Probes," *Materials Characterization*, **44**, pp. 59–85 (2000).
- [112] D. N. Seidman, "From Field-Ion Microscopy of Single Atoms to Atom-Probe Tomography: A Fifty Year Journey," *Review of Scientific Instruments*, **78**, pp. 030,901:1–3 (2007).
- [113] J. W. Leggoe, "Nth-Nearest Neighbor Statistics for Analysis of Particle Distribution Data Derived from Micrographs," *Scripta Materialia*, **53**, pp. 1263–1268 (2005).
- [114] J. Ohser and F. Mücklich, *Statistical Analysis of Microstructures in Materials Science*, Wiley, New York (2000).
- [115] M. K. Miller and E. A. Kenik, "Atom Probe Tomography: A Technique for Nanoscale Characterization," *Microscopy & Microanalysis*, **10**, pp. 336–341 (2004).
- [116] K. L. Clarkson, "Proc. 31st IEEE Symp. on Foundations of Computer Science," in *Proc. 31st IEEE Symposium on Foundations of Computer Science*, pp. 387–395, Pittsburgh, PA (1992).
- [117] C. B. Barber, D. P. Dobkin, and H. Huhdanpaa, "The Quickhull Algorithm for Convex Hulls," *ACM Transactions on Mathematical Software*, **22**, pp. 469–483 (1996).
- [118] M. J. D. Powell, "A Direct Search Optimization Method that Models the Objective and Constraint Functions by Linear Interpolation," in *Advances in Optimization and*

- Numerical Analysis* (edited by S. Gomez and J. P. Hennart), pp. 51–67, Kluwer Academic, Dordrecht (1994).
- [119] A. Lin and S.-P. Han, “On the Distance between Two Ellipsoids,” *SIAM Journal on Optimization*, **13**, pp. 298–308 (2002).
- [120] K.-A. Sohn, B. Jüttler, M.-S. Kim, and W. Wang, “Computing Distances between Surfaces Using Line Geometry,” in *PG 2002* (edited by S. Coquillart, H.-Y. Shum, and S.-M. S.-M. Hu), pp. 236–245, IEEE Computer Society (2002).
- [121] E. Jones, T. Oliphant, P. Peterson, et al., “SciPy: Open source scientific tools for Python,” (2001–).
- [122] V. Mohles, “The Critical Resolved Shear Stress of Single Crystals with Long-Range Ordered Precipitates Calculated by Dislocation Dynamics Simulations,” *Materials Science and Engineering A*, **365**, pp. 144–150 (2004).
- [123] R. W. Balluffi, S. M. Allen, and W. C. Carter, *Kinetics of Materials*, Wiley-Interscience, Hoboken (2005).
- [124] H. A. Calderon, P. W. Voorhees, J. L. Murray, and G. Kostorz, “Ostwald Ripening in Concentrated Alloys,” *Acta Metallurgica et Materialia*, **42**, pp. 991–1000 (1994).
- [125] A. Umantsev and G. B. Olson, “Ostwald Ripening in Multicomponent Alloys,” *Scripta Metallurgica et Materialia*, **29**, pp. 1135–1140 (1993).
- [126] A. J. Ardell, “Precipitate Coarsening in Solids: Modern Theories, Chronic Disagreement with Experiment,” in *Phase Transformations '87* (edited by G. W. Lorimer), pp. 485–494, The Institute of Metals, London (1988).
- [127] A. J. Ardell, “Temporal Behavior of the Number Density of Particles During Ostwald Ripening,” *Materials Science and Engineering A*, **238**, pp. 108–120 (1997).

- [128] A. J. Ardell and V. Ozolins, "Trans-Interface Diffusion-Controlled Coarsening," *Nature Materials*, **4**, pp. 309–316 (2005).
- [129] R. A. Karnesky, D. Isheim, and D. N. Seidman, "Direct Measurement of 2-Dimensional and 3-Dimensional Interprecipitate Distance Distributions from Atom-Probe Tomographic Reconstructions," *Applied Physics Letters*, **90** (2007).
- [130] E. Nembach, *Particle Strengthening of Metals and Alloys*, John Wiley & Sons, Inc. (1997).
- [131] G. Schmitz and P. Haasen, "Decomposition of an Al–Li Alloy—The Early Stages Observed by HREM," *Acta Metallurgica et Materialia*, **40**, pp. 2209–2217 (1992).
- [132] C. Booth-Morrison, J. Weninger, C. K. Sudbrack, Z. Mao, R. D. Noebe, and D. N. Seidman, "Effects of Solute Concentrations on Kinetic Pathways in Ni–Al–Cr Alloys," *Submitted to Acta Materialia* (2007).
- [133] K. E. Yoon, C. K. Sudbrack, R. D. Noebe, and D. N. Seidman, "The Temporal Evolution of the Nanostructures of Model Ni–Al–Cr and Ni–Al–Cr–Re Superalloys," *Zeitschrift für Metallkunde*, **96**, pp. 481–485 (2005).
- [134] C. S. Sudbrack, T. D. Ziebell, R. D. Noebe, and D. N. Seidman, "Effects of a Tungsten Addition on the Morphological Evolution, Spatial Correlations, and Temporal Evolution of a Model Ni–Al–Cr Superalloy," *Acta Materialia*, **Submitted** (2007).
- [135] K. Yoon, R. D. Noebe, and D. N. Seidman, "Effects of a Rhenium Addition on the Temporal Evolution of the Nanostructure and Chemistry of a Model Ni–Cr–Al Superalloy, I. Experimental Observations," *Acta Materialia*, **55**, pp. 1145–1157 (2007).
- [136] K. Yoon, R. D. Noebe, and D. N. Seidman, "Effects of a Rhenium Addition on the Temporal Evolution of the Nanostructure and Chemistry of a Model Ni–Cr–Al Superalloy,

- II. Analysis of the Coarsening Behavior,” *Acta Materialia*, **55**, pp. 1159–1169 (2007).
- [137] J. Alkember, V. A. Snyder, N. Akaiwa, and P. W. Voorhees, “Dynamics of Late-Stage Phase Separation: A Test of Theory,” *Physical Review Letters*, **82**, pp. 2725–2728 (1999).
- [138] D. Rowenhorst, J. Kuang, K. Thornton, and P. Voorhees, “Three-Dimensional Analysis of Particle Coarsening in High Volume Fraction Solid-Liquid Mixtures,” *Acta Materialia*, **54**, pp. 2027–2039 (2006).
- [139] N. Sano, Y. Hasegawa, K. Hono, H. Jo, K. Hirano, H. W. Pickering, and T. Sakurai, “Precipitation Processes of Al–Sc Alloys,” *Journal de Physique*, **C6**, pp. 337–342 (1987).
- [140] T. Torma, E. Kovács-Csetényi, T. Turmezey, T. Ungár, and I. Kovács, “Hardening mechanisms in Al–Sc alloys,” *Journal of Materials Science*, **24**, pp. 3924–3927 (1989).
- [141] Z. Yin, Q. Pan, Y. Zhang, and F. Jiang, “Effect of Minor Sc and Zr on the Microstructure and Mechanical Properties of Al–Mg Based Alloys,” *Materials Science and Engineering A*, **280**, pp. 151–155 (2000).
- [142] K. Kendig and D. Miracle, “Strengthening Mechanisms of an Al–Mg–Sc–Zr Alloy,” *Acta Materialia*, **50**, pp. 4165–4175 (2002).
- [143] S. Lathabai and P. Lloyd, “The Effect of Scandium on the Microstructure, Mechanical Properties and Weldability of a Cast Al–Mg Alloy,” *Acta Materialia*, **50**, pp. 4275–4292 (2002).
- [144] K.-D. Woo, S.-W. Kim, and T. Lou, “Mechanical Properties and Deformation Behavior of Al–4Mg–0.4Sc–1.5MM Alloy at Room Temperature,” *Materials Science and Engineering A*, **334**, pp. 257–261 (2002).

- [145] K. Yu, W. Li, S. Li, and J. Zhao, "Mechanical Properties and Microstructure of Aluminum Alloy 2618 with Al₃(Sc, Zr) Phases," *Materials Science and Engineering A*, **368**, pp. 88–93 (2004).
- [146] P. Cavaliere, "Effect of Minor Sc and Zr Addition on the Mechanical Properties of Friction Stir Processed 2024 Aluminium alloy," *Journal of Materials Science*, **41**, pp. 4299–4302 (2006).
- [147] S. Senkova, O. Senkov, and D. Miracle, "Cryogenic and Elevated Temperature Strengths of an Al–Zn–Mg–Cu Alloy Modified with Sc and Zr," *Metallurgical and Materials Transactions A*, **37**, pp. 3569–3575 (2006).
- [148] W. Liang, Q. Pan, Y. He, Z. Zhu, and Y. Liu, "Effect of Predeformation on Microstructure and Mechanical Properties of AlCuLiZr Alloy Containing Sc," *Materials Science and Technology*, **23**, pp. 395–399 (2007).
- [149] C. L. Fu, "Electronic, elastic, and fracture properties of trialuminide alloys: Al₃Sc and Al₃Ti," *Journal of Materials Research*, **5**, pp. 971–979 (1990).
- [150] E. P. George, D. P. Pope, C. L. Fu, and J. H. Schneibel, "Deformation and Fracture of L1₂ Trialuminides," *ISIJ International*, **31**, pp. 1063–1075 (1991).
- [151] K. Fukunaga, M. Kolbe, K. Yamada, and Y. Miura, "Temperature Dependence of Dislocation Dissociation Mode in L1₂ Trialuminides," *Materials Science and Engineering A*, **234-236**, pp. 594–597 (1997).
- [152] K. Fukunaga, T. Shouji, and Y. Miura, "Temperature Dependence of Dislocation Structure of L1₂–Al₃Sc," *Materials Science and Engineering A*, **239-240**, pp. 202–205 (1997).

- [153] K. Venkateswarlu, L. C. Pathaka, A. K. Raya, G. Dasa, P. K. Verma, M. Kumar, and R. N. Ghosha, "Microstructure, Tensile Strength and Wear Behaviour of Al-Sc Alloy," *Materials Science and Engineering A*, **383**, pp. 374–380 (2004).
- [154] V. Mohles, "Simulations of Dislocation Glide in Overaged Precipitation-Hardened Crystals," *Philosophical Magazine A*, **81**, pp. 971–990 (2001).
- [155] V. Mohles and E. Nembach, "The Peak- and Overaged States of Particle Strengthened Materials: Computer Simulations," *Acta Materialia*, **49**, pp. 2405–2417 (2001).
- [156] V. Mohles, "Orowan Process Controlled Dislocation Glide in Materials Containing Incoherent Particles," *Materials Science and Engineering A*, **309-310**, pp. 265–269 (2001).
- [157] A. Fuchs and D. Ronnpagel, "Comparison Between Simulation Calculations and Measurements Concerning Athermal Yielding of Precipitation Hardening of Cu-Co Single Crystals," *Materials Science and Engineering A*, **164**, pp. 340–345 (1993).
- [158] R. A. Karnesky, C. K. Sudbrack, and D. N. Seidman, "Best-Fit Ellipsoids of Atom-Probe Tomographic Data to Study Coalescence of γ' ($L1_2$) Precipitates in Ni-Al-Cr," *Scripta Materialia*, **Accepted April 2007** (2007).
- [159] D. Tabor, "The Physical Meaning of Indentation and Scratch Hardness," *British Journal of Applied Physics*, **7**, pp. 159–166 (1956).
- [160] C. B. Fuller, *Temporal Evolution of the Microstructures of Al(Sc,Zr) Alloys and Their Influences on Mechanical Properties*, Ph.D. thesis, Northwestern University (2003).
- [161] M. A. Meyers and K. K. Chawla, *Mechanical Metallurgy: Principles and Applications*, Englewood Cliffs, Paramus, NJ (1984).

- [162] P. B. Hirsch and F. J. Humphreys, "Plastic Deformation of Two-Phase Alloys Containing Small Nondeformable Particles," in *The Physics and Strength of Plasticity* (edited by A. Argon), pp. 189–216, MIT Press, Cambridge, MA (1969).
- [163] V. Mohles, "Computer Simulations of Particle Strengthening: The Effects of Dislocation Dissociation on Lattice Mismatch Strengthening," *Materials Science and Engineering A*, **319-321**, pp. 206–210 (2001).
- [164] V. Mohles, "Computer Simulations of Particle Strengthening: Lattice Mismatch Strengthening," *Materials Science and Engineering A*, **319-321**, pp. 201–205 (2001).
- [165] V. Mohles, "Computer Simulations of the Glide of Dissociated Dislocations in Lattice Mismatch Strengthened Materials," *Materials Science and Engineering A*, **324**, pp. 190–195 (2002).
- [166] V. Mohles, "Superposition of Dispersion Strengthening and Size-Mismatch Strengthening: Computer Simulations," *Philosophical Magazine Letters*, **83**, pp. 9–19 (2003).
- [167] V. Mohles, *Computer Simulations of Dislocation Glide in Particle Strengthened Metal Crystals*, Ph.D. thesis (2003).
- [168] V. Mohles, *Continuum Scale Simulation of Engineering Materials: Fundamentals — Microstructures — Process Applications*, vol. 17, chap. Dislocation dynamics simulations of particle strengthening, pp. 375–396, Wiley-VCH, Berlin (2004).
- [169] K. E. Knipling, D. C. Dunand, and D. N. Seidman, "Criteria for Developing Castable, Creep-Resistant Aluminum-Based Alloys—A Review," *Zeitschrift für Metallkunde*, **97**, pp. 246–265 (2006).
- [170] D. J. Chakrabarti, J. T. Staley, S. F. Baumann, R. R. Sawtell, P. E. Bretz, and C. L. Jensen, "Superplastic Aluminum Products and Alloys," US Patent 5,055,257 (1991).

- [171] J. Rösler and E. Arzt, “The Kinetics of Dislocation Climb Over Hard Particles—I. Climb Without Attractive Particle-Dislocation Interaction,” *Acta Metallurgica*, **36**, pp. 1043–1051 (1988).
- [172] J. Cadek, *Creep in Metallic Materials*, Elsevier, New York (1988).
- [173] W. C. Oliver and W. D. Nix, “High Temperature Deformation of Oxide Dispersion Strengthened Al and Al–Mg Solid Solutions,” *Acta Metallurgica*, **30**, pp. 1335–1347 (1982).
- [174] A. H. Clauer and N. Hansen, “High Temperature Strength of Oxide Dispersion Strengthened Aluminium,” *Acta Metallurgica*, **32**, pp. 269–278 (1984).
- [175] J. Rosler, R. Joos, and E. Arzt, “Microstructure and Creep Properties of Dispersion-Strengthened Aluminum Alloys,” *Metallurgical Transactions A*, **23**, pp. 1521–1539 (1992).
- [176] Y. Li and T. G. Langdon, “Creep Behavior of an Al–6061 Metal Matrix Composite Reinforced with Alumina Particulates,” *Acta Materialia*, **45**, pp. 4797–4806 (1997).
- [177] A. B. Pandey, R. S. Mishra, A. G. Paradkar, and Y. R. Mahajan, “Steady State Creep Behaviour of an Al–Al₂O₃ Alloy,” *Acta Materialia*, **45**, pp. 1297–1306 (1997).
- [178] F. A. Mohamed, “On Creep Behavior in Powder Metallurgy 6061 Al,” *Scripta Materialia*, **38**, pp. 457–463 (1998).
- [179] Z. Y. Ma and S. C. Tjong, “Creep Deformation Characteristics of Discontinuously Reinforced Aluminium-Matrix Composites,” *Composites Science and Technology*, **61**, pp. 771–786 (2001).
- [180] O. D. Sherby and E. M. Taleff, “Influence of Grain Size, Solute Atoms and Second-Phase Particles on Creep Behavior of Polycrystalline Solids,” *Materials Science and*

- Engineering A*, **322**, pp. 89–99 (2002).
- [181] E. Arzt and J. Rösler, “The Kinetics of Dislocation Climb Over Hard Particles—II. Effects of an Attractive Particle-Dislocation Interaction,” *Acta Metallurgica*, **36**(4), pp. 1053–1060 (1988).
- [182] J. Rösler and E. Arzt, “A New Model-Based Creep Equation for Dispersion Strengthened Materials,” *Acta Metallurgica et Materialia*, **38**(4), pp. 671–683 (1990).
- [183] D. C. Dunand and A. M. Jansen, “Creep of Metals Containing High Volume Fractions of Unshearable Dispersoids—Part I. Modeling the Effect of Dislocation Pile-Ups Upon the Detachment Threshold Stress,” *Acta Materialia*, **45**(11), pp. 4569–4581 (1997).
- [184] R. A. Karnesky, D. N. Seidman, and D. C. Dunand, “Creep of Al–Sc Microalloys with Rare-Earth Element Additions,” *Materials Science Forum*, **519-521**, pp. 1035–1040 (2006).
- [185] D. Bergner and N. van Chi, “Untersuchungen zur Diffusion von 3d-Metallen in Al,” *Wissenschaftliche Zeitschrift der Pädagogischen Hochschule*, **15** (1977).
- [186] T. Marumo, S. Fujikawa, and K. Hirano, “Diffusion of Zirconium in Aluminum,” *Journal of the Japan Institute of Light Metals*, **23**, pp. 17–25 (1973).
- [187] A. Redsten, E. M. Klier, A. M. Brown, and D. C. Dunand, “Mechanical Properties and Structure of Cast Oxide-Dispersion-Strengthened Aluminum,” *Materials Science and Engineering A*, **201**(1–2), pp. 88–102 (1995).
- [188] B. Q. Han and D. C. Dunand, “Microstructure and Mechanical Properties of Magnesium Containing High Volume Fractions of Ytria Dispersoids,” *Materials Science and Engineering A*, **277**, pp. 297–304 (2000).

- [189] S. Arakawa, T. Hatayama, K. Matsugi, and O. Yanagisawa, "Effect of Heterogeneous Precipitation on Age-Hardening of Al_2O_3 Particle Dispersion Al-4 Mass% Cu Composite Produced by Mechanical Alloying," *Scripta Materialia*, **42**(8), pp. 755–760 (2000).
- [190] J. M. G. de Salazar and M. I. Barrena, "Role of Al_2O_3 Particulate Reinforcements on Precipitation in 7005 Al-Matrix Composites," *Scripta Materialia*, **44**(10), pp. 2489–2495 (2001).
- [191] J. P. Unsworth and S. Bandyopadhyay, "Effect of Thermal Aging on Hardness, Tensile, and Impact Properties of an Alumina Microsphere-Reinforced Aluminum Metal-Matrix Composite," *Journal of Materials Science*, **29**(17), pp. 4645–4650 (1994).
- [192] C. Goujon and P. Goeuriot, "Influence of the Content of Ceramic Phase on the Precipitation Hardening of Al Alloy 7000/ AlN Nanocomposites," *Materials Science and Engineering A*, **356**, pp. 399–404 (2003).
- [193] U. Lagerpusch, V. Mohles, D. Baither, B. Anczykowski, and E. Nembach, "Double Strengthening of Copper by Dissolved Gold-Atoms and by Incoherent SiO_2 -Particles: How do the Two Strengthening Contributions Superimpose?" *Acta Materialia*, **48**, pp. 3647–3656 (2000).
- [194] U. Lagerpusch, V. Mohles, and E. Nembach, "On the Additivity of Solid Solution and Dispersion Strengthening," *Materials Science and Engineering A*, **319-321**, pp. 176–178 (2001).
- [195] J. C. Huang and A. J. Ardell, "Addition Rules and the Contribution of δ' Precipitates to Strengthening of Aged Al-Li-Cu Alloys," *Acta Metallurgica*, **36**, pp. 2995–3006 (1988).

- [196] J. Cadek, K. Kucharova, and K. Milicka, "Creep in Copper Dispersion Strengthened with Fine Alumina Particles and Reinforced with Alumina Short Fibres—An ODS Copper Matrix Composite," *Journal of Alloys and Compounds*, **378**, pp. 123–126 (2004).
- [197] L. M. Peng and S. J. Zhu, "Creep of Metal Matrix Composites Reinforced by Combining Nano-Sized Dispersoids with Micro-Sized Ceramic Particulates or Whiskers (Review)," *International Journal of Materials & Product Technology*, **18**, pp. 215–254 (2003).
- [198] J. Rosler and M. Baker, "A Theoretical Concept for the Design of High-Temperature Materials by Dual-Scale Particle Strengthening," *Acta Materialia*, **48**, pp. 3553–3567 (2000).
- [199] K. Kucharová, J. Cadek, and S. J. Zhu, "The Load Transfer Effect in the True Threshold Creep Behaviour of an Al–8.5 Fe–1.3 V–1.7 Si Alloy Reinforced with Alumina Short Fibres," *Journal of Materials Science*, **38**, pp. 3535–3543 (2003).
- [200] E. A. Marquis, *Microstructural Evolution and Strengthening Mechanisms in Al–Sc and Al–Mg–Sc Alloys*, Ph.D. thesis, Northwestern University (2002).
- [201] R. W. Hyland, Jr., M. Asta, S. M. Foiles, and C. L. Rohrer, "Al(f.c.c.):Al₃Sc(L12) Interphase Boundary Energy Calculations," *Acta Materialia*, **46**, pp. 3667–3678 (1998).
- [202] X. D. Zhang and G. Sauthoff, "Analysis of Relationships Between Cohesive Energy, Elastic Moduli and Lattice Parameter of Some High Temperature Intermetallics," *Intermetallics*, **3**, pp. 137–140 (1995).
- [203] Y. Harada and D. C. Dunand, "Thermal Expansion of Al₃Sc and Al₃(Sc_{0.75}X_{0.25})," *Scripta Materialia*, **48**, pp. 219–222 (2003).

- [204] J. Røyset and N. Ryum, "Some comments on the misfit and coherency loss of Al₃Sc particles in Al–Sc alloys," *Scripta Materialia*, **52**, pp. 1275–1279 (2005).
- [205] J. Dundurs, "Elastic Interaction of Dislocations with Inhomogeneities," in *Mathematical Theory of Dislocations* (edited by T. Mura), pp. 70–115, ASME, New York (1969).
- [206] T. F. Kelly and M. K. Miller, "Atom Probe Tomography," *Review of Scientific Instruments*, **78**, pp. 031,101:1–20 (2007).
- [207] D. N. Seidman, "Three-Dimensional Atom-Probe Tomography: Advances and Applications," *Annual Review of Materials Research*, **37**, pp. 127–158 (2007).
- [208] M. K. Miller, B. D. Wirth, and G. R. Odette, "Precipitation in Neutron-Irradiated Fe–Cu and Fe–Cu–Mn Model Alloys: A Comparison of APT and SANS Data," *Materials Science and Engineering A*, **353**, pp. 133–139 (2003).
- [209] R. P. Kolli and D. N. Seidman, "Comparison of Compositional and Morphological Atom-Probe Tomography Analyses for a Multicomponent Fe–Cu Steel," *Microscopy & Microanalysis*, **Submitted**, (2007).
- [210] F. Soisson, A. Barbu, and G. Martin, "Monte Carlo Simulations of Copper Precipitation in Dilute Iron–Copper Alloys During Thermal Ageing and Under Electron Irradiation," *Acta Materialia*, **44**, pp. 3789–3800 (1996).
- [211] E. Cadel, D. Lemarchand, S. Chambreland, and D. Blavette, "Atom Probe Tomography Investigation of the Microstructure of Superalloys N18," *Acta Materialia*, **50**, pp. 957–966 (2002).
- [212] A. Heinrich, T. Al-Kassab, and R. Kirchheim, "Investigation of the Early Stages of Decomposition of Cu–0.7at.% Fe with the Tomographic Atom Probe," *Materials Science*

- and Engineering A*, **353**, pp. 92–98 (2003).
- [213] D. Wolde-Giorgis, T. Al-Kassab, and R. Kirchheim, “Nucleation and Growth in Cu–0.7at.% Ti as Studied with the Tomographic Atom Probe,” *Materials Science and Engineering A*, **A353**, pp. 152–157 (2003).
- [214] M. Dumont, W. Lefebvre, B. Doisneau-Cottignies, and A. Deschamps, “Characterisation of the Composition and Volume Fraction of η' and η Precipitates in an Al–Zn–Mg Alloy by a Combination of Atom Probe, Small-Angle X-Ray Scattering and Transmission Electron Microscopy,” *Acta Materialia*, **53**, pp. 2881–2892 (2005).
- [215] D. Isheim, G. Hsieh, R. D. Noebe, and D. N. Seidman, “Nanostructural Temporal Evolution and Solute Partitioning in Model Ni-Based Superalloys Containing Ruthenium, Rhenium, and Tungsten,” in *Solid-Solid Phase Transformations in Inorganic Materials*, vol. 1 (edited by J. M. Howe, D. E. Laughlin, J. K. Lee, D. J. Srolovitz, U. Dahmen, and W. A. Soffa), pp. 309–314, TMS, Warrendale, PA (2005).
- URL <http://nucapt.northwestern.edu/refbase/show.php?record=187>
- [216] S. D. Erlach, H. Leitner, M. Bischof, H. Clemens, F. Danoix, D. Lemarchand, and I. Siller, “Comparison of NiAl Precipitation in a Medium Carbon Secondary Hardening Steel and C-Free PH13–8 Maraging Steel,” *Materials Science and Engineering: A*, **429**, pp. 96–106 (2006).
- [217] E. V. Pereloma, I. B. Timokhina, K. F. Russell, and M. K. Miller, “Characterization of Clusters and Ultrafine Precipitates in Nb-Containing C–Mn–Si Steels,” *Scripta Materialia*, **54**, pp. 471–476 (2006).
- [218] A. Andersson, K. Stiller, and M. Hättstrand, “Comparison of Early Stages of Precipitation in Mo-Rich and Mo-Poor Maraging Stainless Steels,” *Surface and Interface*

- Analysis*, **39**, pp. 195–200 (2007).
- [219] D. Blavette, F. Vurpillot, P. Pareige, and A. Menand, “A Model Accounting for Spatial Overlaps in 3D Atom-Probe Microscopy,” *Ultramicroscopy*, **89**, pp. 145–153 (2001).
- [220] C. K. Sudbrack, K. E. Yoon, R. D. Noebe, and D. N. Seidman, “Temporal Evolution of the Nanostructure and Phase Compositions in a Model Ni–Al–Cr Alloy,” *Acta Materialia*, **54**, pp. 3199–3210 (2006).
- [221] Z. Mao, C. K. Sudbrack, K. E. Yoon, G. Martin, and D. N. Seidman, “The Mechanism of Morphogenesis in a Phase Separating Concentrated Multi-Component Alloy,” *Nature Materials*, **6**, pp. 210–216 (2007).
- [222] J. Z. Zhu, T. Wang, A. J. Ardell, S. H. Zhou, Z. K. Liu, and L. Q. Chen, “Three-Dimensional Phase-Field Simulations of Coarsening Kinetics of γ' Particles in Binary Ni–Al Alloys,” *Acta Materialia*, **52**, pp. 2837–2845 (2004).
- [223] R. E. Beddoe, P. Haasen, and G. Kostorz, “Early Stages of Decomposition in Ni–Al Single Crystals Studied by Small-Angle Neutron Scattering,” in *Decomposition of Alloys: The Early Stages*, vol. 2 of *Acta-Scripta Metallurgica Proceedings Series* (edited by P. Haasen, V. Gerold, R. Wagner, and M. F. Ashby), pp. 233–238, Pergamon, Oxford (1984).
- [224] C. Schmuck, F. Danoix, P. Caron, A. Hauet, and D. Blavette, “Atomic Scale Investigation of Ordering and Precipitation Processes in a Model Ni–Cr–Al Alloy,” *Applied Surface Science*, **94–95**, pp. 273–279 (1996).
- [225] C. K. Sudbrack, K. E. Yoon, R. D. Noebe, and D. N. Seidman, “The Temporal Evolution of the Nanostructure of a Model Ni–Al–Cr Superalloy,” *TMS Letters*, **1**, pp. 25–26 (2004).

URL <http://nucapt.northwestern.edu/refbase/show.php?record=199>

- [226] C. K. Sudbrack, R. D. Noebe, and D. N. Seidman, “Temporal Evolution of Sub-Nanometer Compositional Profiles Across the γ/γ' Interface in a Model Ni–Al–Cr Superalloy,” in *Solid-Solid Phase Transformations in Inorganic Materials*, vol. 2 (edited by J. M. Howe, D. E. Laughlin, J. K. Lee, D. J. Srolovitz, U. Dahmen, and W. A. Soffa), pp. 543–548, TMS, Warrendale, PA (2005).

URL <http://nucapt.northwestern.edu/refbase/show.php?record=180>

- [227] C. K. Sudbrack, R. D. Noebe, and D. N. Seidman, “Compositional Pathways and Capillary Effects During Isothermal Precipitation in a Nondilute Ni–Al–Cr Alloy,” *Acta Materialia*, **55**, pp. 119–130 (2007).
- [228] D. Blavette, B. Deconihout, A. Bostel, J. M. Sarrau, M. Bouet, and A. Menand, “The Tomographic Atom Probe: A Quantitative Three-Dimensional Nanoanalytical Instrument on an Atomic Scale,” *Review of Scientific Instruments*, **64**, pp. 2911–2919 (1993).
- [229] A. Cerezo, T. J. Godfrey, S. J. Sijbrandij, G. D. W. Smith, and P. J. Warren, “Performance of an Energy-Compensated Three-Dimensional Atom Probe,” *Review of Scientific Instruments*, **69**, pp. 49–58 (1998).
- [230] O. C. Hellman, J. B. du Rivage, and D. N. Seidman, “Efficient Sampling for Three-Dimensional Atom Probe Microscopy Data,” *Ultramicroscopy*, **95**, pp. 199–205 (2003).
- [231] J. F. Nye, *Physical Properties of Crystals: Their Representation by Tensors and Matrices*, Oxford University Press, Oxford (1985).
- [232] W. H. Press, S. A. Teukolsky, W. T. Vetterling, and B. P. Flannery, *Numerical Recipes: The Art of Scientific Computing*, 1 edn., Cambridge University Press, Cambridge (1986).

- [233] K. M. Bowkett and D. A. Smith, *Field-Ion Microscopy*, North-Holland, Amsterdam (1970).
- [234] H. J. Bunge, *Texture Analysis in Materials Science: Mathematical Methods*, Butterworths, Boston (1982).
- [235] J. Taylor, *An Introduction to Error Analysis: The Study of Uncertainties in Physical Measurements*, University Science Books (1997).
- [236] P. Bevington and D. Robinson, *Data Reduction and Error Analysis for the Physical Sciences*, McGraw-Hill Education (2002).
- [237] M. Lucas and J. Hubbard, *Absolute BSD: The Ultimate Guide to FreeBSD*, No Starch Press (2002).
- [238] G. Lehey, *The Complete FreeBSD, Fourth Edition*, O'Reilly Media, Inc. (2003).
- [239] Y. Korff, P. Hope, and B. Potter, *Mastering FreeBSD and OpenBSD Security*, O'Reilly Media, Inc. (2004).
- [240] D. Barrett and R. Silverman, *SSH, The Secure Shell: The Definitive Guide*, O'Reilly (2001).
- [241] H. Dwivedi, *Implementing SSH: Strategies for Optimizing the Secure Shell*, Wiley (2003).
- [242] J. T's, R. Eckstein, and D. Collier-Brown, *Using Samba, Second Edition*, O'Reilly Media, Inc. (2003).
- [243] C. Pilato, B. Collins-Sussman, and B. Fitzpatrick, *Version Control with Subversion*, O'Reilly Media, Inc. (2004).
- [244] A. Butcher, *Sams Teach Yourself MySQL in 21 Days*, Sams (2002).
- [245] M. Widenius and D. Axmark, *MySQL Reference Manual*, O'Reilly Media, Inc. (2002).

- [246] A. S. Pachev, *MySQL Enterprise Solutions*, Wiley (2003).
- [247] J. Horn and M. Grey, *MySQL: Essential Skills*, McGraw-Hill Osborne Media (2004).
- [248] J. Zawodny and D. Balling, *High Performance MySQL*, O'Reilly Media, Inc. (2004).
- [249] *MySQL Administrator's Guide and Language Reference*, MySQL Press (2006).

APPENDIX A

Best-Fit Ellipsoids of Atom-Probe Tomographic Data to Study**Coalescence of γ' ($L1_2$) Precipitates in Ni–Al–Cr**

One of the principle challenges that analyzing three-dimensional atom-probe tomographic (APT) results poses is the amount of raw data that the instruments are now able to collect [206, 207]; we have collected continuous data sets as large as 2.1×10^8 properly ranged atoms from a single specimen. It is necessary to extract information about spatial and compositional measures, such as precipitate size from these data sets. A common method to measure the size of precipitates is to calculate a single radius of gyration (or, from this, the Guinier radius) [95, 115]. While this technique works well for equiaxed, spheroidal precipitates [208, 209], many alloy systems investigated by APT have non-spherical features [210–218]. Improperly reconstructed data sets, which have preferential evaporation or local-magnification effects, may also exhibit non-spherical features [219]. Techniques that measure the angular eccentricity of features can be used to quantify the accuracy of a reconstruction. The radius of gyration technique does not, however, retain three-dimensional information concerning precipitate orientation.

In this article, a more general alternative to the radius of gyration is presented and applied. Best-fit ellipsoids have equivalent centroids, moments of inertia, and principle axes for arbitrarily shaped precipitates. The crystallographic orientations of the resulting ellipsoids are then used to study the coagulation-coalescence coarsening mechanism in a Ni-Al-Cr

alloy, which occurs when the γ' -precipitate number density is large ($> 10^{24} \text{ m}^{-3}$) and the edge-to-edge distance between adjacent γ' -precipitates is small ($< 2 \text{ nm}$) [220, 221].

In lattice kinetic Monte Carlo simulations, a coagulation-coalescence coarsening mechanism is reported [221]. This mechanism is caused by non-equilibrium overlapping diffusion fields, which originate from the long-range vacancy-solute binding energies and a small mean edge-to-edge interprecipitate distance. The non-equilibrium concentration profiles observed at the γ' -precipitate/ γ -matrix interfaces lead to a higher interfacial free energy than for fully equilibrated γ' -precipitates. The excess free energy of the region of overlapping concentration profiles (“diffuse neck”) can decrease by changing the concentration thereof into a well-formed neck [221]. Phase-field simulations find that the rate of γ' -precipitate coalescence is increased when the γ/γ' -interfacial width is increased artificially, thereby increasing the overlapping diffusion fields [222]. While nanometer-sized coagulated γ' -precipitates might have been observed experimentally, past studies only commented on whether precipitates appeared to be non-equiaxed [223–225], necked [226, 227], or chemically ordered [220]. They did not explore the crystallographic orientation for precipitate coagulation.

Dr. Chantal Sudbrack prepared a Ni-5.2 Al-14.2 Cr (at.%) alloy, aged it, and performed field-ion microscopy and atom probe tomographic experiments on it. After she reconstructed the data, I performed the data analysis that this appendix describes. She initially implemented the ellipsoid method (with minor consultation from me) and source code is given in her thesis. I re-did this analysis and also extracted the orientational information that is presented here.

The alloy was melted under an Ar atmosphere and chill cast. Its chemical composition was verified by inductively coupled plasma spectroscopy. The alloy was homogenized for 24 h at 1300°C, which resulted in coarse grains (0.5–2 mm diameter). After homogenization, the alloy was annealed at 900°C (γ -phase field) and water quenched to ambient temperature. The solutionized alloy was sectioned and aged for 4 h at 600°C and then quenched. This treatment leads to the greatest percentage of γ' -precipitates that are interconnected by necks ($30 \pm 4\%$) [220]. The specimens were cut, ground, and then electropolished into APT tips. Three separate APT runs of ca. 3×10^6 atoms were collected on a first-generation 3-D APT [228, 229] at a specimen temperature of 40.0 ± 0.3 K, a pulse fraction of 19%, and a pulse repetition rate of 1.5 kHz. The computer programs *IVAS* (Imago Scientific Instruments) and *ADAM* [68] were used to analyze APT data. The γ/γ' interface is delineated using a 9 at.% Al isoconcentration surface [230] and the atoms contained within the γ' -surface were exported and segmented into individual γ' -precipitates by a modified envelope algorithm [94, 95, 115, 200].

The γ' -precipitates are divided into three classes: (i) single γ' -precipitates (uncoagulated, without a concave neck) that are not cut by the surface of the analyzed volume; (ii) two or more coalesced γ' -precipitates that are interconnected by a concave neck; (iii) γ' -precipitates cut by the analysis volume boundary. Class (i) accounts for 42% of γ' -precipitates analyzed, class (ii) accounts for 28% of the γ' -precipitates analyzed, and only 12% of them are formations of more than two γ' -precipitates (the largest of which is made up of five distinguishable γ' -precipitates). The best-fit ellipsoid method yields quantitative results for all three classes; particularly class (ii), which is important for understanding the coagulation-coalescence mechanism of γ' -precipitate coarsening.

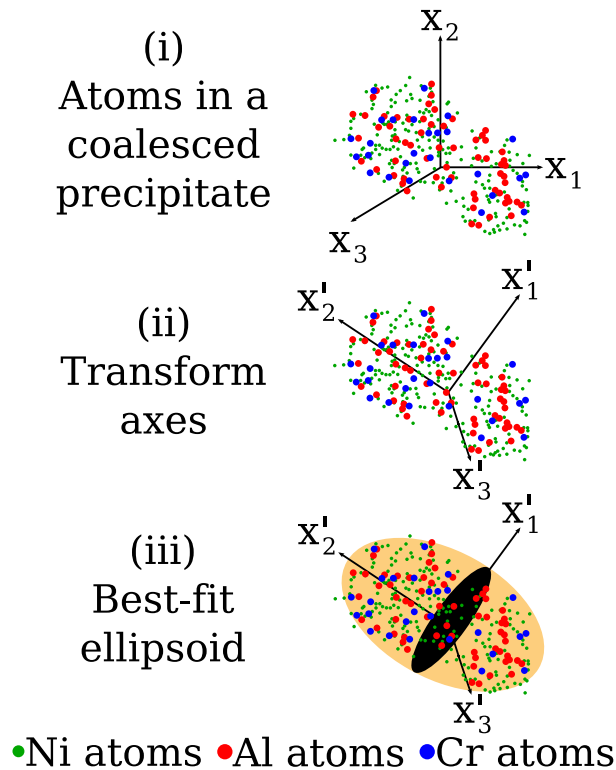


Figure A.1. The best-fit ellipsoid of a precipitate is determined in three steps: (i) for a reference set of axes (X_1 , X_2 , and X_3), identify the x_1 , x_2 , x_3 coordinates of all atoms in a precipitate and its center of mass to obtain a moment of inertia tensor (L) (Eqs. A.1–A.3); (ii) the orientation of the principle axes (X'_1 , X'_2 , and X'_3) of the ellipsoid axes construct a Jacobian transformation matrix that will diagonalize L . (iii) the lengths of the major and minor semi-axes of the best-fit ellipsoid are found from the eigenvalues of the transformed matrix. (Eq. A.4).

A schematic that explains the fitting of an equivalent ellipsoid to atoms of coagulated and coalesced precipitates is presented in Fig. A.1. For a reference space defined by Cartesian axes X_1 , X_2 , X_3 (typically the analysis direction and the two orthogonal principle directions of the area detector), the major and minor axes of the best-fit ellipsoid of a precipitate containing N atoms are determined directly from its eigenvalues (λ_1 , λ_2 , λ_3), also referred to as the principle axes [231]. The principle axes are segments along the transformed

Cartesian X'_1 , X'_2 , and X'_3 axes and are obtained from the diagonalization of the characteristic length matrix, L (also known as the inertia tensor). This diagonalization is obtained by a Jacobian transformation [232] of a symmetric second-rank tensor, as follows:

$$(A.1) \quad L = \begin{bmatrix} l_{11} & l_{12} & l_{13} \\ l_{12} & l_{22} & l_{23} \\ l_{13} & l_{23} & l_{33} \end{bmatrix} \xrightarrow{\text{transform}} \begin{bmatrix} \lambda_1 & 0 & 0 \\ 0 & \lambda_2 & 0 \\ 0 & 0 & \lambda_3 \end{bmatrix} ;$$

where the characteristic lengths, l_{jk} , are calculated from the positions of i^{th} atom in the reference space ($x_1(i)$, $x_2(i)$, and $x_3(i)$), relative to a precipitate's center of mass ($x_1(\text{com})$, $x_2(\text{com})$, and $x_3(\text{com})$), averaged over N atoms, employing:

$$(A.2) \quad l_{kk} = \frac{1}{N} \sum_i \left(\sum_{j \neq k} (x_j(i) - x_j(\text{com}))^2 \right)$$

$$(A.3) \quad l_{jk} = -\frac{1}{N} \sum_i \left((x_j(i) - x_j(\text{com})) (x_k(i) - x_k(\text{com})) \right) \quad \text{for } j \neq k$$

The diagonalization of the L matrix follows a procedure outlined in Ref. [232]. The transformation matrix used for this diagonalization yields the orientation of the ellipsoid with respect to the reference state. Defining $\lambda_1 \geq \lambda_2 \geq \lambda_3$, the semi-axes (S_i) of the best-fit ellipsoid are given by:

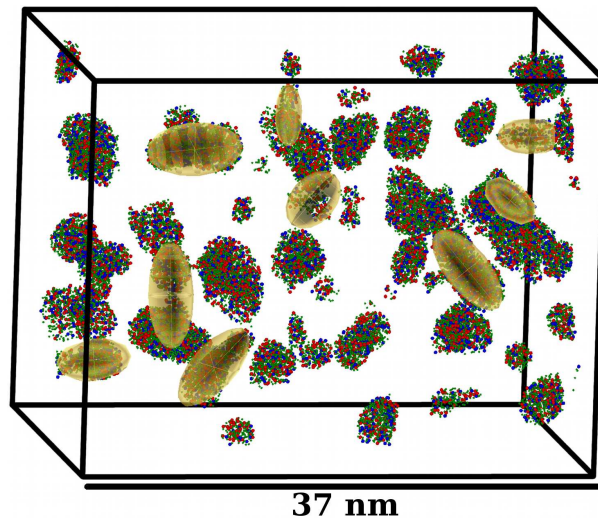


Figure A.2. A representative data set for a Ni-5.2 Al-14.2 Cr (at.%) alloy, whose thermal history is discussed in the text. The coloring scheme matches that of Fig. A.1, with Ni atoms in green, Al atoms in red, and Cr atoms in blue. The atoms in the γ -matrix (FCC) are omitted for clarity. The gold colored best-fit ellipsoids indicate those γ' (L1₂) precipitates that are interconnected by necks.

$$(A.4) \quad S_i = \sqrt{\frac{5}{2} (\lambda_j + \lambda_k - \lambda_i)} \quad \text{for } j \neq k;$$

where $S_3 \geq S_2 \geq S_1$ are the major semi-axis and two minor semi-axes, respectively.

Figure A.2 shows a reconstruction of one APT data set where ellipsoids have been fit to interconnected γ' -precipitates. As is seen, the best-fit ellipsoid retains 3-D size and crystallographic orientation information that is jettisoned by other techniques [95, 115].

Single γ' -precipitates that are not cut by the analysis volume have aspect ratios of $\frac{S_3}{S_2} = 1.5 \pm 0.5$ and $\frac{S_2}{S_1} = 1.3 \pm 0.2$. The closeness of these values to unity is consistent with equiaxed, uncoagulated precipitates.

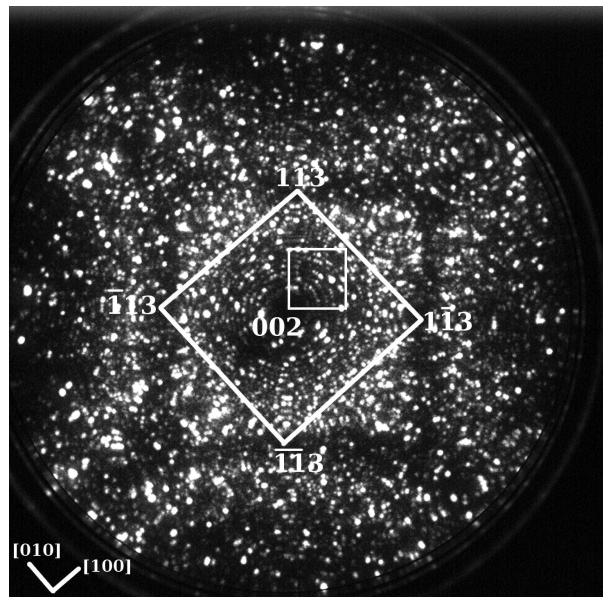


Figure A.3. An FIM image, centered on the 002 pole, taken before APT analysis. The small square denotes the area and orientation for the data set in Fig. A.1. The larger square connects the 113 family of poles and the edges of this square give the [010] and [100] directions.

Coalesced γ' -precipitates that are interconnected by necks have aspect ratios of $\frac{s_3}{s_2} = 2.9 \pm 0.9$ and $\frac{s_2}{s_1} = 1.3 \pm 0.3$. The ratio for $\frac{s_3}{s_2}$ is about twice the same ratio for uncoagulated precipitates, but $\frac{s_2}{s_1}$ is about the same for the two classes. This demonstrates that a majority of these consist of two equiaxed γ' -precipitates that have coagulated and undergone coalescence.

Precipitates that are cut by the edge of the analysis volume can serve as a check of the best-fit ellipsoid method. These have $\frac{s_3}{s_2} = 2.2 \pm 0.8$ and $\frac{s_2}{s_1} = 1.4 \pm 0.4$ because the majority are equiaxed, uncoagulated γ' -precipitates that are, on average, cut in two by the analysis boundary. Sampling bias by coagulated γ' -precipitates is small, as they make up a minority of precipitates and many can be isolated (if their concave necks are in the analysis volume).

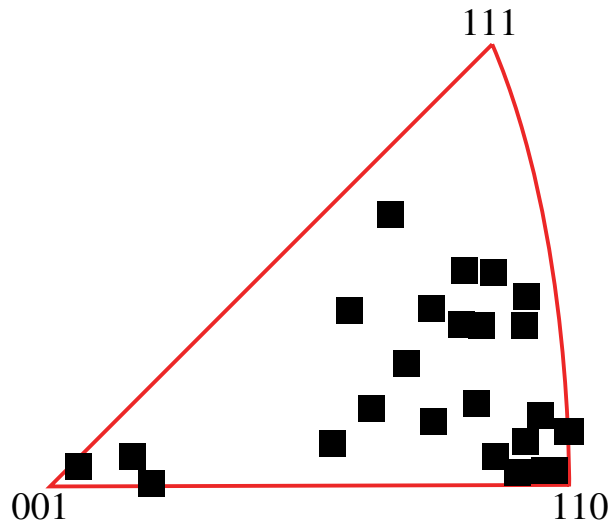


Figure A.4. An inverse pole figure for all interconnected γ' ($L1_2$) precipitates in this study, presented in the standard stereographic triangle. There is a preference for coagulation along and close to $\langle 110 \rangle$ -type directions, which is consistent with a diffusion controlled mechanism for coagulation.

It is useful to relate the axes of the analysis volume with specific crystallographic directions to study the orientation of γ' -precipitate coagulation. The analysis direction, which was chosen near the 002 crystallographic pole, provides us with the [001] direction. The [010] and [100] directions can be deduced from a Field-Ion Microscope (FIM) image (Fig. A.3) [233] to within $1\text{--}4^\circ$. FIM micrographs also demonstrate that local magnification effects are negligible in this alloy, which is consistent with the small lattice parameter misfit, $\delta = 0.0006 \pm 0.0004$ [220].

The rotation matrix used in the best-fit ellipsoid method yields the Bunge Euler angles [234] for the major principle axis of the γ' -precipitate with respect to this crystallographically-resolved reference system. From these, an inverse pole figure (Fig. A.4) shows the orientations of γ' -precipitates that are the result of the coagulation-coalescence coarsening. There

is a preference for coagulation along the $\langle 110 \rangle$ -type directions. 30% of the coalesced precipitates are within 10° and 71% are within 15° of $\langle 110 \rangle$ -type directions. In the FCC structure of the γ -matrix, $\langle 110 \rangle$ is the fastest diffusion path for solute clusters, and is therefore consistent with the model presented in Ref. [221]. Some γ' -precipitates coagulated along $\langle 100 \rangle$, which is the next-fastest diffusion path and none coagulated along $\langle 111 \rangle$, which is a slower path.

No crystallographic orientational preference was found for single, uncoagulated γ' -precipitates. This supports, once more, the equiaxed nature of γ' -precipitates and the proper reconstruction approach (with negligible local magnification) for analyzing the raw APT data. The γ' -precipitates that are cut by the analysis boundary show a preference for the $[100]$ direction, as that direction makes up the majority of the analysis frustum's surface.

The measurement of size and orientation of non-spheroidal precipitates in APT data requires more spatial information to be preserved than for the commonly used methods currently reported to date. We have demonstrated that the best-fit ellipsoid technique preserves the center of gravity, moment of inertia, and principle axes of any precipitate. The technique is applied to specific results for a Ni-Al-Cr alloy with both uncoagulated equiaxed γ' -precipitates and nonequiaxed lobed precipitates that formed through a coagulation-coalescence coarsening mechanism.

APPENDIX B

Error Analysis

Error is sometimes omitted or incorrectly used in the applied sciences, but the consistent and correct use of error is important when comparing experimental data with each other or to a model. This appendix serves as a very brief primer in error analysis, with examples given for creep experiments. More details are given in Refs. [235, 236].

B.1. Error Propagation

To measure statistical dispersion of a quantity, i , we use the standard deviation, σ_i . Given F , a value defined by an arbitrary function of variables ($F = f(u, v, \dots)$, with u, v, \dots being variables, each of which can have an error), the standard deviation of F , σ_F is:

$$\begin{aligned}\sigma_F &= \sqrt{\lim_{n \rightarrow \infty} \left[\frac{1}{n} \sum_{i=1}^n (F_i - \bar{F})^2 \right]} \\ &\approx \sqrt{\sigma_u^2 \left(\frac{\partial F}{\partial u} \right)^2 + \sigma_v^2 \left(\frac{\partial F}{\partial v} \right)^2 + \dots + 2\sigma_{uv} \left(\frac{\partial F}{\partial u} \right) \left(\frac{\partial F}{\partial v} \right)}.\end{aligned}$$

Assuming the errors $\sigma_u, \sigma_v, \dots$ are uncorrelated:

$$\sigma_F \approx \sqrt{\sigma_u^2 \left(\frac{\partial F}{\partial u} \right)^2 + \sigma_v^2 \left(\frac{\partial F}{\partial v} \right)^2 + \dots}$$

Uncertainty estimates based on algebraic manipulations are listed in Table B.1

Table B.1. Estimates of propagated error for common algebraic manipulations

Function, $F = f(u, v)$	Estimated Uncertainty, σ_F
$u \pm v$	$\sqrt{\sigma_u^2 + \sigma_v^2}$
$u^i v^j$	$u^i v^j \sqrt{\left(i \frac{\sigma_u}{u}\right)^2 + \left(j \frac{\sigma_v}{v}\right)^2}$
$\ln u$	$\frac{\sigma_u}{u}$
$\exp u$	$\sigma_u \exp u$

B.2. Least-Squares Fits

In a weighted least-squares fit, the parameters (A, B, \dots) of a function ($f(x)$) of the independent variable x are varied to minimize the sum of squares of residuals, χ^2 :

$$\chi^2 = \sum_i \left(\frac{y_i - f(x_i)}{\sigma_i} \right)^2;$$

where y_i is the measured dependent quantity (χ^2 has been weighted by $1/\sigma_i^2$, assigning more significance to observations with lower uncertainty). In the case of the linear function, $f(x) = A + Bx$, the uncertainties of the fitting parameters are given as:

$$\sigma_A = \sqrt{\frac{1}{\Delta} \sum_i \frac{x_i^2}{\sigma_i^2}}$$

$$\sigma_B = \sqrt{\frac{1}{\Delta} \sum_i \frac{1}{\sigma_i^2}};$$

with:

$$\Delta = \sum_i \frac{1}{\sigma_i^2} \sum_i \frac{x_i^2}{\sigma_i^2} - \left(\sum_i \frac{x_i}{\sigma_i^2} \right)^2.$$

Nonlinear equations may often be algebraically transformed to linear equations or software might be used to estimate the fitting parameter uncertainty in nonlinear fits.

B.3. Errors in Creep Experiments

B.3.1. Applied Stress, σ

The applied stress, σ is defined as:

$$\sigma = \frac{L}{A}$$

$$\sigma_{\sigma} = \sqrt{\sigma^2 \left(\left(\frac{\sigma_L}{L} \right)^2 + \left(\frac{\sigma_A}{A} \right)^2 \right)};$$

where L is the load and A is the area. The load is defined by the lever equation:

$$L = ax + b$$

$$\sigma_L = \sqrt{\left(L^2 \left(\left(\frac{\sigma_a}{a} \right)^2 + \left(\frac{\sigma_x}{x} \right)^2 \right) \right) + \sigma_b^2};$$

where x is the load on the far end of the arm and a and b are both the fitting parameters from the creep frame calibration. Note that σ_x varies on which set of particular weights are use, but is smaller than the uncertainty in the frame calibration and so is neglected.

B.3.1.1. Cylindrical samples. For cylindrical samples, A is given as:

$$A = \pi \left(\frac{d}{2} \right)^2$$

$$\sigma_A = 2A \frac{\sigma_d}{d};$$

where d and σ_d are the diameter of the sample and its error, as obtained from measuring with calipers.

B.3.2. Strain Rate

Because the uncertainty in length measurements are similar and small, the uncertainty in strain rate is taken as the maximum of the fitting error and of the minimal strain rate that is measurable over the duration of an experiment.

B.3.3. Threshold Stress

The threshold stress, σ_{th} , is found by a weighted least-squares linear fit through $\sqrt[n]{\dot{\epsilon}}$ vs. σ . The weight should be $\frac{1}{\sigma^2 \sqrt[n]{\dot{\epsilon}}}$. This is the default weighting of most graphing software which allow you to specify error in the ordinate. Note that Microsoft Excel should be avoided, as it makes incorrect weighted fits. Most recent versions of analysis software made for scientists, including Grace and Microcal Origin will give the correct fit. σ_σ was given above. $\sigma_{\sqrt[n]{\dot{\epsilon}}}$ is:

$$\sigma_{\sqrt[n]{\dot{\epsilon}}} = \frac{\sqrt[n]{\dot{\epsilon}} \sigma_{\dot{\epsilon}}}{n \dot{\epsilon}}.$$

n is the imposed stress exponent ($n = 4.4$ for Al). This weighted fit should yield a slope, s , and an intercept, i , and errors. Then:

$$(B.1) \quad \sigma_{th} = -\frac{i}{s}$$

$$(B.2) \quad \sigma_{\sigma_{th}} = \sqrt{\sigma_{th}^2 \left(\left(\frac{\sigma_i}{i} \right)^2 + \left(\frac{\sigma_s}{s} \right)^2 \right)}$$

Table B.2. Example creep data (for Al-600 Sc-200 Gd with $\langle R \rangle = 3.6 \pm 0.4$ nm precipitates [9])

σ (MPa)	$\dot{\epsilon}$ (10^{-9} s^{-1})	$\sqrt[4.4]{\dot{\epsilon}}$ ($10^{-3} \text{ s}^{-\frac{1}{4.4}}$)
36.5	4 ± 2	12 ± 2
37.4	10 ± 5	15 ± 2
38.2	317 ± 3	33.34 ± 0.07
39.6	9000 ± 4	71.32 ± 0.01

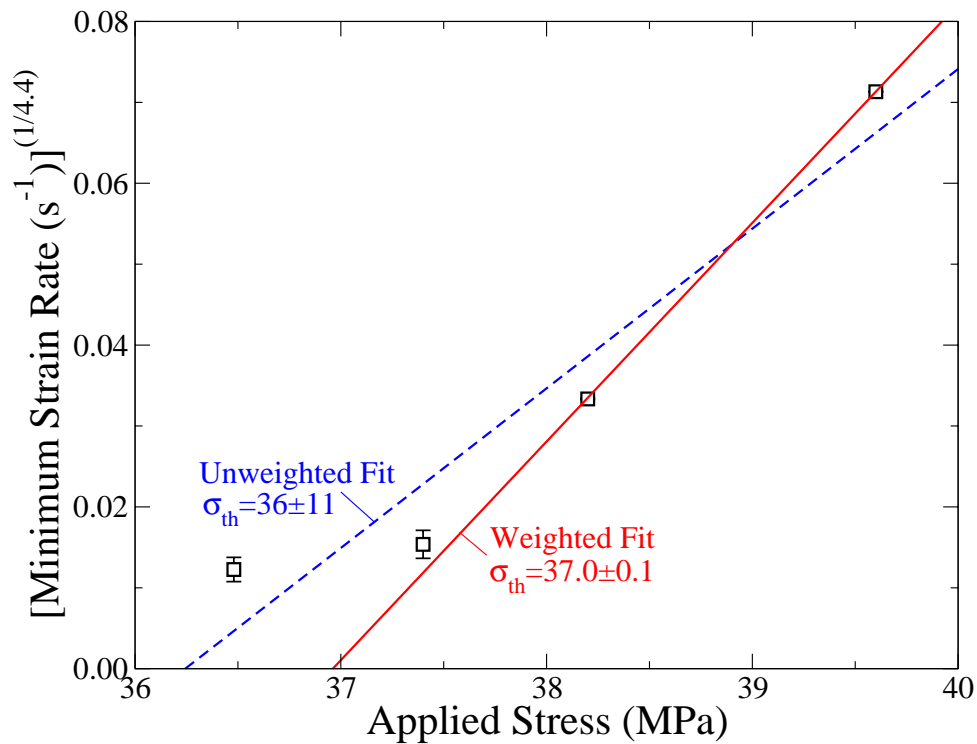


Figure B.1. Unweighted and weighted fits for the creep data presented in Table B.2.

B.3.4. Example

Table B.2 contains an example set of minimum strain rate creep data for an Al-600 Sc-200 Gd alloy with $\langle R \rangle = 3.6 \pm 0.4$ nm precipitates [9]. The experimental uncertainty in $\dot{\epsilon}$ is algebraically transformed using a rule in Table B.1 and is plotted in Fig. B.1. Unweighted and

weighted fits are compared. The weighted fit takes into account the high relative certainty in the measured strain rate for faster strain rates (under larger applied stresses). This reduces the uncertainty in the fitting parameters, which reduces the uncertainty in the threshold stress (as calculated using Eq. B.2).

APPENDIX C

Source Code for Interprecipitate Distance Measurement

```

#!/usr/bin/env python

#####
#                               PROGRAM INFORMATION                               #
#####
#
# Calculates minimum distances between ellipsoids
#
# Usage: interppt
#
# Requires: Python & several libraries.
#
# These are easy to install in most Linux distros
#
# For Mac and Windows, enthon is nice:
#
# <http://code.enthought.com/enthon/>
# Input: 'transform3d.txt', contains 4x4 transformation matrices for ppts
# Output: 'allspacings.csv', spreadsheet containing all distances
#
# 'minspacings.csv', the shortest distance for each ppt
#
# Richard Karnesky
# Released under the GPL
# http://www.gnu.org/copyleft/gpl.html
# Created: 2005-12-15
# Updated: 2007-03-20
#

```

```

# Notes:
# * transform3d.txt
# * Is usually generated by a modified version of precip.py (from IVAS)
# * This is available on ARC
# * I do not own the copyright, so can't publish my modifications
# * The only significant modification is to write out transform3d.txt
# * Alternatively, see Chantal Sudbrack's thesis for ellipsoid fitting
# * Convex hull/Delaunay spacings
# * These can be extracted with hull [1] or qhull [2]
# [1] <http://www.cs.att.com/netlib/voronoi/hull.html>
# [2] <http://www.qhull.org/>
#
# Possible improvements:
# * Optimize
# * Thread – this will make it faster on multiprocessor machines
# * Make minspacings.csv use the csv writer
# * Optionally only do the minimization on ppts which are "close enough"
# * Optionally exclude outer-most ppts on hull to eliminate bias
# * User-friendliness
# * Specify files for input/output
# * GUI (?)

#####
#                                     IMPORTS                                     #
#####

from LinearAlgebra import inverse
from math import sqrt
from scipy.optimize import fmin_cobyla
from scipy import alltrue, dot, linalg, zeros
from string import split, strip

```

```

from csv import writer

try:
    # Import Psyco if available (it will speed things up)
    import psyco
    psyco.full()
except ImportError:
    pass

#####
#                               DEFINITIONS                               #
#####
# Distance between two points with different transformations
# The two points are in a single array:
# [x1_1,x1_2,x1_3, x2_1,x2_2,x2_3]
def distance(x, transform1, transform2):
    x1 = zeros(4,float)
    x2 = zeros(4,float)
    for i in range(3):
        x1[i]=x[i]
        x2[i]=x[i+3]
    x1[3] = 1.
    x2[3] = 1.
    r=dot(transform1 ,x1)-dot(transform2 ,x2)
    return sqrt(sum(r**2))

# The constraints are that x,y,z lies on a unit sphere, centered at (0,0,0)
def con1(x, transform1, transform2):
    return -abs(sum(x[:3]**2)-1)
def con2(x, transform1, transform2):
    return -abs(sum(x[3:]**2)-1)

```

```

#####
#                               MAIN PROGRAM                               #
#####

# Input & output files
infile = open('transform3d.txt', 'r')
lines = infile.readlines()
infile.close()

outfile = open('minspacings.csv', 'w')
outfile2 = writer(open("allspacings.csv", "wb"))

heading = "PPT, Nearest_PPT, Edge-to-Edge_(nm), Nearest_PPT, Cen-to-Cen_(nm)\n"
outfile.writelines(heading)

print heading,

# Allocate arrays
num = len(lines)
transforms = zeros((num/4,4,4),float) # 4x4 3D transformation matrices
spacings = zeros((num/4),float)      # minimum edge-to-edge spacings
allspacings = zeros((num/4),float)   # ALL edge-to-edge spacings
censpacings = zeros((num/4),float)   # minimum center-to-center spacings
# used for initial guess
cen1 = zeros(4,float)
cen2 = zeros(4,float)
p0 = zeros(6,float)

# Fill the array of transformation matrices
i = 0
while i < num:
    for j in range(4):
        elem = split(lines[i+j])
        for k in range(4):

```

```

        transforms[i/4][j][k]=float(elem[k].strip(', '))
    i += 4
print transforms
# Iterate over every ellipsoid
iter = 0
count = 0
for transform1 in transforms:
    minspacing = 1.7E308
    mincenspacing = 1.7E308
    currentpnt = 0
    inv1 = linalg.inv(transform1)
    # Compare it to every other ellipsoid
    for transform2 in transforms:
        if alltrue(transform1 == transform2):
            woot=0
        else:
            # initial guess for two points in untransformed space, p0
            # We use cen-to-cen, which is a better guess than we need
            inv2 = linalg.inv(transform2)
            for i in range(3):
                cen1[i]=transform1[i][3]
                cen2[i]=transform2[i][3]
            centocen=cen2-cen1
            centocen[3]=1.
            dir1 = dot(inv1, centocen)
            point1 = dir1/sqrt(sum(dir1[:3]**2))
            centocen=-centocen
            centocen[3]=1.
            dir2 = dot(inv2, centocen)
            point2 = dir1/sqrt(sum(dir2[:3]**2))

```

```

for i in range(3):
    p0[i]=point1[i]
    p0[i+3]=point2[i]

# Shortest cen-to-cen distance
censpacing = sqrt(sum(centocen[:3]**2))
if (censpacing < mincenspacing):
    mincenspacing = censpacing
    nearestcenppt = currentppt

# Find shortest distance between the two ellipsoids
y = fmin_cobyla(distance, p0, [con1, con2], args=(transform1, transform2),
               rhobeg=1, rhoend=1e-4, iprint=0, maxfun=1e4)
spacing = distance(y, transform1, transform2)
allspacings[currentppt] = spacing
allspacings[iter] = 0
if (spacing < minspacing):
    minspacing = spacing
    nearestppt = currentppt
currentppt += 1
outfile2.writerow(allspacings)
spacings[iter] = minspacing
censpacings[iter] = mincenspacing
data = "%s,%s,%.2f,%s,%.2f\n" % (str(iter), str(nearestppt), spacings[iter],
                               str(nearestcenppt), censpacings[iter])
outfile.writelines(data)
print data,
iter += 1
outfile.close()

```

APPENDIX D

Source Code for Dual-Strengthening Creep Model

This notebook currently calculates the critically resolved shear stress felt by a dislocation due to the lattice and modulus mismatches of the first through fourth nearest neighbor Al_3Sc precipitates (a 3x3 plane of precipitates assumed to be normal to the vector between the 1nn and the closest point on the dislocation and 1 precipitate directly behind the 1nn).

```
In[1] := Remove["*"]
```

Material Properties

```
In[2] := T = 300 + 273.15;
```

$$a_{\text{Al3Sc}} = 4.103 \times 10^{-10};$$

$$r_{\text{barAl3Sc}}[r_] = \sqrt{\frac{2}{3}} r;$$

$$r_{\text{Al3Sc}} = 9.6 \times 10^{-9} \text{ (* Default radius (9.6 nm) [m] *)};$$

```
In[3] := aAl = 4.049 × 10-10 (* Lattice paramter [m] *);
```

$$b_{\text{Al}} = \frac{a_{\text{Al}}}{\sqrt{2}} \text{ (* Length of a Burgers vector (Yes, I know it is 0.286 nm -- this just keeps } a_{\text{Al}} \text{ and } b_{\text{Al}} \text{ consistent) [m] *)};$$

$$G_0 = 25.4 \times 10^9;$$

$$T_m = 933;$$

$$G_{\text{Al}} = G_0 * (1 + -0.5 * ((T - 300)/T_m)); \text{ (* Shear Modulus (25.4 GPa, From Frost & Ashby) [Pa] *)}$$

$$\nu_{\text{Al}} = 0.34;$$

$$L_{\text{Al}} = 1.8 \times 10^{-4} + 2.364 \times 10^{-5} * (T - 300) + 4.164 \times 10^{-9} * (T - 300)^2 + 8.27 \times 10^{-12} * (T - 300)^3;$$

$$\begin{aligned}
\text{In[4]} := \chi_{\text{Al}} &= 100 \times 10^9; \\
\delta_{\text{Al3Sc}} &= \frac{a_{\text{Al3Sc}} * (1 + 1.6 \times 10^{-5} * (T - 300))}{a_{\text{Al}} * (1 + L_{\text{Al}})} - 1; \\
\epsilon_{\text{Al3Sc}} &= \frac{\delta_{\text{Al3Sc}}}{1 + \frac{4 * G_{\text{Al}}}{3 * \chi_{\text{Al}}}} (* - 0.0064 \text{ Constrained Lattice Mismatch} *); \\
f_{\text{Al3Sc}} &= 0.003 (* \text{Volume Fraction (0.0071, from EAM)} *); \\
\lambda_{\text{Al3Sc}}[r_-] &= 2 * r_{\text{barAl3Sc}}[r] * \left(\sqrt{\frac{\pi}{4 * f_{\text{Al3Sc}}}} - 1 \right) (* \text{Inter - precipitate spacing (m)} *); \\
G_{\text{Al3Sc}} &= 68 \times 10^9; \\
\nu_{\text{Al3Sc}} &= 0.2;
\end{aligned}$$

Critically Resolved Shear Stress Equation

We let x =the distance along the dislocation line from the center

y =the distance between a plane of reinforcements and the center of the particle

z =the distance the center of the particle lies above or below the dislocation

r =the radius of the Al_3Sc precipitate.

Nembach (5.41b) gives the resolved shear stress for an edge dislocation due to the lattice mismatch of a particle:

$$\begin{aligned}
\text{In[5]} := \Gamma &= \frac{G_{\text{Al}}}{G_{\text{Al3Sc}}} \\
k_m &= 3 - 4 * \nu_{\text{Al}} \\
k_p &= 3 - 4 * \nu_{\text{Al3Sc}} \\
\alpha &= \frac{\Gamma * (k_m + 1) - (k_p + 1)}{\Gamma * (k_m + 1) + (k_p + 1)} \\
\beta &= \frac{\Gamma * (k_m - 1) - (k_p - 1)}{\Gamma * (k_m + 1) + (k_p + 1)} \\
\text{Energy}[x_-, y_-, z_-, R_-] &= \\
&= \frac{G_{\text{Al}} * b_{\text{Al}}^2}{\pi * (k_m + 1) * (1 - \beta^2)} \left((\alpha + \beta^2) \text{Log} \left[\frac{y^2 + z^2}{y^2 + z^2 - R^2} \right] + (\alpha + \beta^2 - 2(1 + \alpha) * \beta) * \frac{r^2 * y^2}{(y^2 + z^2)^2} - \right. \\
&\quad \left. \frac{1}{2} * (1 + \alpha) * \left(1 - \beta - \frac{(1 - \alpha) * (1 - \beta)}{1 + \alpha - 2\beta} \right) * \frac{r^2 * z^2}{(y^2 + z^2)^2} \right) \\
F[x_-, y, z_-, R_-] &= -r * \partial_y \text{Energy}[x, y, z, R]
\end{aligned}$$

$$\text{In}[6] := \tau_{\epsilon}[x_{-}, y_{-}, z_{-}, r_{-}] = \left(F[x, y, z, R]/b_{Al}/\lambda_{Al3Sc}[R] - \frac{6 * G_{Al} * \epsilon_{Al3Sc} * R^3}{(x^2 + y^2 + z^2)^{\frac{5}{2}}} * y * z \right) * 10^{-6}$$

$$\sigma_{\epsilon}[x_{-}, y_{-}, z_{-}, r_{-}] = \frac{2 * G_{Al} * \epsilon_{Al3Sc} * r^3}{(x^2 + y^2 + z^2)^{\frac{5}{2}}} \begin{pmatrix} (x^2 + y^2 + z^2) - 3 * x^2 & -3 * x * y & -3 * x * z \\ -3 * x * y & (x^2 + y^2 + z^2) - 3 * y^2 & -3 * y * z \\ -3 * x * z & -3 * y * z & (x^2 + y^2 + z^2) - 3 * z^2 \end{pmatrix} * 10^{-6}$$

$$\tau_{\epsilon\text{check}}[x_{-}, y_{-}, z_{-}, r_{-}] = \sigma_{\epsilon}[x, y, z, r][[2, 3]] * \text{Cos}[0] + \sigma_{\epsilon}[x, y, z, r][[2, 3]] * \text{Sin}[0]$$

$$\tau_{\epsilon}[x, y, z, r_{Al3Sc}] == \tau_{\epsilon\text{check}}[x, y, z, r_{Al3Sc}] (* \text{Return true if } \tau_{\epsilon} \text{ is correct} *)$$

$$\text{In}[7] := \tau_{\epsilon_{1nn}}[x_{-}, y_{-}, z_{-}, r_{-}] = \tau_{\epsilon}[x, y, z, r]$$

$$\text{In}[8] := \tau_{\epsilon_{2nn}}[x_{-}, y_{-}, z_{-}, r_{-}] = \tau_{\epsilon}[x + \lambda_{Al3Sc}[r], y, z, r] + \tau_{\epsilon}[x - \lambda_{Al3Sc}[r], y, z, r] + \tau_{\epsilon}[x, y, z + \lambda_{Al3Sc}[r], r] + \tau_{\epsilon}[x, y, z - \lambda_{Al3Sc}[r], r];$$

$$\text{In}[9] := \tau_{\epsilon_{3nn}}[x_{-}, y_{-}, z_{-}, r_{-}] = \tau_{\epsilon}[x, y + \lambda_{Al3Sc}[r], z, r];$$

$$\text{In}[10] := \tau_{\epsilon_{4nn}}[x_{-}, y_{-}, z_{-}, r_{-}] = \tau_{\epsilon}[x + \lambda_{Al3Sc}[r], y, z + \lambda_{Al3Sc}[r], r] + \tau_{\epsilon}[x - \lambda_{Al3Sc}[r], y, z + \lambda_{Al3Sc}[r], r] + \tau_{\epsilon}[x + \lambda_{Al3Sc}[r], y, z - \lambda_{Al3Sc}[r], r] + \tau_{\epsilon}[x - \lambda_{Al3Sc}[r], y, z - \lambda_{Al3Sc}[r], r];$$

$$\text{In}[11] := \tau_{\epsilon_{\text{total}}}[x_{-}, y_{-}, z_{-}, r_{-}] = \tau_{\epsilon_{1nn}}[x, y, z, r] + \tau_{\epsilon_{2nn}}[x, y, z, r] + \tau_{\epsilon_{3nn}}[x, y, z, r] + \tau_{\epsilon_{4nn}}[x, y, z, r];$$

$$\text{In}[12] := \tau_{\epsilon_{\text{average}}}[x_{-}, y_{-}, z_{-}, r_{-}] = \text{Mean}[\text{Table}[\tau_{\epsilon_{\text{total}}}[x, y, z, r], \{x, (-\lambda_{Al3Sc}[r]/2), (\lambda_{Al3Sc}[r]/2), \lambda_{Al3Sc}[r]/100\}]]; \\ \tau_{\epsilon_{\text{back}}}[x_{-}, y_{-}, z_{-}, r_{-}, d_{-}] = 3.06 * \text{Mean}[\text{Table}[\text{Abs}[\tau_{\epsilon_{\text{average}}}[x, (r + d), (r + d) * \text{Tan}[\theta], r]], \{\theta, -\pi/2 + \pi/100, 0 - \pi/100, \pi/100\}]];$$

$$\text{In}[13] :=$$

$$\text{Table}[\tau_{\epsilon_{\text{back}}}[x_{-}, y_{-}, z_{-}, r, b_{Al}], \{r, 1 * 10^{-9}, 35 * 10^{-9}, 5 * 10^{-10}\}] \\ \text{Table}[\tau_{\epsilon_{\text{back}}}[x_{-}, y_{-}, z_{-}, r, 5 * b_{Al}], \{r, 1 * 10^{-9}, 35 * 10^{-9}, 5 * 10^{-10}\}] \\ \text{Table}[\tau_{\epsilon_{\text{back}}}[x_{-}, y_{-}, z_{-}, r, 10 * b_{Al}], \{r, 1 * 10^{-9}, 35 * 10^{-9}, 5 * 10^{-10}\}]$$

APPENDIX E

Computing Facilities of the Northwestern University Center for Atom-Probe Tomography

Because atom-probe tomographic datasets are large and because the Northwestern University Center for Atom-Probe Tomography (NUCAPT) is a user facility with high throughput, the computing facilities that the author helped to setup for NUCAPT are somewhat advanced. The facilities were created to scale to handle not only the larger number of users and larger amounts of data than the Seidman group had used for older generations of atom-probe tomographs, but also to allow future growth of the facility. Fig. E.1 depicts the various computers that are part of the facility. The changes made to the computers provided by Imago as part of the instrument purchase and the workstations purchased separately are discussed briefly. At the heart of the NUCAPT computing facility, the fileserver ARC will then be discussed in more depth.

E.1. Changes to Imago Computers

E.1.1. Archival of LSS Data

The LEAP System Server (LSS) both directly controls and monitors the various subsystems (vacuum, laser, high voltage pulsing system, cryo, motion and control, data acquisition, etc.) of the LEAP. It is networked to the LEAP Client Computer (LCC), but is not directly accessible

E.1.2. Changes to the LCC

The LCC is the intermediary between the user of the LEAP and the LSS. It displays the instrument status and keeps logs of vacuum and temperature conditions. Larger LCD monitors are installed on the NUCAPT LCC to provide more space for charts to be displayed during a run. The LCC is currently a “single-user” machine that is typically left logged in so that log files can be generated. After a run, the RRAW and RHIT data files that the LEAP generates on the LSS are copied to the LCC. The NUCAPT LCC has an additional 500 GB drive that is used to store a larger backlog of RHIT files than the factory default permitted. Read-only access to this data is permitted from computers with a Cook hall IP address. End users will typically read this data on a NUCAPT workstation (section E.2) in IVAS and will generate reconstructions which are saved to the server, ARC.

The LCC also hosts a MySQL database of all LEAP specimens and runs. The factory-installed setup used the root account without a password and allowed network access. NUCAPT’s version has removed remote access from root and requires a password for local root access. A “LEAP” account is allowed to SELECT/UPDATE/INSERT/DELETE rights to the specimen database from any NUCAPT workstation. This allows users to remotely browse and update the specimen database. A third “ARC” account is allowed read-only access to the column that contains the number of good hits for each experiment, which allows a running total to be displayed on the website. Both of these accounts are also password protected, but the passwords are generally shared between NUCAPT users.

There are minor tweaks to the user permissions on the NUCAPT LCC, but the most significant changes are third-party software that has been installed or updated. In addition to Symantec

AntiVirus and the Sunbelt Kerio software firewall, the following free and open source programs are installed:

- 7-ZIP, for data compression and decompression
- AMANDA, for backup of the Documents and Settings folder, the database backups, the log files, and the INI (settings) files for the Imago software
- FILEZILLA, for file transfers
- PUTTY, for remote SSH access to ARC

E.2. Workstations

NUCAPT's workstations are listed in black in Fig. E.1. The Macintosh machines were purchased from Apple, the AMD machines from Monarch, and the Intel machine from Dell. Processors and system RAM are listed. Each workstation has a high performance NVIDIA graphics card with 256 MB of video RAM (GeForce 6800 GT or Quadro FX 3000, depending on the workstation). The Windows machines are on the NUCAPT Windows domain (run by the server, ARC, using samba), which allows users to login with the same username/password to any workstation and to see their same data (which is kept on ARC). The machines have small hard disks, as all user data is stored on the server. However, the "Documents and Settings" directory is still backed up via AMANDA for redundancy. These machines are chiefly used to run IVAS, but they also have a variety of third-party software. In addition to the utilities installed on the LCC (Section E.1.2), they have:

- ABIWORD, a lightweight word processor
- CYGWIN, a Linux-like environment

- ENTHON, a distribution of the PYTHON programming language with scientific libraries (for interprecipitate analysis and other methods developed at NUCAPT)
- GIMP, a bitmap graphics editor
- GNUMERIC, a lightweight spreadsheet
- INKSCAPE, a vector graphics editor
- MOZILLA FIREFOX, a web browser
- MOZILLA SUNBIRD, for scheduling instrument time
- MOZILLA THUNDERBIRD, an email client
- OPENOFFICE.ORG, an office suite
- VIM, a text editor

and other software. Two of the workstations have ULTRAVNC, which allows NUCAPT users to access the machines from anywhere in the world and perform data analysis.

The Macintosh workstations are not currently part of the domain, so separate accounts are currently needed. OS X does allow LDAP authentication, so this annoyance could be addressed if they were to see heavier usage.

E.3. Server

E.3.1. Server System

The main NUCAPT server was purchased from eRacks, but it has had a number of hardware upgrades (including the addition of a second RAID array and tape backup drives). It runs FREEBSD 6.2 [237–239] and can be administered both locally and via SSH [240, 241] (and, for some applications, via the web). A majority of applications have been installed from

the `PORTS` system and the configuration files are in `/usr/local/etc`. Prior to software installation and updates from `PORTS`, the admin should issue the command `cd /usr/ports && sudo make update`. After this command completes, `PORTINSTALL` may be used to install a new package and `portupgrade -i aRr` will interactively (asking the admin if they want to upgrade each package) upgrade all installed packages and their recursive dependencies. While `MONIT` attempts to maintain uptime for the various service daemons, upgrading may cause temporary outages (and some upgrades may require programs that depend on them to also be upgraded or for configuration files to be updated, potentially extending downtime). Because of this, upgrades should be done only during scheduled maintenance, when the change is to an application that will not impact the daemons, or when there are known vulnerabilities in the package. The command `portaudit` may be used to check for vulnerabilities. If there are vulnerable packages, they may be upgraded by the command `portupgrade -iRr packagename`

The root user gets emailed security reports. This should be checked periodically:

- `sudo su`
- `setenv MAIL /var/mail/root`
- `mutt`

E.3.2. User Accounts: Lightweight Directory Access Protocol, Windows Domain and File Sharing, SSH/SFTP, and Logging

`OPENLDAP` is an implementation of the Lightweight Directory Access Protocol (LDAP). This stores the account information (including the username, password, group membership,

home directory, and shell) of NUCAPT users. This information is used for logins into the Windows workstations that are part of the NUCAPT Windows domain, SFTP access, and calendar modifications.

SAMBA [242] is used for SMB (Windows file sharing) and to control the NUCAPT domain. To add a new user (typically someone who has been freshly trained to use the LEAP tomograph) to the NUCAPT domain, the customized `sudo smbldap-adduser` script may be used. This script will ask for and store values for a username, password (or it may auto-generate a password), full name, and CUPS account number. It will automatically run the standard `smbldap-useradd` script to setup the user's account. There are also `smbldap` scripts to perform other user or group tasks (add, del, mod, show). To change a user's password, issue the command `sudo smbldap-passwd [username]`. To add a workstation to the NUCAPT domain, `sudo smbldap-useradd -w [machinename]` is used. This script requires no other input, but to modify or delete the account, a `$` must be appended to the machine name. On the workstation that is to be added to the Windows domain, the System Properties may be accessed from right-clicking on My Computer or by using the Control Panel. The Computer Name tab will allow the workstation name to be set to the `machinename` that was used in `SMLDAP-USERADD` and the domain name may be set to NUCAPT. Windows will prompt for the username and password of a domain administrator. When the workstation is rebooted, it will join the NUCAPT domain.

OPENSSH provides secure shell (SSH) and secure file transfer (SFTP). NUCAPT users have the `RSSH` shell by default. This means that they cannot obtain an interactive shell, and are only able to use SFTP services. This allows them to upload files to or download files from NUCAPT from anywhere in the world. Certain users have the `bash` shell so that they may

use `RSYNC` or `SUBVERSION` [243] (such users might eventually be migrated to the `SCPONLY` shell, or to obtain an interactive shell for administrative purposes.

E.3.2.1. Server Storage. ARC currently has two RAID-5 arrays, mounted as `/u1` (1.3 TB capacity, which is used for the user profiles (the Documents and Settings folder in Windows) and for archives) and `/u2` (2.6 TB capacity, which is used for the “public” share and for user directories). Under `/u2` are directories for the letters a–z and under these are the user directories. A user directory may contain `AnalyzedData` (a legacy from older versions of `IVAS` and `ROOT`), `screenshots`, `temp` (which some `IVAS` scripts still expect to find), `incoming`, and `outgoing` directories, in addition to files and directories added by the user. To allow `userone` to upload files to `usertwo`, an admin may execute the commands:

- `cd /u2/u/usertwo/`
- `sudo mkdir -p incoming/userone`
- `sudo chown userone:Domain\ Users incoming/userone`
- `sudo chmod 770 incoming/userone/`
- `sudo ln -s /u2/u/usertwo/incoming/userone \`
`/u2/u/userone/outgoing/usertwo`

Additionally, a user may post something to the web by placing it in their `~/outgoing/www` directory. The content will be available under `http://arc.nucapt.northwestern.edu/~username`.

E.3.2.2. Usage Tracking. Users are billed for use of NUCAPT workstations. The PC usage tracking is automated. When a user logs in to a NUCAPT workstation, `/u2/public` is automatically mounted. When they logout, it is unmounted. These transactions are recorded in `SAMBA`’s logs. On the first of each month, custom scripts (`SAMBA_BILL.[PY|SH]`) create and

email a list with workstation usage by user, rounded in 0.25 h increments and a spreadsheet with a more detailed usage report.

E.3.3. Reliability and Backup

The RAID-5 arrays in ARC allow a single drive to fail and be replaced before data loss occurs. 3DM2 monitors the original RAID array (mounted as /u1) and will email the administrator when there are problems. The second RAID array is self-monitored and will automatically swap in a hot spare drive. Promise WEBPAM is used to monitor the new RAID (mounted as /u2). This software is currently running on the AP-FIM PC. ARC does not use it because there were issues getting the array detected in the FREEBSD version of WEBPAM. The second RAID array and the AP-FIM PC are plugged into a personal router, so that the array is not visible to the external network. The health of the boot drive, all drives in the original RAID array, and many of the workstations have their health monitored by SMARTMONTTOOLS.

AMANDA (the Advanced Maryland Automatic Network Disk Archiver) is used to backup the server and selected directories on networked clients to an Overland Storage ARCvault24 tape drive. The client software may be installed on other workstations and the disklist on ARC (/etc/amanda/ARCvault24/disklist) may be updated to add more clients in the future. AMRECOVER is used to easily recover files using an index that lists files, backup dates, and the tape that they are on. A typical session looks like:

- `$ sudo amrecover -C ARCvault24 \`
- `-s arc.nucapt.northwestern.edu -t arc.nucapt.northwestern.edu`
- `amrecover> sethost arc.nucapt.northwestern.edu`

- `amrecover> setdisk /u1/karnesky`
- `amrecover> add file_or_directory_to_recover`
- `amrecover> extract`

If `amrecover` has difficulties, whole backup images may be restored using `AMRESTORE`. Finally, the archive formats are standard `TAR` archives which can be manually decompressed. A Dell PowerVault 122T had initially been used for backups, but was replaced with the higher capacity (in terms of both number of tapes in a carousel and the size of a tape) `ARCvault24`. This drive is now used for the longterm archival of data (such as all data from former group members and `RHIT` and `RRAW` data). `SCREEN` is used to start a session that is persistent to disconnection. The tape might be loaded manually or with the `MTX` program that interacts with the tape changer. The program `MT` can directly interact with the tape loaded into the read/write tape drive slot of the changer:

- `mt -f /dev/nsa1 rewind`
- `mt -f /dev/nsa1 erase`
- `mt -f /dev/nsa1 rewind`

Finally, `GNU TAR` is used to archive files:

- `cd /DIRECTORYTOARCHIVE`
- `gtar -cvpf /dev/nsa1 -label="archive-2007-01_1: LSS:2006-04" .`

Some users have laptops and other machines that can not be backed up at night with the standard `AMANDA` cronjob, as they cannot be contactec by `ARC` during the default backup time. A majority of these clients use `RSYNC` to backup a selection of files to their user directory

on ARC during the daytime when they have network access. This usage of disk space on ARC and the requirement of the user having a shell that can execute `rsync` might be disadvantages that must be weighed against advantages of `RSYNC`, including the ability for clients to push backups to ARC whenever they wish and the easier firewall and port forwarding setup on the client than AMANDA. The users data is additionally backed up to tape when their user directory on ARC is backed up by AMANDA.

The boot drive in ARC is not in a RAID system. It is backed up by AMANDA, but a disk image and a cloned drive are useful to quickly bring it back up online. A disk image is stored on `/u1/archive/`, but new images can be created using `DCFLDD` periodically to stay up-to-date. To create a space-efficient image, `BZIP2` compression is used. It works best when the slack space has been overwritten with zeros using the command `dd if=/dev/zero > /tmp/zero && rm /tmp/zero`. The image may then be created using the command `dclfd if=/dev/ad0 | bzip2 > /u1/archive/ARC_boot_date.bz2`. The image may be copied to another machine with `DCFLDD` (or any program that can read `DD` images) and put onto a new hard drive using the command `bzip2 -cd ARC_boot_date.bz2 | dclfd of=/dev/new_harddrive`.

E.3.4. Web Site

The NUCAPT website is hosted on the `APACHE HTTP SERVER`. The web-based applications utilize the `MYSQL` [244–249] database software and are largely written in `PHP`. The site was designed to be editable by any member of the Seidman group and some other users of NUCAPT. Many pages are kept in `MEDIAWIKI`, the same software that hosts Wikipedia. This

was patched to offer a custom navigation menu and to allow for page access restriction (to disallow reading of sensitive pages (such as comments on Imago's software) by users who are not logged in). Extensions to MediaWiki (located in the `extensions` subdirectory and called by `LocalSettings.php` within the MediaWiki installation directory) allow the use of RSS feeds (to track APEX news), Google Maps, CAPTCHA (completely automated public Turing test to tell computers and humans apart) to prevent spam URLs from being added to talk pages, special permissions for talk pages, citation generation, and the display of a count of all "good hits" collected by the LEAP tomograph. MEDIAWIKI accounts are separate from other accounts on NUCAPT and are added by any of the several wiki administrators. An account is required to edit pages and to view restricted pages. No account is needed to view unrestricted pages or to edit talk pages. Because anonymous edits are allowed to talk pages, recent changes should be monitored (via RSS or some other means).

E.3.5. Literature Database

I am one of the lead developers of REFBASE, a literature database. This allows the use storage and retrieval of both citation metadata and copies of references. References may be exported to desktop reference management software and the use of bibliographic standards allow it to gracefully interact with third-party tools such as LIBX and ZOTERO. Citations can be automatically imported from a number of formats. There are two copies of REFBASE installed. One is publicly readable, but requires an account to add or edit records. It tracks the latest stable release of REFBASE and provides a large database that is easily readable by anyone. The second copy allows for anonymous submissions, but is kept to a small number of references which are less easy to be read by others. This allows a low barrier for useful submissions

to the database, but prevents spam from impacting the larger database. The records in the second installation of rebase are manually reviewed by someone who has write access to the public copy of REFBASE. This second copy of REFBASE is also a testbed for a future version, as it tracks the “bleeding-edge” SUBVERSION branch. REFBASE user accounts are different from all other user accounts. Record adds may be monitored by email and/or RSS.

E.3.6. Other Web Services

E.3.6.1. Time Sheets. TIMESHEET.PHP has been occasionally used to log the time spent assisting external users. As the facility manager now handles most of this assistance himself, it has not been used since October 2006. If it continues to go unused, it should be uninstalled (an alternative means for reporting billable hours to the facility manager might also need to be implemented).

E.3.6.2. Statistics of Web Site Access. AWSTATS is used to track the usage of the website. It can be accessed from 129.105.37.xxx IP addresses. Hosts within this range are also ignored for statistical purposes (so that the numbers are not artificially inflated by the internal use of the site).

E.3.6.3. Reserving Facility Instrument Time. The system to schedule instrument time and group meetings is also web-based. The calendar files utilize the iCalendar format and can be changed by authenticated users with LDAP accounts using MOZILLA SUNBIRD or other calendaring software that supports WebDAV. Changes to the files are committed to a SUBVERSION repository. Mistakes can therefore be reverted by any NUCAPT user with a copy of SUBVERSION (although patience and a text editor are also useful). Each day, a PYTHON

script archives events that are over four weeks old to an archive calendar that is also kept in version control. This keeps the working calendar files small (so fast to retrieve and edit), but retains a log of all scheduled usage. The web-based PHP iCALENDAR is used to look at the schedule without special software, but cannot yet be used to edit the schedule.

E.3.7. Mailing Lists

MAILMAN is used to maintain mailing lists. There are private lists for the Dunand and Seidman groups, the AI subgroup, NUCAPT users, and the second copy of REFBASE. There are public lists for the main copy of REFBASE and for a general atom probe tomography mailing list (although the archives of the latter are kept private to list members). The [HT://DIG](http://DIG) search engine can be used to search the list archives from the NUCAPT website.

APPENDIX F

Colophon

This manuscript was typeset by using \LaTeX (specifically \TeX LIVE 2007) with a number of extension packages. The thesis template was authored by Miguel Lerma, in Northwestern's Math Department.

The text body is Bitstream Charter. Greek and Mathematical symbols use the Math Design fonts.

Most graphs were prepared using GRACE, although some were prepared using MATPLOTLIB and PYTHON. Most atom probe visualizations were generated in IVAS, but some were prepared in APEX. GIMP and INKSCAPE were used for bitmap and vector graphics (respectively).

RICHARD ALBERT KARNESKY, JR.

Dept. of Materials Science and Engineering
Northwestern University
2220 Campus Drive
Evanston, IL 60208

<http://nucapt.northwestern.edu/karnesky>
e-mail: karnesky@gmail.com
phone: (847) 491-3575
fax: (847) 467-2269

EDUCATION

- Northwestern University** — Evanston, IL Sep 2002 – Oct 2007
Doctor of Philosophy, Materials Science and Engineering
Mechanical Properties and Microstructure of Al-Sc with Rare-Earth Element and Al₂O₃ Additions
Advisors: Profs. David C. Dunand David N. Seidman
- California Institute of Technology** — Pasadena, CA Sep 1998 – Jun 2002
Bachelor of Science, Engineering and Applied Science
Advisor: Prof. Ersan Üstündag

RESEARCH EXPERIENCE

- Postdoctoral Scholar, Sandia National Laboratory** — Livermore, CA Oct 2007 – Present
- Ph.D. Candidate, Northwestern University** — Evanston, IL Sep 2002 – Oct 2007
- Utilized atom-probe tomography (APT) and transmission electron microscopy (TEM) to measure the composition and morphology of nanometer-scale precipitates in Al-Sc-RE.
 - Measured the elevated temperature creep and the ambient temperature strength (yield stress and microhardness) of alloys.
 - Correlated microscopic information with mechanical properties through computer models.
- Research Assistant, California Institute of Technology** — Pasadena, CA Jan 2000 – Sep 2002
- Programmed the *SMARTS Expert System* to assist in neutron diffraction experiments.
 - Studied beam divergence of the SMARTS neutron diffractometer.
 - Assisted in collection and analysis of neutron diffraction data for residual stresses.
- Research Assistant, LIGO** — Hanford, WA Jun 1999 – Sep 1999
- Formulated optimal epoxy bonding techniques to couple magnets and standoffs to test masses used in the high vacuum Laser Interferometer Gravitational Wave Observatories.

ACHIEVEMENTS AND AWARDS

- Winner of the John E. Hilliard Symposium (Northwestern University, 2007)
- Walter P. Murphy Graduate Fellowship (Northwestern University, 2002–2007)
- TMS Travel Award (2005)
- HREM Winter School Travel Award (Arizona State University, 2005)
- Director of Residence Life and Master of Student Houses Award (Caltech, 2002)
- Ricketts House President (Caltech, 2001–2002)

PUBLICATIONS

1. R. A. Karnesky, D. Isheim, D. N. Seidman. "Direct Measurement of 2-Dimensional and 3-Dimensional Interprecipitate Distance Distributions from Atom-Probe Tomographic Reconstructions" *Appl Phys Lett*, **91**(1), 013111:1–3 (2007)
2. R. A. Karnesky, C. K. Sudbrack, D. N. Seidman. "Best-Fit Ellipsoids of Atom-Probe Tomographic Data to Study Coalescence of γ' ($L1_2$) Precipitates in Ni–Al–Cr" *Scripta Mater*, **57**(4), 353–356 (2007)
3. R. A. Karnesky, L. Meng, D. C. Dunand. "Strengthening Mechanisms in Aluminum Containing Coherent Al_3Sc Precipitates and Incoherent Al_2O_3 Dispersoids" *Acta Mater*, **55**(4), 1299–1308 (2007)
4. R. A. Karnesky, M. E. van Dalen, D. C. Dunand, D. N. Seidman. "Effects of Substituting Rare-Earth Elements for Scandium in a Precipitation-Strengthened Al 0.08 at.% Sc Alloy" *Scripta Mater*, **55**(5), 437–440 (2006)
5. R. A. Karnesky, D. N. Seidman, D. C. Dunand. "Creep of Al-Sc Microalloys with Rare-Earth Element Additions" *Mat Sci Forum*, **519-521**, 1035–1040 (2006).
6. E. Üstündag, R. A. Karnesky, M. R. Daymond, I. C. Noyan. "Dynamical Diffraction Peak Splitting in Time-Of-Flight Neutron Diffraction" *Appl Phys Lett*, **89**(23), 233515 (2006)
7. R. A. Karnesky, G. Martin, D. N. Seidman. "Time to Achieve a Steady State in the Stationary State" *Scripta Mater*, In preparation, (2007)
8. R. A. Karnesky, D. C. Dunand. "Mechanical Properties of Al–Sc with Rare-Earth Element Additions at Ambient and Elevated Temperature", In preparation, (2007)
9. R. A. Karnesky, D. N. Seidman. "Precipitate Coarsening in Al–Sc–Er Alloys", In preparation, (2007)
10. R. A. Karnesky, V. Mohles, D. N. Seidman, D. C. Dunand. "Precipitation Strengthening in Al–0.09% Sc–0.03% Er: Experiments and Simulations", In preparation, (2008)
11. R. A. Karnesky, K. E. Knipling, D. C. Dunand, D. N. Seidman. "Precipitate Strengthening Model for Al–Zr–Sc Using Experimentally Determined Microstructures", In preparation, (2008)

PRESENTATIONS

1. R. A. Karnesky, D. N. Seidman, D. C. Dunand
"Nanostructural Evolution and Creep of Al-Sc Microalloys with Rare-Earth Additions"
International Conference on Aluminum Alloys, 2006 (Vancouver).
2. R. A. Karnesky, D. C. Dunand
"Creep Model for Alloys Strengthened with Fine Coherent Precipitates and Coarse Incoherent Dispersoids"
TMS Materials Science & Technology, 2005 (Pittsburgh).
3. R. A. Karnesky, L. Meng, D. N. Seidman, D. C. Dunand
"Mechanical Properties of a Heat-Treatable Al-Sc Alloy Reinforced with Al_2O_3 "
TMS Materials Science & Technology, 2003 (Chicago).
4. D. C. Dunand, M. E. van Dalen, R. A. Karnesky, D. N. Seidman
"Temporal Evolution of Microstructure and Mechanical Properties in Al Strengthened with Sc, Er and Yb"
MRS, 2006 (Boston).
5. D. N. Seidman, M. E. van Dalen, R. A. Karnesky, D. C. Dunand
"Rare-Earth Additions to Al-Sc Alloys for Creep-Resistance above 300"
TMS Materials Science & Technology, 2005 (Pittsburgh).
6. E. Üstündag, R. A. Karnesky, I. C. Noyan, M. A. M. Bourke, D. W. Brown
"Effect of Beam Divergence on Strain Data from Neutron Diffraction"
Denver X-Ray Conference, 2002 (Denver).